Head Office: Università degli Studi di Padova

Department of Chemical Sciences

Ph.D. COURSE IN: Science and Engineering of Materials and Nanostructures
SERIES: XXXIV

Synthesis and Applications in Electrocatalysis of 3D Multifunctional Carbon Architectures

Coordinator: Ch.mo Prof. Giovanni Mattei
Supervisor: Ch.mo Prof. Stefano Agnoli

Ph.D. student : Jiajia Ran

Contents

List of acronyms and abbreviations

2D	Two-Dimensional
3D	Three-Dimensional
ATM	Ammonium tetrathiomolybdate
BE	Binding Energy
BET	Brunauer Emmett Teller
BJH	Barrett Joyner Halenda
BSE	Backscattered Electrons
CE	Counter electrode
CNT	Carbon nanotube
CP	Chronopotentiometry
CV	Cyclic Voltammetry
CVD	Chemical vapor deposition
DMF	N,N-dimethylformamide
EC	Electrochemical
EDX	Energy dispersive X-ray spectroscopy
EIS	Electrochemical Impedance Spectroscopy
FE-SEM	Field-Emission Scanning Electron Microscopy
G	Graphene
GAs	Graphene aerogels
GC	Glassy carbo
GCE	Glassy carbon electrode
GO	Graphene Oxide
GOAMs	Graphene Oxide Aerogel Microspheres
HER	Hydrogen Evolution Reaction
LDH	Layered Double Hydroxide
LSV	Linear Sweep Voltammetry
NPs	Nano Particles
NR	Nanorings
OER	Oxygen Evolution Reaction
ORR	Oxygen reduction reaction
PEC	Photoelectron catalytic
prGOAMs	Partial reduced-Graphene Oxide Aerogel Microspheres
rGO	Reduced GO

RHE	Reversible Hydrogen Electrode
SCE	Standard Calomel Electrode
SE	Secondary Electrons
SEM	Scanning Electron Microscopy
STEM	Scanning Transmission Electron Microscopy
TEM	Transmission Electron Microscopy
TEM	Transmission Electron Microscopy
TMDC	Transition metals dichalcogenide
WE	Working electrode
WS	Water splitting
XAFS	X-Ray Absorption Fine Structure
XPS	X-Ray Photoemission Spectroscopy
XRD	X-Ray Diffraction
η_{10}	Overpotentials at 10 $mAcm^{-2}$

Abstract

In this thesis, I have been focusing on the investigation of 3D graphene aerogel nanoarchitectures to be used as advanced supports for heterogeneous catalysis. The combination of 3D graphene nanostructures with noble-metal-free electrocatalysts materials can produce systems with a large surface area, but also provide an architecture with tailored porosity, offering an efficient interaction with the electrolyte, which requires a combination of micro- and meso-porosity. Moreover, the crosslink within the 3D graphene network can avert the degradation of the catalytic performance caused by the re-stacking of graphene sheets or the coarsening of the hosted active phases. In this work, I have exploited a combined technique for the preparation of 3D graphene aerogels: electrospraying and freeze casting. Both steps are extremely cheap and quick, very suitable for a fast and continuous production (e.g. hundreds of mg per hour of material produced with lab scale equipment). Nonetheless, these extreme high productivity and cost effectiveness do not come at the expenses of materials properties: a mesoporous hierarchical morphology perfectly suited for the interactions with electrolyte can be easily realized and also the atomic composition can be tuned with high flexibility, resulting in the synthesis of complex nanocomposites designed at multiple scales.

The thesis is divided in four main chapters.

Chapter 1 is an introduction and summary of the preparation and application of 3D graphene aerogel composite materials, and explains its application scope and collocation within the broader context of modern catalysis. In addition, it also provides some basic information about the materials studied and the basic principles behind their design. Moreover, GOAMs with well-controlled morphologies and highly ordered structures will be introduced, display a quite unique center-diverging microchannel *dandelion-like* structure.

In Chapter 2, we investigated the preparation of innovative hybrid electrocatalysts coupling TMDCs nanosheets with GOAMs (TMDC/GOAM) by electrospray and freeze casting techniques. The aim is to prove that it is possible to integrate into the GOAM graphene network the functional properties of active electrocatalysts without altering the microchannel central divergence morphology. The procedure of incorporation has been optimized using exfoliated $MoSe_2$, and subsequently it was successfully extended to other exfoliated TMDCs, i.e., MoS_2, WS_2 and WSe_2. The aim was to create a hybrid material where electronic contacts among the two pristine materials are established in a 3D architecture, to test any improvement in the HER activity while maintaining accessible the TMDC catalytic sites. The final materials were used to prepare an electrode suitable for the HER characterization. Interestingly,

the adopted approach, based on combining electrospraying with freeze-casting techniques, successfully, provides stable electrodes where the *dandelion-like* structure is retained. After a heat treatment, the scaffold transform into a partially reduced one (prGOAM) which increases the mechanical stability of the assembly while maintaining the same 3D structure. The actual HER tests on TMDC/prGOAMs display an interesting improvement of the HER activity in an acidic environment compared to the pristine TMDC, confirming a kind of synergetic interaction between the TMDC catalyst and the scaffold. Moreover, the comparison of the HER results of TMDC/prGOAM modified electrodes with those obtained from TMDC/prGO and TMDC/Vulcan analogous hybrid materials (benchmark samples) allowed us to demonstrate the role of the 3D architecture in the catalytic HER performance. More interestingly, this 3D architecture is also preserved after the electrochemical tests. The hybrid electrocatalysts were also HER verified under light in PEC tests displaying interesting results.

In Chapter 3, we made a step forward and propose a synthesis strategy to control not only the morphology of the nanocomposite, but also the chemistry of the active phase. To achieve this goal, we envisaged a *fully* bottom-up approach for preparing the MoS_2 phase decorating the 3D GOAM scaffold, which is based on a molecular precursor, e.g. ATM, ($(NH_4)_2MoS_4$). The advantages of this approach to prepare the hybrid MoS_2/prGOAM materials are: i) fine and homogeneous dispersion of MoS_2 on the graphenic support, ii) higher scalability of the preparation procedure, and shorter preparation time since there is no need to prepare the TMDC by a lengthy and expensive exfoliation procedure, iii) possibility to introduce a large variety of dopants into the MoS_2 moiety. The resulting materials with both tailored morphology and chemistry demonstrated to be outstanding catalyst for the HER, superior to previous top-down MoS_2 (in Chapter 2) based catalysts. The as-prepared catalysts were evaluated by structural characterization covering characterized by SEM, EDX, BET, XRD, Raman and XPS.

In Chapter 4, in order to study the general applicability of our materials, we have studied the development of a heterostructure constructed by CoAl-LDH NR supported on GOAMs as a highly efficient electrocatalyst for water oxidation. The presence of negatively charged GOAMs can play an import role in supporting and dispersing positively charged CoAl-LDH NR. The as-prepared electrocatalyst, denoted as CoAl-LDH NR/GOAMs, inherits the special centre-diverging microchannel 3D structure from GOAMs, with numerous CoAl-LDH NR decorating quite homogeneously the GO surface. As a result, the CoAl-LDH NR/prGOAMs (treated in oven at 200 ℃ in inert atmosphere) exhibit a remarkable electrocatalytic activity in the OER, which is attributed both to the peculiar centre-diverging mesoporous structure of the carbon scaffold, which allows an easy access to the active sites and an optimal mass transport, and to the presence of many catalytically active sites associated with the nanorings.

The general conclusions and perspectives of this work are summarized in Chapter 5.

Chapter 1

Introduction

1. Introduction

With fast growth of the global population and the massive combustion of fossil fuels, several efforts have been devoted to develop clean and renewable energies, such as solar and wind energy. However, their power output is intermittent and fluctuant, easily influenced by the climate and location, which impede their massive permeate to the modern grid system.[1–4] In addition, to manage the issue of the greenhouse effect, new energy carriers with low carbon emission have been intensively studied. Catalytic water splitting to generate hydrogen as a fuel has been considered as the sustainable and remarkable approach to offer a promising strategy and has already captured a primary place in the scientific community.[5 – 7] For an efficient water splitting the electrochemical route is the most promising one. The two electrodic reactions are the cathodic HER and the anodic OER, but to reduce the energy requirements by minimizing the required overpotential, highly efficient electrocatalysts are needed.[8] Currently, noble metals (such as Pt, Ir, Ru) at the catode and their oxides (IrO_2, RuO_2) at the anode represent the best electrocatalysts for HER and OER.[9,10] Nevertheless, the high cost and scarcity of these noble metal-based catalysts impact on their large-scale commercial applications.[9] To replace these noble metal-based electrocatalysts, designing durable, efficient and economically desirable non-noble metal-based electrocatalysts for complete water splitting is thereby highly demanded.

Besides catalytic active materials, a porous support is also an important component of the electrodes. Owing to gas bubbles adhering to catalyst surfaces, gaseous electrodes run actually on the solid-liquid-gas phase interface, where the triple pathways of electron, ion, and gas are necessary.[11-13] To this end, 3D electrodes have attracted considerable attentions due to high specific surface area and the resulting high loading capacity of active materials.[14-17] A suitable 3D porous support/substrate/collector is vital for boosting practicable catalytic electrolysis towards industry. Currently, water splitting is carried out mainly using catalyst-loaded macroporous supports, e.g. nickel/titanium foams [18,19] and carbon cloths/papers.[20] The selectable supports are rather limited and urgent to be extended.

Graphene, a 2D monolayer sheet of sp^2-bonded carbon atoms arranged in a honeycomb lattice, has attracted increasing attention in recent years mainly due to its extraordinary electrical and thermal conductivities,[21,22] huge mechanical strength,[23] large specific surface area,[24] and potentially low manufacturing cost.[25] In particular, graphene and graphene-based composites have been widely studied as promising materials for several devices, e.g. for chemical adsorption,[26,27] energy storage,[28–30] batteries,[31,32] and sensors.[33,34] In these studies, graphene can play the role of enhancer of the conductivity or can act itself as an electroactive center. Usually, for applied materials in each of the above applications, large surface area and fast electrolyte transport are required, in order to obtain high reaction rate and good performances. However, the graphene sheets on the electrode usually aggregate in a layer-by-layer fashion because of their strong π-π interaction, forming compact films and so reducing the effective surface area. Therefore, graphene and graphene based composite materials possessing 3D porous architectures hold great potential as high-performance electrodes due to their distinct advantages of high specific surface area, high conductivity, excellent thermal and chemical stability, good biocompatibility, and abundant functional sites (e.g., absorption and/or activation sites).[35–37]

3D GAs assembled by 2D graphene sheets have ultra-high porosity and large specific surface area. Many studies have reported the use of GAs for energy storage. Yang et al. prepared GAs for energy storage materials with stable shapes.[38] Zhong et al. studied the excellent performance of GAs in energy management.[39] Dong,[40] Yang,[41] Xu,[42] and Wang [43] et al. studied the application of GAs in thermal energy storage and energy management through different preparation and research methods.

In order to get the utmost out of high specific surface area and porous structure of graphene aerogel, Liao et al. [44] investigated GOAMs with well-controlled morphologies and highly ordered structures. The GOAMs display a quite unique "center-diverging microchannel" *dandelion-like* structures which eventually enhance the electrocatalytic performance and improving an effective dispersion of an active phase. Therefore, combining the GOAMs with other materials to prepare aerogel microsphere hybrids can not only broaden the applications of graphene materials, but also open up potential applications for aerogels.

In the following, the general methods to prepare 3D graphene composite materials will be first reported. In the second part of this chapter, the peculiar GOAMs materials will be addressed, being them the core of this thesis.

1.1 Preparation and application of 3D graphene composite materials

The combination of 3D graphene oxide and other materials such as polymers, [45] metal oxides, [46–48] two-dimensional transition metal carbides or nitrides, [49,50] 2D transition metal sulfides, [51,52] has attracted wide attention from researchers and the application fields have been continuously expanding.

GO composites can be readily fabricated into 3D interconnecting networks by one of the following methods: hydrothermal assembly,[53] organic sol-gel method,[54] templating method [55] and 3D printing technology [56] to improve the mechanical and thermal stabilities.

The many efforts that have been made in order to prepare 3D graphene composite materials is justified by their peculiar properties, e.g. low density, good electrical and thermal conductivity and high surface area, which make them versatile materials in many applications such as energy storage, catalysis and adsorption.

1.1.1 Hydrothermal-assembly method

Hydrothermal-assembly has been recognized for a long time as one of the most effective strategies for "bottom-up" nanotechnology. This technique is based on the use of aqueous solutions at pressure and temperature higher than ambient. Given its unique 2D structure and outstanding properties, graphene is naturally a versatile nanoscale building block for self-assembly. Mixed hydrogels of rGO and other materials are first prepared, and then hybrid aerogels are obtained by freeze drying or supercritical drying.

Ma et al. [57] have developed Fe_3O_4 decorated rGO nanospheres (Fe_3O_4-NS/rGO) via a facile one-pot solvothermal synthetic method, as shown in Figure 1.1, which were employed in anode bio-electrocatalysts of microbial fuel cells. The Fe_3O_4-NS/rGO anode at the optimized ratio (1.5:1) yields the maximum power density 1837.4 mW/m^2 at the scan rate of 1 mV/s, which is much higher compared to other literature anodes.

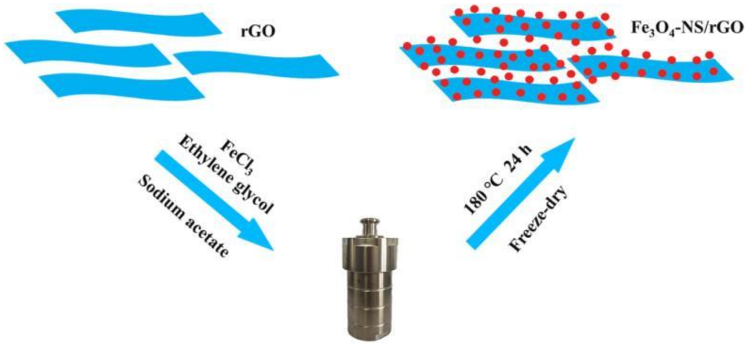

Figure 1.1 Schematic illustration for the preparation and formation of Fe_3O_4-NS/rGO composites.[57]

Narugopal et al. [58] have synthesized a nitrogen-doped entangled graphene framework, decorated with mixed NiFe-LDH nanostructures by an *in situ* solvothermal procedure followed by freeze-drying at high vacuum and low temperature. The freeze-drying procedure contributed to prevent the restacking of the GO sheets and to form a high surface area nitrogen-doped graphene scaffold where the NiFe-LDHs were homogeneously dispersed, as shown in Figure 1.2. The prepared material showed a high specific surface area (547m^{2}g^{-1}) and an excellent OER performance (the overpotential was 290 mV at the current density of 10 mAcm^{-2}, and the Tafel slope was 68 mV/Dec).

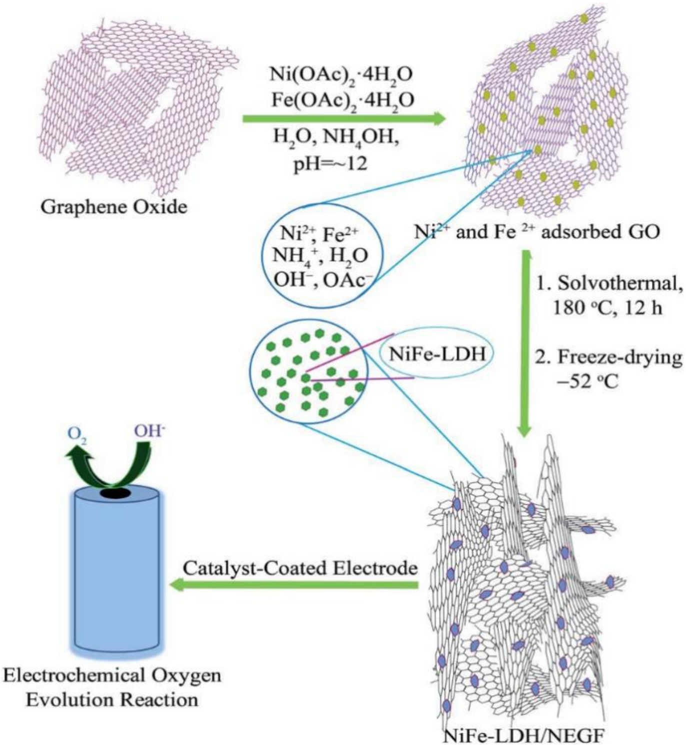

Figure 1.2 Schematic representation of the synthesis of the NiFe-LDH-anchored N-doped 3D entangled GO framework (NiFe-LDH/NEGF) and its application as an efficient OER electrocatalyst.[58]

Ren et al [59] reported a low-cost method for fabricating 3D free-standing nickel nanoparticle/GA composite materials prepared through a one-pot hydrothermal synthesis: the graphene sheets were assembled into the GA while the nickel ion were reduced forming metallic nanoparticles on the carbon scaffold. The final product could be applied in ethanol fuel cells, and it showed a high peak current density at 6 mA cm^{-2} for ethanol oxidation under the test conditions (i.e. 0.1 M ethanol in 0.1 M NaOH solution).[59] The final material involves three important peculiarities: firstly, the Ni nanoparticles which have good catalytic activity for ethanol electro-oxidation; secondly, the high electrical conductivity that ensures high current loads, and thirdly, the 3D porous network which enables maximum accessibility for active species to the catalysts and enhances the mass transfer of reactants. In Figure 1.3 a photo of the 3D aerogel is presented, which shows the shape and dimensions of the material (a diameter of about 20 mm), which is floating in water and magnetically active.

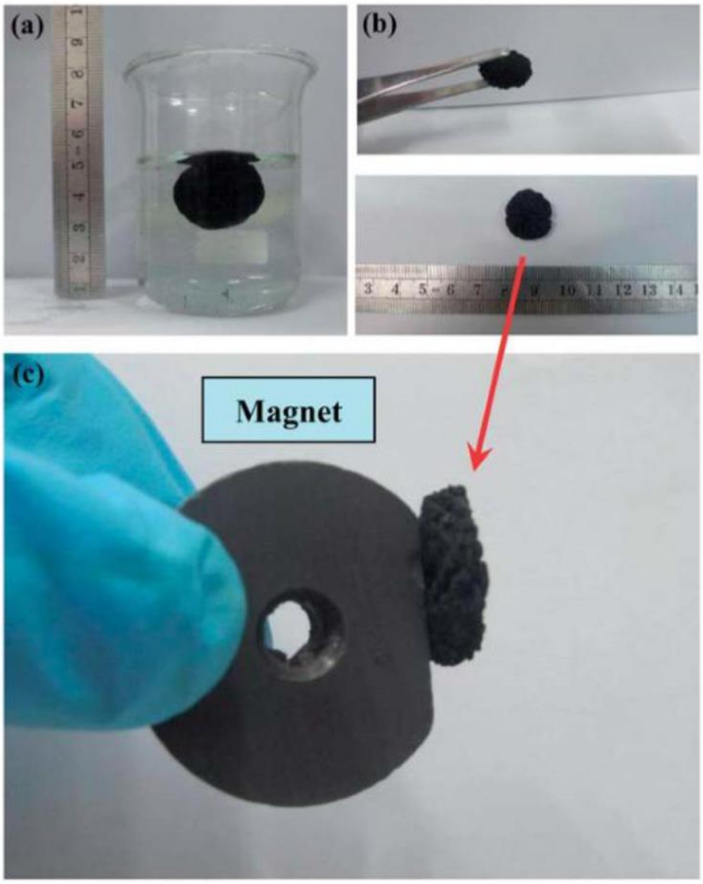

Figure 1.3 Digital images of the as-prepared 3D Ni/graphene aerogel. [59]

Yin et al. [60] prepared an iron nitride (FeNx)/NGA hybrid by a simple two-step hydrothermal method, in which iron phthalocyanines were uniformly dispersed on the GO surface with the assistance of π–π stacking and by the interactions with oxygen-containing functional groups. Such materials was used as catalyst for the oxygen reduction reaction, and its catalytic performance was comparable to that of commercial Pt/C catalysts. It is worth noting that the Pt/C catalysts showed a significant current shift in presence of methanol, indicating that methanol oxidation reaction occurred, while no significant change was observed in the ORR current of the FexN/NGA hybrid. The results show that the methanol cross-tolerance of the hybrid is better than that of Pt/C, as shown in Figure 1.4, which is a very notable feature for the application of these materials as cathodic catalysts in methanol fuel cells.

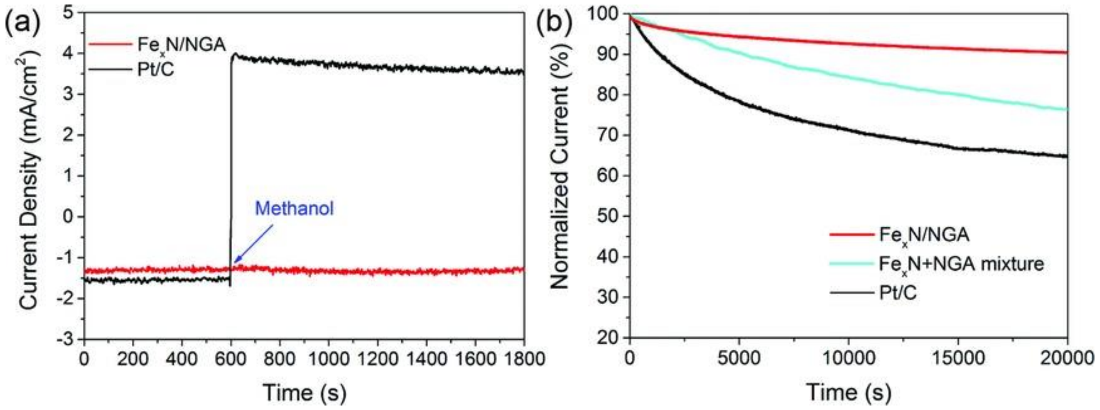

Figure 1.4 a) Chronoamperometric responses of FexN/NGA and Pt/C at −0.25 V vs Ag/AgCl in O_2-saturated 0.1 m KOH followed by addition of 3 M methanol. b) Current-time responses of Fe_xN/NGA and Pt/C at −0.4 V vs Ag/AgCl in O_2-saturated 0.1 m KOH at 1600 rpm.[60]

Xu et al. [61] have prepared MoS_2 and rGO aerogel composite materials (MoS_2/rGO) by a simple hydrothermal method. These MoS_2/rGO hybrid nanostructures have outstanding HER electrocatalytic activity, with an onset overpotential of about 105 mV, a small Tafel slope of 51 mV/dec, and a large exchange current density (j_0) of 3.28×10^{-5} A/cm^2, as shown in Figure 1.5. The excellent electrochemical performance of MoS_2/rGO is attributed to the 3D porous hybrid structure, which enhances the conductivity from graphene to MoS_2 and HER activity.

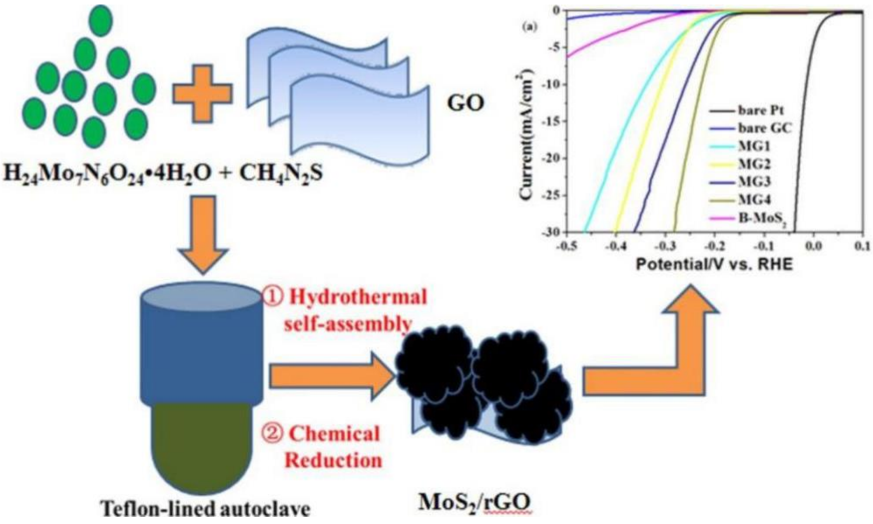

Figure 1.5 Schematic illustration of the preparation of MoS_2/rGO aerogels and linear sweep voltammetries showing the activity in acid conditions towards the hydrogen evolution reaction.[61]

Zhao et al. [62] proposed a composite nanocatalyst made up by MoS_2 nanosheets installed into a 3D GA. The material was prepared by a two-step procedure: first a GA was obtained from a GO solution after solvothermal treatment and then the resulting GA monolith was used for the deposition of MoS_2 again by the solvothermal method starting from ammonium heptamolybdate and thiourea. The highly flexible graphene sheets forming the aerogel are tightly interconnected in a 3D manner preventing the restacking of graphene, and providing a large surface area for growing MoS_2 nanosheets. The resultant MoS_2 supported on 3D GA (GA-MoS_2) composite possesses uniform high and homogeneous dispersion of MoS_2 and excellent electron transfer properties, exhibiting high catalytic performance and strong stability for electrocatalytic application in the HER.

1.1.2 Organic sol-gel method

Organic sol-gel chemistry involves the polymerization of organic precursors to form a highly cross-linked organic gel, which can then be dried and pyrolyzed to form a carbon aerogel. When the organic precursors are added to a suspension of GO, polymerization occurred primarily on the GO surface, both coating the nanosheets and forming junctions between adjacent bundles. Upon drying and pyrolysis, the organic coating and junctions are converted to carbon, yielding the aerogel.

Marcus et al. [54] have reported the preparation of ultra-low-density 3D macroassemblies of GO sheets, which exhibit high electrical conductivity (87 S/m), large internal surface areas (584 m^2/g) and a high pore volume (2.96 cm^3/g). These materials are synthesized as monolithic structures from suspensions of single-layer GO in which organic sol-gel chemistry is used to cross-link the individual sheets, as shown in Figure 1.6. The graphene aerogels exhibit an improvement of the bulk electrical conductivity of more than 2 orders of magnitude compared to those 3D graphene networks prepared with physical cross-links alone.

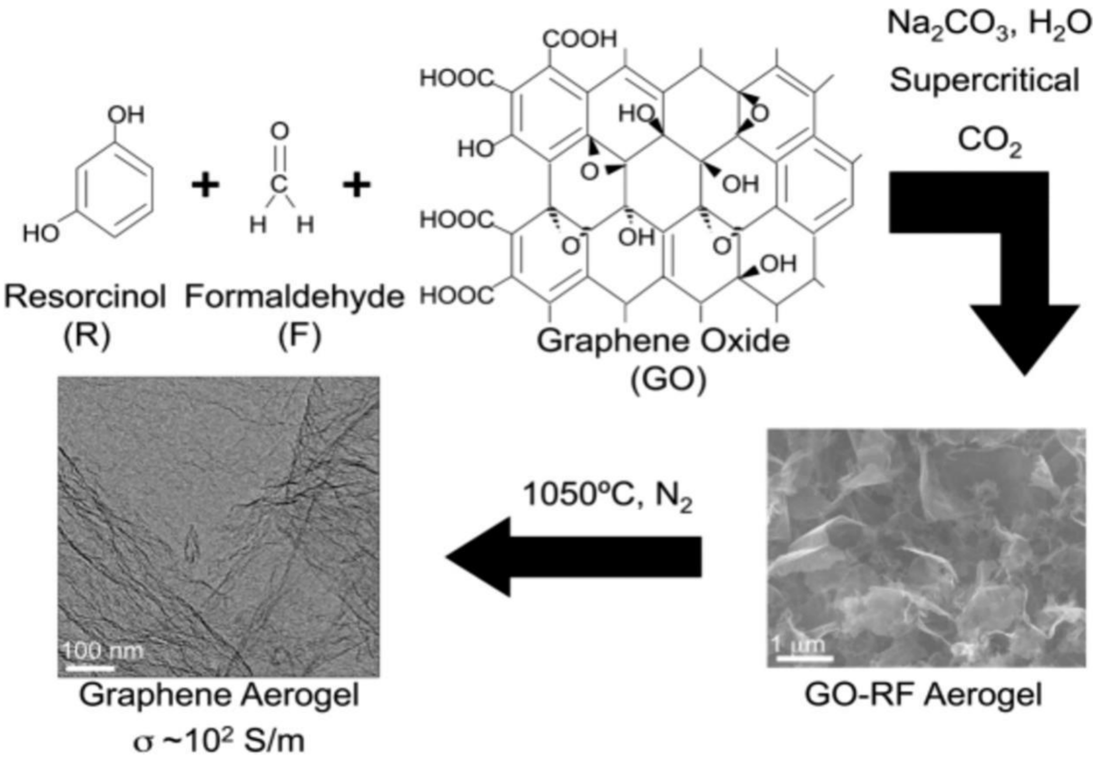

Figure 1.6 Schematic representation of the synthesis of the GO-Resorcinol formaldehyde (GO-RF) aerogel.[54]

Graphene aerogels synthesized by chemical route using GO as precursor are also called as chemically converted graphene aerogels (CCGA). Liu et al. [63] have reported to prepare pure 3D CCGA with a facile and scalable method from high concentration gel precursors with HI acid as the reducing reagent and the assistance of freeze-drying method, as shown in Figure 1.7. The CCGA exhibits many interesting properties, including high compressive strength (106.1 kPa under a strain of 80%), large compression deformation, variable and ultralow electric resistance (6.6 Ω at a compressive strain of 90%), fast and high oil absorption capacity. The CCGA adsorption amount of bean oil, pump oil, toluene, acetone, N,N-Dimethylformamide (DMF), n-heptane and n-hexane solvents is approximately 40 times its own weight.

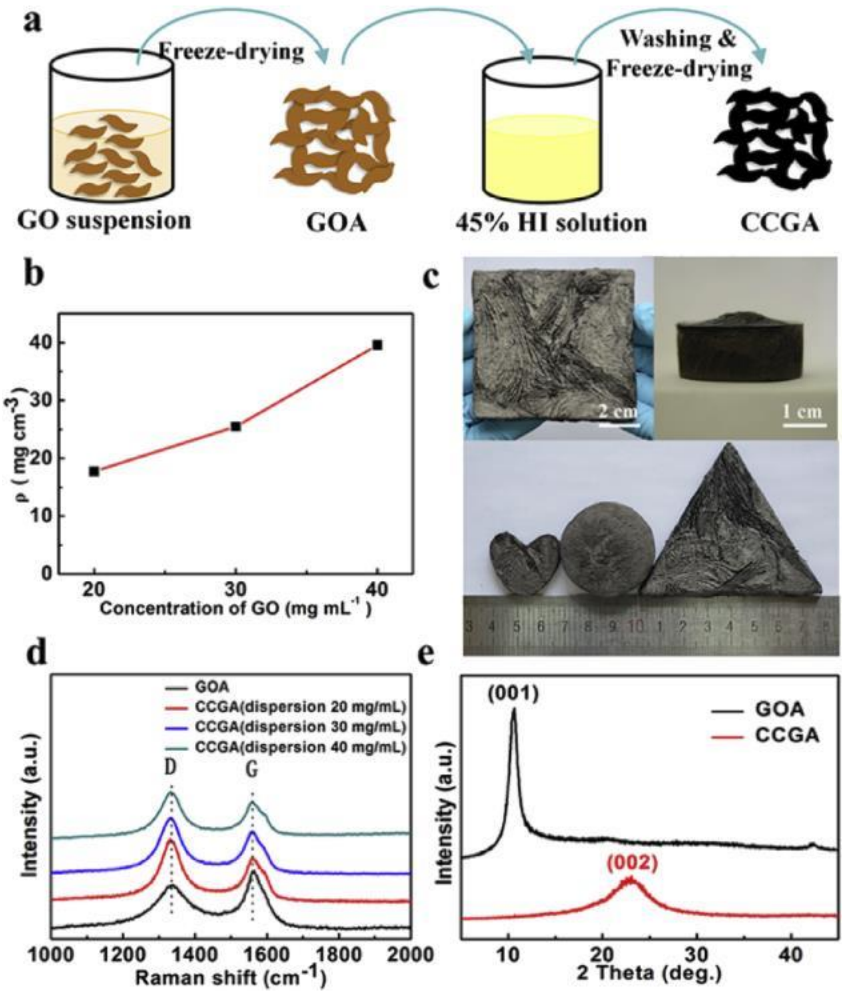

Figure 1.7 (a) Illustration of the fabrication process of the aerogel. (b) The plot of CCGA density versus the initial GO concentration. (c) A photograph showing different shapes and sizes of CCGA. (d) The Raman spectra of GOA and CCGA (initial GO concentration of 20 mg mL^{-1}, 30 mg mL^{-1} and 40 mg mL^{-1}). (e) XRD patterns of the GOA and the CCGA.[63]

Liu et al. [64] have synthesized Nitrogen-doped 3D graphene frameworks (N-3D GFs) by a simple two-step route (Figure 1.8): using polystyrene colloidal particles as a sacrificial template, following heating in NH_3. The N-3D GFs exhibits superior lithiumion storage performance and improved rate capability: it delivers a high specific capacity of 1094 mAhg^{-1} after 100 cycles at 200 mAg^{-1} and excellent rate performance (480 mAhg^{-1} at 2000 mAg^{-1} and 691 mAhg^{-1} after 500 cycles at 1000 mAg^{-1}) when used as anode for lithium-ion batteries.

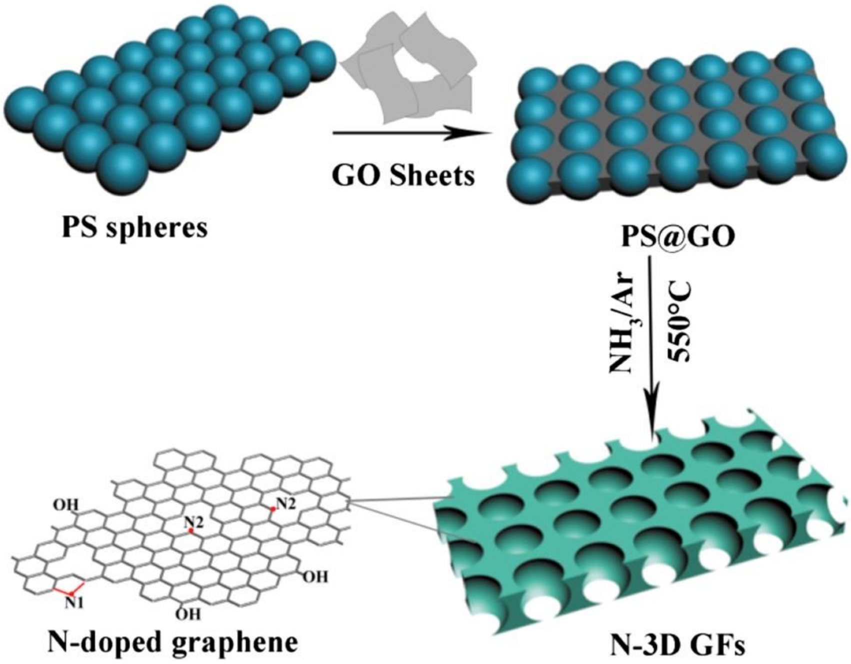

Figure 1.8 Schematic illustration of the synthesis process for N-3D GFs.[64]

1.1.3 Templating method

The template assisted synthesis of nanomaterials has been a cutting-edge technology developed since the 1990s.[65,66] It is also a very effective nanomaterials synthesis method that has been widely used in recent years. It is a relatively simple and easy procedure that has made the fabrication of rather sophisticated nanomaterials accessible to almost any laboratory. Templates can be produced by the self-assembly of several objects such as nanoparticles or macromolecules, or by synthetic procedures guided by special forces (dispersive, electrostatic etc) or intrinsic anisotropic properties (chemical reactivity, mechanical properties etc.). Alternatively, template synthesis requires access to instrumentation for the bottom up synthesis of materials such as physical of chemical vapor deposition (e.g. sputtering, molecular beam epitaxy, etc) or electrochemical deposition, using a nanoporous membrane as a template to produce replica made of various materials, namely, conductive polymers, metals, semiconductors, and carbon.

The template method determines the morphology of products, mainly by controlling the nucleation and growth during nanomaterial preparation. The general routes for nanomaterial synthesis by using the template method are generally divided into three steps:

- first, the template is prepared;
- second, some common synthetic approach such as sol-gel, [67] CVD, [55]

hydrothermal method [68] and freeze-dry [69] methods are used to synthesize the targeted product under the function of template;

- finally, the template is removed.

1.1.3.1 Sol-gel template method

Sol-gel template method is a simple, highly versatile synthetic technique for creating periodic structures with nanometer-to-submicrometer features in three dimensions. It is used to synthesize highly ordered porous materials with a wide range of pore sizes, morphologies, and compositions.

Shao et al. [67] successfully assembled GO hollow spheres using polystyrene spheres as templates to create 3D arrays of graphene spheres (see Figure 1.9). Compared with planar stacked graphene sheets, the hollow spherical graphene shells can provide more free space between the spheres, which results in a larger accessible surface area (440 m^2 g^{-1}) for adsorption of electrolyte ions in supercapacitors. Electrochemical tests show that the graphene hollow spheres exhibit a high specific capacitance of 273 Fg^{-1} at a low current density of 0.5 A g^{-1} and 197 F g^{-1} at a high current density of 10 A g^{-1}, respectively, and excellent electrochemical stability (retaining 95% of their initial capacitance even after 5000 cycles).

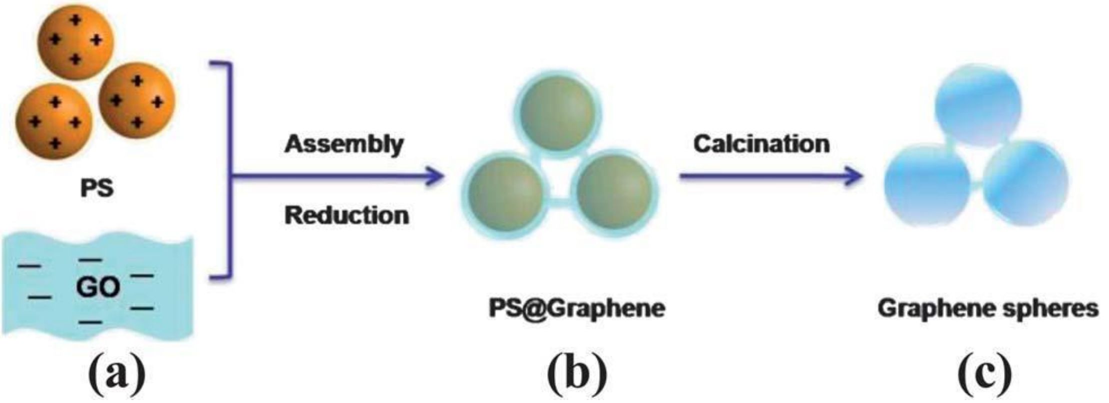

Figure 1.9 Illustration of the preparation process of GO hollow spheres. (a) PS spheres and GO are mixed; (b) GO shells are formed on the PS spheres; and (c) PS spheres are removed to obtain spherical GO shells.[67]

Hong et al [70] prepared a functionalized GA with high porosity and hydrophobicity by surface treatment of self-assembled graphene oxide aerogels. The surface functionalization consisted in the grafting of siloxanes species containing a long chain fluorinated aliphatic substituent. The as-made GA exhibited a low density of 14.4 mg cm^{-3} and mechanical stability as it can stand 2600 times its own weight. Most importantly, this material possessed high absorption ability for several oils and organic solvents, and it could be regenerated by drying at above the melting point of the absorbed species. Hence, it can be used for clearing spilled oils and other pollutants. This behaviour was associated with the synergistic action of high porosity and high surface area which results from the 3D macroporous framework, and the chemical affinity of the hydrophobic functionalized surface for oils-solvents. The regeneration capability was attributed to the strong covalent bonds that build up the network of the surface-modified GA, which ensure chemical and mechanical durability. Figure 1.10 (left) shows the adsorption capacity of the GA for an oil blue N dye and figure 1.10 (right) shows the compressive stress–strain curve of the fluorinated GA.

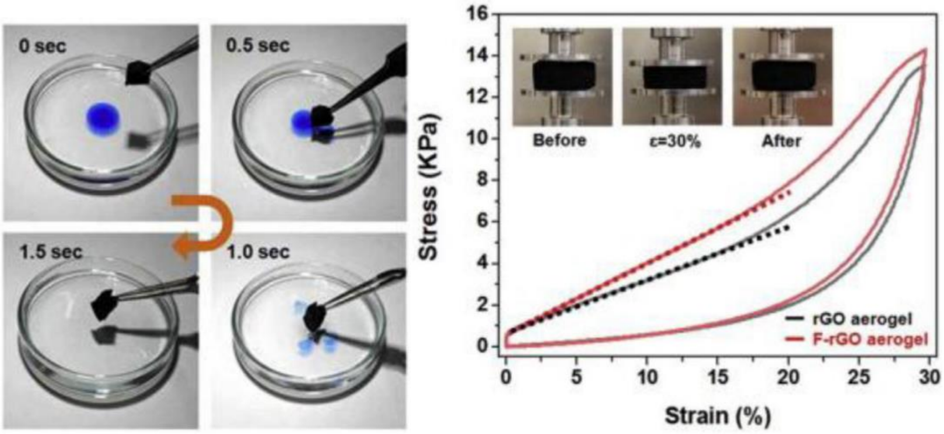

Figure 1.10 Left: Oil absorption test of the aerogel. Oil (stained with Oil blue N dye) floating on water was completely absorbed within 1.5 s. Right: Compressive stress–strain curves of the rGO aerogel (black) and Functionalized-rGO aerogel (red) performed by a dynamic mechanical analyzer with 30% strain in compression. Inset: images from before/after the 30% strain compression test.[70]

1.1.3.2 CVD method

The template-assisted chemical vapor deposition method uses low-molecular-weight organics such as CH_4, C_2H_5OH or C_2H_2 as the carbon source to deposit carbon layers on the surface of metals that are known to easily form graphene such as Cu or Ni by high-temperature cracking. Then the template is removed by etching, obtaining a 3D interconnected graphene structure.

Cao et al. [55] demonstrated a novel 3D graphene structure in a facile CVD procedure by using Ni foam as a template and ethanol as the carbon source as ethanol-CVD. Such 3D graphene structures demonstrated to be excellent templates for the construction of graphene/metal oxide hybrids, which can be used as supercapacitor electrodes. Nickel oxide (NiO) has been deposited on the 3D graphene networks by electrochemical method. The 3D graphene porous structure with a large surface area (2630 m^2 g^{-1}), a high specific capacitance (816 F g^{-1} at 5 mV s^{-1}which allows the rapid access of electrolyte ions to the NiO surface. The obtained NiO/graphene hybrids exhibited a stable cycling performance even after 2000 cycles. Figure 1.11 illustrates the fabrication of 3D graphene networks on Ni foam by ethanol-CVD.

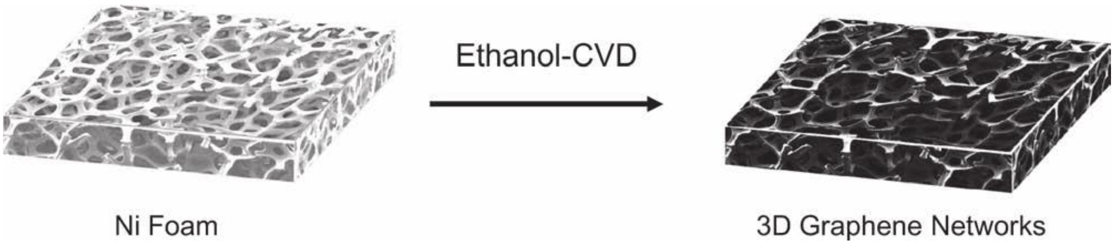

Figure 1.11 Schematic illustration of the synthesis of 3D graphene networks on Ni foam by ethanol-CVD.[55]

Yang et al. [71] reported that different type of graphene frameworks can be combined together. Actually, they realized a hybrid graphene aerogel (HG) made of self-assembled GO nanosheets and nanoplatelets (GNP) using as main scaffold a graphene foam (GF), which was obtained via CVD using a porous nickel template (Figure 1.12). Both the GF and HG aerogels display huge surface area, hydrophilic surface, and mechanical stability and they were used to host a paraffinic wax (PW) to create composite materials. Interestingly, the thermal properties of the HG/PW composite were much better than pure PW (+574% thermal conductivity) and GF/PW composite (+98%) and also the shape stability was greatly improved. Finally, given the high optical adsorption of graphene, the composite showed interesting performances as energy conversion and storage materials.

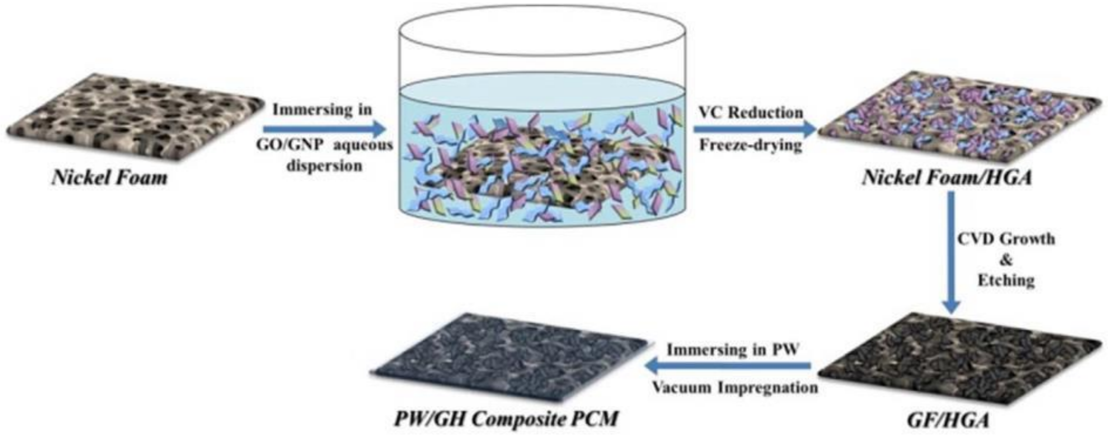

Figure 1.12 Schematic illustration of the preparation of GH and PW/GH composite PCMs.[71]

1.1.3.3 Hydrothermal reduction method

The template-assisted hydrothermal reduction method has been widely used for the synthesis of carbon spheres (CSs) at relatively low temperature (160–200 °C) due to its low cost and high efficiency. It is a feasible strategy for the preparation CSs, applicable to large scale industrial production at low cost.

Liang et al. [68] successfully prepared nitrogen-doped porous carbon spheres (NPCSs) by a facile hydrothermal method through the assistance of a triblock copolymer F108 as soft template, as shown in Figure 1.13. The obtained NPCSs have a high specific surface area of 1481 $m^2\ g^{-1}$ and nitrogen-doped concentration of 2.4 at%. As electrode material for supercapacitors, the NPCSs present a high specific capacitance (365 $F\ g^{-1}$ at 0.5 $A\ g^{-1}$) and outstanding cycling stability (93.9% retention after 10000 cycles). In addition, these NPCSs showed interesting performances as adsorbents, catalysts, and systems for water purification and energy storage and conversion.

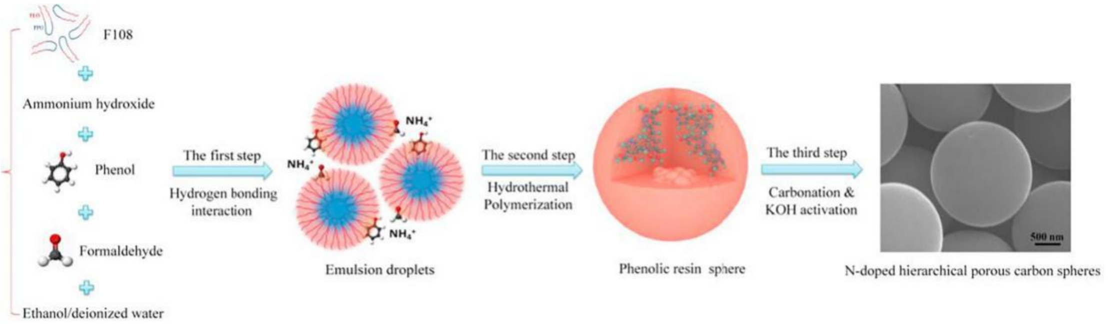

Figure 1.13 The preparation process of NPCSs using the hydrothermal method.[68]

Wu et al [72] presented some GAs with good catalytic activity for the catalytic reduction of 4-nitrophenol, good photocatalytic degradation of methyl orange and capacity to remove oils and dyes from water. The GAs, which were decorated with Cu nanoparticles to impart also improved catalytic activity, were prepared through a reduction and self-assembly process, and then freeze dried to impart the desired morphology. As it is shown in figure 1.14, these GAs have high absorption capacities for oils and dyes because of their porosity, hydrophobicity and high surface areas.

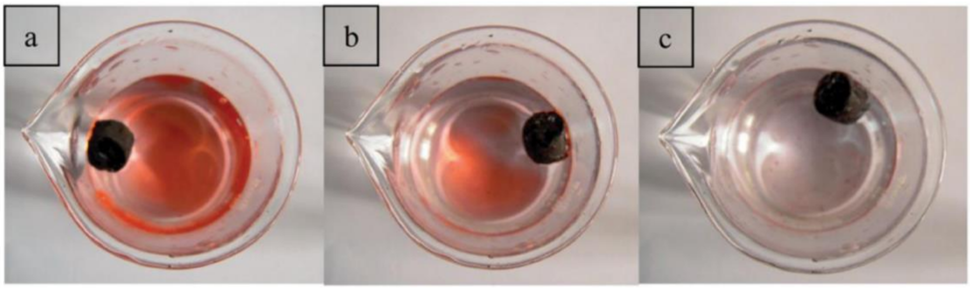

Figure 1.14 Photos of the absorption of diesel oil by GA over time (Sudan III was

added to the oil for better observation) after 0, 1 and 4 min, respectively.[72]

1.1.3.4 Freeze drying method

The use of freezing of colloids to template the porosity in materials is known as ice-templating or freeze-casting. The basic idea is to obtain a porosity that is a replica of the ice crystals, by freezing a suspension and subsequently removing the ice crystals by sublimation.

Qiu et al. [73] reported that the combination of graphene oxide chemistry, namely the presence of polar groups that can be used for hydrogen bonds and a variety of dispersive interactions, and ice physics can form super-light and ultra-elastic graphene-based cell structures, as shown in Figure 1.15. The unique biomimetic hierarchical structure endows this new class of elastomers with exceptionally high energy absorption capability (the graphene elastomer with a density of 5.1 mg cm^{-3} gives an energy loss coefficient of 82.5% at the first compressive cycle and 65% after four cycles of compression) and good electrical conductivity (0.12 S cm^{-1}), at a density of 5.1 mg cm^{-3}.

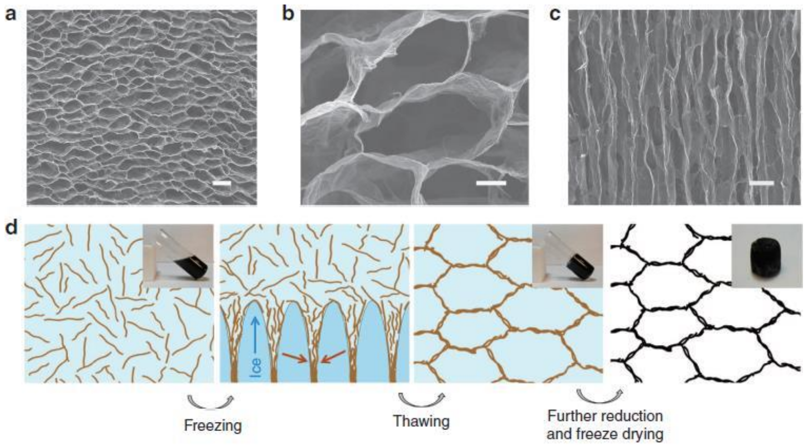

Figure 1.15 Morphology and formation mechanism of the cork-like GO elastomer.[73] Scale bars, 50 mm (a,c) and 10 mm (b).

Li et al.[74] prepared hybrid aerogel microspheres from GO and $Ti_3C_2T_x$ MXene by rapid freezing combined with electrospraying, as shown in Figure 1.16. This method allows preparing a large amount of GO-based hybrid aerogel microspheres without inducing any reduction of the GO moiety, like it general happens in the case of solvo/hydrothermal methods. The resulting materials have been used for electromagnetic screening since the unique aerogel structure not only provides the advantage of a light weight, but also extends the attenuation path when electromagnetic waves enter the material. As microwaves adsorbers, these hybrid hydrogels have achieved minimum reflection loss of -49.1 dB at 14.2 GHz at a thickness of 1.2 mm.

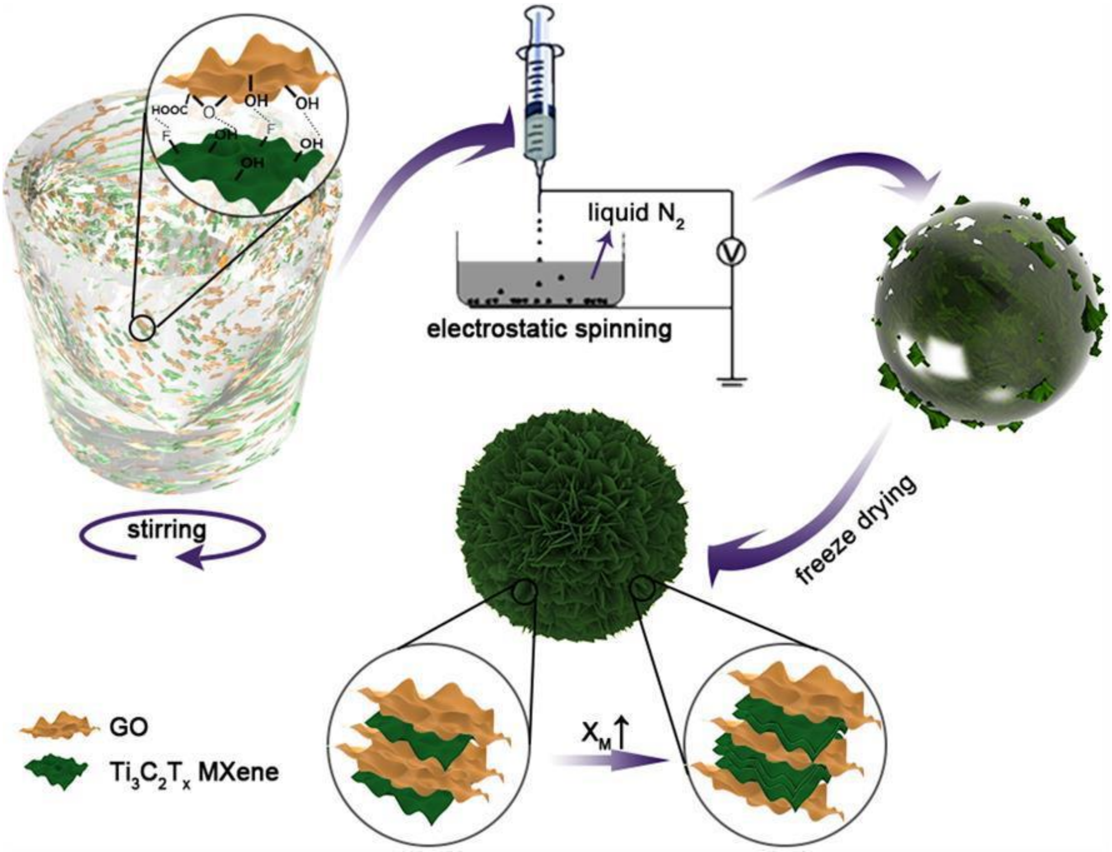

Figure 1.16 The assembly mechanism of M@GAMS during processing.[74]

1.1.4 3D printing technology

Quite interestingly, freeze drying based technique can be combined with the emerging 3D printing techniques allowing to produce materials with special morphological features form the nano to the microscopic scale, which can be quite useful for the realization of functional components of practical devices or (micro)objects for a variety of applications form MEMS to energy storage and conversion, from sensors to micromechanics.

An extrusion-based 3D printing technique, known as “direct ink writing” was applied to construct cellular elastomeric architectures and lightweight composites. This technique employs a three-axis motion stage to assemble 3D structures by robotically extruding a continuous ‘ink’ filament through a micronozzle at room temperature in a layer-by-layer scheme.

Zhu et al. [56] reported the preparation of graphene aerogel microlattices, by a 3D printing technique of direct ink writing to form an engineered structure, as shown in

Figure 1.17. The 3D printed graphene aerogels not only provide the advantage of a light-weight, but also exhibit supercompressibility (up to 90% compressive strain). Moreover, even though a high surface area is preserved, the Young’ s modulus of these graphene aerogels is an order of magnitude higher compared to bulk graphene materials with comparable geometric density.

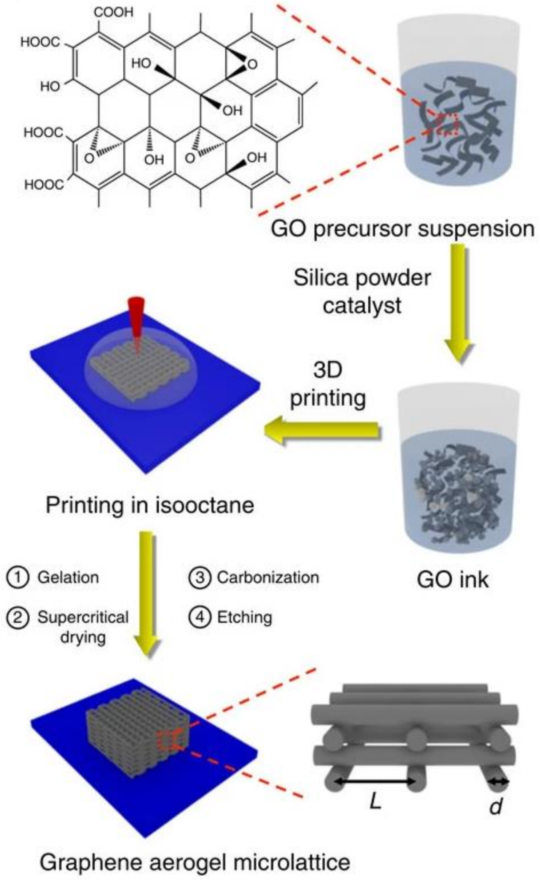

Figure 1.17 Fabrication strategy and GO ink’s rheological properties.[56]

Yao et al. [75] reported a surface-functionalized 3D-printed GA (SF-3D GA), as shown in Figure 1.18. It achieves a surface capacitance of 2195 mF cm^{-2} at a high current density of 100 mA cm^{-2}, and an ultra-high intrinsic capacitance of 309.1 μF cm^{-2} under a load of 12.8 mg cm^{-2}. The device assembled with SF-3D GA as the anode and 3D printed GA decorated with MnO_2 as the cathode is superior to operating carbon-based supercapacitors having an ultra-high power density of 164.5 mW cm^{-2}, and achieving a high energy density of 0.65 mWh cm^{-2}.

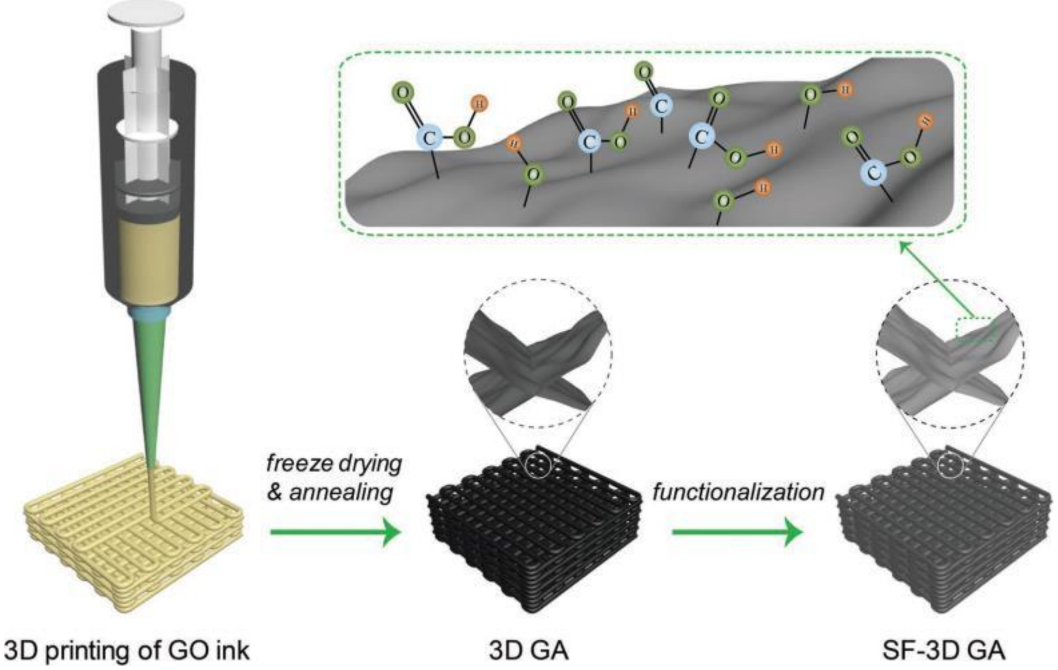

Figure 1.18 Schematic illustration of preparing SF-3D GA.[75]

1.2 Preparation and application of 3D graphene aerogel microsphere hybrids

Graphene aerogel microspheres (GAMs) are highly porous systems with bulk density as low as 0.0018 g cm^{-3}.[76] They are mostly prepared starting from GO and for this reason they are often referred as GOAMs, even if in literature many different acronyms are present. The pore size of the GOAMs can range from nano- to micrometers. The unique ultralight and high porous structure ensure high moisture and water uptake capacity. The GOAMs have many unique properties compared with those of GAs, which can be used in various applications, where dimension and textural properties are key factors. Most routes to produce the GOAMs are based on emulsion-gelation, injection dropping and electrospraying.

1.2.1 Emulsion-Gelation

The emulsion gelation technique is based on the formation of oil-in-water droplets, which act as soft template and the hydrogel crosslinks around them. The microspheres obtained by this method are generally small in size, ranging from a few microns to tens of microns, which are suitable for large scale production.

Zeng et al. [77] synthesized porous phloroglucinol-resorcinol-formaldehyde (PRF) aerogel microspheres (called by the authors as CPRF) by inverse microemulsion method and using as template a polymer such as PEG-200, as shown in Figure 1.19. The result is the formation of CPRF microspheres with a unique 3D structure that can be easily tuned in terms of pore dimensions (10-35 nm), pore volume and surface areas in a wide range Such microspheres exhibit a high specific surface area (up to 798.3 m^2g^{-1}) characterized by mesopores, resulting an excellent support for electrocatalysis. As an example, they were used to support Pt nanoparticles to be used in alkaline conditions for the oxygen reduction reaction. Comparing commercial Pt/amorphous carbon catalysts with such Pt/CPRF microspheres, it turns out that the latter show a much higher electrochemically active surface area and higher mass activity.

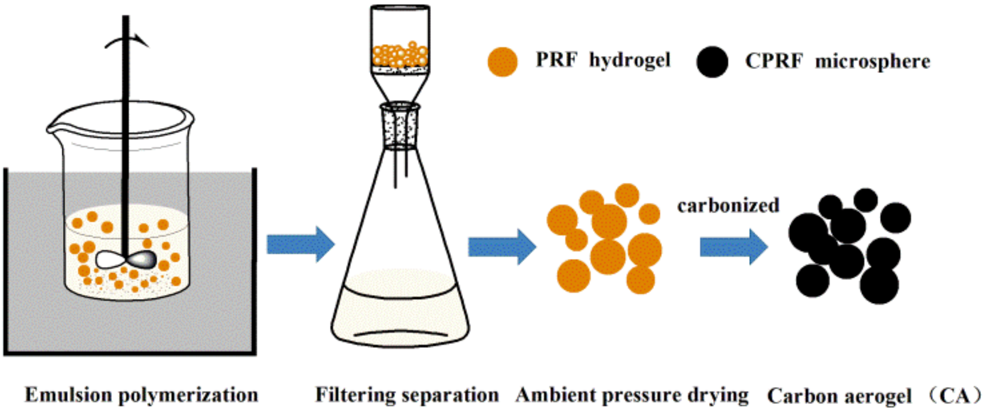

Figure 1.19 Diagram of the processing method used for the preparation of CPRF microspheres.[77]

Zhai et al. [78] combined water-in-oil (W/O) emulsification process and freeze-drying process to prepare cross-linked superhydrophobic polyvinyl alcohol (PVA)/cellulose nanofibril (CNF) aerogel microspheres, as shown in Figure 1.20. The prepared PVA/CNF microspheres have ultra-low densities ranging from 4.66 to 16.54 mg/cm^3, which demonstrated an ultrahigh crude oil absorption capacity (up to 116 times compared to their own weight).

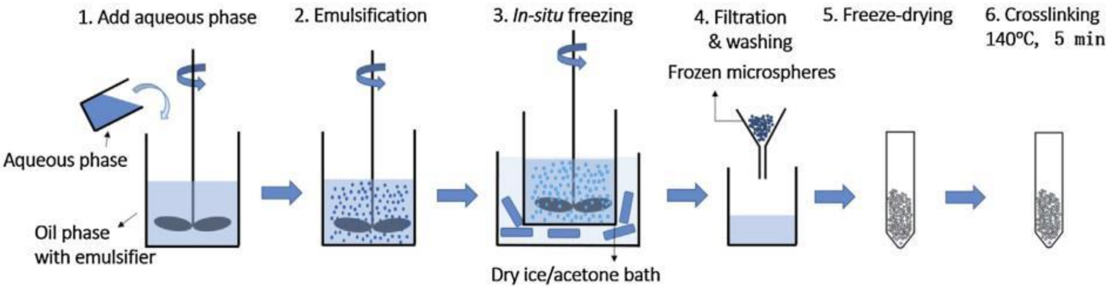

Figure 1.20 Schematic description of the synthesis route of the PVA/CNF aerogel microspheres via the emulsification process combined with freeze-drying.[78]

Yue et al. [79] have prepared urchin-like reduced graphene oxide microspheres (UrGOMS) with adjustable size and structure by a simple water-in-oil (W/O) emulsion technology, as shown in Figure 1.21. The structure has a high specific surface area (356.33m^2 g^{-1}) and bulk density (1.37g cm^{-3}). When used as an electrode material in supercapacitors, the UrGOMS exhibits high volume capacitances of 527.6 F cm^{-3} and 452.1 F cm^{-3} at 10 mV s^{-1} and 0.2 A g^{-1}, respectively. In addition, they also exhibit excellent long-term cycle stability (the capacity retention rate is about 99.43% after 5000 cycles).

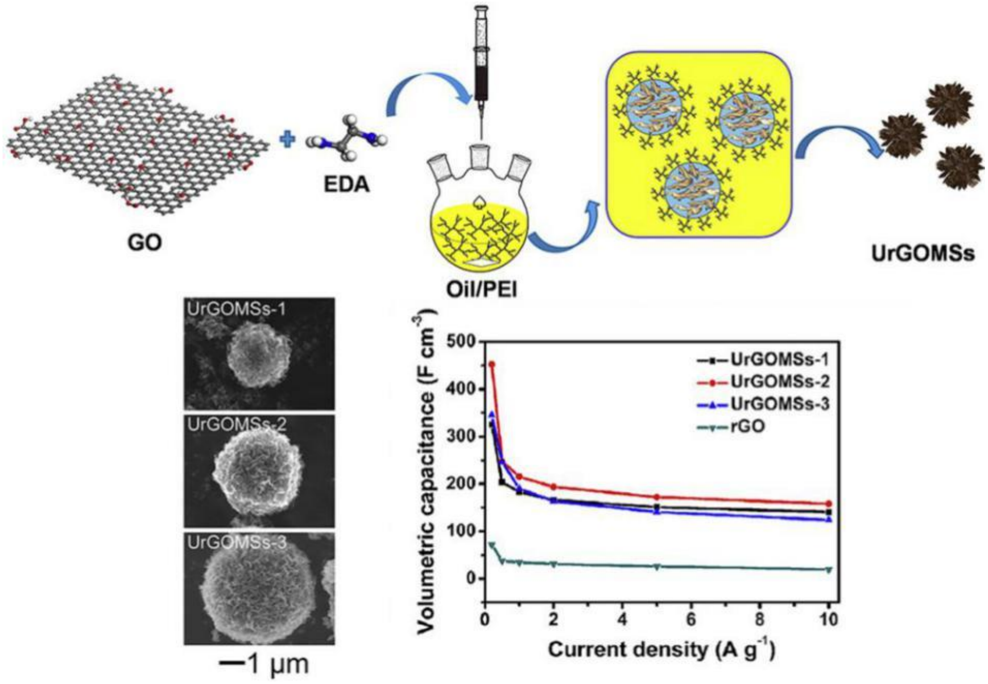

Figure 1.21 Schematic of the fabrication process of the UrGOMSs and Volumetric capacitance of the UrGOMSs and rGO electrodes as a function of the current density.[79]

1.2.2 Injection Dropping

The injection dropping is one of the first example of GAM preparation method. This method is based on a simple injection equipment that extrudes the precursor droplets, and then the final aerogel microspheres are obtained by *in-situ* freezing and followed by lyophilization. This method is simple and widely used. However, the size of the GAMs is generally rather large, and the preparation efficiency is low.

Through the encapsulation of GO into sodium alginate (SA), Fei et al.[80] have prepared composite GO-SA hydrogels and aerogels (by lyophilization of the hydrogels) (Figure 1.22). The SA was transformed into a hydrogel through the standard $CaCl_2$ hardening technique. The resulting materials were used as an adsorbent to remove ciprofloxacin from aqueous solutions. The maximum adsorption capacities of GO-SA aerogel and GO-SA hydrogel reached 55.55 and 86.12 mg/g, respectively. The adsorption capacity of GO-SA composite gel is about 7 to 9 times higher than that of SA only. Moreover, these graphene composite materials can remove organic pollutants from aqueous solutions.

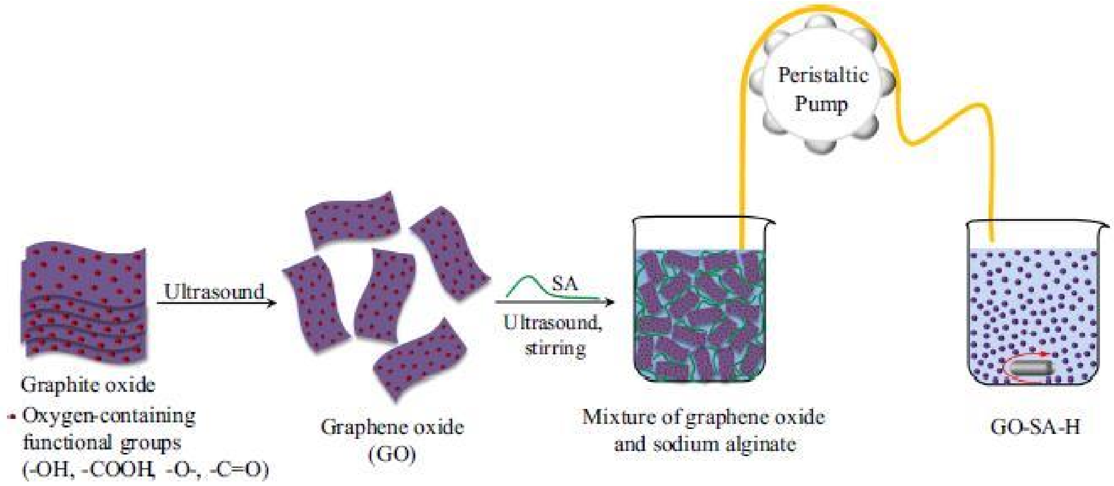

Figure 1.22 Schematic diagram of the preparation process of GO-SA-H.[80]

Zhao et al.[81] have prepared millimeter-scale superelastic GOAMSs, which exhibited an interesting response to external stimuli and high versatility of applications (in wireless electrostatic charge manipulation, fast oil/organic solvent adsorption with high capacity, effective electrode materials in battery, and strain sensors). As shown in Figure 1.23, GSs are obtained by wet spinning of GO solution (i.e. by injecting the precursor solution into a rotating coagulation bath of 5 wt% $CaCl_2$ solution), then drying and thermal annealing. The GOAMs have a special core-shell structure made by a thin continuous and compact skin supported on a highly porous core, which results in excellent elasticity and high specific strength. Both horizontally and vertically assembled sphere arrays exhibit superelasticity comparable to that of a single sphere, allowing it to fully recover under 95% strain, and even after 1000 compression cycles under 70% strain. Given these quite unique mechanical, electric, and porosity properties, they can be used as adsorbents materials for electromechanical devices and supports for electrochemical applications.

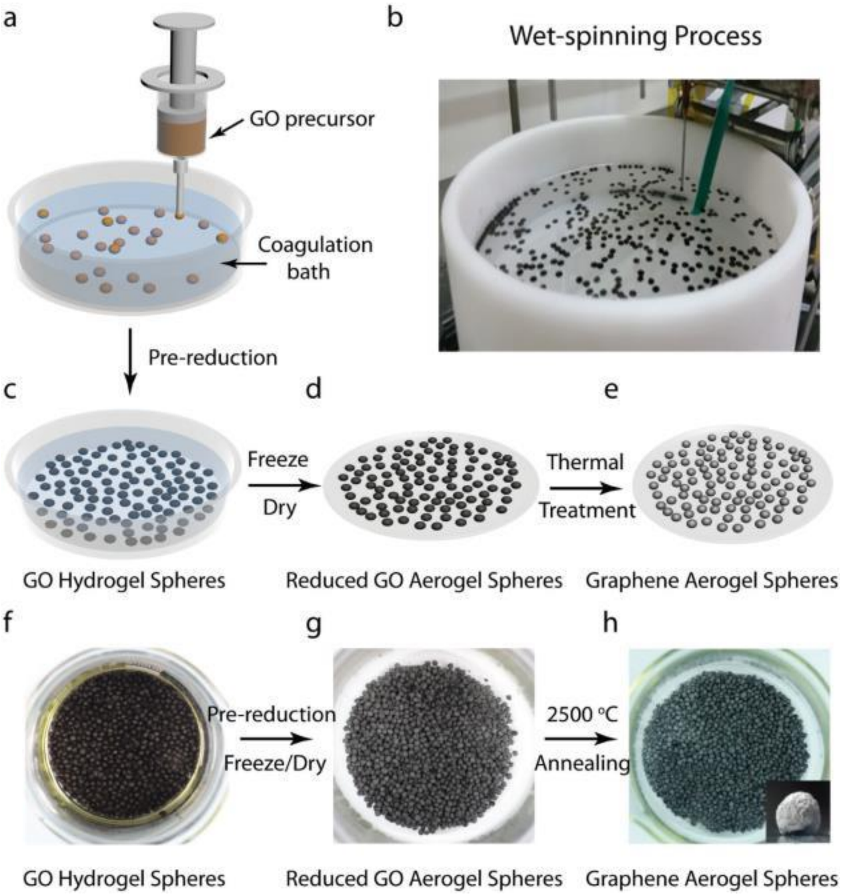

Figure 1.23 a) Scheme and b) digital photo of the wet-spinning process of GO hydrogel spheres. c-e) Schematic illustration of the preparation process of GO aerogel spheres from GO hydrogel spheres. Digital photos of f) freshly formed GO hydrogel spheres, g) rGO aerogel spheres (VcNa), and h) GO aerogel spheres after 2500 0C annealing. The inset in (h) is a photo of a single GO aerogel sphere.[81]

1.2.3 Electrospraying method

Electrospraying, also called electrohydrodynamic (EHD) or EHD atomization (EHDA), is a sister technology to electrospinning and is a very promising technique for the preparation of micro- and nanoparticles. It is based on the use of a high electric field to break up an electrically conductive solution. The particle size is controlled by varying solution properties such as concentration, conductivity surface tension, as well as processing parameters, such as flow rate and applied voltage, geometrical configuration. The solution flows through an emitter, in general a needle or small capillary, and a high voltage is applied to the emitter tip and an electrical field is established with the grounded collector. When the energy of the electric field overcomes the surface tension of the solution, the solution breaks into small charged microdroplets. The so formed aerosol can be used for the preparation of materials with microsphere morphology, in general by directing the microdroplet in a receiving liquid where the chemical (cross-linking) or physical (e.g. freezing) solidification can take place. Liao et al. [44] combined the electrostatic spray method and freeze-drying method to prepare GOAMs with a centrally diverging micro-channel structure and later He et al. [82] used such microspheres to deposit by a solvothermal method Pt nanoparticle, which demonstrated to be more performing than analogous nanoparticles supported on standard carbon materials as elctrocatalysts for the oxidation of methanol.

Zhou et al. [83] have synthesized reduced graphene oxide aerogel microspheres (rGOAM), as shown (Figure 1.24) using an electrospraying method, where the charged droplets of a GO suspension were directed into an isooctane bath containing a curing (Ca^{2+}) and reducing agent (ascorbic acid) that promoted the crosslinking between GO sheets and formation of a stable material. The resulting rGOAMs found several applications such as water remediation and as micromotors for active transport and microassembly. In the first case, the rGOAMs were able to adsorb up to 60 mg/g of rhodamine B form water solution, and the removal rate reached 89.2% within 120 min, indicating its considerable adsorption ability.

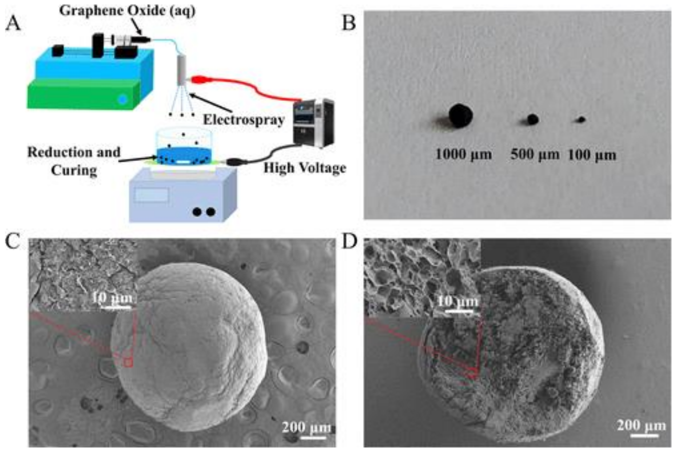

Figure 1.24 (A) Schematic of the fabrication process of the rGOAMs. (B) Photograph of as-prepared rGOAMs with different sizes. SEM images of (C) external morphology and (D) cross profile of rGOAMs. Inset images are the partial enlargements.[83]

Benefiting from the ultralight weight of the aerogel and low fluid resistance on the water surface, the rGOAMs show a high motion speed (up to 17.60 mm/s) under the action of light in the NIR. Taking advantage of the photothermal conversion capacity of the rGOAM under an asymmetric light field, it is capable of moving either on the water surface driven by the Marangoni effect or under the water via light-manipulated density change. The motion direction and speed on water as well as the “start/stop” state can be precisely steered by NIR light. The possibility of moving precisely the rGOAMs associated with their high surface area and porosity paves the way also to the applications of these materials as micro-cargo able to transport and organize matter at the microscopic scale.

Liao et al. [44] have prepared GOAMs with a unique well-defined center-diverging microchannel microstructure (*dandelion-like*) through a synthesis route involving electrospray followed by freeze-casting with an isotropic radial gradient. This is actually the preparation method adopted in this thesis (see Chapter 2). After a two-step thermal reduction (in a vacuum oven for 60 min at 120 ℃ , 60 min at 150 ℃ , and 120 min at 180 ℃ ; in a microwave oven for 1 min at a power of 700 W in the atmosphere of Ar), the lightweight rGO aerogel microspheres were obtained with the "center-diverging microchannel" microstructure retained. Due to their highly porous, layered and hydrophobic structure, rGOAMs show excellent adsorption capacity for various organic solvents and oils, up to 60-214 g per gram of rGOAMs (Figure 1.25), showing potential applications in environment protection and water remediation.

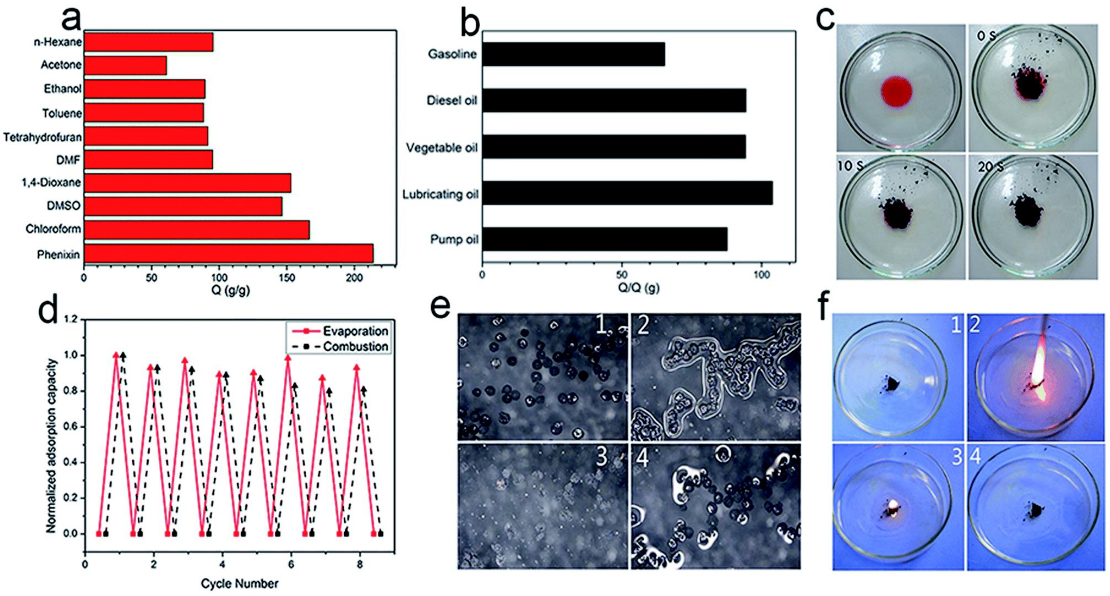

Figure 1.25 (a and b) Absorption capacities of rGOAMs for a range of organic liquids and oils; (c) absorption process of pump oil (dyed with Sudan red III) in water by the rGOAMs within 20 s; (d) recyclability of rGOAMs for the absorption of n-hexane and diesel oil under evaporation and combustion cycles, respectively; (e) pictures of the evaporation process of n-hexane adsorbed rGOAMs (recorded by digital microscope); (f) pictures of the combustion process of diesel oil adsorbed rGOAMs.[44]

1.3 The application of 3D graphene aerogel microsphere hybrids to electrocatalytic water splitting

Water electrolysis is one of the most exciting scientific achievement due to the clean inherent aspects of the electrochemically breaking of H_2O into H_2 and O_2. The only starting material is H_2O and low-cost electricity from solar, wind and hydropower or photovoltaics can be used to sustain the electrochemical process.[84–86] Generally, water electrolysis is carried out in a quartz cell consisting of a cathode and anode in which the HER and OER take place.[87] In order to increase the reaction rate, catalysts must be used in order to reduce the overpotential. Besides catalytic active materials, a porous support is also an important component of catalytic electrodes. Graphene materials possessing 3D porous architectures hold great potential as support materials due to their distinct advantages, e.g. high specific surface area, high conductivity, excellent thermal and chemical stability, good biocompatibility and abundant functional sites. Although there are a large number of reports on the application of 3D graphene aerogel microspheres, only few have addressed catalytic water splitting. Hereafter the most prominent examples are briefly summarized.

Park et al. [88] have successfully prepared highly porous $MoSe_2$-rGO-CNT microspheres by a spray pyrolysis process (Figure 1.26). The high aspect ratio CNTs produced a porous, spherical backbone for the composite powders that minimized the stacking of rGO nanosheets. The CNTs and rGO nanosheets also minimized the growth of $MoSe_2$ nanocrystals. The $MoSe_2$-rGO-CNT composite possesses more active sites because of a large electrochemical surface area and ultrafine $MoSe_2$ nanocrystals, which provide an outstanding catalytic HER activity (an overpotential of 0.24 V at a current density of 10 mA cm^{-2}, Tafel slope of 53 mV dec^{-1}). It compares very favourably to $MoSe_2$-CNT (η_{10} 0.26 V, 76 mV dec^{-1}), $MoSe_2$-rGO (η_{10} 0.32 V, 86 mV dec^{-1}), and bare $MoSe_2$ (η_{10} 0.33 V, 115 mV dec^{-1}).

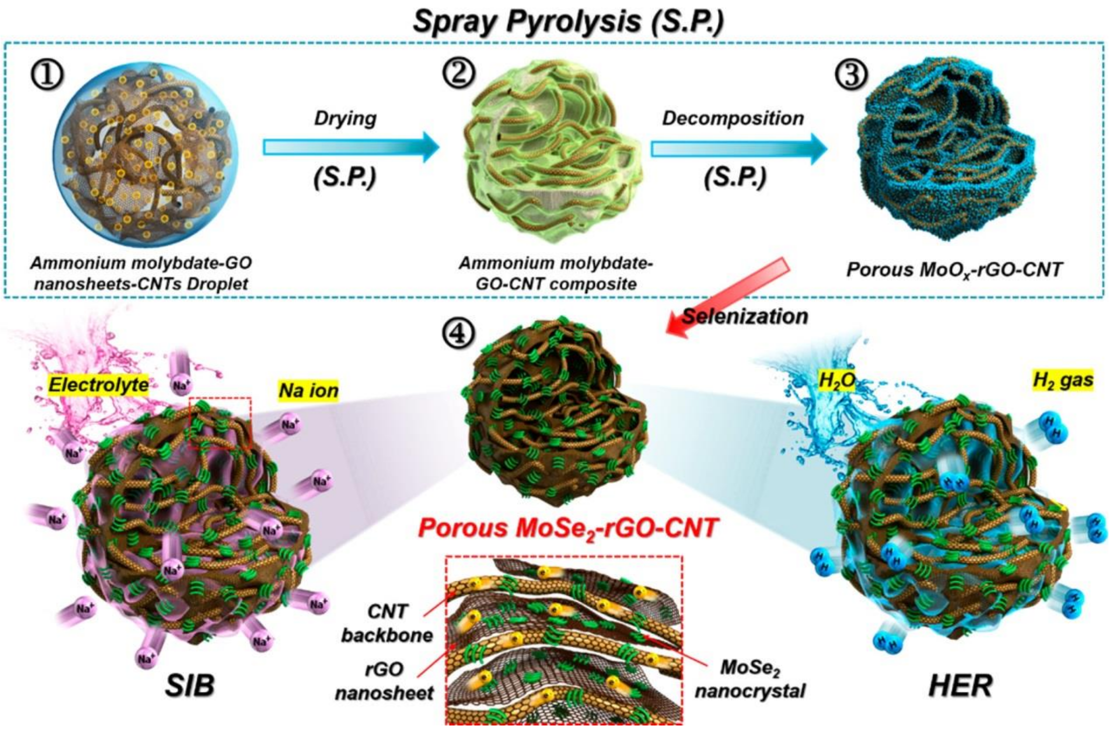

Figure 1.26 Formation Mechanism of Highly Porous MoSe$_2$-rGO-CNT Composite by Spray Pyrolysis Process and Subsequent One-Step Post-Treatment.[88]

As a co-author in the previous paper, [89] we have reported reported a successful route to disperse Ti$_3$C$_2$T$_x$ MXene nanosheets within a GO aerogel having a special centre-diverging microchannel 3D structure (Figure 1.27). The prepared GOAMs, with a radius of a few hundreds of μm, can be easily obtained by a bottom-up approach combining two subsequent steps, i) the electrospraying of GO suspensions and ii) the freeze-casting. Then studied the impact of 3D mesoporous microsphere networks on HER performance. Compared with bulk Ti$_3$C$_2$T$_x$ or Ti$_3$C$_2$T$_x$/GO hybrid aerogels, the as-prepared Ti$_3$C$_2$T$_x$/rGOAMs display improved HER activity, which confirms the advantages of using aerogel microspheres for electrochemical applications. The improved activitie in HER performance may be attributed to the highly ordered centre diverging microsphere structure and low valence state Ti. The strategy of constructing the MXene/graphene aerogel microsphere into 3D network to improve the HER properties can be easily extended to the combination of GOAMs with different TMDCs and a variety of 2D catalysts, which we have confirmed in the next studies.

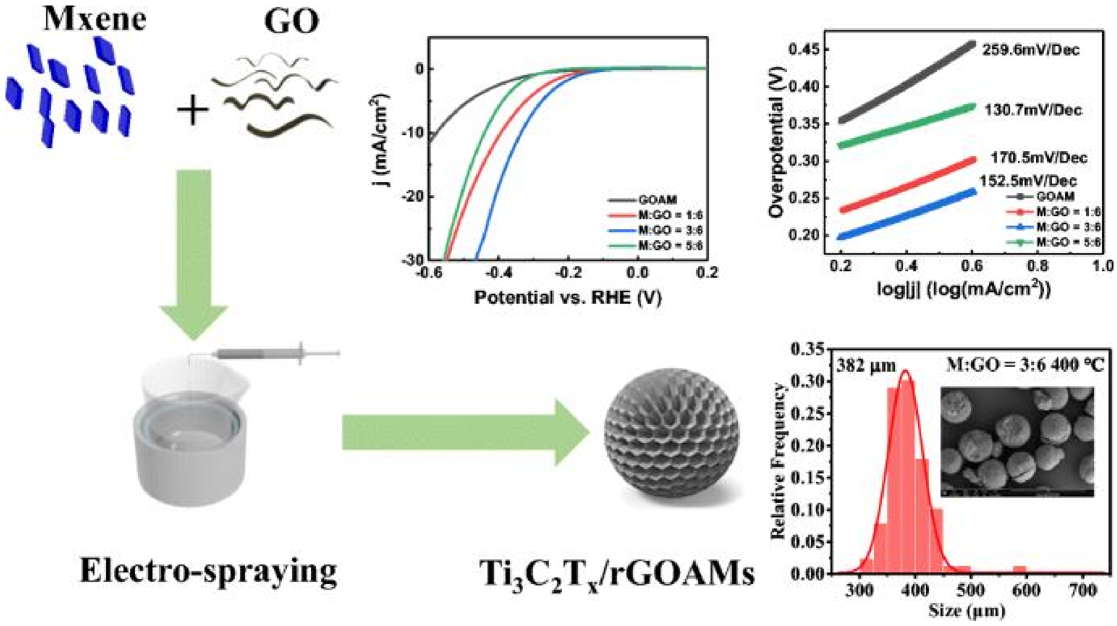

Figure 1.27 Schematic of the fabrication process of the $Ti_3C_2T_x$/rGOAMs and The LSV curves and Tafel plots of the $Ti_3C_2T_x$/GOAMs.[89]

Reference

(1) Mahmood, N.; Wang, Z.; Hassan, S. T. Renewable Energy, Economic Growth, Human Capital, and CO2 Emission: An Empirical Analysis. *Environ. Sci. Pollut. Res.* **2019**, *26* (20), 20619–20630. https://doi.org/10.1007/s11356-019-05387-5.

(2) Nazir, M. S.; Mahdi, A. J.; Bilal, M.; Sohail, H. M.; Ali, N.; Iqbal, H. M. N. Environmental Impact and Pollution-Related Challenges of Renewable Wind Energy Paradigm – A Review. *Sci. Total Environ.* **2019**, *683*, 436–444. https://doi.org/10.1016/j.scitotenv.2019.05.274.

(3) Nazir, M. S.; Ali, Z. M.; Bilal, M.; Sohail, H. M.; Iqbal, H. M. N. Environmental Impacts and Risk Factors of Renewable Energy Paradigm—a Review. *Environ. Sci. Pollut. Res.* **2020**, *27* (27), 33516–33526. https://doi.org/10.1007/s11356-020-09751-8.

(4) Al-Badi, A. H.; Ahshan, R.; Hosseinzadeh, N.; Ghorbani, R.; Hossain, E. Survey of Smart Grid Concepts and Technological Demonstrations Worldwide Emphasizing on the Oman Perspective. *Appl. Syst. Innov.* **2020**, *3* (1), 1–27. https://doi.org/10.3390/asi3010005.

(5) Faber, M. S.; Jin, S. Earth-Abundant Inorganic Electrocatalysts and Their Nanostructures for Energy Conversion Applications. *Energy Environ. Sci.* **2014**, *7* (11), 3519–3542. https://doi.org/10.1039/c4ee01760a.

(6) Dresselhaus, M. S.; Thomas, I. L. Alternative Energy Technologies. Dresselhaus2001. *Nature* **2001**, *414* (6861), 332–337.

(7) Wei, S.; Qi, K.; Jin, Z.; Cao, J.; Zheng, W.; Chen, H.; Cui, X. One-Step Synthesis of a Self-Supported Copper Phosphide Nanobush for Overall Water Splitting. *ACS Omega* **2021**, *1* (6), 1367–1373. https://doi.org/10.1021/acsomega.6b00366.

(8) Jin, H.; Wang, J.; Su, D.; Wei, Z.; Pang, Z.; Wang, Y. In Situ Cobalt-Cobalt Oxide/N-Doped Carbon Hybrids as Superior Bifunctional Electrocatalysts for Hydrogen and Oxygen Evolution. *J. Am. Chem. Soc.* **2015**, *137* (7), 2688–2694. https://doi.org/10.1021/ja5127165.

(9) You, B.; Jiang, N.; Sheng, M.; Bhushan, M. W.; Sun, Y. Hierarchically Porous Urchin-Like Ni2P Superstructures Supported on Nickel Foam as Efficient Bifunctional Electrocatalysts for Overall Water Splitting. *ACS Catal.* **2016**, *6* (2), 714–721. https://doi.org/10.1021/acscatal.5b02193.

(10) Hou, Y.; Lohe, M. R.; Zhang, J.; Liu, S.; Zhuang, X.; Feng, X. Vertically Oriented Cobalt Selenide/NiFe Layered-Double-Hydroxide Nanosheets Supported on Exfoliated Graphene Foil: An Efficient 3D Electrode for Overall Water Splitting. *Energy Environ. Sci.* **2016**, *9* (2), 478–483. https://doi.org/10.1039/c5ee03440j.

(11) Lu, Z.; Zhu, W.; Yu, X.; Zhang, H.; Li, Y.; Sun, X.; Wang, X.; Wang, H.; Wang, J.; Luo, J.; Lei, X.; Jiang, L. Ultrahigh Hydrogen Evolution Performance of Under-Water "Superaerophobic" MoS2 Nanostructured Electrodes. *Adv. Mater.* **2014**, *26* (17), 2683–2687. https://doi.org/10.1002/adma.201304759.

(12) Li, Y.; Zhang, H.; Xu, T.; Lu, Z.; Wu, X.; Wan, P.; Sun, X.; Jiang, L. Under-Water Superaerophobic Pine-Shaped Pt Nanoarray Electrode for Ultrahigh-Performance Hydrogen Evolution. *Adv. Funct. Mater.* **2015**, *25* (11), 1737–1744. https://doi.org/10.1002/adfm.201404250.

(13) Shi, Y.; Zhang, B. Recent Advances in Transition Metal Phosphide Nanomaterials: Synthesis and Applications in Hydrogen Evolution Reaction. *Chem. Soc. Rev.* **2016**, *45* (6), 1529–1541. https://doi.org/10.1039/c5cs00434a.

(14) Koh, C. S. L.; Lee, H. K.; Phan-Quang, G. C.; Han, X.; Lee, M. R.; Yang, Z.; Ling, X. Y. SERS- and Electrochemically Active 3D Plasmonic Liquid Marbles for Molecular-Level Spectroelectrochemical Investigation of Microliter Reactions. *Angew. Chemie - Int. Ed.* **2017**, *56* (30), 8813–8817. https://doi.org/10.1002/anie.201704433.

(15) Chen, L. F.; Feng, Y.; Liang, H. W.; Wu, Z. Y.; Yu, S. H. Macroscopic-Scale Three-Dimensional Carbon Nanofiber Architectures for Electrochemical Energy Storage Devices. *Adv. Energy Mater.* **2017**, *7* (23), 1–31. https://doi.org/10.1002/aenm.201700826.

(16) Yang, J. C.; Mun, J.; Kwon, S. Y.; Park, S.; Bao, Z.; Park, S. Electronic Skin: Recent Progress and Future Prospects for Skin-Attachable Devices for Health Monitoring, Robotics, and Prosthetics. *Adv. Mater.* **2019**, *31* (48), 1–50. https://doi.org/10.1002/adma.201904765.

(17) Wan, C.; Cai, P.; Wang, M.; Qian, Y.; Huang, W.; Chen, X. Artificial Sensory Memory. *Adv. Mater.* **2020**, *32* (15), 1–22. https://doi.org/10.1002/adma.201902434.

(18) Li, Y.; Zhang, H.; Jiang, M.; Zhang, Q.; He, P.; Sun, X. 3D Self-Supported Fe-Doped Ni2P Nanosheet Arrays as Bifunctional Catalysts for Overall Water Splitting. *Adv. Funct. Mater.* **2017**, *27* (37), 1–8. https://doi.org/10.1002/adfm.201702513.

(19) Lu, W.; Liu, T.; Xie, L.; Tang, C.; Liu, D.; Hao, S.; Qu, F.; Du, G.; Ma, Y.; Asiri, A. M.; Sun, X. In Situ Derived Co B Nanoarray: A High-Efficiency and Durable 3D Bifunctional Electrocatalyst for Overall Alkaline Water Splitting. *Small* **2017**, *13* (32), 1–8. https://doi.org/10.1002/smll.201700805.

(20) Wang, J.; Zhong, H. X.; Wang, Z. L.; Meng, F. L.; Zhang, X. B. Integrated Three-Dimensional Carbon Paper/Carbon Tubes/Cobalt-Sulfide Sheets as an Efficient Electrode for Overall Water Splitting. *ACS Nano* **2016**, *10* (2), 2342–2348. https://doi.org/10.1021/acsnano.5b07126.

(21) Geim, A. K.; Novoselov, K. S. The Rise of Graphene PROGRESS. *Nat. Mater.* **2007**, *6* (3), 183–191.

(22) Balandin, A. A.; Ghosh, S.; Bao, W.; Calizo, I.; Teweldebrhan, D.; Miao, F.; Lau, C. N. Superior Thermal Conductivity of Single-Layer Graphene. *Nano Lett.* **2008**, *8* (3), 902–907. https://doi.org/10.1021/nl0731872.

(23) Lee, C.; Wei, X.; Kysar, J. W.; Hone, J. Of Monolayer Graphene. *Science (80-.).* **2008**, *321* (July), 385–388.

(24) Stoller, M. D.; Park, S.; Zhu, Y.; An, J.; Ruoff, R. S. Graphene-Based Ultracapacitors. **2008**, 6–10.

(25) Park, S.; Ruoff, R. S. Erratum: Chemical Methods for the Production of Graphenes (Nature Nanotechnology (2009) 4 (217-224)). *Nat. Nanotechnol.* **2010**, *5* (4), 309. https://doi.org/10.1038/nnano.2010.69.

(26) Zhuang, Y. T.; Jiang, R.; Wu, D. F.; Yu, Y. L.; Wang, J. H. Selenocarrageenan-Inspired Hybrid Graphene Hydrogel as Recyclable Adsorbent for Efficient Scavenging of Dyes and Hg 2+ in Water Environment. *J. Colloid Interface Sci.* **2019**, *540*, 572–578. https://doi.org/10.1016/j.jcis.2019.01.060.

(27) Yu, X.; Wei, Y.; Liu, C.; Ma, J.; Liu, H.; Wei, S.; Deng, W.; Xiang, J.; Luo, S. Ultrafast and Deep Removal of Arsenic in High-Concentration Wastewater: A Superior Bulk Adsorbent of Porous Fe2O3 Nanocubes-Impregnated Graphene Aerogel. *Chemosphere* **2019**, *222*, 258–266. https://doi.org/10.1016/j.chemosphere.2019.01.130.

(28) Zhang, W.; Feng, P.; Chen, J.; Sun, Z.; Zhao, B. Electrically Conductive Hydrogels for Flexible Energy Storage Systems. *Prog. Polym. Sci.* **2019**, *88*, 220–240. https://doi.org/10.1016/j.progpolymsci.2018.09.001.

(29) Liu, L.; Zheng, K.; Yan, Y.; Cai, Z.; Lin, S.; Hu, X. Graphene Aerogels Enhanced Phase Change Materials Prepared by One-Pot Method with High Thermal Conductivity and Large Latent Energy Storage. *Sol. Energy Mater. Sol. Cells* **2018**, *185* (November 2017), 487–493.

https://doi.org/10.1016/j.solmat.2018.06.005.

(30) Yang, J.; Qi, G. Q.; Liu, Y.; Bao, R. Y.; Liu, Z. Y.; Yang, W.; Xie, B. H.; Yang, M. B. Hybrid Graphene Aerogels/Phase Change Material Composites: Thermal Conductivity, Shape-Stabilization and Light-to-Thermal Energy Storage. *Carbon N. Y.* **2016**, *100*, 693–702. https://doi.org/10.1016/j.carbon.2016.01.063.

(31) Yuan, Y.; Lv, H.; Xu, Q.; Liu, H.; Wang, Y. G. A Few-Layered MoS 2 Nanosheets/Nitrogen-Doped Graphene 3D Aerogel as a High Performance and Long-Term Stability Supercapacitor Electrode. *Nanoscale* **2019**, *11* (10), 4318–4327. https://doi.org/10.1039/c8nr05620j.

(32) Yao, W.; Zhang, F.; Qiu, W.; Xu, Z.; Xu, J.; Wen, Y. General Synthesis of Uniform Three-Dimensional Metal Oxides/Reduced Graphene Oxide Aerogels by a Nucleation-Inducing Growth Strategy for High-Performance Lithium Storage. *ACS Sustain. Chem. Eng.* **2019**, *7* (1), 847–857. https://doi.org/10.1021/acssuschemeng.8b04467.

(33) Yan, S.; Zhang, G.; Li, F.; Zhang, L.; Wang, S.; Zhao, H.; Ge, Q.; Li, H. Large-Area Superelastic Graphene Aerogels Based on a Room-Temperature Reduction Self-Assembly Strategy for Sensing and Particulate Matter (PM2.5 and PM10) Capture. *Nanoscale* **2019**, *11* (21), 10372–10380. https://doi.org/10.1039/c9nr02071c.

(34) Xiao, Z.; Zhou, W.; Zhang, N.; Zhang, Q.; Xia, X.; Gu, X.; Wang, Y.; Xie, S. All-Carbon Pressure Sensors with High Performance and Excellent Chemical Resistance. *Small* **2019**, *15* (13), 1–7. https://doi.org/10.1002/smll.201804779.

(35) Chowdhury, S.; Balasubramanian, R. Three-Dimensional Graphene-Based Macrostructures for Sustainable Energy Applications and Climate Change Mitigation. *Prog. Mater. Sci.* **2017**, *90*, 224–275. https://doi.org/10.1016/j.pmatsci.2017.07.001.

(36) Lu, Y.; Ma, Y.; Zhang, T.; Yang, Y.; Wei, L.; Chen, Y. Monolithic 3D Cross-Linked Polymeric Graphene Materials and the Likes: Preparation and Their Redox Catalytic Applications. *J. Am. Chem. Soc.* **2018**, *140* (37), 11538–11550. https://doi.org/10.1021/jacs.8b06414.

(37) Yousefi, N.; Lu, X.; Elimelech, M.; Tufenkji, N. Environmental Performance of Graphene-Based 3D Macrostructures. *Nat. Nanotechnol.* **2019**, *14* (2), 107–119. https://doi.org/10.1038/s41565-018-0325-6.

(38) Yang, J.; Li, X.; Han, S.; Yang, R.; Min, P.; Yu, Z. Z. High-Quality Graphene Aerogels for Thermally Conductive Phase Change Composites with Excellent Shape Stability. *J. Mater. Chem. A* **2018**, *6* (14), 5880–5886.

https://doi.org/10.1039/c8ta00078f.

(39) Zhong, Y.; Zhou, M.; Huang, F.; Lin, T.; Wan, D. Effect of Graphene Aerogel on Thermal Behavior of Phase Change Materials for Thermal Management. *Sol. Energy Mater. Sol. Cells* **2013**, *113*, 195–200. https://doi.org/10.1016/j.solmat.2013.01.046.

(40) Li, A.; Dong, C.; Dong, W.; Atinafu, D. G.; Gao, H.; Chen, X.; Wang, G. Hierarchical 3D Reduced Graphene Porous-Carbon-Based PCMs for Superior Thermal Energy Storage Performance. *ACS Appl. Mater. Interfaces* **2018**, *10* (38), 32093–32101. https://doi.org/10.1021/acsami.8b09541.

(41) Yang, J.; Li, X.; Han, S.; Zhang, Y.; Min, P.; Koratkar, N.; Yu, Z. Z. Air-Dried, High-Density Graphene Hybrid Aerogels for Phase Change Composites with Exceptional Thermal Conductivity and Shape Stability. *J. Mater. Chem. A* **2016**, *4* (46), 18067–18074. https://doi.org/10.1039/c6ta07869a.

(42) Xu, Y.; Fleischer, A. S.; Feng, G. Reinforcement and Shape Stabilization of Phase-Change Material via Graphene Oxide Aerogel. *Carbon N. Y.* **2017**, *114*, 334–346. https://doi.org/10.1016/j.carbon.2016.11.069.

(43) Wang, X.; Cheng, X.; Li, Y.; Li, G.; Xu, J. Self-Assembly of Three-Dimensional 1-Octadecanol/Graphene Thermal Storage Materials. *Sol. Energy* **2019**, *179* (November 2018), 128–134. https://doi.org/10.1016/j.solener.2018.12.041.

(44) Liao, S.; Zhai, T.; Xia, H. Highly Adsorptive Graphene Aerogel Microspheres with Center-Diverging Microchannel Structures. *J. Mater. Chem. A* **2016**, *4* (3), 1068–1077. https://doi.org/10.1039/c5ta09540a.

(45) Md Said, N. H.; Liu, W. W.; Khe, C. S.; Lai, C. W.; Zulkepli, N. N.; Aziz, A. Review of the Past and Recent Developments in Functionalization of Graphene Derivatives for Reinforcement of Polypropylene Nanocomposites. *Polym. Compos.* **2021**, *42* (3), 1075–1108. https://doi.org/10.1002/pc.25922.

(46) Lin, X.; Sun, M.; Sun, S.; Zhang, Z. Graphene Promoted Triphasic N/Ti3+-TiO2 Heterostructures: In-Situ Hydrothermal Synthesis and Enhanced Photocatalytic Performance. *J. Alloys Compd.* **2019**, *785*, 732–741. https://doi.org/10.1016/j.jallcom.2019.01.266.

(47) Liu, C.; Zhang, L.; Liu, R.; Gao, Z.; Yang, X.; Tu, Z.; Yang, F.; Ye, Z.; Cui, L.; Xu, C.; Li, Y. Hydrothermal Synthesis of N-Doped TiO2 Nanowires and N-Doped Graphene Heterostructures with Enhanced Photocatalytic Properties. *J. Alloys Compd.* **2016**, *656*, 24–32. https://doi.org/10.1016/j.jallcom.2015.09.211.

(48) Zhao, L.; Wang, Z. B.; Liu, J.; Zhang, J. J.; Sui, X. L.; Zhang, L. M.; Gu, D. M.

Facile One-Pot Synthesis of Pt/Graphene-TiO2 Hybrid Catalyst with Enhanced Methanol Electrooxidation Performance. *J. Power Sources* **2015**, *279*, 210–217. https://doi.org/10.1016/j.jpowsour.2015.01.023.

(49) Liu, C.; Wu, W.; Shi, Y.; Yang, F.; Liu, M.; Chen, Z.; Yu, B.; Feng, Y. Creating MXene/Reduced Graphene Oxide Hybrid towards Highly Fire Safe Thermoplastic Polyurethane Nanocomposites. *Compos. Part B Eng.* **2020**, *203* (October), 108486. https://doi.org/10.1016/j.compositesb.2020.108486.

(50) Sharifuzzaman, M.; Chhetry, A.; Zahed, M. A.; Yoon, S. H.; Park, C. I.; Zhang, S.; Chandra Barman, S.; Sharma, S.; Yoon, H.; Park, J. Y. Smart Bandage with Integrated Multifunctional Sensors Based on MXene-Functionalized Porous Graphene Scaffold for Chronic Wound Care Management. *Biosens. Bioelectron.* **2020**, *169* (September), 112637. https://doi.org/10.1016/j.bios.2020.112637.

(51) Oliveira, F. M.; Gusmaõ, R. Recent Advances in the Electromagnetic Interference Shielding of 2D Materials beyond Graphene. *ACS Appl. Electron. Mater.* **2020**, *2* (10), 3048–3071. https://doi.org/10.1021/acsaelm.0c00545.

(52) Nawz, T.; Safdar, A.; Hussain, M.; Lee, D. S.; Siyar, M. Graphene to Advanced Mos2: A Review of Structure, Synthesis, and Optoelectronic Device Application. *Crystals* **2020**, *10* (10), 1–31. https://doi.org/10.3390/cryst10100902.

(53) Xu, Y.X.; Sheng, K.X.; Li, C.; Shi, G. . Elf-Assembled Graphene Hydrogel via a One-Step Hydrothermal Process. *ACS Nano* **2010**, *4* (7), 4324–4330.

(54) Worsley, M. A.; Pauzauskie, P. J.; Olson, T. Y.; Biener, J.; Satcher, J. H.; Baumann, T. F. Synthesis of Graphene Aerogel with High Electrical Conductivity. *J. Am. Chem. Soc.* **2010**, *132* (40), 14067–14069. https://doi.org/10.1021/ja1072299.

(55) Cao, X.; Shi, Y.; Shi, W.; Lu, G.; Huang, X.; Yan, Q.; Zhang, Q.; Zhang, H. Preparation of Novel 3D Graphene Networks for Supercapacitor Applications. *Small* **2011**, *7* (22), 3163–3168. https://doi.org/10.1002/smll.201100990.

(56) Zhu, C.; Han, T. Y. J.; Duoss, E. B.; Golobic, A. M.; Kuntz, J. D.; Spadaccini, C. M.; Worsley, M. A. Highly Compressible 3D Periodic Graphene Aerogel Microlattices. *Nat. Commun.* **2015**, *6*, 1–8. https://doi.org/10.1038/ncomms7962.

(57) Ma, J.; Shi, N.; Jia, J. Fe3O4 Nanospheres Decorated Reduced Graphene Oxide as Anode to Promote Extracellular Electron Transfer Efficiency and Power Density in Microbial Fuel Cells. *Electrochim. Acta* **2020**, *362*, 137126. https://doi.org/10.1016/j.electacta.2020.137126.

(58) Manna, N.; Ayasha, N.; Singh, S. K.; Kurungot, S. A NiFe Layered Double Hydroxide-Decorated N-Doped Entangled-Graphene Framework: A Robust Water Oxidation Electrocatalyst. *Nanoscale Adv.* **2020**, *2* (4), 1709–1717. https://doi.org/10.1039/c9na00808j.

(59) Ren, L.; Hui, K. S.; Hui, K. N. Self-Assembled Free-Standing Three-Dimensional Nickel Nanoparticle/Graphene Aerogel for Direct Ethanol Fuel Cells. *J. Mater. Chem. A* **2013**, *1* (18), 5689–5694. https://doi.org/10.1039/c3ta10657h.

(60) Yin, H.; Zhang, C.; Liu, F.; Hou, Y. Hybrid of Iron Nitride and Nitrogen-Doped Graphene Aerogel as Synergistic Catalyst for Oxygen Reduction Reaction. *Adv. Funct. Mater.* **2014**, *24* (20), 2930–2937. https://doi.org/10.1002/adfm.201303902.

(61) Xu, X.; Sun, Y.; Qiao, W.; Zhang, X.; Chen, X.; Song, X.; Wu, L.; Zhong, W.; Du, Y. 3D MoS 2 -Graphene Hybrid Aerogels as Catalyst for Enhanced Efficient Hydrogen Evolution. *Appl. Surf. Sci.* **2017**, *396*, 1520–1527. https://doi.org/10.1016/j.apsusc.2016.11.201.

(62) Zhao, Y.; Xie, X.; Zhang, J.; Liu, H.; Ahn, H. J.; Sun, K.; Wang, G. MoS2 Nanosheets Supported on 3D Graphene Aerogel as a Highly Efficient Catalyst for Hydrogen Evolution. *Chem. - A Eur. J.* **2015**, *21* (45), 15908–15913. https://doi.org/10.1002/chem.201501964.

(63) Liu, Y.; Shi, Q.; Hou, C.; Zhang, Q.; Li, Y.; Wang, H. Versatile Mechanically Strong and Highly Conductive Chemically Converted Graphene Aerogels. *Carbon N. Y.* **2017**, *125*, 352–359. https://doi.org/10.1016/j.carbon.2017.09.072.

(64) Liu, X.; Wu, Y.; Yang, Z.; Pan, F.; Zhong, X.; Wang, J.; Gu, L.; Yu, Y. Nitrogen-Doped 3D Macroporous Graphene Frameworks as Anode for High Performance Lithium-Ion Batteries. *J. Power Sources* **2015**, *293*, 799–805. https://doi.org/10.1016/j.jpowsour.2015.05.074.

(65) Kim, T. W.; Kleitz, F.; Paul, B.; Ryoo, R. MCM-48-like Large Mesoporous Silicas with Tailored Pore Structure: Facile Synthesis Domain in a Ternary Triblock Copolymer-Butanol-Water System. *J. Am. Chem. Soc.* **2005**, *127* (20), 7601–7610. https://doi.org/10.1021/ja042601m.

(66) Dong, A.; Ren, N.; Tang, Y.; Wang, Y.; Zhang, Y.; Hua, W.; Gao, Z. General Synthesis of Mesoporous Spheres of Metal Oxides and Phosphates. *J. Am. Chem. Soc.* **2003**, *125* (17), 4976–4977. https://doi.org/10.1021/ja029964b.

(67) Shao, Q.; Tang, J.; Lin, Y.; Zhang, F.; Yuan, J.; Zhang, H.; Shinya, N.; Qin, L. C. Synthesis and Characterization of Graphene Hollow Spheres for Application

in Supercapacitors. *J. Mater. Chem. A* **2013**, *1* (48), 15423–15428. https://doi.org/10.1039/c3ta12789c.

(68) Liang, Z.; Zhang, L.; Liu, H.; Zeng, J.; Zhou, J.; Li, H.; Xia, H. Soft-Template Assisted Hydrothermal Synthesis of Size-Tunable, N-Doped Porous Carbon Spheres for Supercapacitor Electrodes. *Results Phys.* **2019**, *12* (January), 1984–1990. https://doi.org/10.1016/j.rinp.2019.01.074.

(69) Yang, Z.; Xia, Y.; Mokaya, R. Zeolite ZSM-5 with Unique Supermicropores Synthesized Using Mesoporous Carbon as a Template. *Adv. Mater.* **2004**, *16* (8), 727–732. https://doi.org/10.1002/adma.200306295.

(70) Hong, J. Y.; Sohn, E. H.; Park, S.; Park, H. S. Highly-Efficient and Recyclable Oil Absorbing Performance of Functionalized Graphene Aerogel. *Chem. Eng. J.* **2015**, *269*, 229–235. https://doi.org/10.1016/j.cej.2015.01.066.

(71) Yang, J.; Qi, G. Q.; Bao, R. Y.; Yi, K.; Li, M.; Peng, L.; Cai, Z.; Yang, M. B.; Wei, D.; Yang, W. Hybridizing Graphene Aerogel into Three-Dimensional Graphene Foam for High-Performance Composite Phase Change Materials. *Energy Storage Mater.* **2018**, *13* (November 2017), 88–95. https://doi.org/10.1016/j.ensm.2017.12.028.

(72) Wu, T.; Chen, M.; Zhang, L.; Xu, X.; Liu, Y.; Yan, J.; Wang, W.; Gao, J. Three-Dimensional Graphene-Based Aerogels Prepared by a Self-Assembly Process and Its Excellent Catalytic and Absorbing Performance. *J. Mater. Chem. A* **2013**, *1* (26), 7612–7621. https://doi.org/10.1039/c3ta10989e.

(73) Qiu, L.; Liu, J. Z.; Chang, S. L. Y.; Wu, Y.; Li, D. Biomimetic Superelastic Graphene-Based Cellular Monoliths. *Nat. Commun.* **2012**, *3*, 1–7. https://doi.org/10.1038/ncomms2251.

(74) Li, Y.; Meng, F.; Mei, Y.; Wang, H.; Guo, Y.; Wang, Y.; Peng, F.; Huang, F.; Zhou, Z. Electrospun Generation of Ti3C2Tx MXene@graphene Oxide Hybrid Aerogel Microspheres for Tunable High-Performance Microwave Absorption. *Chem. Eng. J.* **2020**, *391* (September 2019), 123512. https://doi.org/10.1016/j.cej.2019.123512.

(75) Yao, B.; Chandrasekaran, S.; Zhang, H.; Ma, A.; Kang, J.; Zhang, L.; Lu, X.; Qian, F.; Zhu, C.; Duoss, E. B.; Spadaccini, C. M.; Worsley, M. A.; Li, Y. 3D-Printed Structure Boosts the Kinetics and Intrinsic Capacitance of Pseudocapacitive Graphene Aerogels. *Adv. Mater.* **2020**, *32* (8), 1–10. https://doi.org/10.1002/adma.201906652.

(76) Cai, H.; Sharma, S.; Liu, W.; Mu, W.; Liu, W.; Zhang, X.; Deng, Y. Aerogel Microspheres from Natural Cellulose Nanofibrils and Their Application as Cell Culture Scaffold. *Biomacromolecules* **2014**, *15* (7), 2540–2547.

https://doi.org/10.1021/bm5003976.

(77) Zeng, M.; Wang, C. Y.; Su, L.; Luo, Z. H.; Wu, J. K.; Yi, Y. Nano-Platinum Catalysts Supported by Carbon Aerogel Microsphere with Adjustable Pore Size Tuned by PEG-200 for Oxygen Reduction Reaction. *ChemistrySelect* **2020**, *5* (29), 9296–9300. https://doi.org/10.1002/slct.202001936.

(78) Zhai, T.; Zheng, Q.; Cai, Z.; Xia, H.; Gong, S. Synthesis of Polyvinyl Alcohol/Cellulose Nanofibril Hybrid Aerogel Microspheres and Their Use as Oil/Solvent Superabsorbents. *Carbohydr. Polym.* **2016**, *148*, 300–308. https://doi.org/10.1016/j.carbpol.2016.04.065.

(79) Yue, F.; Gao, G.; Li, F.; Zheng, Y.; Hou, S. Size-Controlled Synthesis of Urchin-like Reduced Graphene Oxide Microspheres with Highly Packed Density by Emulsion-Assisted in-Situ Assembly and Their Supercapacitor Performance. *Carbon N. Y.* **2018**, *134*, 112–122. https://doi.org/10.1016/j.carbon.2018.03.074.

(80) Fei, Y.; Li, Y.; Han, S.; Ma, J. Adsorptive Removal of Ciprofloxacin by Sodium Alginate/Graphene Oxide Composite Beads from Aqueous Solution. *J. Colloid Interface Sci.* **2016**, *484*, 196–204. https://doi.org/10.1016/j.jcis.2016.08.068.

(81) Zhao, X.; Yao, W.; Gao, W.; Chen, H.; Gao, C. Wet-Spun Superelastic Graphene Aerogel Millispheres with Group Effect. *Adv. Mater.* **2017**, *29* (35), 1–9. https://doi.org/10.1002/adma.201701482.

(82) He, M.; Fei, G.; Zheng, Z.; Cheng, Z.; Wang, Z.; Xia, H. Pt Nanoparticle-Loaded Graphene Aerogel Microspheres with Excellent Methanol Electro-Oxidation Performance. *Langmuir* **2019**, *35* (10), 3694–3700. https://doi.org/10.1021/acs.langmuir.9b00021.

(83) Zhou, X.; Li, Z.; Tan, L.; Zhang, Y.; Jiao, Y. Near-Infrared Light-Steered Graphene Aerogel Micromotor with High Speed and Precise Navigation for Active Transport and Microassembly. *ACS Appl. Mater. Interfaces* **2020**, *12* (20), 23134–23144. https://doi.org/10.1021/acsami.0c04970.

(84) Lewis, N. S. Solar Energy Use. *Science (80-.).* **2007**, *798* (1), 798–802. https://doi.org/10.1126/science.1137014.

(85) Chen, Y. X.; Lavacchi, A.; Miller, H. A.; Bevilacqua, M.; Filippi, J.; Innocenti, M.; Marchionni, A.; Oberhauser, W.; Wang, L.; Vizza, F. Nanotechnology Makes Biomass Electrolysis More Energy Efficient than Water Electrolysis. *Nat. Commun.* **2014**, *5* (May), 1–6. https://doi.org/10.1038/ncomms5036.

(86) Chen, C.; Tao, L.; Du, S.; Chen, W.; Wang, Y.; Zou, Y.; Wang, S. Advanced

Exfoliation Strategies for Layered Double Hydroxides and Applications in Energy Conversion and Storage. *Adv. Funct. Mater.* **2020**, *30* (14), 1–18. https://doi.org/10.1002/adfm.201909832.

(87) Vincent, I.; Bessarabov, D. Low Cost Hydrogen Production by Anion Exchange Membrane Electrolysis: A Review. *Renew. Sustain. Energy Rev.* **2018**, *81* (February 2017), 1690–1704. https://doi.org/10.1016/j.rser.2017.05.258.

(88) Park, G. D.; Kim, J. H.; Park, S. K.; Kang, Y. C. MoSe2 Embedded CNT-Reduced Graphene Oxide Composite Microsphere with Superior Sodium Ion Storage and Electrocatalytic Hydrogen Evolution Performances. *ACS Appl. Mater. Interfaces* **2017**, *9* (12), 10673–10683. https://doi.org/10.1021/acsami.7b00147.

(89) Cheng, Y.; Zhan, Y.; Ran, J. J.; Wang, Z.; Agnoli, S.; Xia, H.; Granozzi, G. Hybrid MXene/Reduced Graphene Oxide Aerogel Microspheres for Hydrogen Evolution Reaction. *Ionics (Kiel).* **2021**, *27* (7), 3099–3108. https://doi.org/10.1007/s11581-021-04062-5.

Chapter 2

Hybrid Transition Metal Dichalcogenide/Graphene Microspheres for Hydrogen Evolution Reaction

2. Hybrid Transition Metal Dichalcogenide/Graphene Microspheres for Hydrogen Evolution Reaction

2.1 Introduction

In the last decade, materials characterized by pores of different size and shapes have received considerable attention from both the academic and industrial world. The porous structure endows such materials with a high surface area and, more importantly, allows a subtle control over mass transport thanks to size exclusion and size dependent permeation. This behavior is of crucial importance for separation, adsorption, gas storage and catalysis, that are key processes involved in different fields, ranging from biology to environmental protection [1 , 2] and from chemistry to energy conversion and storage,[3–5] as reviwed in detail in the first chapter of this thesis.

Porous materials based on carbon are particularly attractive. The low density, the high strength per weight and the ability to bind with various atoms through different hybrid orbitals (sp^n) make carbon an extraordinarily versatile building block for the construction of porous structures with intriguing morphologies and multifunctional properties. Graphene (G) has been the most studied carbon allotrope of the last fifteen years. This interest is due to the G peculiar physicochemical properties (electronic and thermal conductivity, mechanical and chemical stability) and to its 2D structure, which results in a very high intrinsic surface area.[6 – 8] The specific theoretical surface area of a single G sheet is 2630 m^2/g, [9] but due to the strong tendency to aggregation, experimental values are generally far below this value. The rational assembly of G based 3D architectures allows preserving the G single layers, while maximizing the accessible surface area, resulting in systems with high porosity.[10] Among the various G based 3D architectures, G aerogels combine the exceptional intrinsic G properties with the specific properties of aerogels (lightness, low dielectric permittivity, etc.).[11 – 14]

Recently, prof. Xia's group have reported the synthesis of GOAMs,[15] i.e., a 3D porous structure with microchannel central divergence, by combining electrospray [16 , 17] with freeze-casting techniques [18] (Figure 2.1). In these 3D architectures, the interconnected G sheets arranged radially forms open ended spheres with a radius of ~100 μm, resembling dandelion blowball. Interestingly, thermal treatment in inert atmosphere [19] can produce partial reduced GO aerogel microspheres (prGOAM). These materials, given their highly porous and hydrophobic structure, have excellent adsorption capacity for various organic solvents and oils, finding applications in environmental pollutant treatment and water purification.[15]

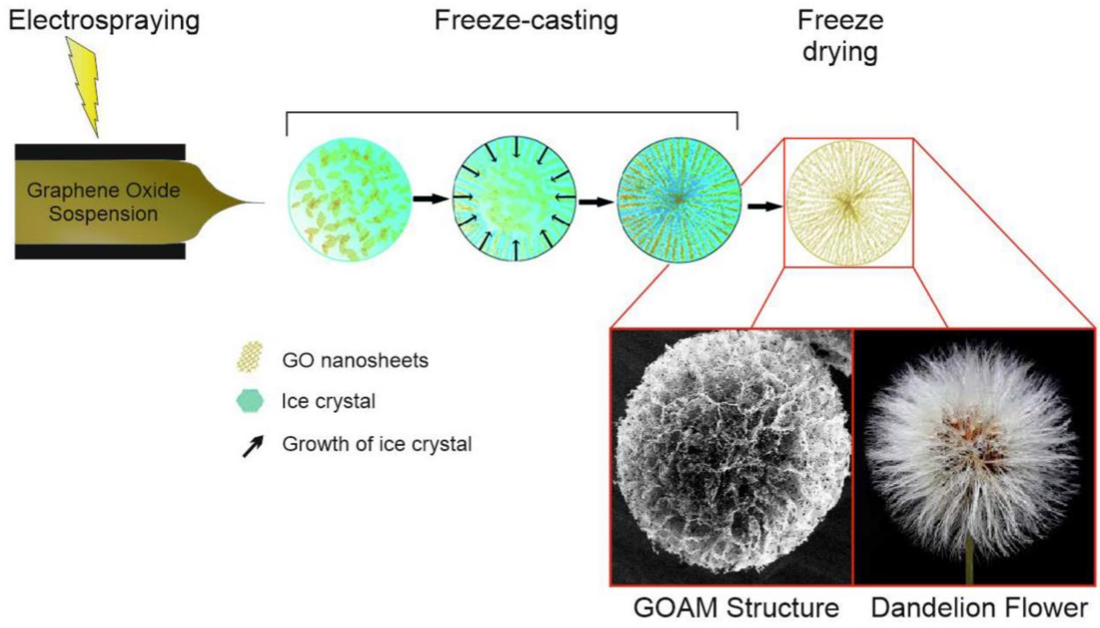

Figure 2.1 Schematic representation of GOAMs synthesis and the final structure of the microspheres showing a kind of resemblance with the dandelion (Taraxacum) flowers.

The coupling of electrospray and freeze casting allows for a high production speed per single unit (single GOAM sphere). By approximating the droplet radius of the starting dispersion with that of the final GOAM structure (~100 μm) and considering a nebulization speed of 0.1 mL/min, a production speed of ~400 units per second is obtained. With this production speed, assuming that the GOAMs structures are arranged on a plane, e.g., a compact hexagonal pattern, the obtained surface coverage speed is ~8 cm^2/min. These values refer to a single electrospray nozzle; therefore, the implementation with a microfabricated nozzle multiplex matrix would increase the production speed in proportion to the number of nozzles.[20 , 21] From this, it follows that this technique can quickly produce a significant amount of a porous carbon material.

Due to its properties and versatility, G is also used in the production of high-performance electrocatalysts for the hydrogen evolution reaction (HER).[22] Among these, transition metal dichalcogenides (TMDCs)/G hybrid systems are widely studied as alternatives to Pt-based electrocatalysts for HER.[23–25] In this work, we report on the preparation of an innovative hybrid electrocatalyst coupling TMDCs nanosheets with dandelion-like prGOAMs (TMDC/prGOAM) by electrospray and freeze casting techniques. The aim is to prove that it is possible to integrate into the prGOAM network the functional properties of catalysts without altering the microchannel central divergence morphology. The procedure of incorporation has been optimized using exfoliated $MoSe_2$, and subsequently it was successfully extended to other exfoliated TMDCs, i.e., MoS_2 , WS_2 and WSe_2 .

The new TMDC/prGOAM catalysts display an interesting improvement of the HER activity in an acidic environment compared to the pristine TMDC, confirming a kind of synergetic interaction between the TMDC catalyst and the G layers. Moreover, the comparison of the HER results of TMDC/prGOAM modified electrodes with those obtained from TMDC/prGO and TMDC/Vulcan analogous hybrid materials (benchmark samples) allowed us to demonstrate the role of the 3D architecture in the catalytic HER performance. More interestingly, this 3D architecture is also preserved after the electrochemical tests. The hybrid electrocatalysts were also HER verified under light in photoelectron catalytic (PEC) tests displaying interesting results.

2.2 Experimental section

2.2.1 Synthesis of Graphene Oxide Aerogel Microspheres (GOAMs)

GOAMs were prepared following a modified version of the procedure by Liao et al..[15] A 6mg/mL GO aqueous suspension was prepared, stirred overnight and then transferred into a syringe with a curved needle connected to a high voltage power supply. The electrospray parameters were as it follows: the flow was set to 0.1 mL/min; the electrospray voltage: 10 kV; the distance between the tip of the syringe and the surface of the collection beaker: 10 cm. The beaker (electrically grounded) containing n-hexane was cooled to − 78 ℃ by an acetone-dry ice bath. Under the action of the electric potential the solution ejected from the tip forms a Taylor cone and then a microjet, which eventually separates into microdroplets.

When the nebulized solution encounters the cold receiving solution, the spherical water microdroplets quickly freeze converting into GO ice microspheres, which were recovered through a metallic sieve and transferred into a cooled vial to avoid the thaw of the sample. Finally, the GOAMs were obtained by removing the water by freeze-drying. It is worth noting that the n-hexane level in the collection beaker significantly decreases for long electrospray-synthesis time (>1 h). Since the distance between the syringe tip and the solution meniscus affects the dimensions of the microstructure, the variation in time of this distance can influence the average size of the microspheres.[15]

2.2.2 Preparation of Exfoliated MX_2 TMDCs (M = Mo, W; X = S, Se)

Exfoliated MX_2 TMDCs nanosheets were obtained from the following bulk materials: MoS_2 , $MoSe_2$, WS_2 and WSe_2. The exfoliation procedure was carried out by Li-intercalation according to a standard protocol.[26 – 30] In a dry-box, 2 mmol of TMDC (average size of 60–90 μm) and 5 mmol of $LiBH_4$ were ground together in a mortar and transferred into a tube. The tube was then connected to a Schlenk line and after three vacuum-N_2 cycles, it was left under N_2 atmosphere and heated into a sand bath at 330 ℃ for 4 days. The resulting solid Li_xMX_2 was poured into 300 mL of Milli-Q water, previously saturated by N_2 bubbling, and the so obtained black suspension was sonicated for 30 min. To remove the generated LiOH, three centrifuge washing cycles were performed (10,000 rpm, RCF 19236-g, 15 min); at the end of each cycle, the supernatant was replaced with 50 mL of degassed Milli-Q water. Finally, the clean TMDC solid was dispersed 100 mL of Milli-Q water and freeze-dried to get a solid powder.

2.2.3 Synthesis of MX_2/GOAM and MX_2 /prGOAM

The TMDC/GOAM samples were obtained by the addition of a defined amount of exfoliated TMDC to the starting GO aqueous solution and following the same procedure described above. The TMDC concentration was optimized in the case of $MoSe_2$, by HER characterizing the final materials: the best electrochemical activity was obtained by using 5 mg/mL (0.02 M). For the successive preparation of the MoS_2/GOAM, WS_2/GOAM and WSe_2/GOAM, the mass concentration was kept constant.

The TMDC/prGOAM samples were obtained from the corresponding TMDC/GOAM systems, after heat treatment in a tubular oven at 450 ℃ (ramp 5 ℃ min^{-1}) for 2 h in an Ar:H_2= 90:10 (100 sccm in total) atmosphere. Two control experiments were performed in the same conditions at 150 and 900 ℃.

The TMDC:C ratio in the nebulized drops during the electrospray step is assumed the same as that of the starting suspension. Therefore, the TMDC:C ratio in TMDC/GOAM and TMDC/prGOAM systems should not deviate significantly from the nominal one of the initial suspensions.

2.2.4 Preparation of Benchmark Samples

The electrocatalytic performances of the $MoSe_2$/prGOAM systems have been compared with some benchmarks based on $MoSe_2$/carbon systems: GO and commercial Vulcan XC-72 (Cabot Corporation, Boston, MA, USA). The $MoSe_2$ /carbon were obtained according to the following procedure: 6 mg of reference carbon material and 5 mg of $MoSe_2$ were ground together in a mortar and the obtained mixture was heated at 450 ℃ in a tubular furnace with a Ar:H_2=90:10 (100 sccm in total) flow for 2 h.

A similar argument to what has been said for the preparation of TMDC/GOAM and TMD/prGOAM is also valid for the benchmark sample TMDC: C ratio.

2.2.5 Physico-Chemical Characterization

Scanning electron microscopy (SEM) micrographs were acquired using a field emission source equipped with a GEMINI column (Zeiss Supra VP35) with an acceleration voltage of 5 kV using secondary electron detection. Energy Dispersive X-ray Analysis (EDX) chemical mapping was recorded on the same instrument using an Oxford Instruments detector. Raman spectra were obtained with a ThermoFisher DXR Raman microscope. The spectra were recorded using a laser with an excitation wavelength of 532 nm (0.1 mW), focused on the sample with a 50× objective (Olympus).

XPS data were acquired in a custom-designed UHV system equipped with an EA 125 Omicron electron analyser with five channeltrons, working at a base pressure of 10^{-10} mbar. Core level photoemission spectra were taken in normal emission using the Mg K α emission line (hv = 1253.6 eV) of a nonmonochromated dual-anode DAR400 X-ray source. High resolution spectra were acquired using 0.5 s dwell time, 0.1 eV energy steps, and 20 eV pass energy. The multipeak analysis of the C 1s, Mo 3d, W 4f, Se 3d and S 2p photoemission lines was performed by means of Voigt functions and subtracting a Shirley background using the KolXPD software.[30]

2.2.6 Electrochemical Characterization

The electrocatalytic studies were performed in a Teflon electrochemical cell (see Figure 2.2b), using a Ag/AgCl (3M KCl) electrode (calibrated as +0.218 V vs. The reversible hydrogen electrode, RHE) and a glassy carbon (GC) rod as reference (RE) and counter electrode (CE), respectively. The working electrode (WE) was prepared by depositing 25 µL of the catalyst ink on a GC electrode (area delimited to 4.5 mm diameter), corresponding to an active material loading of 142 µg cm^{-2} . The catalyst ink was formulated by dispersing 10 mg of sample and 20 µL of Nafion in 1 mL of ethanol, then drop casted on the WE, and finally dried in vacuum. To deposit undamaged GOAMs, it was necessary to widen the hole of the micropipette tip. Due to the typical GOAMs' size (~100 μ m) it was rather difficult to create a mechanically stable and homogeneous layer of uniform thickness on the WE: to achieve the goal the just drop-casted layer was added with 50 µL of ethanol. The HER measurements were carried out in N_2-saturated 0.5 M H_2SO_4 solution at room temperature.

Polarization curves were recorded from +0.05 V to −0.30 V vs. RHE using a scan rate of 0.005 V s^{-1} . Polarization curves with the same parameters were recorded in the presence of white LED (light intensity equal to 97 mW cm^{-2} for PEC measurements (Figure 2.2a). Cyclic voltammetry (CV) curves under light exposure were recorded from +0.05 V to − 0.15 V vs. RHE using a scan rate of 0.005 Vs^{-1} to investigate the photodegradation process of $MoSe_2$/prGOAM. The distance between the LED and the WE in electrolyte was about 2 cm. Due to the equilibrium potential for HER, the overpotential values (η) reported below are equal to the electrochemical potential in absolute value.

The potential scan was carried out employing a potentiostat Autolab PGSTAT204 (Metrohm). The potentiostat unit was paired to the optical desk to control the LED during PEC measurements. Currents presented in the text are normalized by the geometrical area and iR-corrected by using the resistance determined by electrochemical impedance spectroscopy (EIS) measurements. EIS was performed at η= 0.28 V (100 kHz to 0.1 Hz) and fitted using a R (RQ) as equivalent circuit.

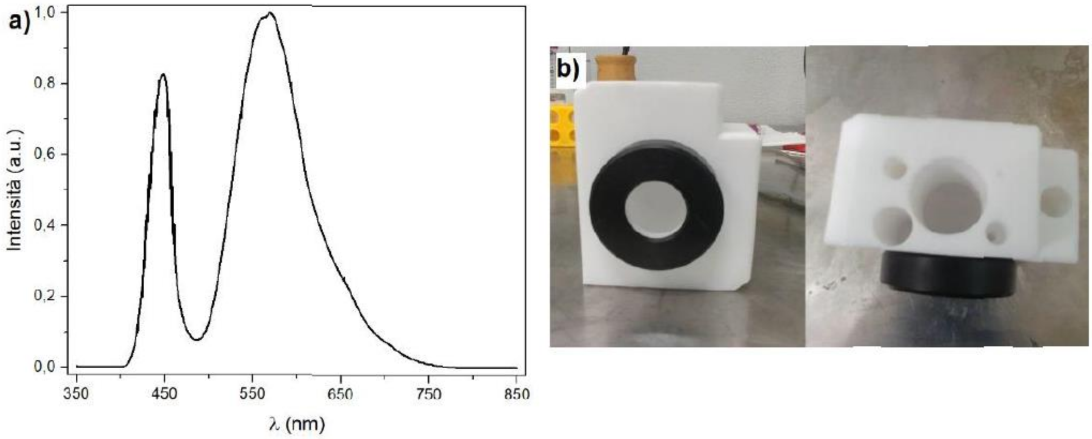

Figure 2.2 (a) Emission spectra of white LED and (b) teflon electrochemical cell with quartz windows for PEC.

2.3 Results and Discussion

2.3.1. Chemical and Structural Characterization

The first step of this study was to test the feasibility to make hybrid TMDC/GOAM systems that preserve the dandelion-like morphology. For the realization of these systems, we have chosen to follow a bottom-up approach. Few-monolayer TMDC and GO were used as building blocks for the target 3D architecture. The search for the optimal TMDC:GO ratio was carried out on the $MoSe_2$/GOAM system taking into consideration both the preservation of the 3D dandelion-like architecture and the HER performance. The preparation of the other TMDC/GOAM systems was subsequently adopted for the same optimized ratio value obtained on $MoSe_2$/GOAM.

The exfoliated $MoSe_2$ nanosheets were obtained as described in the Section 2 and characterized by SEM, Raman and XPS, comparing the data with those measured on analogous bulk materials. Chemical exfoliation produces few layer thick nanosheets that according to the SEM images (Figure 2.3a), have an average lateral size in the micrometer range.

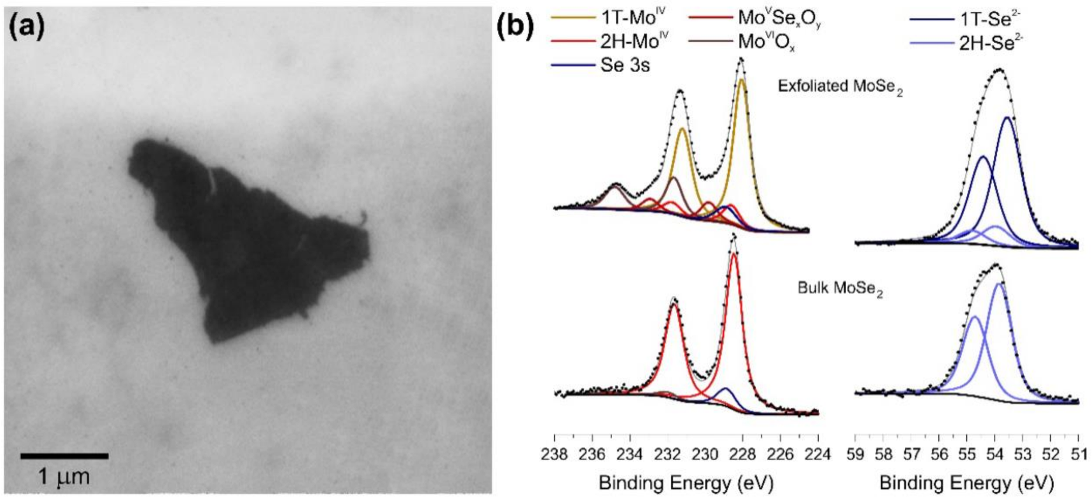

Figure 2.3 (a) Typical SEM image of the exfoliated $MoSe_2$ supported on an Au substrate; (b) XPS characterization of exfoliated and bulk $MoSe_2$. On the left the Mo 3d region, on the right the Se 3d region.

The exfoliated TMDCs samples are typically composed of a mixture of 1T and 2H polymorphs, which can be identified by Raman spectroscopy: in Figure 2.4 we report the Raman spectra of the bulk $MoSe_2$ and of the exfoliated sheets. The Raman spectrum of bulk $MoSe_2$ shows three signals at 167, 241 and 285 cm^{-1} , which can be associated, respectively, with the E_{1g} , A_{1g} and E_{2g} normal modes of the 2H-$MoSe_2$. After exfoliation, the normal modes E_{1g} and A_{1g} of the 2H phase (171 and 238 cm^{-1}) , and the modes J_1 , J_2 , J_3 and A_{1g} of the 1T phase (108, 154, 228 and 287 cm^{-1}) become visible.[31] The Raman spectrum of the exfoliated sample reported in Figure 2.4b is compatible with the literature data of few-layers $MoSe_2$ [32] and show the typical feature of both polymorphs.

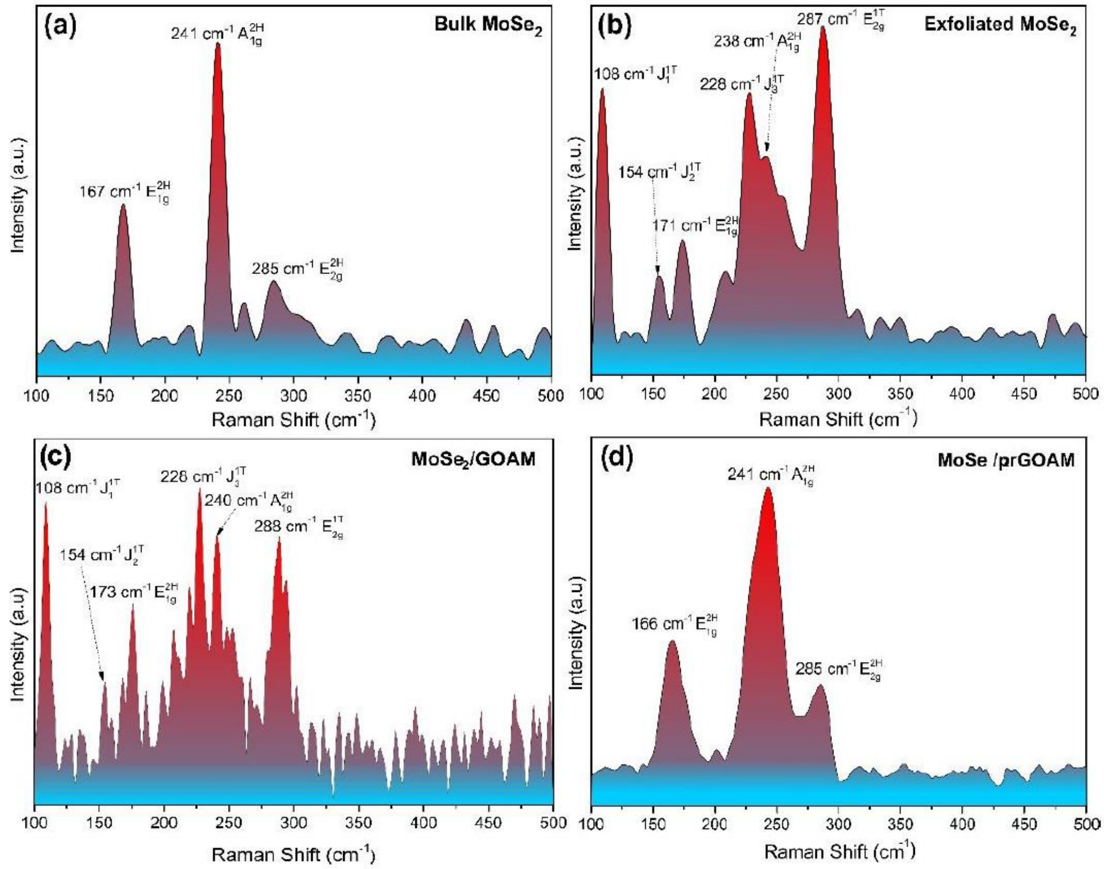

Figure 2.4 Raman spectra of bulk MoSe$_2$ (a), exfoliated MoSe$_2$ (b), MoSe$_2$/GOAM hybrid (c) and MoSe$_2$/prGOAM hybrid samples (d).

An alternative and more quantitative evaluation of the exfoliated material was obtained using XPS (Figure 2.3b), which allows calculating the 2H:1T ratio and the amount of oxide formed as a consequence of air exposure (see Tables 2.1 and 2.2 for details). The Mo 3d region of the MoSe$_2$ bulk material can be deconvoluted in two doublets and a single peak at a binding energy (BE) of about 229 eV corresponding to the Se 3s signal. The main doublet, with the Mo 3d$_{5/2}$ and 3d$_{3/2}$ peaks centered at 228.5 eV and 231.6 eV, is attributed to Mo (IV) species of 2H-MoSe$_2$; the high BE doublet (232.0–234.2 eV) is relative to molybdenum (VI) oxide deriving from surface oxidation.[33 , 34] As mentioned above, the intercalation of Li ions induces the 2H → 1T phase transition, which causes the appearance of 1T-MoSe$_2$ signals in the spectra of the exfoliated sample. In the Mo 3d photoemission line, a doublet with peaks centered at 228 eV and 231.2 eV corresponding to the Mo (IV) 3d$_{5/2}$ and 3d$_{3/2}$ and a peak at 228.6 eV relative to the Se 3s have to be included in the fitting procedure.[35] The analysis of the Se 3d core level is analogous to that of Mo 3d; for the bulk MoSe$_2$ material only one doublet with peaks centered at 53.8 eV and 54.7 eV is identified, which is associated with Se^{2-} ions of 2H-MoSe$_2$, while for the exfoliated sample, a second doublet at lower BE (53.5 and 54.4 eV) corresponding to the 1T-$MoSe_2$ [35] phase is observed. In Table 2.1 we report the 2H:1T ratio determined by XPS. It is possible to quantify the degree of the 2H→1T transformation (final 88% of 1T), with only a limited oxidation of the material.

Table 2.1 Binding Energy (BE) values and composition of Mo 3d core level of the XPS data shown in Figure 2.3b of the main text. The reported BE values error is ±0.1 eV. Percentage value of non-oxidized Mo and 2H: 1T ratio of $MoSe_2$ are reported as well.

	Exfoliated WSe_2		**Bulk WSe_2**	
Mo 3d	**BE (eV)**	**%**	**BE (eV)**	**%**
1T-Mo^{IV}	228.0	66.0	-	-
2H-Mo^{IV}	228.6	8.6	228.5	97.0
$Mo^{V}Se_xO_y$	229.8	8.4	-	-
$Wo^{VI}O_x$	231.8	17.0	232.0	3.0
1T:2H	88:12		0:100	
W^{IV}/W	75%		97%	

Table 2.2 Se 3d BE values and surface composition of the XPS data shown in Figure 2b of the main text shown in Figure 2.3b. Se 3s BE values are reported as well. The BE values error is ±0.1 eV.

	Exfoliated WSe_2		**Bulk WSe_2**	
Se 3d	**BE (eV)**	**%**	**BE (eV)**	**%**
1T-Se^{2-}	53.5	86.9	-	-
2H-Se^{2-}	53.9	13.1	53.8	100
2H-Se 3s	228.8	-	229.2	-

Different samples of $MoSe_2$/GOAMs were prepared, changing the concentration of exfoliated $MoSe_2$ in the initial suspension while keeping the GO concentration constant (6 mg/mL). The samples were later characterized by SEM (Figure 2.5) and by EDX chemical mapping (Figure 2.6). The 3, 5, 7 and 9 mg/mL $MoSe_2$ concentrations were tested to find the TMDC:GO ratio range that preserves the dandelion-like morphology. The morphological GOAM features are conserved until 7 mg/mL $MoSe_2$ concentration.

Outside this range, a Taylor cone instability, and the absence of microstructure in the final material were observed. In detail, using the 9 mg/mL $MoSe_2$ concentrations, aggregates of irregular shapes and different sizes were observed (Figure 2.5d).

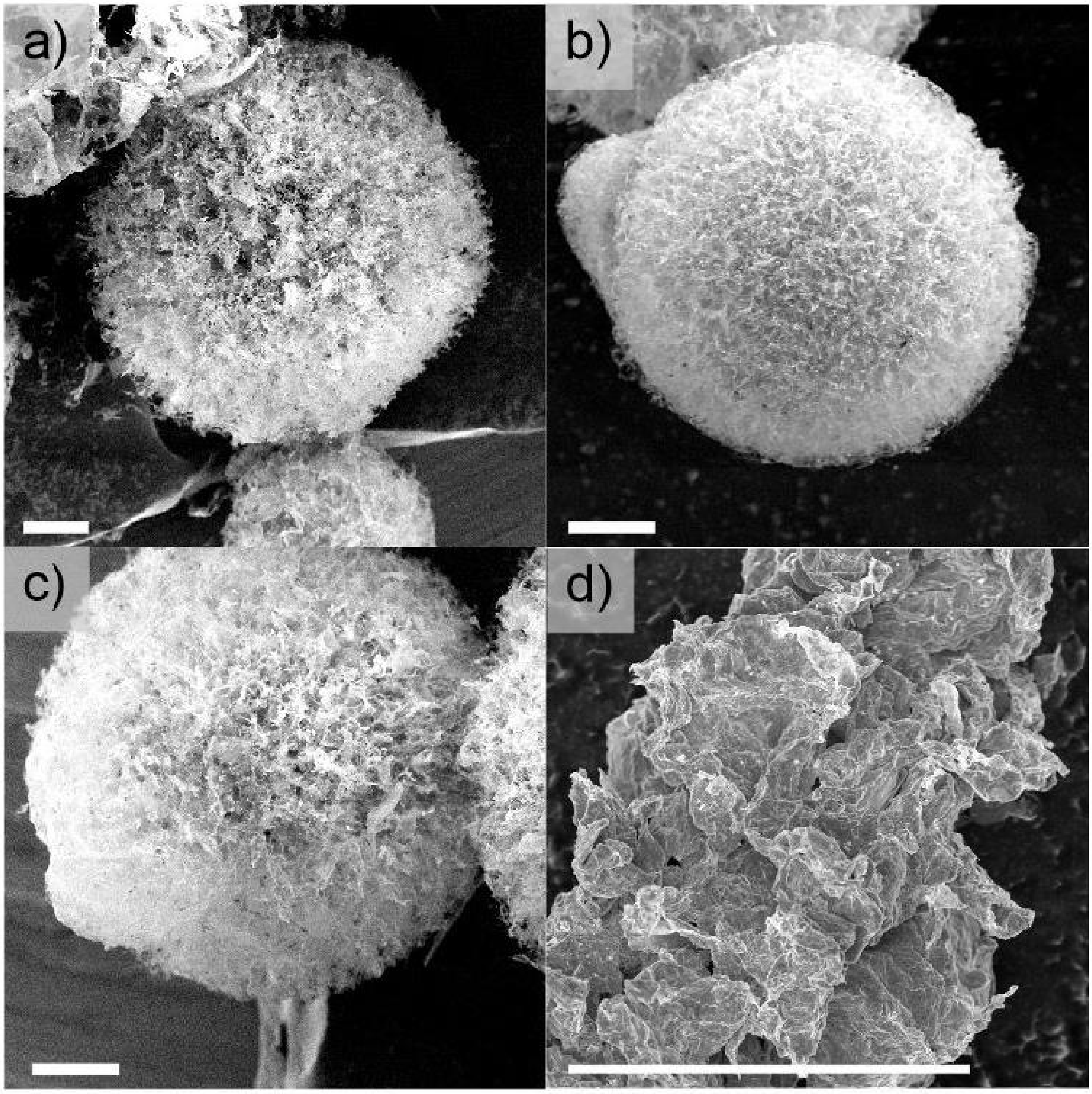

Figure 2.5 (a–d) SEM images of $MoSe_2$/GOAM samples, obtained using respectively the 3, 5, 7, and 9 mg/mL solution of $MoSe_2$. Scale bars are 50 μm.

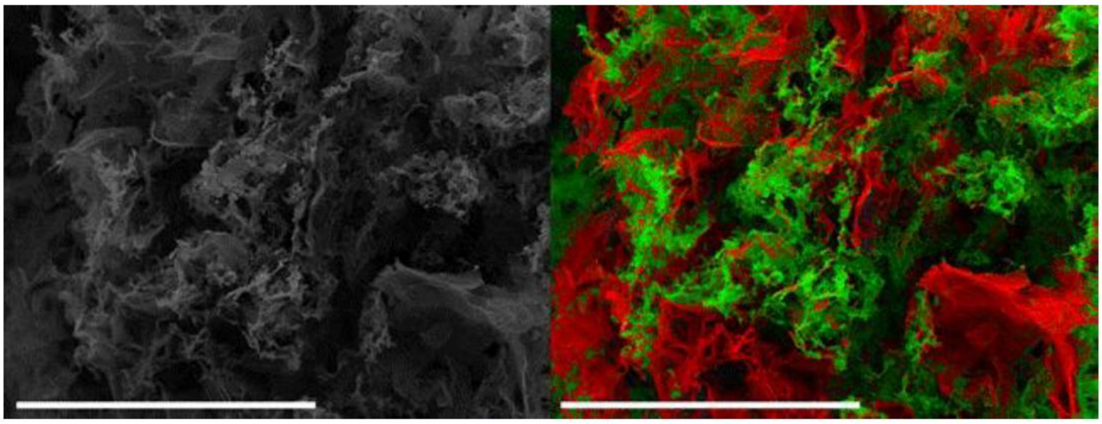

Figure 2.6 SEM and EDX chemical map of the 5 mg/mL $MoSe_2$/GOAM sample, showing the overlap of C (red) and Mo (green) signals. Scale bars are 50 µm.

As for the actual mechanism of the formation of the hybrid materials, we can propose that during the freeze-casting step, the expanding ice crystals create contact zones between the GO sheets and the exfoliated TMDC, promoting their interaction through van der Waals forces. If enough carboxyl groups (from GO) make substantial crosslinking between the GO sheets, during the subsequent lyophilisation, when the ice compression relaxes, the established crosslinking points allow preserving the central diverging microchannel structure. Therefore, when a high TMDC concentration is reached, the formation of sufficient crosslinking points might be inhibited.

However, the as-prepared $MoSe_2$/GOAM systems are not suitable for electrochemical investigations since they are mechanically unstable, and the microstructure is completely lost when the samples are dispersed in polar solvents (water, ethanol, DMF). These solvents compete with the weak interactions (H-bonds) of the crosslinking points in the GOAM structure, inducing the separation of the GO sheets. Thence, the obtained TMDC/GOAM composites were annealed to stabilize the GOAM structure, causing a covalent crosslinking between graphene sheets.[36 , 37] while partially reducing the GO to prGO. We explored the best annealing temperature in the case of $MoSe_2$/rGOAM samples by using a tubular oven in an $Ar:H_2$= 90:10 flow (100 sccm in total) for 2 h at different temperatures (150, 450, 900 ℃). The new $MoSe_2$/prGOAM materials allowed preparing a stable catalyst ink to test their HER activities (vide infra). In addition, the heat treatment induces a partial reduction of GO to prGO, so partially healing the graphene structure and restoring the electrical conductivity.[19 , 38] The XPS and Raman spectra were used to characterize the annealing process at 450 ℃: the increase of Csp^{x}/CO_x peaks area ratio in XPS spectra (Figure 2.7 and Table 2.3), and the decrease in the D/G and D/G peak intensity ratio in the Raman signals (see Figure 2.8 and Table 2.5) confirms the partial establishment of the sp^2 network following the 450 ℃ annealing .[39] Additionally, the analysis of the second-order Raman data of graphene suggests the presence of 2–3 layers of graphene-related material; this value is invariant to the annealing process.[40] Interestingly, the SEM micrographs in Figure 2.9 and Figure 2.12 show that the annealing preserves the dandelion-like morphology. The EDX chemical maps in Figure 2.10 show the dispersion of the exfoliated $MoSe_2$ sheets in the rGOAMs: actually, it is possible to identify features of about 1 μm, compatible with exfolia ted $MoSe_2$, which decorate the GO sheets, most probably through plane-to-plane interactions. Figure 2.11 shows an optical microscope image of a section of a single $MoSe_2$/prGOAM included in the epoxy resin; this image further proves that the presence of TMDC does not alter the formation of centrally diverging microchannels.

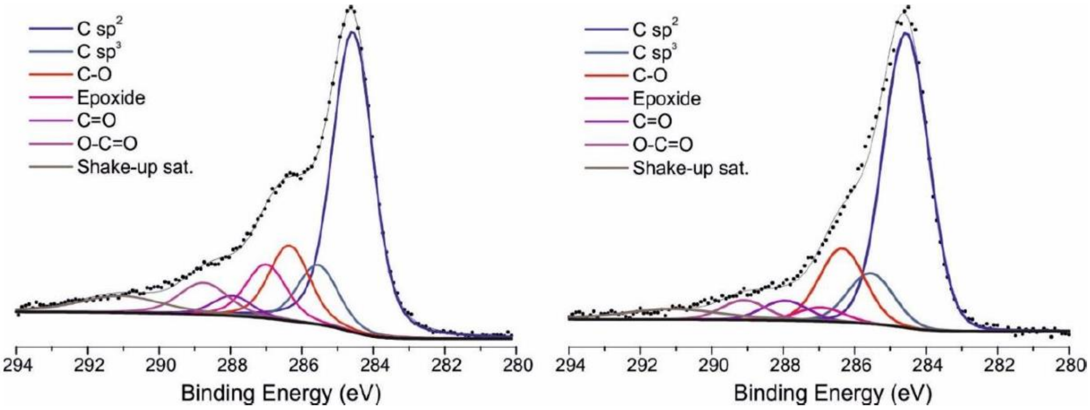

Figure 2.7 XPS spectra of the C 1s region of GO (left) and of the $MoSe_2$/prGOAM sample reduced to 450 ℃ (right).

Table 2.3. BE values and composition of C 1s photoemission line. The reported values error is ±0.1 eV.

	GO		$MoSe_2$ /prGOAM	
C 1s	**BE (eV)**	**%**	**BE (eV)**	**%**
C sp^2	284.6	54.5	284.5	62.3
C sp^3	285.6	10.9	285.5	10.8
C-O	286.4	13.8	286.4	15.6
Epoxide	287.0	8.9	287.0	2.9
C=O	288.0	4.7	288.0	4.3

O-C=O	288.8	7.2	289.0	4.2
C sp ^{x} /CO $_x$	1.9		2.7	

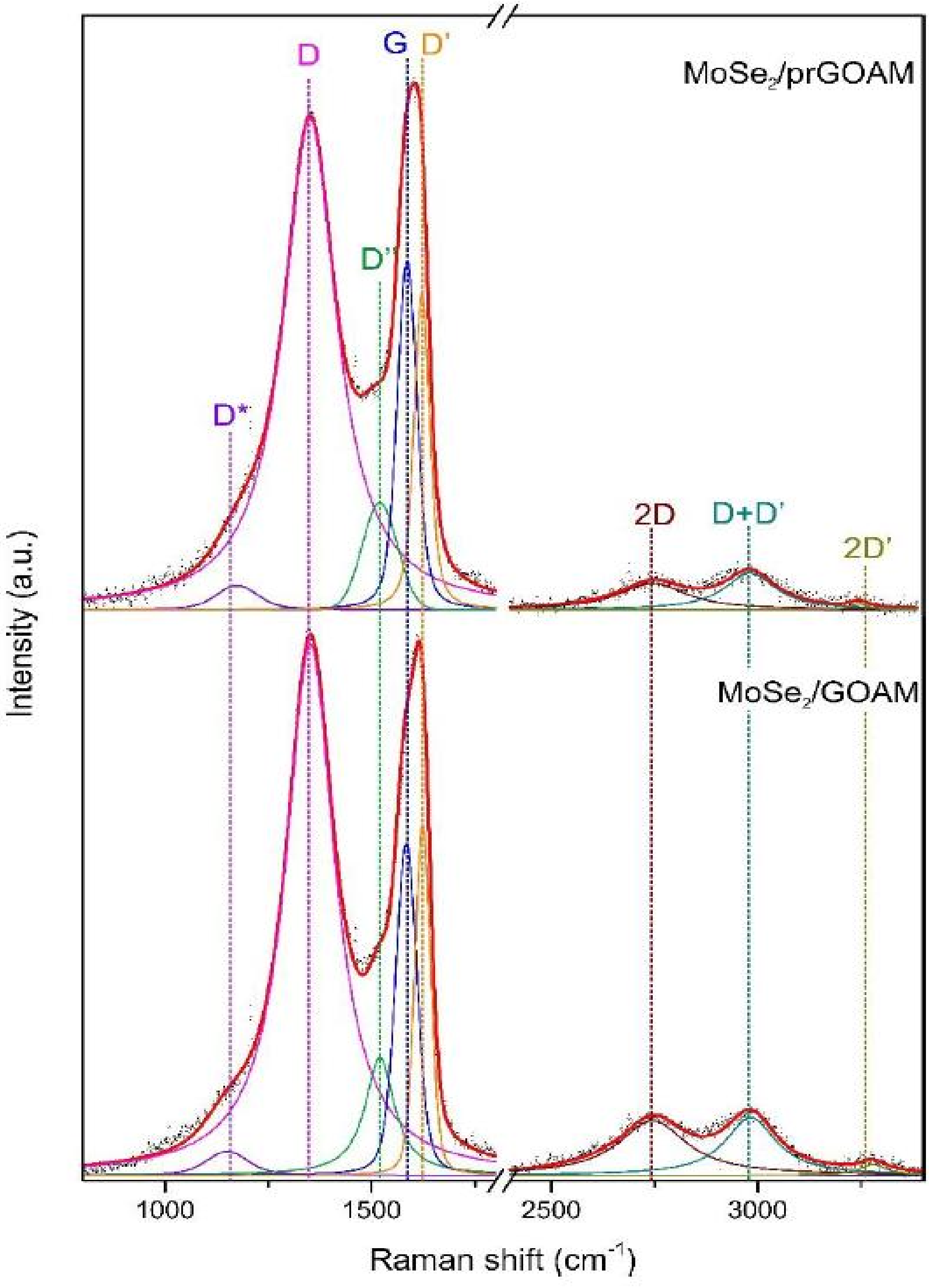

Figure 2.8 Deconvolution of the Raman spectrum of graphene oxide of MoSe$_2$/GOAM and MoSe$_2$/prGOAM reduced to 450 ℃ (right).

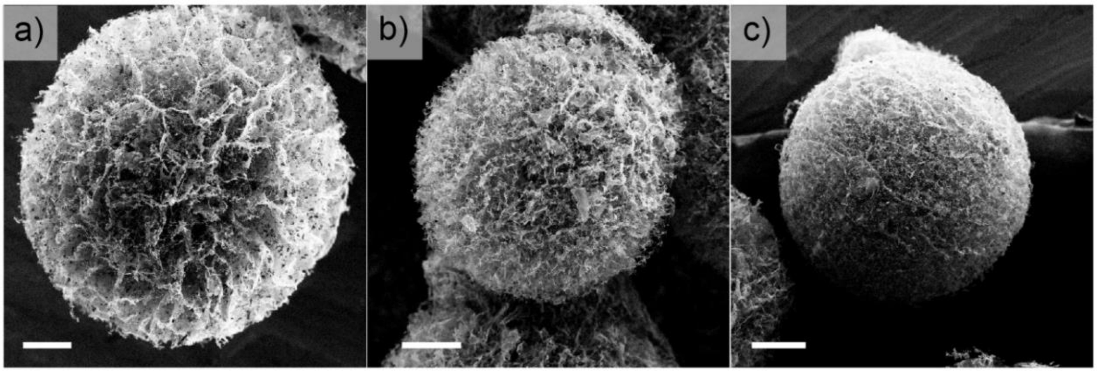

Figure 2.9 SEM images of $MoSe_2$/prGOAM samples reduced to 450 ℃ in the atmosphere Ar:H_2= 90:10 (100 sccm in total). $MoSe_2$/prGOAM samples obtained using a 3(a), 5(b), and 7 mg/mL (c) concentration of $MoSe_2$. Scale bars are 50 μm.

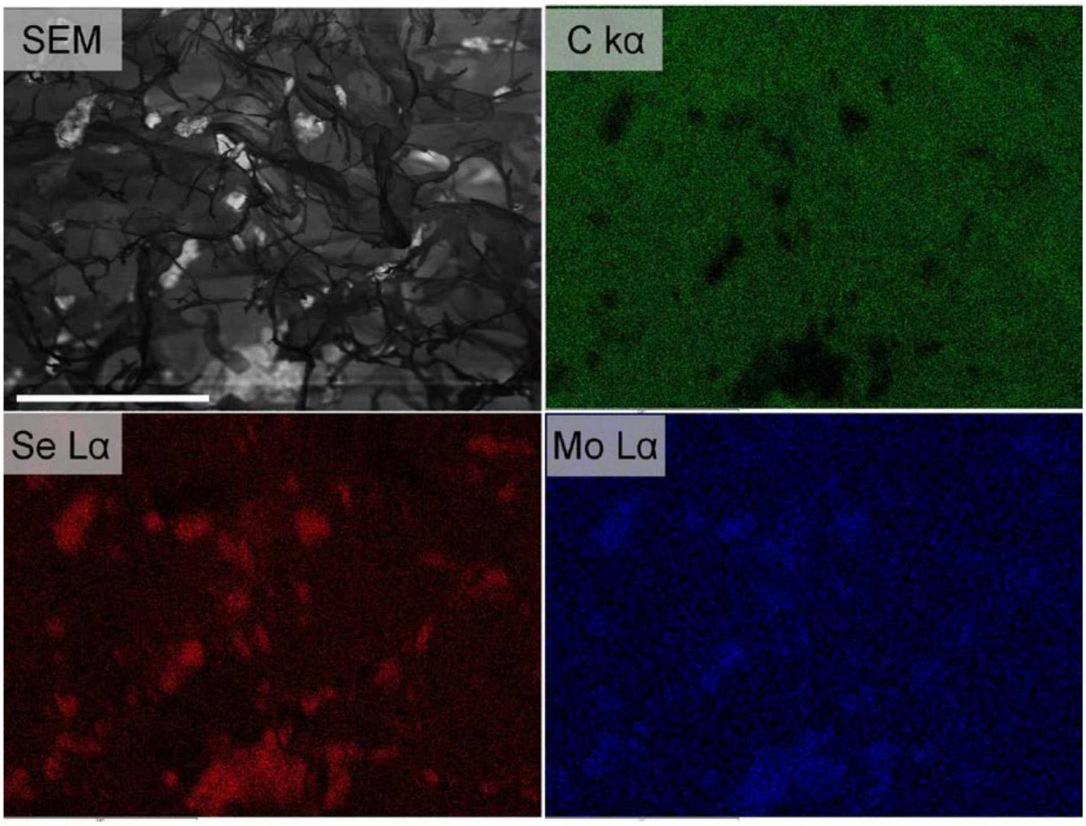

Figure 2.10 SEM images and EDX chemical map of the 5 mg/mL $MoSe_2$/prGOAM. EDX showing the maps of C (green) and Mo (blue) and Se (red) signals. Scale bars are 20 μm.

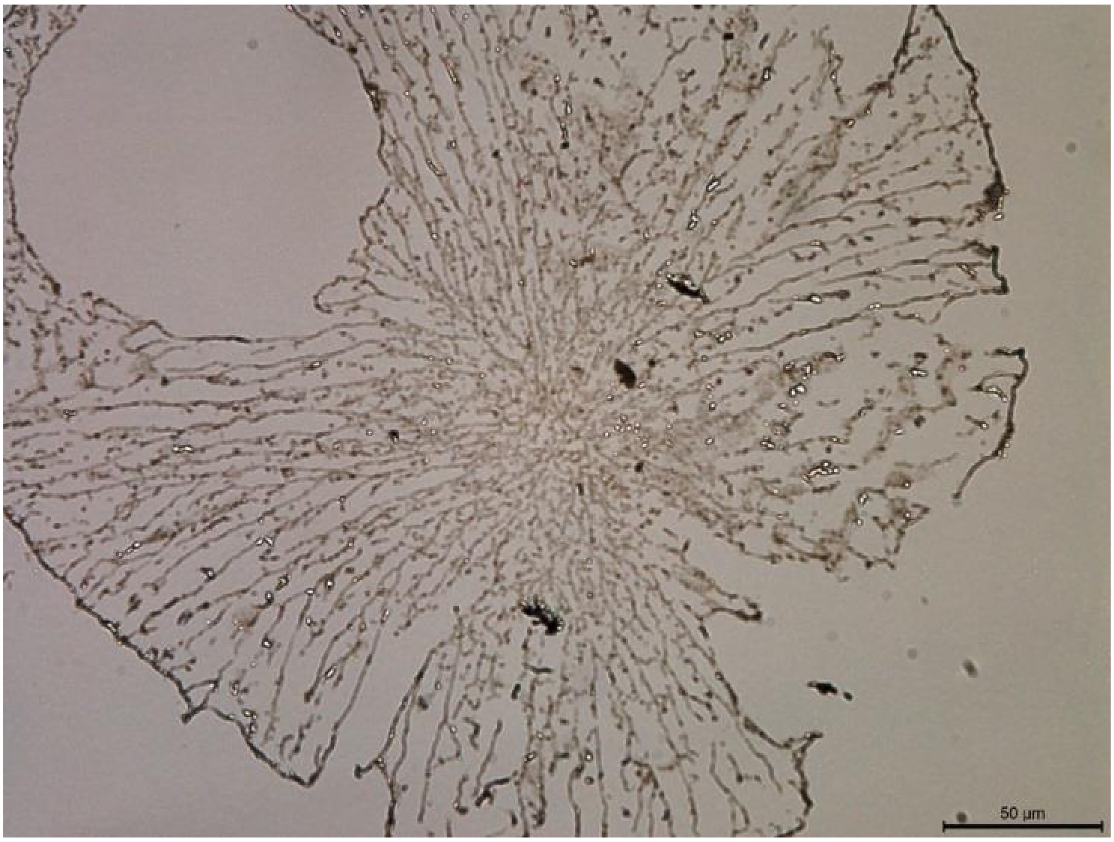

Figure 2.11 Optical microscope image (63x) of $MoSe_2$/prGOAM samples obtained by reduction at 450 ℃ with different scale bars.

Finally, the thermal treatment induces the 1T- to 2H-$MoSe_2$ phase transition [41] (see Raman in Figure 2.4), thus replacing the metallic phase, which typically shows better electrocatalytic performances, with the semiconducting polymorph, which on the other hand exhibits photoactivity (vide infra).[35]

2.3.2. Electrocatalytic HER Characterization

The $MoSe_2$/prGOAM systems can be dispersed in ethanol without losing their dandelion-like morphology, and even after the electrocatalytic test, no substantial differences could be observed (see Figure 2.12).

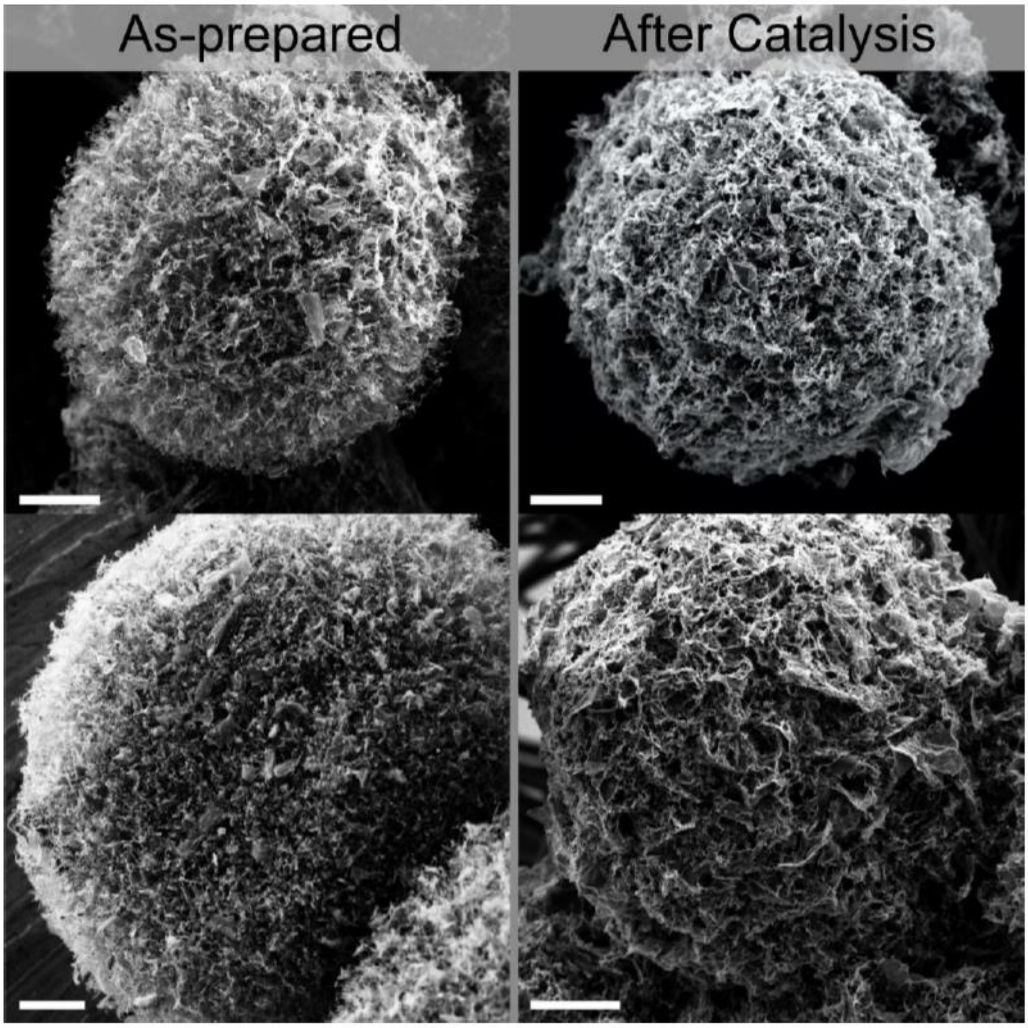

Figure 2.12 Comparison of the SEM images of the $MoSe_2$/prGOAM sample before and after the electrochemical tests. The reference sample is that obtained by heat treatment at 450 ℃ using a 5 mg/mL solution of $MoSe_2$. Scale bar are 50 μm.

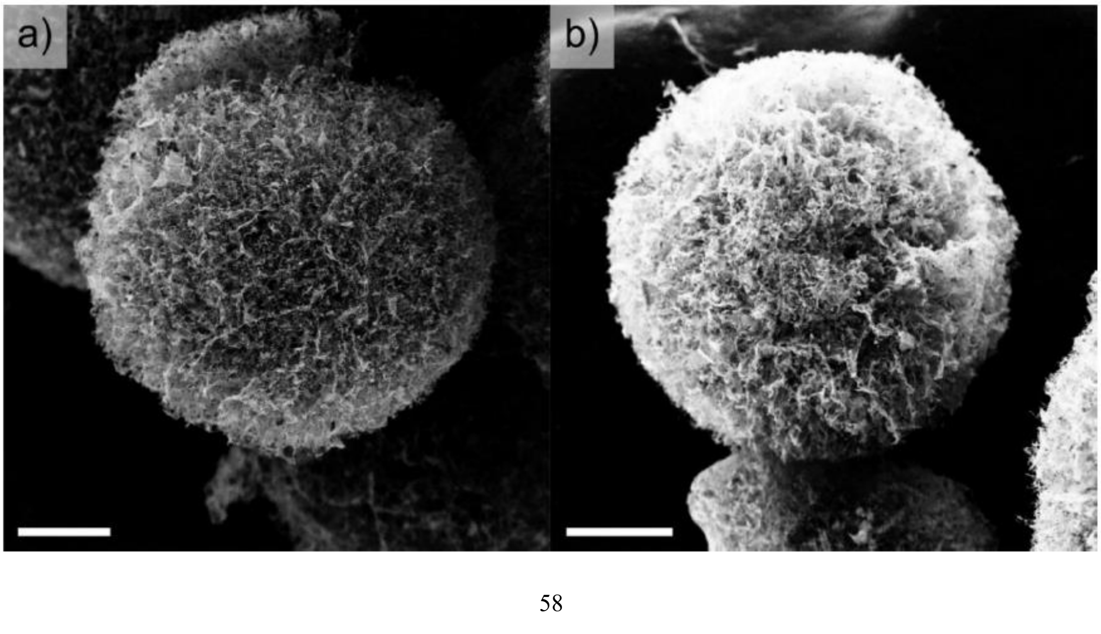

Figure 2.13 SEM images of $MoSe_2$/prGOAM samples obtained by reduction at 150 °C (left) and 900 °C (right). Scale bars are 100 μm.

Figure 2.16a shows the polarization curves of the $MoSe_2$/prGOAM systems obtained using different concentrations of $MoSe_2$, after annealing at 450 ℃; being the $MoSe_2$ nanosheet mostly present as 2H polymorph, we monitored PEC behavior as well, using a white LED to illuminate the working electrode (see Figure 2.2). As for performance descriptors, we report the Tafel slopes and the overpotentials at 10 $mAcm^{-2}$ (η_{10}). The activity parameters obtained from the polarization curves are shown in Table 2.6. The sample obtained using a $MoSe_2$ concentration of 5 mg/mL shows the best performances. Under illumination, all samples show an improvement of η_{10} of about 11% and a gain in terms of current density ($+j_{10}$) ranging from +3 to +7 mA/cm^2 ; the $+j_{10}$ value was obtained considering the j increase under light vs. dark at the value of η_{10} recorded in the dark condition. This result could find an explanation reminding what has been said for the mechanical stability of $MoSe_2$/GOAMs. The concentration of $MoSe_2$ included in the carbon structure influences the number of crosslinking points in the G network. A lower interconnection between the G sheets limits the possible electrons percolation paths in the hybrid system. Therefore, an excessive concentration limits the movement of electrons while a low concentration disadvantages the number of available catalytic sites. Based on the significant improvement under light, we retained that also a stability test was useful to understand if the TMDCs can degde under illumination. In detail, further polarization curves were acquired after 1000 CVs under light exposure (Figure 2.14 and Table 2.4). An η_{10} shift of 5 and 9 mV respectively for the light and dark condition and a decrease of $+j_{10}$ value of 1.3 mA/cm^2 are registered. The material used as WE was also characterized by Raman after the EC test (Figure 2.15 and Table 2.5); no significant variation was observed concerning the already discussed $MoSe_2$/prGOAM spectra (Figures 2.4 and 2.8). These results confirm a substantial stability under light exposure, proving that no significant photodegradation process occurs for $MoSe_2$/prGOAM.

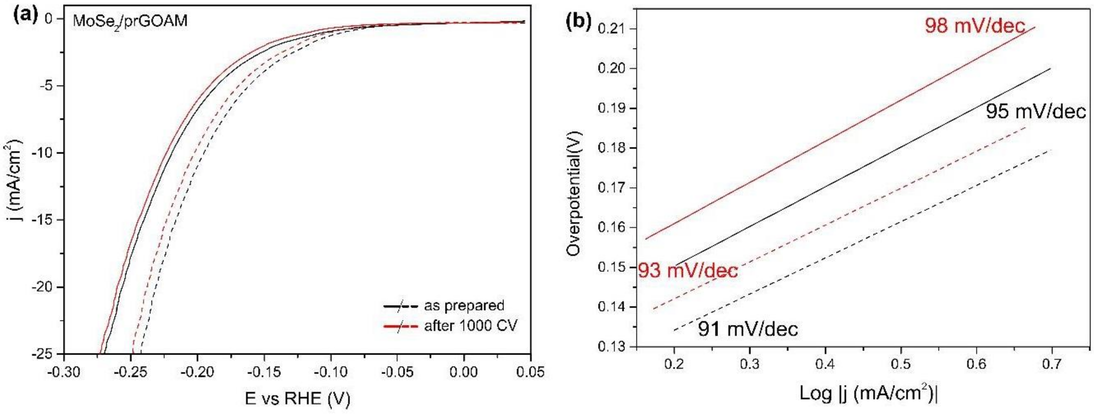

Figure 2.14 Polarization curves (a) and Tafel plots (b) for HER of as-prepared MoSe$_2$/prGOAM samples annealed at 450 ℃ (black) and after 1000 CVs under light exposure (red). Solid lines represent experiments in dark conditions, dashed lines the PEC-HER measurements performed under illumination.

Table 2.4 HER activity parameters of MoSe$_2$/prGOAM from data reported in Figure 2.14.

	η_{10} (mV)	**Tafel slope (mV/dec)**	**η_{10} LED (mV)**	**Tafel Slope LED (mV/dec)**	**$+j_{10}$ (mA/cm^2)**
MoSe$_2$ /prGOAM	-220 (5)	95 (1)	-194 (5)	91 (1)	6.6
MoSe$_2$ /prGOAM (post EC)	-225 (5)	98 (2)	-203 (5)	93 (1)	5.3

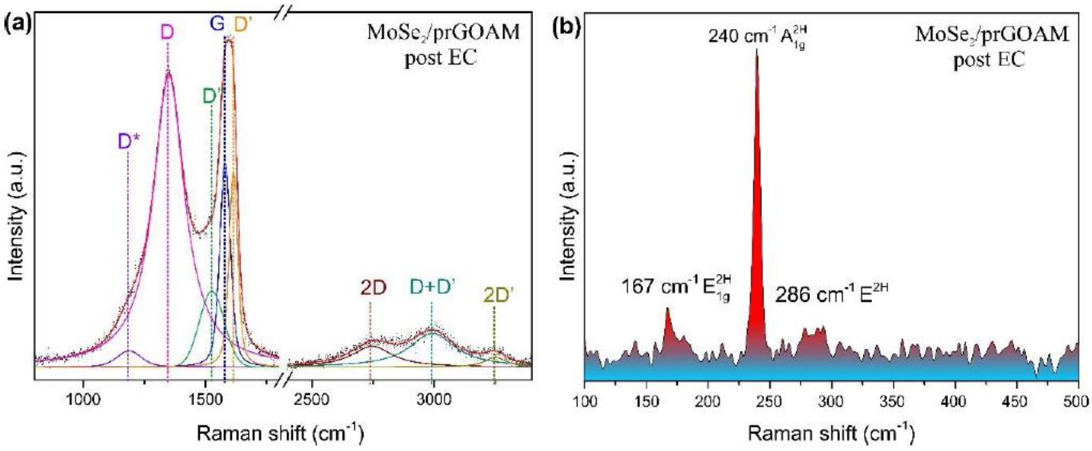

Figure 2.15 (a) Raman spectra of graphene oxide and (b) MoSe$_2$ of MoSe$_2$/prGOAM reduced to 450 ℃ after 1000 CVs under light exposure.

Table 2.5 Fitting parameters calculated for MoSe$_2$/GOAM and MoSe$_2$/prGOAM in the Raman spectra in Figure 2.8 and 2.15.

	ν (cm^{-1})									
	D*	**D**	**D’**	**D”**	**G**	**2D**	**2D’**	**I_D/I_G**	**$I_{D'}/I_G$**	**ν 2D − 2 ν D**
MoSe$_2$ /GOAM	1150	1351	1624	1520	1584	2744	3178	1.58	1.05	42
MoSe$_2$ /prGOAM	1174	1351	1622	1520	1585	2744	3190	1.41	0.90	42
MoSe$_2$ /prGOAM (post EC)	1187	1351	1622	1522	1584	2775	3249	1.42	0.93	43

Table 2.6 HER activity parameters of MoSe$_2$ /prGOAM from data reported in Figure 2.16a.

MoSe$_2$ Conc.	**η_{10} (mV)**	**η_{10} LED (mV)**	**$+j_{10}$ (mA/cm^2)**	**afel Slope (mV/dec)**	**Tafel Slope LED**

					(mV/dec)
3 mg/mL	276 (5)	247 (5)	3.6	182 (1)	177(1)
5 mg/mL	220 (5)	194 (5)	6.6	95 (2)	91 (1)
7 mg/mL	241 (5)	215 (5)	4.4	163 (1)	157 (1)

After finding the optimal $MoSe_2$ concentration, we also explored the role of the different annealing temperatures (150, 450, 900 ℃) (Figure 2.16c): the results displayed definitely give the best performances after a 450 ℃ annealing (remind that the SEM images do not show any change in the morphology at different temperature, Figure 2.9 and Figure 2.12). According to the literature, the electronic conductivity of the reduced GO depends significantly on the annealing temperature, passing from 400 Scm^{-1} after annealing at 900 ℃ to values lower than 50 Scm^{-1}at temperatures below 450 ℃ .[19 , 38] On the other hand, 200 °C sets the threshold for the 1T → 2H transition in exfoliated $MoSe_2$.[41] Therefore, 450 ℃ might represent a compromise between the transformation from GO to prGO and polymorphic transformation of $MoSe_2$. On the other hand, higher temperature treatments may also induce defects healing, which can be counterproductive in electrocatalysis.[38 , 41 – 43] The tested temperatures allow investigating the limit cases illustrated above: at 150 ℃, 1T - $MoSe_2$ should be preserved, but the electronic conductivity of the GO should be relatively low, while at 900 ℃, the opposite situation should occur.

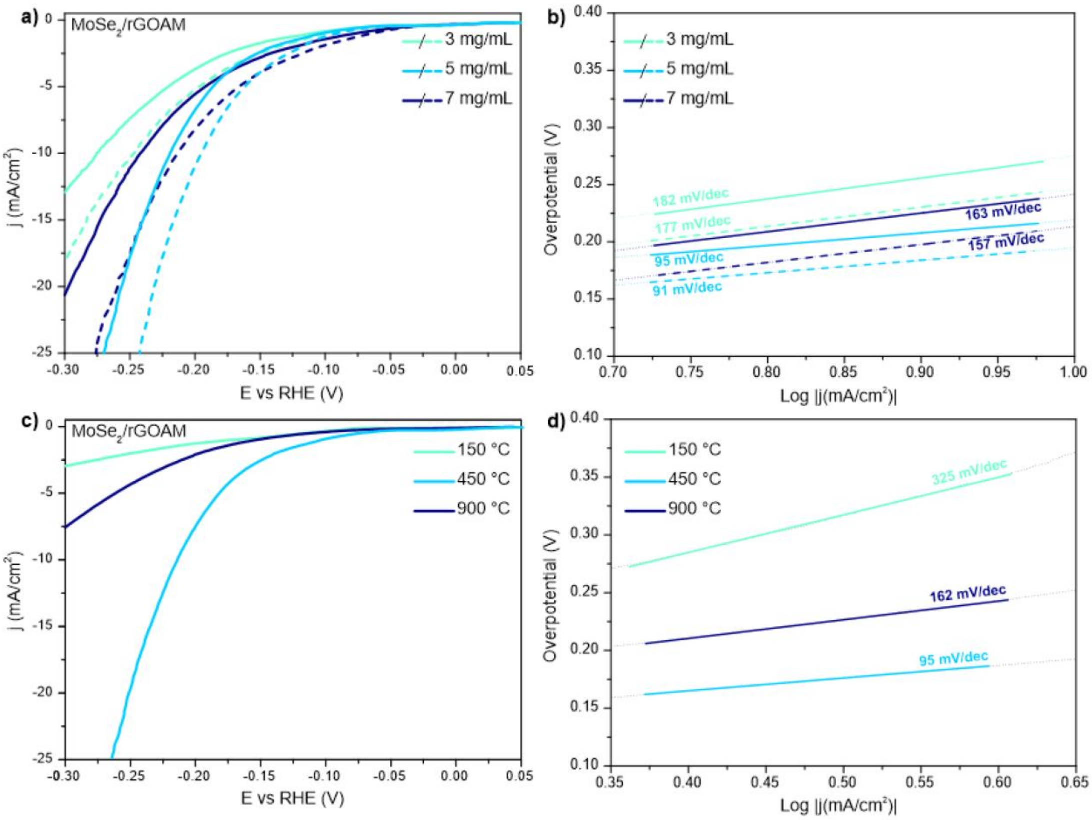

Figure 2.16 Polarization curves (a) and Tafel plots (b) for hydrogen evolution reaction (HER) of $MoSe_2$/prGOAM samples annealed at 450 ℃ obtained by using different concentrations of $MoSe_2$. Solid lines represent experiments in dark conditions, dashed lines the PEC-HER measurements performed under illumination. Polarization curves (c) and Tafel plot (d) for HER of $MoSe_2$/prGOAM samples obtained with 5 mg/mL $MoSe_2$ and different annealing temperatures.

In addition to η_{10} values, also the Tafel slopes for temperatures different from 450 ℃ (see Figure 2.16d) give an important feedback: they are not attributable to the typical mechanisms for HER (see the electrochemical data in Table 2.7). The sample reduced at 150 °C shows the worst performances, with a maximum current density (at − 0.4 V vs. RHE) lower than the 10 mA/cm^2 and with a Tafel slope greater than 300 mV/dec. This behavior is mainly attributable to the low electronic conductivity of GO sheets treated at low temperatures.[19] On the other hand, the sample reduced at 900 ℃ shows η_{10} values of about 330 mV and a Tafel slope of about 160 mV/dec. The poor performance is probably due to the strong prGO hydrophobicity, which limits the permeation of the electrolyte into the microchannels. On the other hand, at 450 ℃, the electronic conductivity and hydrophobicity of the prGO are sufficiently balanced, and the corresponding $MoSe_2$/prGOAM sample shows a η_{10} value of 220 mV and a Tafel slope of 95 mV/dec. This value suggests a Volmer-Heyrovsky mechanism for the

HER with the adsorption process as rate determining step.

Table 2.7 HER activity parameters of $MoSe_2$/prGOAM from data reported in Figure 2.16c.

Annealing T (℃)	**η_{10} (mV)**	**Tafel Slope (mV/dec)**
150		325(1)
450	220 (5)	95 (2)
900	332 (5)	162(1)

To understand if the dandelion-like morphology brings some advantage to the electrocatalytic performance, we compared the $MoSe_2$/prGOAM with some benchmark materials. $MoSe_2$/C systems where C is either GO and commercial Vulcan XC-72 have been prepared, as described in the Experimental Section, using either exfoliated $MoSe_2$ (e-$MoSe_2$) or bulk $MoSe_2$ (b-$MoSe_2$) as the active material and using the same annealing conditions as in the optimized $MoSe_2$/prGOAM sample. The tested benchmark samples are e-$MoSe_2$/prGO, e-$MoSe_2$/Vulcan and b-$MoSe_2$/Vulcan. The polarization curves of the different samples are shown in Figure 2.17, and the related electrochemical data are summarized in Table 2.8.

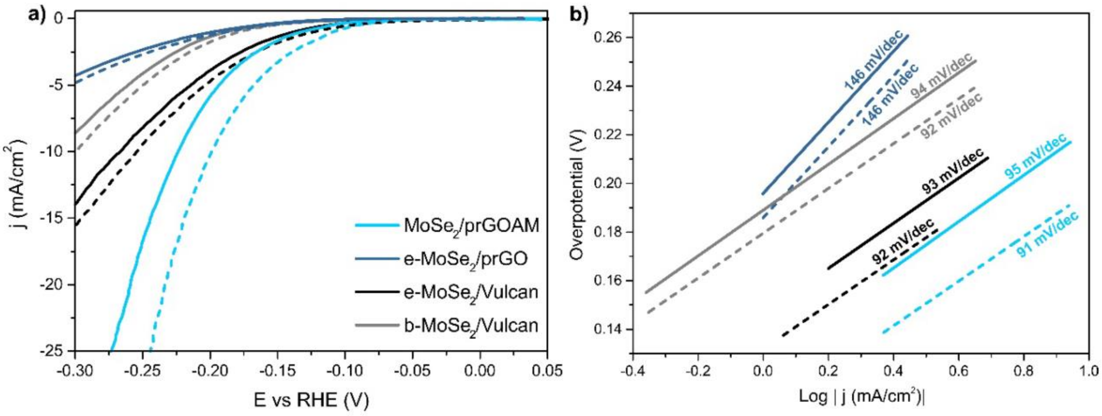

Figure 2.17 (a) Polarization curves for $MoSe_2$/prGOAM and the benchmark systems (see text). The dashed curves were obtained by illuminating the working electrode with white light (see Experimental Section); (b) related Tafel plots.

Table 2.8 HER and PEC-HER activity parameters from data reported in Figure 2.17.

	η_{10} (mV)	Tafel Slope (mV/dec)	η_{10} LED (mV)	Tafel Slope LED (mV/dec)	$+j_{10}$ (mA/cm^2)	j_0 (μA/cm ^{2})	j_0 LED (μA/cm ^{2})
e-MoSe$_2$ /prGO	393 (5)	146 (2)	382 (5)	146 (2)	0.8	46 (3)	53 (3)
b-MoSe$_2$ /Vulcan	314 (5)	92 (1)	299 (5)	92 (1)	1.5	10 (1)	11 (1)
e-MoSe$_2$ /Vulcan	266 (5)	93 (1)	254 (5)	92 (1)	1.5	27 (4)	37 (3)
MoSe$_2$ /prGOAM	220 (5)	95 (1)	194 (5)	91 (1)	6.6	47 (2)	73 (4)

The e-MoSe$_2$/prGO and MoSe$_2$/prGOAM systems differ by their preparation procedures: in the former, the hybrid system is realized by grinding and therefore, the relative final structure is a simple arrangement of 2D units without a particular order; in the latter, instead, the sheets of MoSe$_2$ and those of GO are arranged inside a 3D spherical microstructure (Figure 2.10), forming channels where the electrolyte can permeate. Figure 2.17a and Table 2.8 show that the 3D structure leads to a significant increase in the electrocatalytic performance.

Figure 2.17 compares the results of MoSe$_2$/prGOAM with those obtained for both e-MoSe$_2$/Vulcan and b-MoSe$_2$/Vulcan systems. Vulcan has two types of porosity, the mesopores (2–50 nm) for the dispersion of the catalysts and the macropores (>50 nm) for the diffusion of reagents and products, designed to optimize electrocatalytic performance in systems such as fuel cells.[44] The MoSe$_2$/prGOAM system shows better performance with a gain of about 50 mV in η_{10} compared to the MoSe$_2$ /Vulcan system. In terms of the Tafel slope (Figure 2.17b), the three systems show similar values (about 90 mV/dec), confirming a Volmer-Heyrovsky mechanism. More differences are observed in terms of exchange current density (j_0): the MoSe$_2$/prGOAM system shows a value of j_0 approximately double than that of the e-MoSe$_2$/Vulcan and about 5-times compared to that of the b-MoSe$_2$/Vulcan.

Considering the PEC behavior (see dashed curves in Figure 2.17), more significant improvements in performance can be noted for the MoSe$_2$/prGOAM system; in particular, an improvement of η_{10} of about 25 mV and a gain in terms of current density ($+j_{10}$) of 6.6 mA/cm^2 are observed, which are superior to all the other systems with the same photoactive component (i.e., MoSe$_2$) but different structure and morphology of the carbon support. The best performance in PEC can be read as an indirect proof of a greater light-harvesting by $MoSe_2$ inside the GOAM architecture.

After optimization of the $MoSe_2$/prGOAM preparation procedures, we extended our investigation to a series of MX_2/prGOAM systems where M = Mo, W; X = S, Se. In the SI, we report a section where an extended characterization of the exfoliated TMDCs is reported (Figures 2.18–2.23 and Tables 2.9–2.14).

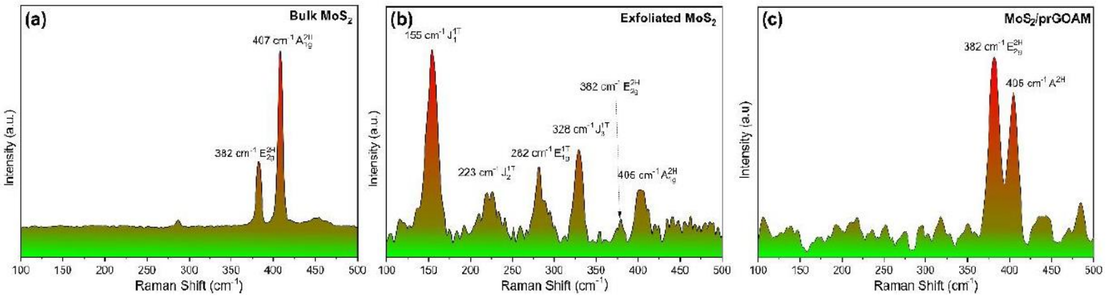

Figure 2.18 Raman spectra of bulk (a), exfoliated (b) and prGOAM hybrid (c) MoS_2 samples.

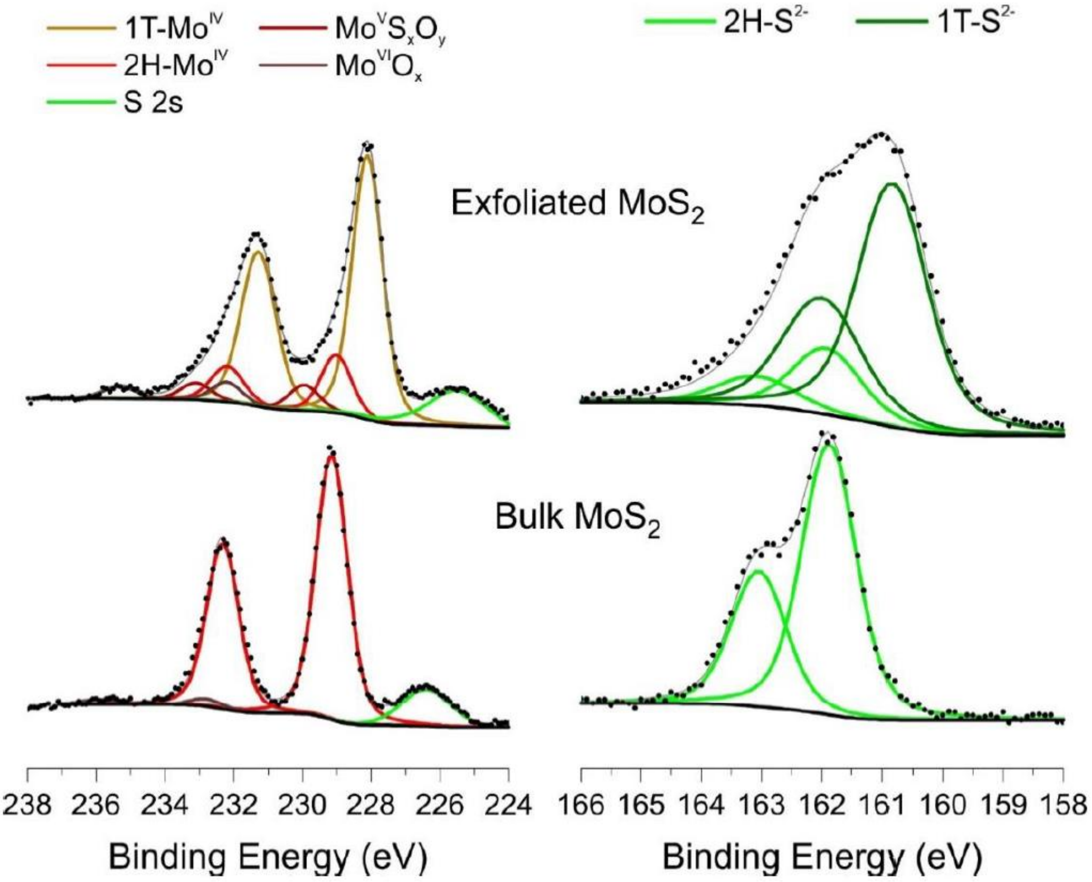

Figure 2.19 XPS spectra of Mo 3d (left) and S 2p (right) regions for exfoliated and bulk MoS_2 samples.

Table 2.9 BE values and composition of Mo 3d core level of MoS_2 samples. The reported BE values error is ±0.1 eV. Percentage value of non -oxidized Mo and 1T:2H ratio of MoS_2 are reported as well.

	Exfoliated MoS_2		**Bulk MoS_2**	
Mo 3d	**BE (eV)**	**%**	**BE (eV)**	**%**
1T-Mo^{IV}	228.1	71.8		
2H-Mo^{IV}	229.1	15.8	229.1	96.1
$Mo^{V}S_xO_y$	35.0	7.1		
$Mo^{VI}O_x$	232.3	5.3	232.3	3.9
1T:2H	82:18		0:100	
Mo^{IV}/Mo	88%		96%	

Table 2.10 BE values and composition of S 2p region of MoS_2 samples. S 2s BE values are reported as well. The error on BE values is ±0.1 eV.

	Exfoliated MoS_2		**Bulk MoS**	
S 2p	**BE (eV)**	**%**	**BE (eV)**	**%**
1T-S^{2-}	160.8	21.0		
2H-S^{2-}	161.9	79.0	161.9	100
S 2s	225.5		226.4	

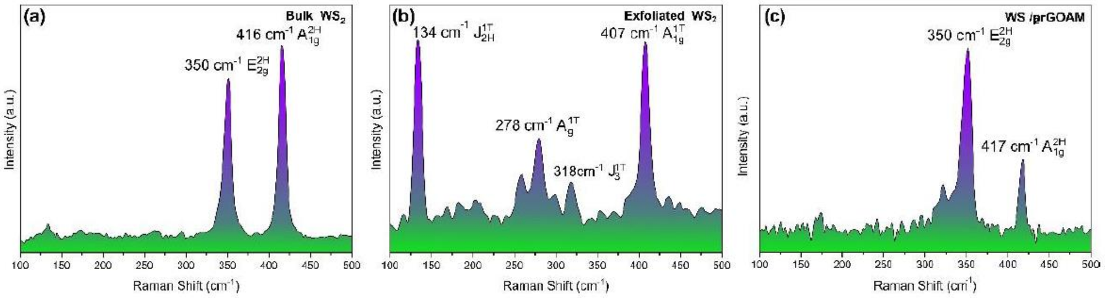

Figure 2.20 Raman spectra of bulk (a), exfoliated (b) and prGOAM hybrid (c) WS$_2$ samples.

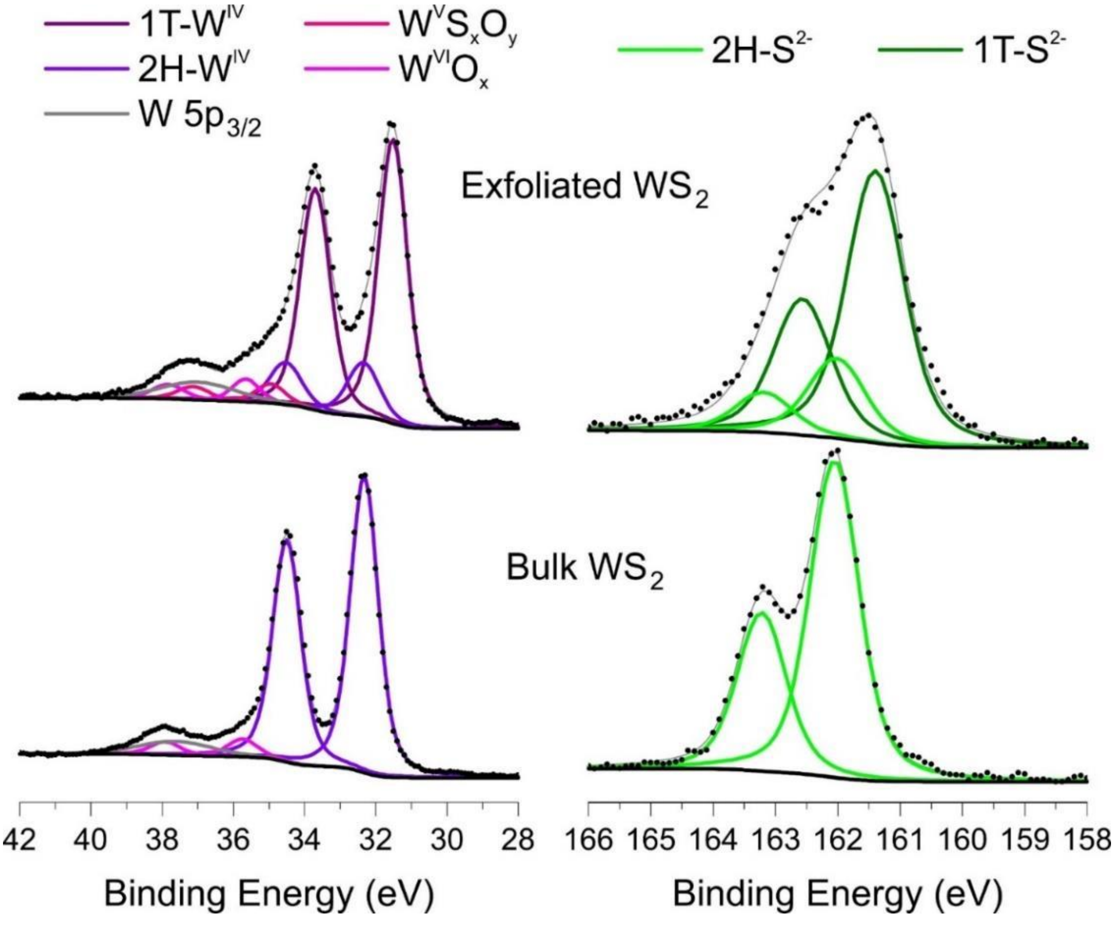

Figure 2.21 XPS spectra of W 4f (left) and S 2p (right) regions for exfoliated and bulk WS$_2$ samples.

Table 2.11 BE values and composition of W 4f core level of WS$_2$ samples. The reported BE values error is ± 0.1 eV. BE of W 5p3/2, percentage value of non - oxidized W and 1T:2H ratio of WS$_2$ are reported as well.

	Exfoliated WS$_2$	**Bulk WS$_2$**

W 4f	BE (eV)	%	BE (eV)	%
1T-W ^{IV}	31.5	74.2	-	
2H-W ^{IV}	32.4	15.5	32.2	94
W V S $_x$ O $_y$	35.0	5.0	-	
W ^{VI} O $_x$	35.7	5.3	35.7	6.0
W 5p 3/2	37.0	-	37.6	-
1T:2H	83:17		0:100	
W ^{IV} /W	90%		94%	

Table 2.12 BE values and composition of S 2p region of WS$_2$ materials. BE values error is ±0.1 eV.

	Exfoliated WS $_2$		Bulk WS $_2$	
S 2p	**BE (eV)**	**%**	**BE (eV)**	**%**
1T-S $^{2-}$	161.4	79.3		
2H-S $^{2-}$	162.0	19.7	162.1	100

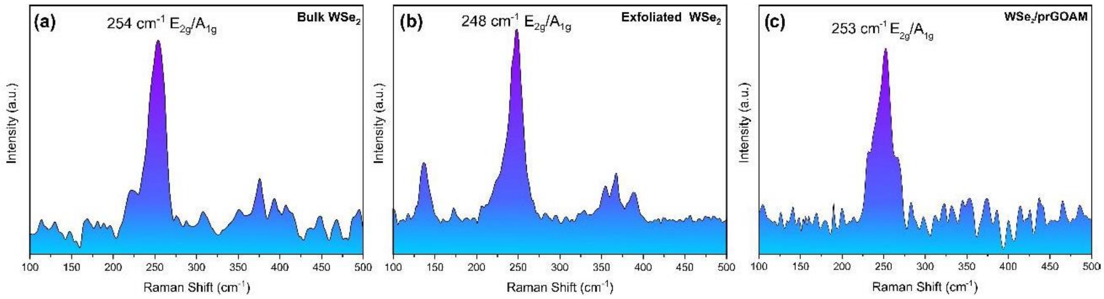

Figure 2.22 Raman spectra of bulk (a), exfoliated (b) and prGOAM hybrid (c) WSe$_2$ samples.

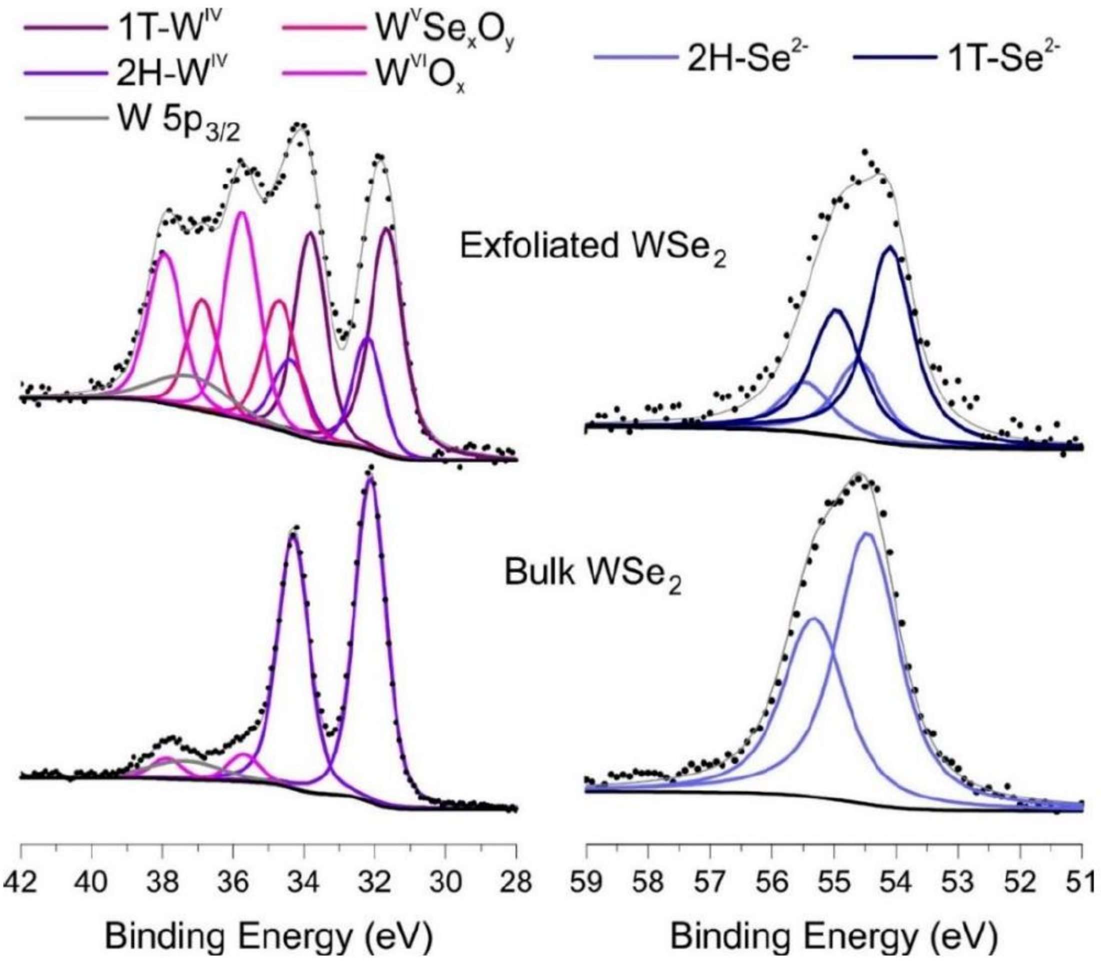

Figure 2.23 XPS spectra of W 4f (left) and Se 3d (right) regions for exfoliated and bulk WSe_2 samples.

Table 2.13 BE values and composition of W 4f core level of WSe_2 samples. The reported BE values error is ± 0.1 eV. BE of W 5p3/2, percentage value of non - oxidized W and 1T:2H ratio of WSe_2 are reported as well.

	Exfoliated WSe_2		**Bulk WSe_2**	
W 4f	**BE (eV)**	**%**	**BE (eV)**	**%**
1T-W^{IV}	31.5	36.5		
2H-W^{IV}	32.2	14.4	32.1	87
$W^{V}S_{x}O_{y}$	34.7	19.3		
$W^{VI}O_{x}$	35.8	29.8	35.7	13

W 5p 3/2	37.2		37.5	
1T:2H	72:28		0:100	
W^{IV}/W	52%		87%	

Table 2.14 BE values and composition of Se 3d region of WSe_2 materials. BE values error is ±0.1 eV.

	Exfoliated WSe_2		**Bulk WSe_2**	
Se 3d	**BE (eV)**	**%**	**BE (eV)**	**%**
$1T\text{-}Se^{2-}$	54.1	71.4		
$2H\text{-}Se^{2-}$	54.6	28.6	54.5	100

The same TMDC mass loading (5 mg/mL) was explored to test the different TMDC/prGOAM systems, without any optimization for the different MX_2. For this reason, the reported data must be considered as explorative. From SEM images and relative EDX data, no relevant changes are observed in the whole MX_2/prGOAM series (Figure 2.24).

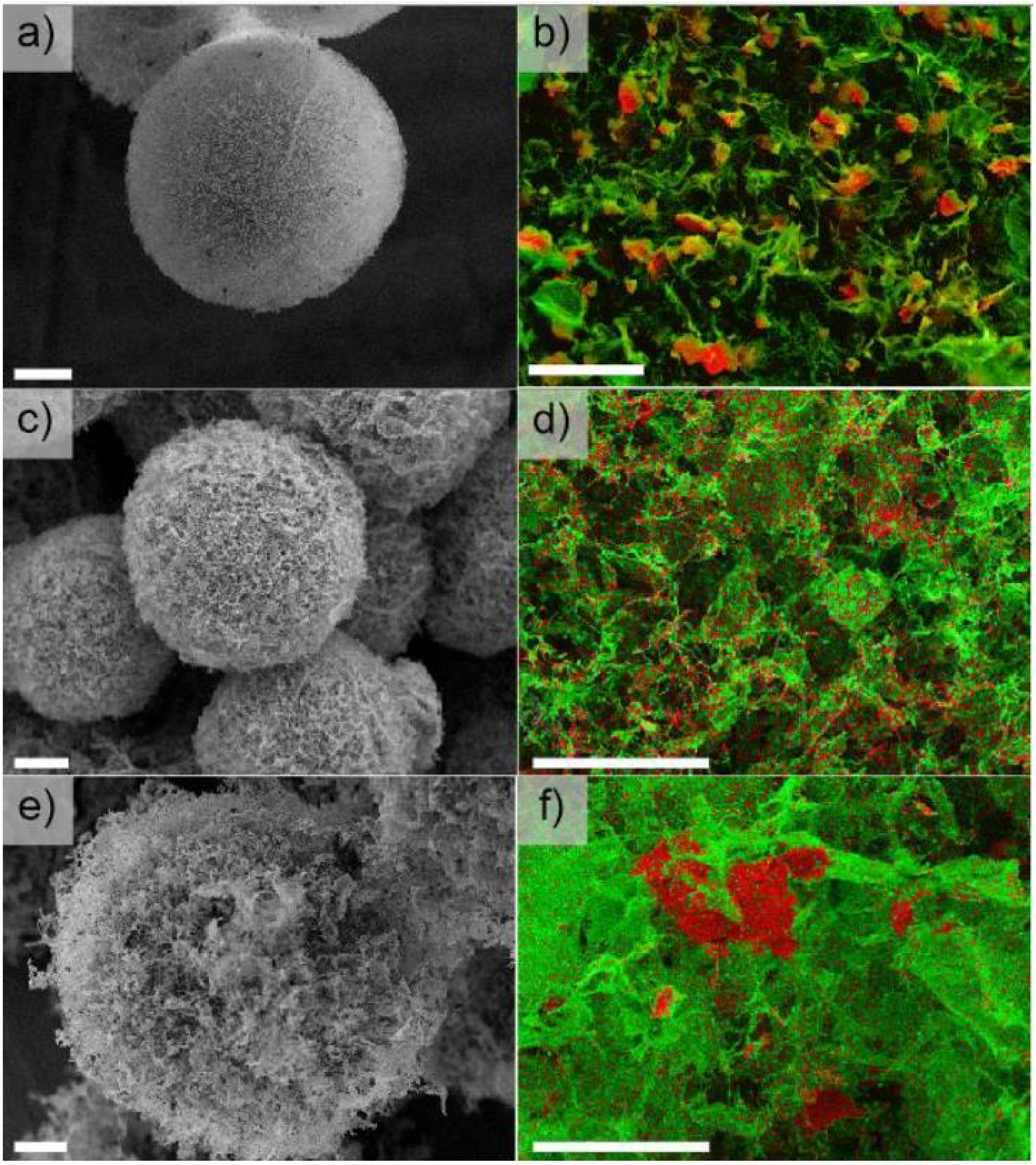

Figure 2.24 SEM images and related EDX maps of the samples (a–b) MoS_2/prGOAM, (c–d) WS_2/prGOAM and (e–f) WSe_2/prGOAM. In EDX maps the green signal correspond to C, while red to Mo or W. Scale bars are 50 µm for SEM images and 20 µm for EDX maps.

The polarization curves of the TMDC/prGOAM samples are shown in Figure 2.25, and the relative electrochemical data are reported in Table 2.15. The reported trend is in agreement with the literature ($MoSe_2$> WS_2> MoS_2> WSe_2).[45] Most probably the reported trend is due to different HER active sites in the different TMDCs. The primary active sites for $MoSe_2$ and WS_2 are both the metal and the chalcogen edges. On the other hand, the active sites for MoS_2 and WSe_2 are only Mo and Se edges, respectively.[45 , 46] However, it must be noted that, with proper optimization, the performances of the other TMDC/prGOAM hybrids could be enhanced, but this goes beyond the purposes of this work.

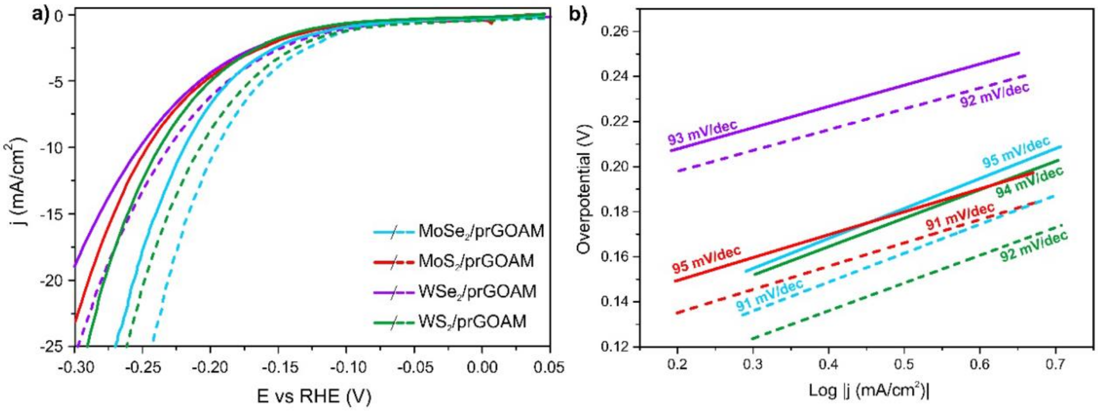

Figure 2.25 (a) Polarization curves for HER and PEC-HER activities of TMDC/prGOAM systems. The dashed curves were obtained by illuminating the working electrode with white light. (b) Tafel plots for electrochemical tests of different TMDCs/prGOAM hybrids.

Table 2.15 Electrochemical data from LSV shown in Figure 2.25.

	η_{10} (mV)	**Tafel Slope (mV/dec)**	**η_{10} LED (mV)**	**Tafel Slope LED (mV/dec)**	**$+j_{10}$ (mA/cm^2)**	**j_0 (μA/cm ^{2})**	**j_0 LED (μA/cm ^{2})**
MoS_2 /prGOAM	246 (5)	95 (2)	230 (5)	91 (2)	3.1	32 (2)	61 (2)
$MoSe_2$ /prGOAM	220 (5)	95 (1)	194 (5)	91 (1)	6.6	47 (2)	73 (4)
$MoSe_2$ /prGOA	237 (5)	94 (1)	208 (5)	92 (1)	6.8	85 (9)	139 (3)
WSe_2 /prGOAM	253 (5)	92 (1)	231 (5)	92 (1)	3.7	81 (6)	174 (4)

In kinetics terms, however, WX_2/prGOAM shows the best performances, with an approximately double value of j 0 compared to MoX_2/prGOAM. Furthermore, considering the PEC behavior, the WS_2/prGOAM is the system with the most remarkable light enhancement, with a reduction of η_{10} value of about 30 mV, a current density gain (+j_{10}) of about 7 mA/cm^2 , and an exchange current increase of about 65 μ A/cm^2. The WSe_2/prGOAM system shows a worse performance concerning WS_2 with a η_{10} value of about 250 mV and a Tafel slope higher than 130 mV/dec. The high Tafel slope is probably to be attributed to the high oxidation degree of exfoliated WSe_2 (about 50%, see XPS data in Table 2.13).

2.4 Conclusions

In this work, we demonstrated that a bottom-up approach based on the use of electrospray and freeze casting techniques starting from GO and exfoliated TMDCs is capable to provide hybrid 3D TMDC/GOAM architectures without significantly altering the dandelion-like microchannel arrangement with central divergence typical of the GOAMs. We have used $MoSe_2$ as benchmark material to optimize many process parameters. Then we have applied the protocol to a wide gamut of other TMDCs materials (i.e., MoS_2, $MoSe_2$, WS_2 and WSe_2). Moreover, such TMDC/GOAM structure can be easily transformed after a thermal annealing at an intermediate temperature (450 ℃, see paragraph 2.2.3) into a mechanically more stable one, i.e., TMDC/prGOAM still retaining the same architecture. Indeed, it is widely reported in the literature that a controlled thermal treatment can substantially improve the mechanical properties of GA by eliminating the oxygen-containing functional groups and promoting π–π stacking interactions between the nanosheets. Moreover, after annealing, covalent crosslinking is established and the electronic conductivity of the sample is increased because of the partial reduction of the GO sheets. Together with the finally tuned wettability of the sample, the annealing procedure makes the TMDC/prGOAM hybrid systems suitable for electrocatalytic experiments: stable electrodes can be prepared and tested (see Figure 2.12). As a consequence of the actual HER screening, we found that the $MoSe_2$ /prGOAM sample provides the best HER performances.

To explore the role of the dandelion-like architecture, we have also compared the HER results of $MoSe_2$/prGOAM with those of related benchmark samples, i.e., hybrid $MoSe_2$/carbon systems where the dandelion-like architecture is not present. Our tests pinpoint better HER performances for the sample with the 3D architecture with respect to the chosen benchmarks. For the sake of honesty, it should be noted that TMDCs/G-based systems with better HER performances with respect to our TMDCs/prGOAM samples are reported in the literature.[47 , 48] However, a full optimization of our 3D catalysts was not carried out, since the main goal of this study was to check the feasibility of preparing HER working electrodes using complex 3D hybrid architectures. Future work is certainly needed for a full optimization of the electrodes by a fine tuning of the graphene/TMDC interactions inside the dandelion-like microspheres.

Reference

(1) Davis, M.E. Ordered porous materials for emerging applications. Nature 2002, 417, 813–821.

(2) Zhang, H.; Cooper, A.I. Synthesis and applications of emulsion-templated porous materials. Soft Matter 2005, 1, 107.

(3) White, R.J.; Luque, R.; Budarin, V.L.; Clark, J.H.; Macquarrie, D.J. Supported metal nanoparticles on porous materials. Methods and applications. Chem. Soc. Rev. 2009, 38, 481–494.

(4) White, R.J.; Budarin, V.; Luque, R.; Clark, J.H.; Macquarrie, D.J. Tuneable porous carbonaceous materials from renewable resources. Chem. Soc. Rev. 2009, 38, 3401.

(5) Bae, Y.; Snurr, R.Q. Development and Evaluation of Porous Materials for Carbon Dioxide Separation and Capture. Angew. Chemie Int. Ed. 2011, 50, 11586–11596.

(6) Novoselov, K.S.; Geim, A.K. The rise of graphene. Nat. Mater 2007, 6, 183–191.

(7) Rao, C.N.R.; Sood, A.K.; Subrahmanyam, K.S.; Govindaraj, A. Graphene: The New Two-Dimensional Nanomaterial. Angew. Chemie Int. Ed. 2009, 48, 7752–7777.

(8) Pumera, M. Graphene-based nanomaterials and their electrochemistry. Chem. Soc. Rev. 2010, 39, 4146.

(9) Stoller, M.D.; Park, S.; Zhu, Y.; An, J.; Ruo_, R.S. Graphene-Based Ultracapacitors. Nano Lett. 2008, 8, 3498–3502.

(10) Liu, L.; Niu, Z.; Zhang, L.; Chen, X. Structural Diversity of Bulky Graphene Materials. Small 2014, 10, 2200–2214.

(11) Worsley, M.A.; Pauzauskie, P.J.; Olson, T.Y.; Biener, J.; Satcher, J.H.; Baumann, T.F. Synthesis of Graphene Aerogel with High Electrical Conductivity. J. Am. Chem. Soc. 2010, 132, 14067–14069.

(12) Gorgolis, G.; Galiotis, C. Graphene aerogels: A review. 2D Mater. 2017, 4, aa7883.

(13) Liu, H.; Qiu, H. Recent advances of 3D graphene-based adsorbents for sample preparation of water pollutants: A review. Chem. Eng. J. 2020, 393, 124691.

(14) Wu,Y.; Zhu, J.; Huang, L.Areview of three-dimensional graphene-based materials: Synthesis and applications to energy conversion/storage and environment. Carbon N. Y. 2019, 143, 610–640.

(15) Liao, S.; Zhai, T.; Xia, H. Highly adsorptive graphene aerogel microspheres with center-diverging microchannel structures. J. Mater. Chem. A 2016, 4, 1068–1077.

(16) Salata, O. V Tools of nanotechnology: Electrospray. Curr. Nanosci. 2005, 1, 25–33.

(17) Almería, B.; Gomez, A. Electrospray synthesis of monodisperse polymer particles in a broad (60 nm–2 _m) diameter range: Guiding principles and formulation recipes. J. Colloid Interface Sci. 2014, 417, 121–130.

(18) Freytag, A.; Sánchez -Paradinas, S.; Naskar, S.; Wendt, N.; Colombo, M.; Pugliese, G.; Poppe, J.; Demirci, C.; Kretschmer, I.; Bahnemann, D.W.; et al. Versatile Aerogel Fabrication by Freezing and Subsequent Freeze-Drying of Colloidal Nanoparticle Solutions. Angew. Chemie Int. Ed. 2016, 55, 1200–1203.

(19) Mattevi, C.; Eda, G.; Agnoli, S.; Miller, S.; Mkhoyan, K.A.; Celik, O.; Mastrogiovanni, D.; Granozzi, G.; Garfunkel, E.; Chhowalla, M. Evolution of Electrical, Chemical, and Structural Properties of Transparent and Conducting Chemically Derived Graphene Thin Films. Adv. Funct. Mater. 2009, 19, 2577–2583.

(20) Deng, W.; Klemic, J.F.; Li, X.; Reed, M.A.; Gomez, A. Increase of electrospray throughput using multiplexed microfabricated sources for the scalable generation of monodisperse droplets. J. Aerosol Sci. 2006, 37, 696–714.

(21) Bocanegra, R.; Galán, D.; Márquez, M.; Loscertales, I.G.; Barrero, A. Multiple electrosprays emitted from an array of holes. J. Aerosol Sci. 2005, 36, 1387–1399.

(22) Huang, H.; Yan, M.; Yang, C.; He, H.; Jiang, Q.; Yang, L.; Lu, Z.; Sun, Z.; Xu, X.; Bando, Y.; et al. Graphene Nanoarchitectonics: Recent Advances in Graphene-Based Electrocatalysts for Hydrogen Evolution Reaction. Adv. Mater. 2019, 31, 1–34.

(23) Wang, R.; Han, J.; Zhang, X.; Song, B. Synergistic modulation in MX2 (where M = Mo orWor V, and X = S or Se) for an enhanced hydrogen evolution reaction. J. Mater. Chem. A 2018, 6, 21847–21858.

(24) Peng, B.; Ang, P.K.; Loh, K.P. Two-dimensional dichalcogenides for light-harvesting applications. Nano Today 2015, 10, 128–137.

(25) Chen, Y.; Yang, K.; Jiang, B.; Li, J.; Zeng, M.; Fu, L. Emerging two-dimensional nanomaterials for electrochemical hydrogen evolution. J. Mater. Chem. A 2017, 5, 8187–8208.

(26) Lukowski, M.A.; Daniel, A.S.; Meng, F.; Forticaux, A.; Li, L.; Jin, S. Enhanced Hydrogen Evolution Catalysis from Chemically Exfoliated Metallic MoS2 Nanosheets. J. Am. Chem. Soc. 2013, 135, 10274–10277.

(27) Tuci, G.; Mosconi, D.; Rossin, A.; Luconi, L.; Agnoli, S.; Righetto, M.; Pham-Huu, C.; Ba, H.; Cicchi, S.; Granozzi, G.; et al. Surface Engineering of Chemically Exfoliated MoS2 in a “Click”: How To Generate Versatile Multifunctional Transition Metal Dichalcogenides-Based Platforms. Chem. Mater. 2018, 30, 8257–8269.

(28) Mosconi, D.; Giovannini, G.; Jacassi, A.; Ponzellini, P.; Maccaferri, N.; Vavassori, P.; Serri, M.; Dipalo, M.; Darvill, D.; De Angelis, F.; et al. Site-Selective Integration of MoS2 Flakes on Nanopores by Means of Electrophoretic Deposition. ACS Omega 2019, 4, 9294–9300.

(29) Garoli, D.; Mosconi, D.; Miele, E.; Maccaferri, N.; Ardini, M.; Giovannini, G.; Dipalo, M.; Agnoli, S.; De Angelis, F. Hybrid plasmonic nanostructures based on controlled integration of MoS2 flakes on metallic nanoholes. Nanoscale 2018, 10, 17105–17111.

(30) Libra, J. KolXPD: Software for Spectroscopy Data Measurement and Processing, Kolibrik.net, s.r.o., Žd’ár nad Sázavou, Czech Republic, (n.d.).

(31) Gupta, U.; Naidu, B.S.; Maitra, U.; Singh, A.; Shirodkar, S.N.; Waghmare, U.V.; Rao, C.N.R. Characterization of few-layer 1T-MoSe2 and its superior performance in the visible-light induced hydrogen evolution reaction. APL Mater. 2014, 2, 092802.

(32) Tonndorf, P.; Schmidt, R.; Böttger, P.; Zhang, X.; Börner, J.; Liebig, A.; Albrecht, M.; Kloc, C.; Gordan, O.; Zahn, D.R.T.; et al. Photoluminescence emission and Raman response of monolayer MoS2, MoSe2, and WSe2. Opt. Express 2013, 21, 4908.

(33) Koroteev, V.O.; Bulusheva, L.G.; Asanov, I.P.; Shlyakhova, E.V.; Vyalikh, D.V.; Okotrub, A.V. Charge transfer in the MoS2/carbon nanotube composite. J. Phys. Chem. C 2011, 115, 21199–21204.

(34) Wang, H.W.; Skeldon, P.; Thompson,G.E. XPS studies of MoS2 formation fromammonium tetrathiomolybdate solutions. Surf. Coatings Technol. 1997, 91, 200–207.

(35) Ambrosi, A.; Sofer, Z.; Pumera, M. 2H ! 1T phase transition and hydrogen evolution activity of MoS2, MoSe2, WS2 and WSe2 strongly depends on the MX 2 composition. Chem. Commun. 2015, 51, 8450–8453.

(36) Zhu, C.; Han, T.Y.-J.; Duoss, E.B.; Golobic, A.M.; Kuntz, J.D.; Spadaccini, C.M.; Worsley, M.A. Highly compressible 3D periodic graphene aerogel microlattices. Nat. Commun. 2015, 6, 6962.

(37) Worsley, M.A.; Olson, T.Y.; Lee, J.R.I.;Willey, T.M.; Nielsen, M.H.; Roberts, S.K.; Pauzauskie, P.J.; Biener, J.; Satcher, J.H.; Baumann, T.F. High Surface Area, sp2-Cross-Linked Three-Dimensional Graphene Monoliths. J. Phys. Chem. Lett. 2011, 2, 921–925.

(38) Pei, S.; Cheng, H. The reduction of graphene oxide. Carbon N. Y. 2012, 50, 3210–3228.

(39) Das, A.; Chakraborty, B.; Sood, A.K. Raman spectroscopy of graphene on di_erent substrates and influence of defects. Bull Mater. Sci. 2008, 31, 579–584.

(40) Malard, L.M.; Pimenta, M.A.; Dresselhaus, G.; Dresselhaus, M.S. Raman spectroscopy in graphene. Phys. Rep. 2009, 473, 51–87.

(41) Yu, Y.; Nam, G.; He, Q.; Wu, X.; Zhang, K.; Yang, Z.; Chen, J.; Ma, Q.; Zhao, M.; Liu, Z.; et al. High phase-purity 1T0-MoS2- and 1T0-MoSe2-layered crystals. Nat. Chem. 2018, 10, 638–643.

(42) Guo, Y.; Sun, D.; Ouyang, B.; Raja, A.; Song, J.; Heinz, T.F.; Brus, L.E. Probing the Dynamics of the Metallic-to-Semiconducting Structural Phase Transformation in MoS2 Crystals. Nano Lett. 2015, 15, 5081–5088.

(43) Ma, Y.; Liu, B.; Zhang, A.; Chen, L.; Fathi, M.; Shen, C.; Abbas, A.N.; Ge, M.; Mecklenburg, M.; Zhou, C. Reversible Semiconducting-to-Metallic Phase Transition in Chemical Vapor Deposition Grown Monolayer WSe2 and Applications for Devices. ACS Nano 2015, 9, 7383–7391.

(44) Soboleva, T.; Malek, K.; Xie, Z.; Navessin, T.; Holdcroft, S. PEMFC catalyst layers: The role of micropores and mesopores on water sorption and fuel cell activity. ACS Appl. Mater. Interfaces 2011, 3, 1827–1837.

(45) Chia, X.; Eng, A.Y.S.; Ambrosi, A.; Tan, S.M.; Pumera, M. Electrochemistry of Nanostructured Layered Transition-Metal Dichalcogenides. Chem. Rev. 2015, 115, 11941–11966.

(46) Tsai, C.; Chan, K.; Abild-Pedersen, F.; Nørskov, J.K. Active edge sites in MoSe2 and WSe2 catalysts for the hydrogen evolution reaction: A density functional study. Phys. Chem. Chem. Phys. 2014, 16, 13156–13164.

(47) Zheng, D.; Cheng, P.; Yao, Q.; Fang, Y.; Yang, M.; Zhu, L.; Zhang, L. Excess Se-doped MoSe2 and nitrogen-doped reduced graphene oxide composite as electrocatalyst for hydrogen evolution and oxygen reduction reaction. J. Alloys Compd. 2020, 848, 156588.

(48) Najafi, L.; Bellani, S.; Oropesa-Nuñez, R.; Ansaldo, A.; Prato, M.; Del Rio Castillo, A.E.; Bonaccorso, F. Engineered MoSe2-Based Heterostructures for

E_cient Electrochemical Hydrogen Evolution Reaction. Adv. Energy Mater. 2018, 8, 1–16

Chapter 3

The Effect of the 3D Nanoarchitecture and Ni-doping on the Hydrogen Evolution Reaction in MoS_2/reduced GO Aerogel Hybrid Microspheres

3. The Effect of the 3D Nanoarchitecture and Ni-doping on the Hydrogen Evolution Reaction in MoS_2/reduced GO Aerogel Hybrid Microspheres

3.1 Introduction

Hydrogen has emerged as the most effective energy vector alternative to fossil fuels because of its high energy density and environmental sustainability, given that its only oxidation product is water.[1] To fulfil the requirements of the *hydrogen economy,*[2] a cheap route to *green* hydrogen production through water splitting (WS) must be developed, possibly using renewable energy sources (sun, wind…). One of the most promising WS processes involves electrolysis,[3] either photoassisted or not, and many efforts are currently taken to develop advanced electrocatalysts able to reduce the overpotential needed to dissociate water into molecular oxygen and hydrogen. The oxygen evolution reaction at the anode is still the bottleneck of the whole process, but there is also much room for the optimization of the electrocatalysts for the hydrogen evolution reaction (HER) at the cathode side.[3–5] The most effective HER electrocatalysts, especially in acid conditions, are based on Pt-group metals (PGMs), which have a long story behind.[6] However, the current challenge is to develop highly active HER catalysts based on materials that are cheap and earth-abundant [7] and that can work in a variety of pH environments. Recently, remarkable advances have been made using transition-metal-dichalcogenides (TMDCs, e.g. MoS_2, $MoSe_2$, $MoTe_2$, WS_2…) as PGM-free HER electrocatalysts.[8–13] Their prototype is MoS_2, which has a relatively low hydrogen adsorption free energy at its edge sites or sulphur vacancies,[14] making it competitive with Pt. However, in MoS_2, both the activity of basal plane and the electron conductivity are rather low, which ultimately limit the overall electrocatalytic performances.[15] To overcome these hurdles, several strategies were proposed, e.g. the combination of MoS_2 with highly conductive materials and the optimization of structure and morphology to maximize the density of active sites.

Several studies sought to improve the electron transfer capabilities of MoS_2 by creating nanocomposites with various conductive materials, e.g. nanoporous carbons,[16] carbon nanotubes,[17] nanoporous metals [18] or mesoporous graphene.[19] Even if significant advances were obtained, MoS_2 nanosheets are intrinsically prone to stack together during the synthesis, given their layered nature, severely limiting the number of the exposed catalytically active sites.[20] On the other hand, integrating MoS_2 nanosheets on 3D conductive *porous* scaffolds can enhance the electron transfer, while maintaining a high dispersion of the sheets because of the restricted movements allowed within the scaffold.[21] Following this idea, MoS_2 was grown on 3D graphene,[22,23] nickel foams [24–27] and silica [28] structures. The most common route to create such nanocomposites consists of mixing the 3D template with an exfoliated TMDC. However, in presence of an intrinsically irregular 3D template, some aggregation of the MoS_2 nanosheets can still persist, reducing the number of the exposed electrocatalytic sites, whereas the use of an ordered (i.e. with a narrow dispersion of pores) 3D template can partially fix this issue. In a previous paper,[29] we reported a successful route to disperse chemically exfoliated TMDC nanosheets within a graphene oxide (GO) aerogel having a special centre-diverging microchannel 3D structure. These GO Aerogel Microspheres (GOAMs), with a radius of a few hundreds of μm, can be easily obtained by a bottom-up approach combining two subsequent steps, i) the electrospraying of GO suspensions and ii) the freeze-casting.[30] Interestingly, the microspheres maintain their shape even after a thermal reduction process (providing partially reduced GOAMs, prGOAMs). Adding exfoliated TMDC during the GOAMs preparation step, TMDC/pr-GOAM hybrids were obtained, which kept their special morphology even during the electrochemical work and achieved better performance in the HER compared to electrodes built with the same materials, i.e. rGO and MoS_2, but without the 3D architecture with mesoscopic centre diverging channels.

Herein, we make a step forward and propose a synthesis strategy to control not only the morphology of the nanocomposite, but also the chemistry of the active phase, realizing quite active bifunctional catalysts. To achieve this goal, we envisaged a *fully* bottom-up approach for preparing the MoS_2 phase decorating the 3D GOAM scaffold, which is based on a molecular precursor, e.g. ammonium tetrathiomolybdate (ATM, $(NH_4)_2MoS_4$)). The advantages of this approach to prepare the hybrid MoS_2/prGOAM materials are: i) fine and homogeneous dispersion of MoS_2 on the graphenic support, ii) higher scalability of the preparation procedure, and shorter preparation time since there is no need to prepare the TMDC by a lengthy and expensive exfoliation procedure, iii) possibility to introduce a large variety of dopants into the MoS_2 moiety. The resulting materials with both tailored morphology and chemistry demonstrated to be outstanding catalyst for the HER, superior to previous top-down MoS_2 based catalysts [29] and similar catalysts found in the literature. In fact, the interaction at the molecular level of ATM with the oxygenated graphene surface, leads to the formation of intimately dispersed nanohybrids with a peculiar composition characterized by the presence of MoO_xS_y species, which according to previous works promote the electroactivity of the MoS_2 basal plane by narrowing the band gap [31] and guaranteeing an efficient interaction with the GO scaffold. Moreover, our bottom-up synthesis allows to introduce easily metal dopants into the growing MoS_2 phase, simply adding a soluble metal salt just before the electrospraying step. A rich literature demonstrates that the modification of MoS_2 with foreign metals can be extremely beneficial for the electrocatalytic activity. As case study we investigated the doping with Ni, which has been widely investigated both theoretically [32] and experimentally [33] even though, different works connect the higher activity to different reasons such as formation of new phases,[33] substitutional doping with consequent modification of structural and electronic properties,[32] complex interaction with oxygen,[34] change in the morphology.[35] This work therefore exemplifies the enormous potential of electrospray and freeze casting for the preparation of highly sophisticated electrocatalytic materials. This technique is extremely cheap and quick, very suitable to a rather fast and continuous production (e.g. hundreds of mg per hour of material produced with lab scale equipment). However, these extreme high productivity and cost effectiveness are not at the expenses of materials properties: as demonstrated here, a mesoporous hierarchical morphology perfectly suited for the interactions with electrolyte can be routinely realized and also the atomic composition can be tuned with high versatility, resulting in the synthesis of sophisticated nanocomposites designed at multiple scales.

3.2 Experimental section

3.2.1 Synthesis of the MoS_2/prGOAMs and Ni-doped MoS_2/prGOAMs

Scheme 3.1 illustrates the synthetic route for the preparation of Ni-doped MoS_2/prGOAMs (Ni doping of 5 at.% vs. Mo). GO, $NiCl_2 6H_2O$ and ammonium thiomolybdate (ATM) in different ratios were used to prepare a series of samples, which in the following are labelled as Ni-doped MoS_2/prGOAM-X-Y (where X indicates the weight percentage of MoS_2, and Y is the annealing temperature). GO, $NiCl_2 6H_2O$ and ATM were added to 10 mL of deionized water, stirred and ultrasonicated at room temperature for 30 minutes to obtain a homogeneous suspension of 7.0 mg mL^{-1}. Table 3.1 summarizes the amount of the reagents used for the different samples. Starting from the precursor solution, a combination of electrospraying, ice templating and thermal annealing was used for the synthesis of the Ni-doped MoS_2/prGOAMs composites. Regarding the electrospraying step, a beaker containing n-hexane was cooled down to -45°C by an acetone/dry ice mixture and used as receiving liquid. Then, the $NiCl_2$/GO/ATM suspension was added to the injection pump of the electrospraying device, which was terminating with a small capillary (nozzle) connected to a high voltage power supply. After a careful optimization, the parameters for the electrospraying procedure were set within the following ranges: flow rate = 6-10 mL h^{-1}; high voltage = 9-12 kV, distance between the receiving liquid and the nozzle = 8-12 cm. Microspheres with different diameters could be prepared by changing these parameters within these ranges. Under the action of the electric field, the electrically conductive suspension is stretched forming a "Taylor cone" and eventually splits into smaller charged droplets that enter the cooling bath, where they are rapidly frozen, producing $NiCl_2$/GO/ATM/ice microspheres. Finally, after rapid filtration, the solid microspheres collected in the cooled n-hexane bath were transferred to a freeze dryer working at -50 ℃ and less than 20 Pa, for 48 h, eventually obtaining the dried $NiCl_2$/ATM/GOAM microspheres ($NiCl_2$ and ATM inside the GOAM). Finally, the dried $NiCl_2$/ATM/GOAMs were heated to 400 ℃, 500 ℃, 600 ℃ or 900 ℃ under an Ar:H_2 = 9:1 (100 sccm in total) atmosphere for 1 h with a heating rate of 5 ℃/min. The thermal decomposition of ATM leads to molybdenum trisulphide (MoS_3), ammonia (NH_3) and hydrogen sulphide (H_2S), in the temperature range between 155 ℃ and 280 ℃ [36,37] according to the following equation:

$(NH_4)_2MoS_4 \rightarrow MoS_3 + 2\ NH_3 + H_2S$ (1)

MoS_3 then decomposes to MoS_2 in a broad temperature range from 300 ℃ to 820 ℃ under inert gas and hydrogen according to the following reaction [37]:

$MoS_3 + H_2 \rightarrow MoS_2 + H_2S$ (2)

On the other hand, nickel chloride is reduced in a temperature range from 300 ℃ to 700 ℃ by hydrogen according to the reaction [38,39]:

$NiCl_2 + H_2 \rightarrow Ni + 2HCl$ (3)

During the heat treatment, the GOAMs are also transformed into prGOAMs,[40] so the final Ni-doped MoS_2/prGOAMs are obtained. For the preparation of MoS_2/prGOAMs, the same procedure was followed simply without adding the $NiCl_2$ in the initial solution.

Table 3.1 The amounts of GO and ATM used to prepare the different samples investigated in this study.

MoS_2 (wt%)	**$NiCl_2 6H_2O$ (mg)**	**GO (mg)**	**ATM (mg)**
20	**2.6**	**70**	**28**
30	**4.5**	**70**	**49**
40	**6.7**	**70**	**73**
50	**9.2**	**70**	**100**

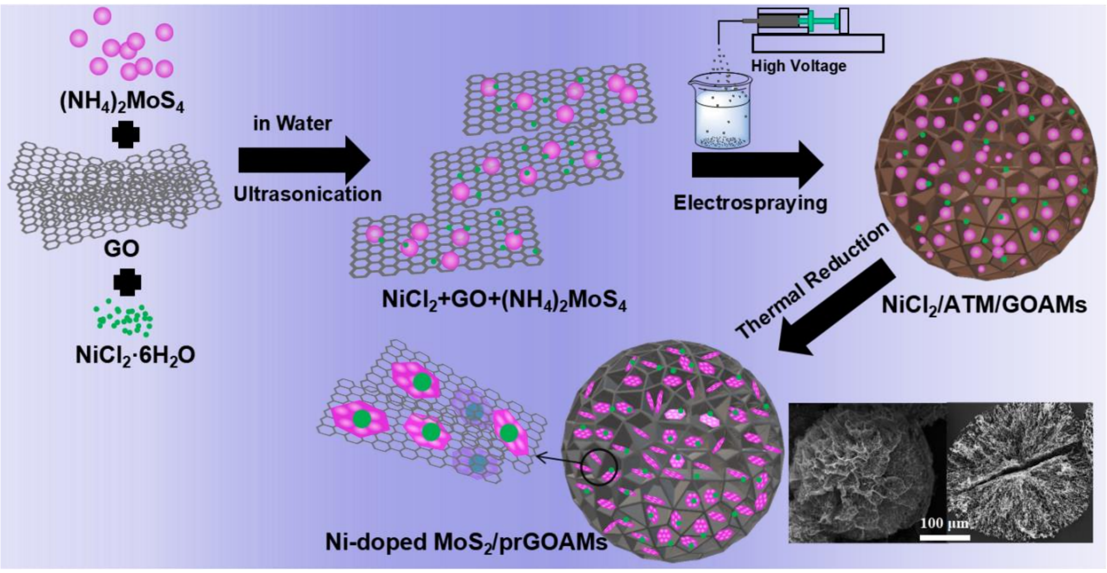

Scheme 3.1 Schematic illustration of the synthesis of the Ni-doped MoS_2/prGOAMs.

3.2.2 Structural and Morphological Characterizations

Scanning Electron Microscopy (SEM) measurements were carried out with a Zeiss Supra VP35 Field-Emission Scanning Electron Microscopy (FE-SEM), equipped with In-Lens, Secondary Electrons (SE), and Backscattered Electrons (BSE) detectors for the imaging (Zeiss, Jena, Germany). Micrographs were obtained with an acceleration voltage of 5 kV using in-lens high-resolution detection. Energy dispersive X-ray spectroscopy (EDX) data were acquired with the same instrument. The surface area measurements were carried out with a Micromeritics ASAP 2020/2010 apparatus using the Brunauer–Emmett–Teller (BET) model for N_2 adsorption measurements. Prior to the adsorption run, the sample was outgassed at 573 K for 20 h.

X-ray diffraction (XRD) patterns were recorded in the diffraction angular range of 5–80°by a PANalytical X ’Pert 3 diffractometer, working in the reflection geometry and equipped with a graphite monochromator on the diffracted beam (Cu Kα radiation, Pananlytical, Almelo, The Netherlands). Raman spectra were collected using a DXR Raman microscope system (Thermo Fisher Scientific, USA) with a 532 nm laser as the photoexcitation source, with 0.5 mW laser power at the sample and a 50× objective lens.

The surface chemical composition of the samples was investigated by XPS using a custom-made system working at a base pressure of 10^{-10} mbar and equipped with an EA 125 Omicron electron analyzer ending with a five channeltron detector. The XPS data were collected at room temperature using the Al Kα line (hν = 1253.6 eV) of a non-monochromatized dual-anode DAR400 X-ray source. High resolution spectra were acquired using 0.1 eV energy steps, and 20 eV pass energy. The multipeak analysis of the C 1s, Ni 2p, Mo 3d and S 2p photoemission lines was performed by means of Voigt functions and subtracting a Shirley background using the XPSPEAK software.

3.2.3 Electrochemical Characterization

The electrochemical (EC) HER measurements were carried out in a custom designed three-electrode cell using an Autolab PGSTAT-204 potentiostat. Graphite was used as counter electrode, whereas an Ag/AgCl $_{(3MKCl)}$ electrode, calibrated with respect to the reversible hydrogen electrode (RHE), was the reference electrode. All potentials reported in the text and figures are referred to the (RHE) and corrected according to the equation: E(RHE) = E(Ag/AgCl) + 0.225 V + 0.059 pH. The EC experiments were carried out in Ar-saturated 0.5 M H_2SO_4 or 1 M KOH solution prepared from high-purity reagents (Sigma-Aldrich) and ultrapure Milli-Q water. The working electrodes were prepared by painting 100 μL of the catalyst ink (which was obtained by dispersing 1 mg of sample and 5 μL of Nafion in 200 μL of DMF, by ultrasonication for powder materials, whereas by gently shaking only for aerogel microspheres) on a 1×l cm carbon cloth (Zoltek Tm P X30 Woven fabric, Hungary). The polarization curves were recorded at a 5 mV/s scan rate. The cycling stability measurements after CV experiments was performed for 1000 cycles with a scan rate of 50 mV/s in the potential range of -0.12 to −0.47 V (vs Ag/AgCl). The stability of the catalysts was tested by chronopotentiometry (CP) at 10 mA cm^{-2}. Curves were iR-corrected using the resistance determined by Electrochemical impedance spectroscopy (EIS).

3.3 Results and Discussion

3.3.1 Physicochemical characterization.

As an example, Figure 3.1a and Figure 3.1c show the SEM micrographs of Ni-doped MoS_2/prGOAM-40%-500 (see the Experimental section for the sample labels), where the typical spherical morphology of the materials (~ 300 μm diameter) is easily recognizable. Furthermore, the inner microstructure of Ni-doped MoS_2/prGOAM-40%-500 can be clearly observed in Figure 3.1d and e, and consists of a highly porous network made up by randomly interconnected graphene sheets. Such structure, resembling a *dandelion blowball,* shows radially oriented microchannels and is the result of the uniform cooling of the $NiCl_2$/GO/ATM/ice microsphere, where the ice crystals grow in the radial direction triggering the self-assembly of $NiCl_2$/GO/ATM blocks, which may organize through electrostatic/dispersive interactions and hydrogen bonds.[29,30] The radially oriented microchannel structure is retained after the removal of the templating ice crystals during the lyophilization step. The SEM images at larger magnification (reported in Figure 3.1f), show that the Ni-doped MoS_2 nanoparticles (*vide infra*), which typically exhibit a brighter contrast, are uniformly dispersed on the prGO surface. Such nanoparticles are often observed on GO wrinkles where sometimes they form larger aggregates, whereas on flatter GO sheets they show a variable size ranging between 20 and 80 nm. Figure 3.1g and h show the SEM image and the corresponding EDX spectra: the total mass percentage of S and Mo is approximately 39.6%, very close to the 40% value expected from the concentration in the precursor suspension, and the atomic ratio of Ni/Mo (5.7%) is very close to the nominal 5%, deriving from the precursor Ni:Mo ratio. Overall, the SEM/EDX investigation suggests that Ni-doped MoS_2 nanoparticles finely decorates the prGO sheets, which are efficiently interconnected creating a series of centre diverging channels.

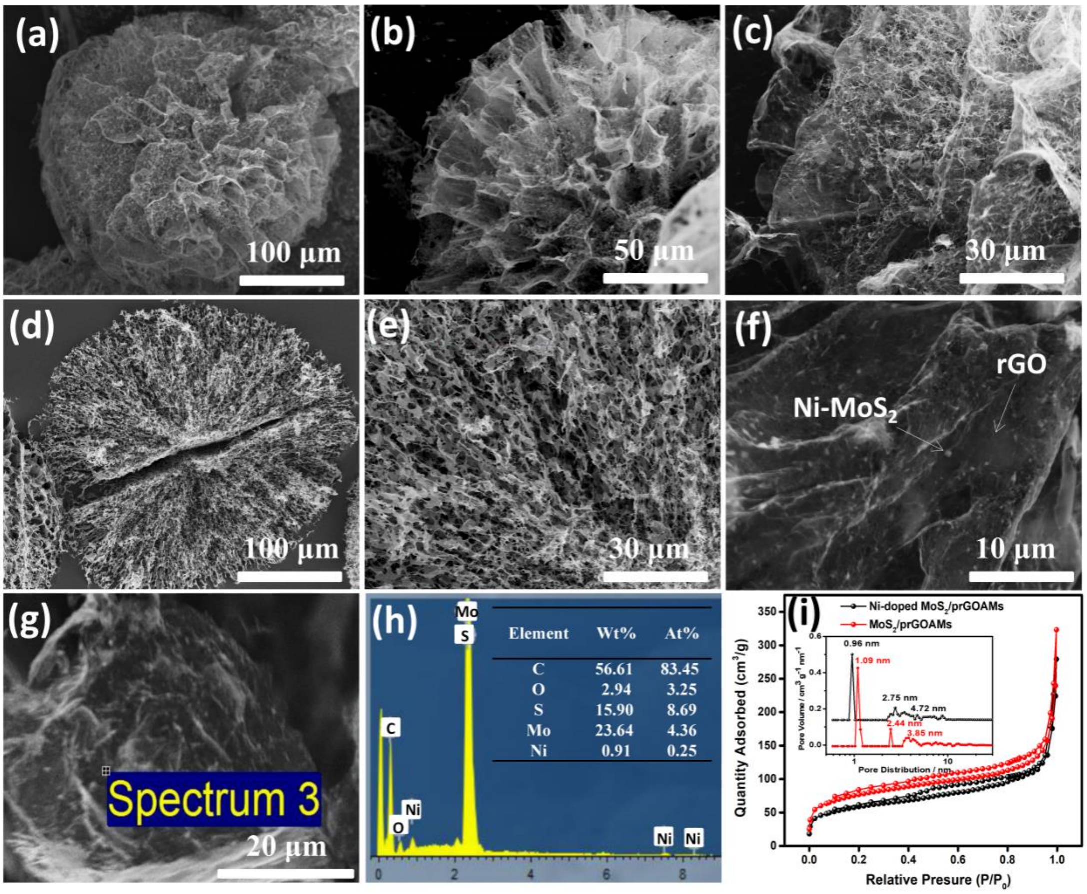

Element	Wt%	At%
C	56.61	83.45
O	2.94	3.25
S	15.90	8.69
Mo	23.64	4.36
Ni	0.91	0.25

Figure 3.1 (a - c) SEM images of typical Ni-doped MoS_2/prGOAM-40%-500 (a: lower magnification; b and c: higher magnification); (d - f) Ni-doped MoS_2/prGOAM-40%-500 aerogel hemispheres made by cracking the microspheres;

(g and h) SEM image and EDX analysis of Ni-doped MoS_2/prGOAM-40%-500; (i) N_2 adsorption-desorption isotherm and pore-size distribution (inset) of Ni-doped MoS_2/prGOAM-40%-500 and MoS_2/prGOAM-40%-500.

Figure 3.2, reports the morphology of the corresponding undoped MoS_2/prGOAM-40%-500 sample to verify that the introduction of the $NiCl_2$ in the precursor solution does not change the morphological features of the materials. In general, by varying the process parameters during the electrospraying process, MoS_2/prGOAMs with different average diameter can be obtained (150 μm (V=13kV, Rate=10 mL h^{-1}), 200 μm (V=12kV, Rate=10 mL h^{-1}), 300 μm (V=10kV, Rate=8 mL h^{-1}) and 400 μm (V=8kV, Rate=8 mL h^{-1}), see Figure 3.3), but still retain the usual spherical shape and microchannel structure. Figure 3.4 shows the EDX spectrum of MoS_2/prGOAM-40%-500, which demonstrates again a good agreement between the nominal and experimental composition values.

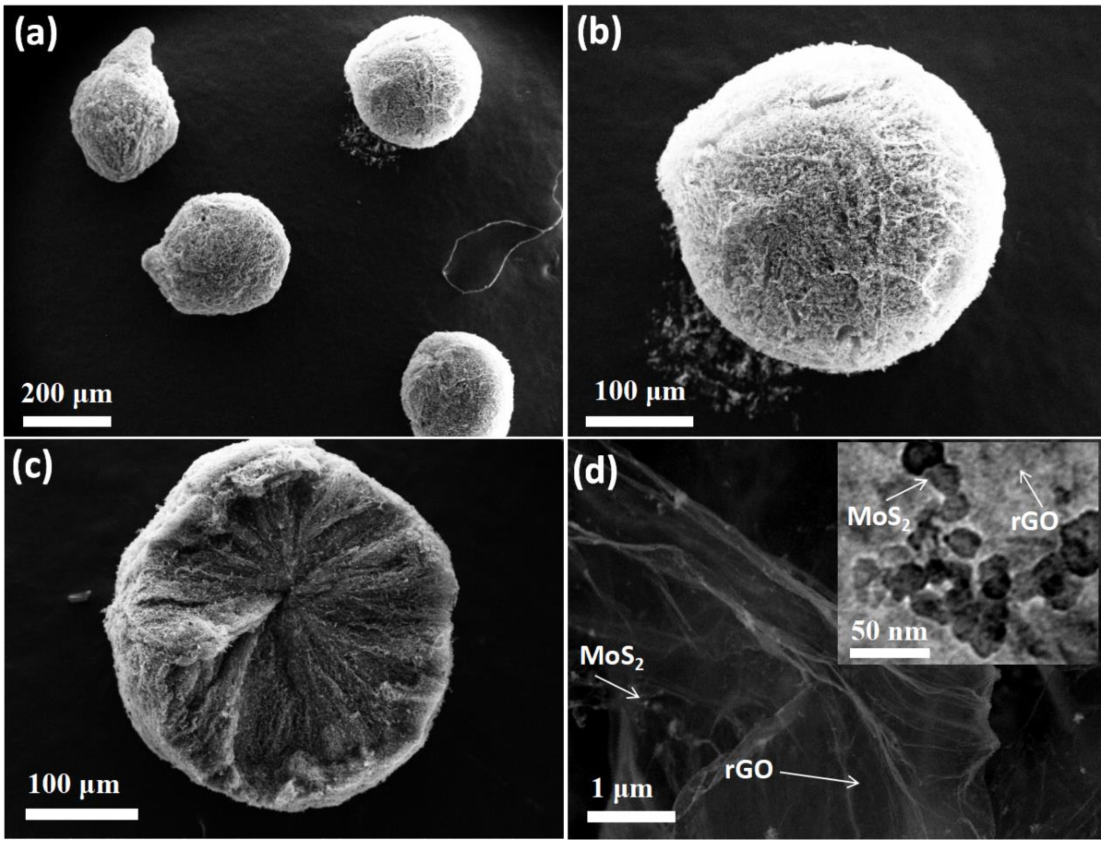

Figure 3.2 (a and b) SEM images of typical MoS_2/prGOAM-40%-500 (a: lower magnification; b: higher magnification); (c and d) SEM images of MoS_2/prGOAMs aerogel hemispheres made by cracking the microspheres. In the inset of d the relative high resolution TEM image is reported.

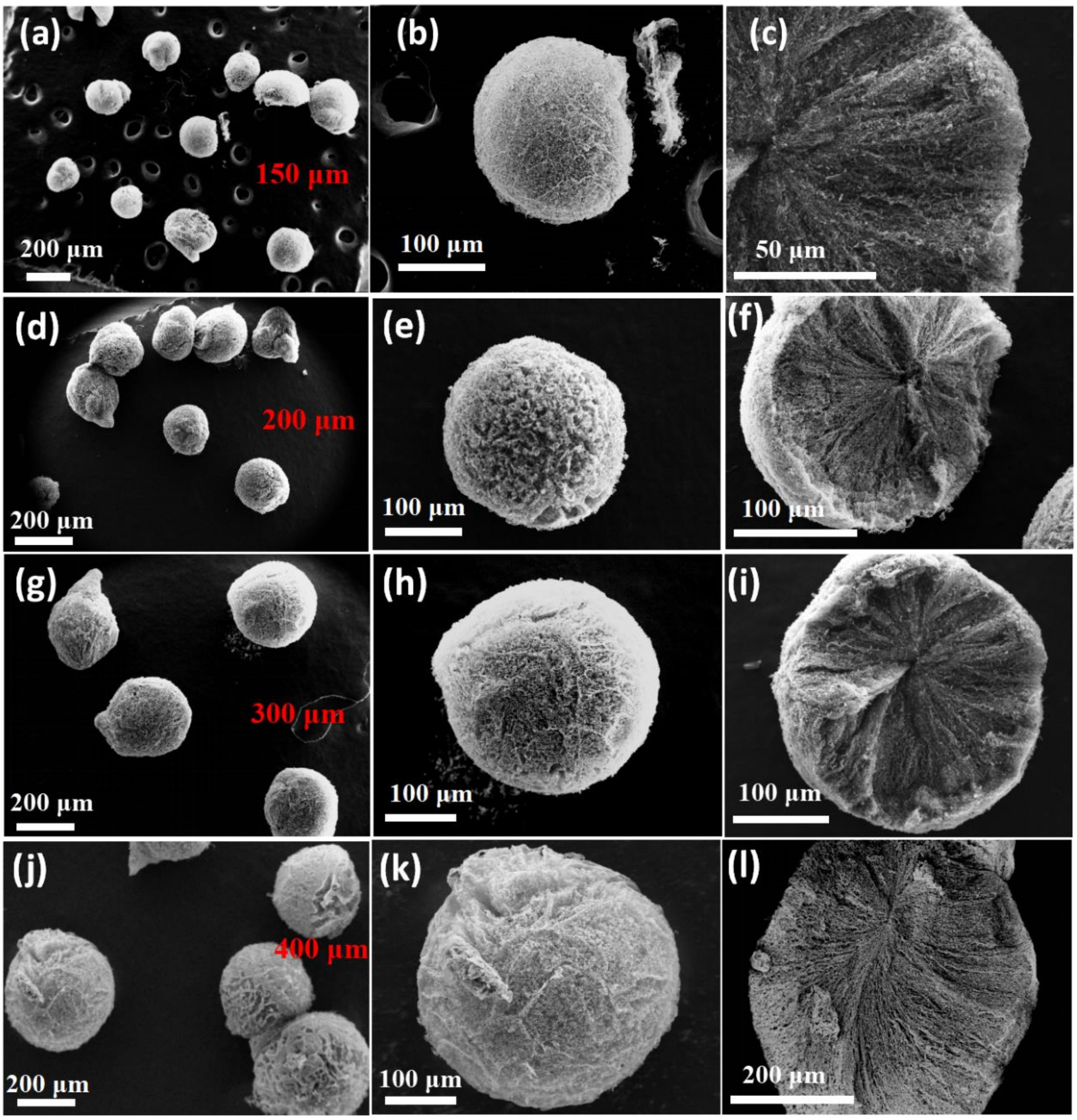

Figure 3.3 SEM images of ATM/GOAMs-30% with a diameter of about 150 μm, (a and b), 200 μm (d and e), 300 μm (g and h) and 400 μm (j and k); (c, f, i and l) SEM images of ATM/GOAMs-30% hemispheres (~150 μm, ~200 μm, ~300 μm and ~400 μm, respectively).

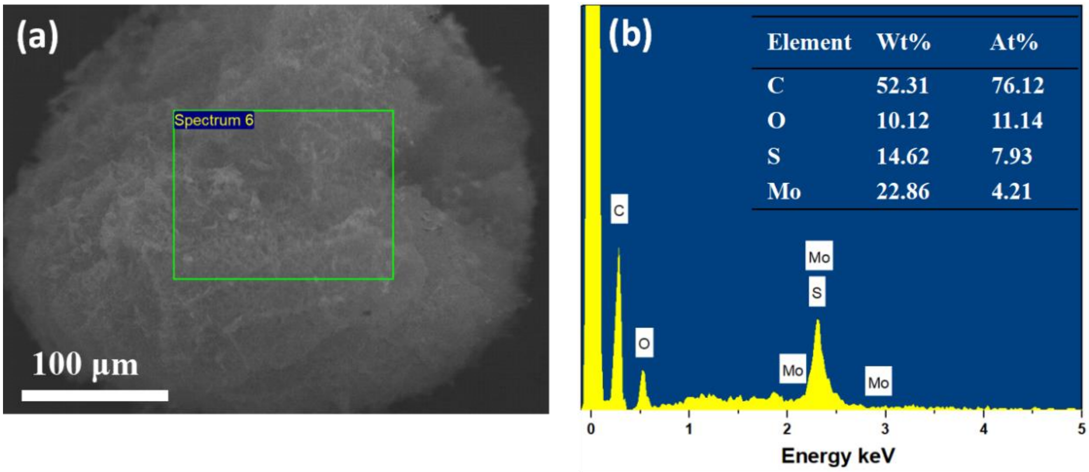

Element	Wt%	At%
C	52.31	76.12
O	10.12	11.14
S	14.62	7.93
Mo	22.86	4.21

Figure 3.4 SEM image and EDX analyses of MoS_2/prGOAM-40%-500.

The porosity of Ni-doped and undoped MoS_2/prGOAM-40%-500 was characterized using nitrogen adsorption experiments (Figure 3.1i). The N_2 adsorption-desorption isotherm of all samples showed a type IV isotherm (according to the IUPAC classification) with a small H3 hysteresis loop extending from $P/P_0 = 0.45$ to 0.95, demonstrating the presence of a mesoporous structure and slit-shaped pores,[41] as expected from the observed morphology. The N_2 adsorption-desorption measurements revealed that the as-prepared Ni-doped and undoped MoS_2/prGOAM-40%-500 hybrid with the diameter of 300 μm had Brunauer-Emmett-Teller (BET) specific surface area of 166 m^2g^{-1} and 170 m^2g^{-1}, respectively, which are higher values than those obtained for 150 μm (144 m^2g^{-1}), 200 μm (151 m^2g^{-1}) and 400 μm (125 m^2g^{-1}) microspheres (Figure 3.5). Moreover, MoS_2/prGOAMs (same diameter of ~300 μm) with different weight percentage of MoS_2 have slightly different BET specific surface area (Figure 3.6). This trend is somehow surprising considering that MoS_2 is much denser than carbon, however it can be partially explained assuming that a larger number of MoS_2 nanoparticles can physically prevent the stacking of the GO sheets on top of each other, allowing the formation of a larger amount of pores as actually confirmed by the presence of a significant tail in the size pore distribution above 3 nm. The pore-size distribution of Ni-doped and undoped MoS_2/prGOAM-40%-500 (300 μm) exhibit a dominant feature around 0.9-1.1 nm, and other weaker features at 2.4-5 nm (inset of Figure 3.1i), suggesting the presence of both micro- and meso-pores. As a result of the BET analyses, we can deduce that the diameter of prGOAMs maximizing the surface areas, is 300 μm, therefore in the following we will focus on this class of materials.

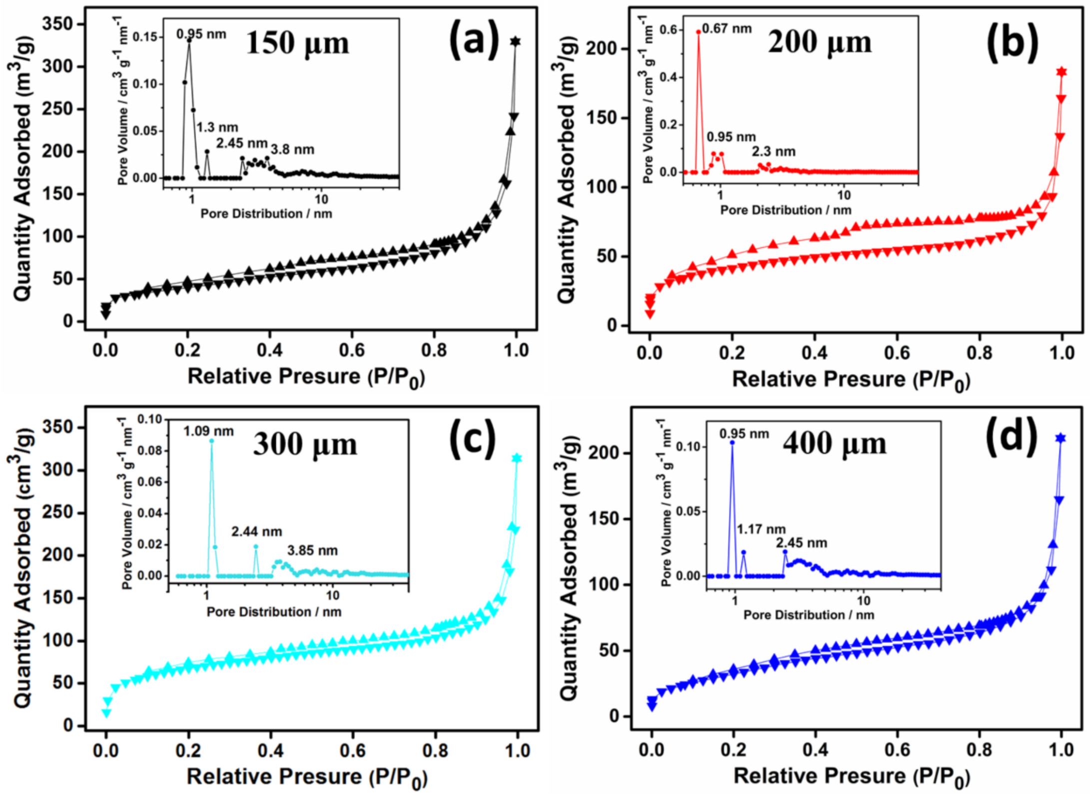

Figure 3.5 N_2 adsorption-desorption isotherm and pore-size distribution (inset) of MoS_2/prGOAM-40%-500 with the diameter of (a) 150 μm, (b) 200 μm, (c) 300 μm and (d) 400 μm.

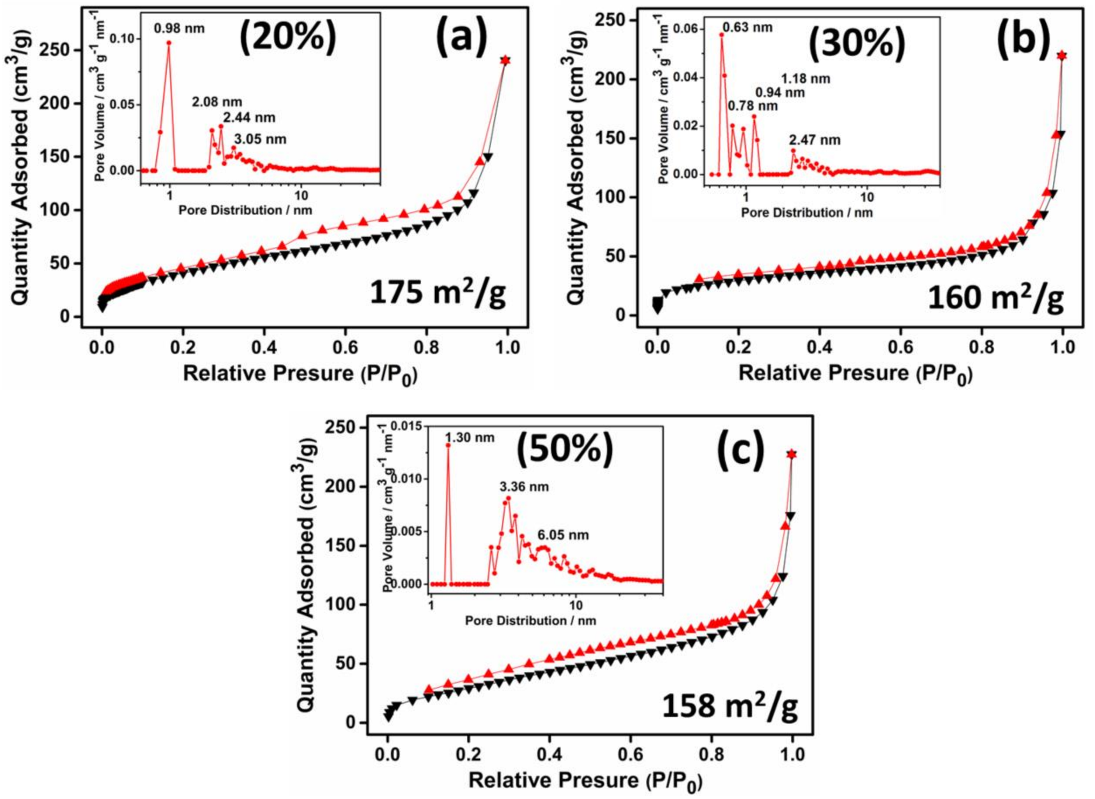

Figure 3.6 N_2 adsorption-desorption isotherm and pore-size distribution (inset) with the same diameter of 300 μm of (a) MoS_2/prGOAM-20%-500, (b) MoS_2/prGOAM-30%-500 and (c) MoS_2/prGOAM-50%-500.

Figure 3.9a shows the XRD pattern of the Ni-doped MoS_2/prGOAM-40%-500 sample. The diffraction peaks at 33.0°, 39.6°and 58.2°correspond to the (100), (103) and (110) planes of 2H-MoS_2, respectively. In the diffraction pattern, weak reflections associated with the formation of a $Ni_xMo_6S_8$ chevrel phase, i.e. a non-stoichiometric mixed metal sulphide, which can often exchange sulphur atoms for oxygen atoms, can be identified as well.[42] In fact, the possibility for both Ni and O to enter the lattice of MoS_2 is also confirmed theoretically: Ni dopants can substitute Mo atoms to occupy the transition metal lattice sites in Ni-doped MoS_2,[32] meanwhile Ni and O atoms can be co-doped into MoS_2 nanosheets.[43]

Figure 3.7 shows the XRD pattern of the MoS_2/prGOAM-30%-500 and MoS_2/prGOAM-40%-500 samples, showing clear diffraction features associated with 2H-MoS_2. It is worth noticing that the intensity of (002) plane peaks of 2H-MoS_2 decreases with increasing graphene amount in the composites, and MoS_2/prGOAM-40%-500 exhibits a larger interlayer spacing than MoS_2/prGOAM-30%-500 as suggested by the shift of (002) diffraction peak from 12.9°to 12.7°. This indicates that graphene inhibits the (002) plane growth of MoS_2 crystals in the hybrids.[44] Finally, the presence of the peak at approximately 26.0°confirms that GO has been converted to prGO.

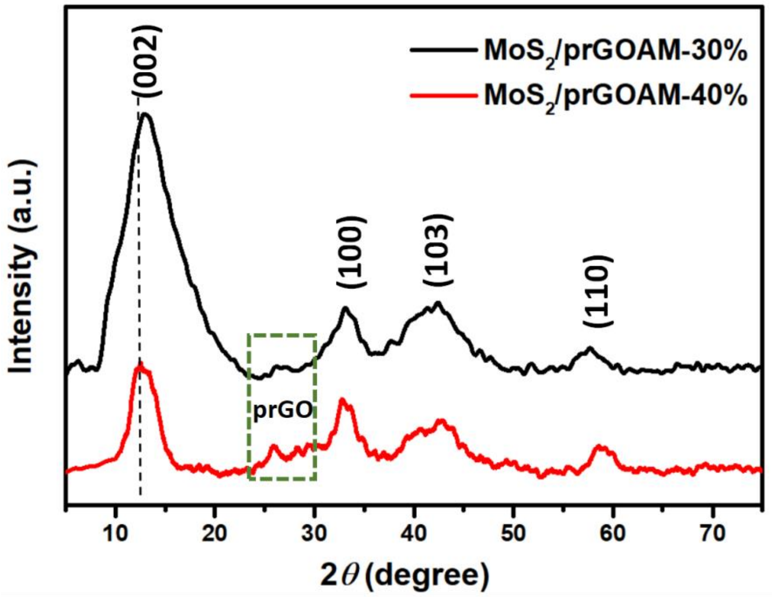

Figure 3.7 XRD pattern of MoS_2/prGOAM-30%-500 and MoS_2/prGOAM-40%-500.

The characteristic Raman peaks of 2H-MoS_2 corresponding to the E^1_{2g} in-plane vibrational mode at 376 cm^{-1} and the A^1_g out-of-plane vibrational modes at 402 cm^{-1} are observed for MoS_2/prGOAM-40%-500 (Figure 3.8) [45,46] in agreement with the XRD data. The ratio between the D and G peak intensity (I_D/I_G) gives important information about the disorder degree and defectivity of the carbon lattice [47]: the I_D/I_G of ATM/GOAMs was 0.96, smaller than that of MoS_2/prGOAMs (I_D/I_G=1.3), which means that there are more defects after the high temperature treatment, which is not unusual in carbon materials and it is due to the formation of small new patches of C sp^2.

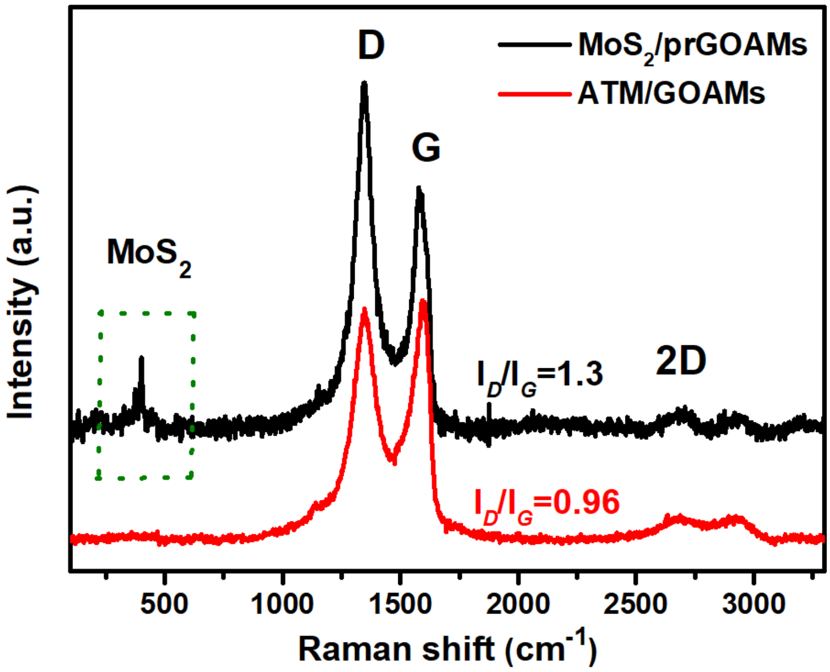

Figure 3.8 Raman spectra of ATM/GOAMs-40% and MoS_2/prGOAMs-40%-500.

For a catalysis-oriented study, exploring the surface composition is mandatory. Figure 3.9c shows the XPS C 1s region of Ni-doped MoS_2/prGOAM-40%-500: different chemical species can be identified, i.e. C sp^2 at a binding energy (BE) of 284.2 eV, C sp^3 at 285.6 eV, C-O (epoxides and alcohols) at 286.9 eV, C=O (carbonyls) at 288.0 eV, HO-C=O (carboxyls) at 289.5 eV and the π-π* satellite at 290.9 eV. The observed relative intensity among the components suggests that the GO sheets have been substantially reduced during the thermal treatment (see for comparison figure 3.11a for the materials before the anneling). The S 2p region (Figure 3.9d) presents two doublets: the former with maxima at 161.5($2p_{3/2}$) eV and 162.6 eV ($2p_{1/2}$) is ascribed to Mo-S bonds, while the latter with maxima at 163.8 eV ($2p_{3/2}$) and 164.9 eV ($2p_{1/2}$) to Mo-S-O.[48,49] Two small additional peaks at 168.1 eV($2p_{3/2}$) and 169.2 eV ($2p_{1/2}$) are due to traces of SO_4^{2-}.[50,51] Figure 3.9e shows the XPS data of the Mo 3d region for Ni-doped MoS_2/prGOAM-40%-500. Apart from the peak at BE of 225.9 eV, which is associated with the S 2s core levels of MoS_2, the remaining eight peaks, are assigned to four 3d doublets of chemically distinct Mo species. The two peaks at 228.7 ($3d_{5/2}$) and 231.9 eV ($3d_{3/2}$), are ascribed to 2H-MoS_2,[48,49,52,53] whereas the Mo $3d_{5/2}$ component at 232.6 eV can be assigned to Mo^{6+} oxidation state and the other peaks (Mo $3d_{5/2}$ at 230.1 eV and 231.6 eV) are due to MoS_3 and to an oxysulfide phase MoO_xS_y, with an effective oxidation state of ca. 5.5^+,[31] in agreement with the analysis of the S 2p spectrum. The oxysulfide phases is likely formed at the edges of MoS_2, either after environmental oxidation or, most likely, at the interface with oxygenated species typical of GO and prGO, and as intrinsic contaminant of the

$Ni_xMo_6S_8$ chevrel phase. Also the Ni $2p_{3/2}$ photoemission line (in Figure 3.9f) was separated into chemically shifted components: two distinct components at BEs of 852.7 and 856.6 eV were identified, which were attributed to Nickel in a mostly sulphur environment, i.e. NiS_xO_y,, and NiO_x species, respectively.[33,54] The other peak centred at 862.2 is a shakeup satellite typical of Ni^{2+} ions surrounded by oxygen atoms.

Table 3.2 summarizes the atomic percentage of the different elements in Ni-doped MoS_2/prGOAM-40%-500 derived from the XPS data. It can be seen that the mass percentage of O and C atoms are 10.55% and 42.25%, respectively, and the total mass of S and Mo is 46.4%. In addition, the measured atomic ratio of Mo:S (1:2.5) is close to the MoS_2 stoichiometric value and the atomic ratio of Ni/Mo (5.3%) is very close to the nominal 5%.

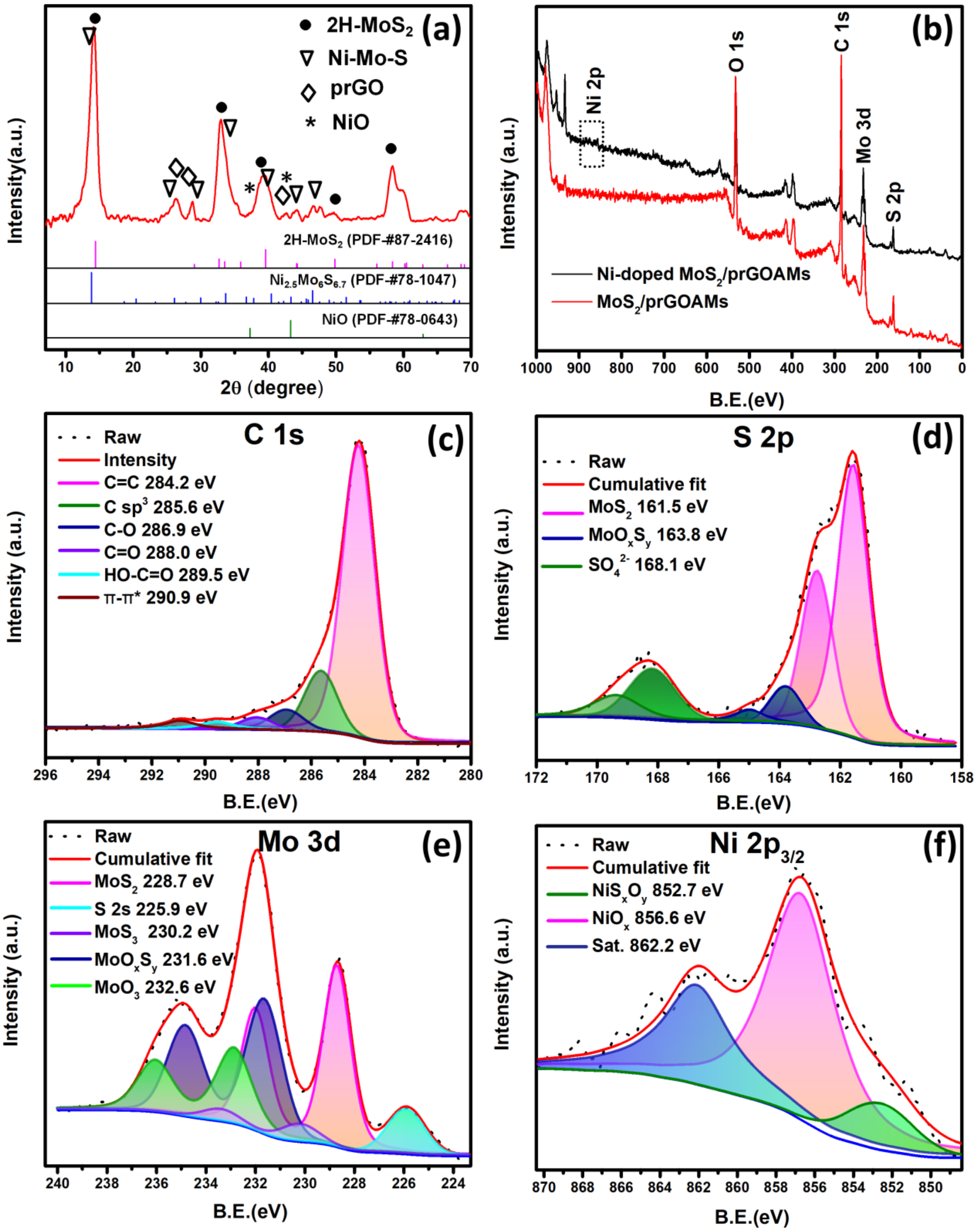

Figure 3.9 (a) XRD pattern of Ni-doped MoS_2/prGOAM-40%-500; XPS broad survey spectrum of Ni-doped and undoped MoS_2/prGOAM-40%-500; XPS data of the C 1s (c), S 2p (d), Mo 3d (e) and Ni 2p (f) regions where the different fitted components are outlined.

Table 3.2 The atom and mass percentages of different elements in Ni-doped MoS_2/prGOAM-40%-500 derived from XPS data.

Element	Atom percentage (%)	Mass percentage (%)
C	68.53	42.25
O	14.18	10.55
S	12.17	24.61
Mo	4.86	21.81
Ni	0.26	0.78

We have also investigated by XPS the undoped MoS_2/prGOAM-40%-500 (Figure 3.10 and Table 3.3). Regarding the Mo 3d region, like in the previous case, we observed several components: the Mo $3d_{5/2}$ peak at 228.8 eV can be assigned to Mo^{4+}, whereas, the other two Mo $3d_{5/2}$ peaks at 229.8 and 231.4 eV having much lower intensities, arise from the chemical environment of Mo atoms in MoS_3 [55] and in a mixed MoO_xS_y phase. Comparing the relative intensity of the oxide and oxysulphides phases in doped vs undoped materials, it is clear that the presence of nickel promotes the introduction of oxygen. This behaviour is not unexpected considering the high oxophilicity of nickel atoms. Finally, the analysis of the C 1s energy region confirms that GO was partially reduced and MoS_2 was successfully synthesized.

The multipeak analysis of the C 1s photoemission spectrum of the pre-heated ATM/GOAM sample is reported in Figure 3.11a: the O-related peaks in the C 1s region of MoS_2/prGOAM-40%-500 (e.g. C-O, C=O and O-C=O groups) have a much lower intensity, suggesting that after the heat treatment the GOAMs were reduced to a large extent to prGOAMs. Moreover, as reported in Table 3.4, the mass percentage of oxygen in ATM/GOAMs is much higher, 27.6% and the C/O ratio changes from 1.8 to 9.8 after GO/ATM is converted to MoS_2/prGOAM-40%-500, confirming that the thermal treatment at 500℃ produces a significant reduction of the GO support. As a further check, in Figure 3.12 and Table 3.5 we report the XPS data of MoS_2/prGOAM-30%-500: the total mass percentage of S and Mo are 30.7%, once again, confirming the good agreement between the expected and actual composition.

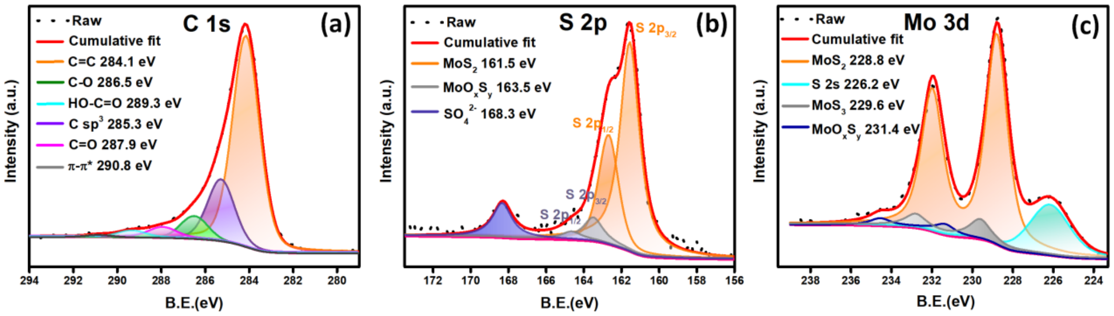

Figure 3.10 XPS data of the C 1s (a), S 2p (b) and Mo 3d (c) regions of MoS_2/prGOAM-40%-500, where the different fitted components are outlined.

Table 3.3 Atom and mass percentages of different elements in MoS_2/prGOAM-40%-500 derived from the XPS data.

Element	Atom percentage (%)	Mass percentage (%)
C	79.7	55.4
O	8.1	7.5
S	8.3	15.3
Mo	3.9	21.8

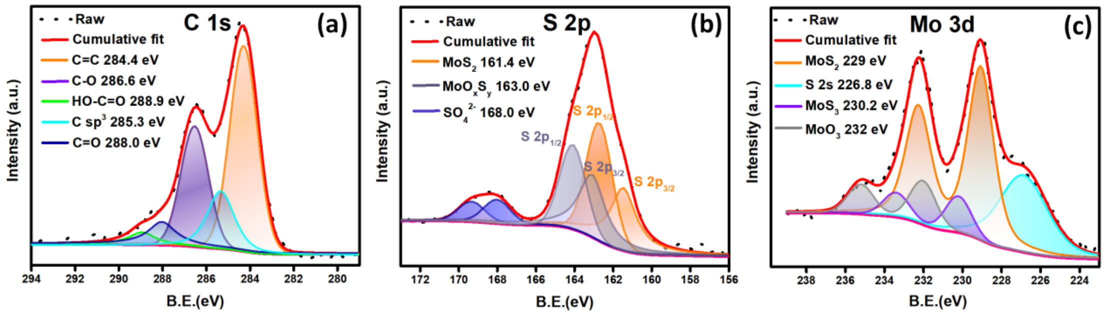

Figure 3.11 XPS data of the Mo 3d (a), S 2p (b) and C 1s (c) regions of ATM/GOAM-40% where the different fitted components are outlined.

Table 3.4 The percentages of different elements in ATM/GOAM-40%.

Element	Atom percentage (%)	Mass percentage (%)

C	55.8	37.3
O	30.9	27.6
S	10.1	18.0
Mo	3.2	17.1

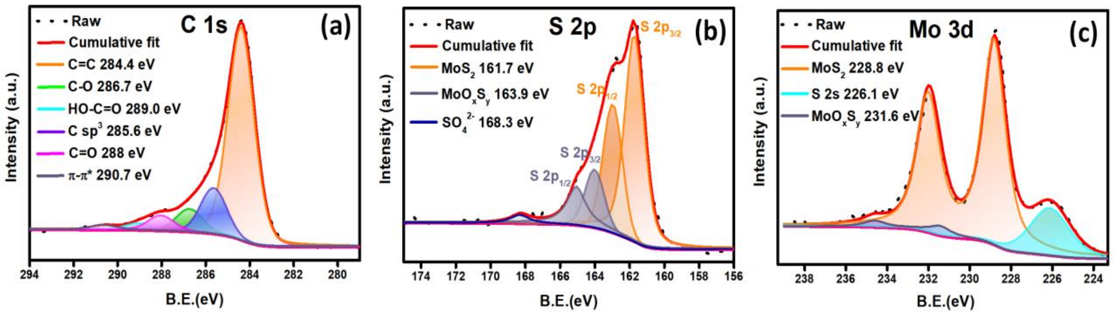

Figure 3.12 XPS data of the Mo 3d (a), S 2p (b) and C 1s (c) regions of MoS_2/prGOAM-30%-500 where the different fitted components are outlined.

Table 3.5 The percentages of different elements in MoS_2/prGOAM-30%-500.

Element	Atom percentage (%)	Mass percentage (%)
C	81.4	60.2
O	9.2	9.1
S	6.3	12.4
Mo	3.1	18.3

In summary, the body of our experimental data suggests that Ni-doped MoS_2/prGOAM-40%-500 is a rather complex nanocomposite, characterized by a unique mesoporous morphology produced by the self-assembly of GO nanosheets, with a very complex chemical composition. In fact, the nickel atoms were introduced as atomic dopant into molybdenum sulphide, which on the other hand, given the synthesis conditions (water environment, mild annealing temperature, presence of Nickel (II) cations) and the intimate interactions with the GO nanosheets, is not phase pure but undergoes a significant oxidation and incorporation of oxygen producing an extended oxysulfide phase. Therefore, the nickel atoms can experience a local chemical environment that can be either oxygen or sulphur rich.

3.3.2 HER electrocatalytic characterization.

To identify the active phases, and understand the role of the morphology and structure of the 3D template, we adopted a reductionist approach and investigated both in alkaline and acid conditions the HER activity of different composite systems, (Figure 3.15), i.e. prGO, prGO and MoS_2 physically mixed powder, MoS_2/prGOAM-40%-500, and Ni-doped MoS_2/prGOAM-40%-500. The Ni-doped MoS_2/prGOAM-40%-500 sample presents the best HER activity with the lowest η_{10} (i.e. the overpotential necessary to reach a current density of 10 mA cm^{-2}) value of 174 mV vs RHE in 0.5 M H_2SO_4 and 160 mV vs RHE in 1 M KOH, compared with the prGO+MoS_2 physically mixed powder (η_{10} of 325 mV vs RHE in 0.5 M H_2SO_4 and 416 mV vs RHE in 1 M KOH) and MoS_2/prGOAM-40%-500 (η_{10} of 189 mV vs RHE in 0.5 M H_2SO_4 and 206 mV vs RHE in 1 M KOH). In Figure 3.13 and Figure 3.14 we report the morphologies of Ni-doped and undoped MoS_2/prGOAM-40%-500 after the HER activity test: both samples maintain their spherical shape and porous network features.

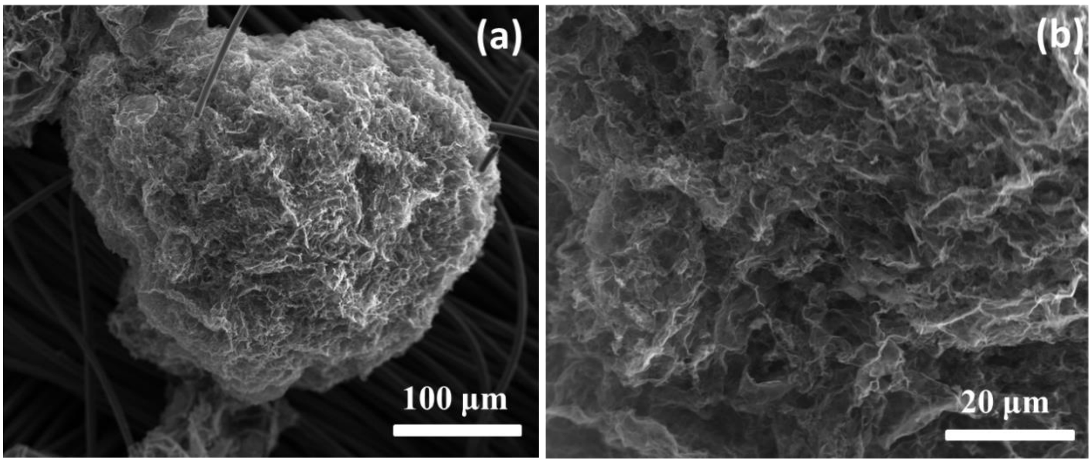

Figure 3.13 SEM images of Ni-doped MoS_2/rGOAMs-40%-500 after electrochemical activity test.

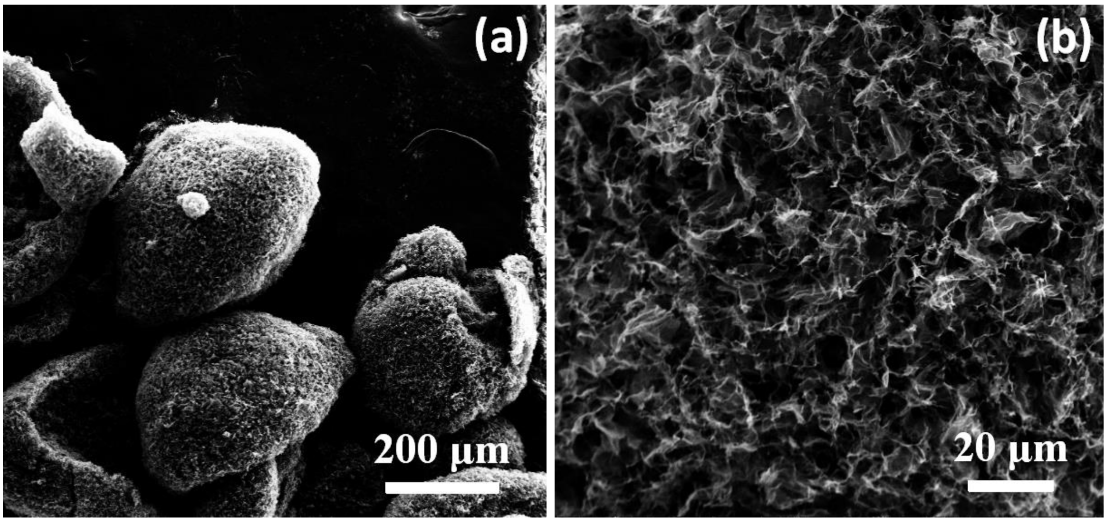

Figure 3.14 SEM images of MoS_2/rGOAMs-40%-500 after electrochemical activity test.

The same conclusions are reached when another figure of merit is taken into consideration, i.e. the Tafel slope, which is often utilized to evaluate the efficiency of the HER.

The linear portions of the Tafel plots (Figure 3.15b and d) were fit to the Tafel equation ($\eta = b \log j + a$), where j is the current density and b is the Tafel slope).[56–58] In acid conditions, the Ni-doped MoS_2/prGOAM-40%-500 exhibits a Tafel slope of 62 mV/dec, which is lower than that of MoS_2/prGOAM-40%-500 (83 mV/dec) and prGO+MoS_2 powder (117 mV/dec). In alkaline medium, the Ni-doped MoS_2/prGOAM-40%-500 exhibits a Tafel slope of 55 mV/dec, which is smaller than MoS_2/prGOAM-50%-500 (84 mV/dec) and prGO+MoS_2 physically mixed powder (143 mV/dec).

In the acidic media, the HER reaction proceeds through three principal reaction steps:

Volmer adsorption step

$$H_3O^+ + e^- \rightarrow H_{ad} + H_2O \qquad (4)$$

Heyrovsky desorption step

$$H_{ad} + H_3O^+ + e^- \rightarrow H_2 + H_2O \qquad (5)$$

Tafel recombination step

$$2H_{ad} \rightarrow H_2 \qquad (6)$$

In alkaline medium, the reaction proceeds as it follows:

Volmer adsorption step

$$H_2O + e^- \rightarrow H_{ad} + OH^- \qquad (7)$$

Heyrovsky desorption step

$$H_{ad} + H_2O + e^- \rightarrow H_2 + OH^- \quad (8)$$

Tafel recombination step

$$2H_{ad} \rightarrow H_2 \qquad (9)$$

where H_{ad} is the hydrogen adsorption site onto the surface of the catalyst. After the first Volmer step, there are two possibilities, i.e. Heyrovsky process, or Tafel recombination step. Depending on the rate-determining step of the HER reaction, the expected value of the Tafel slope should be 120 mV/dec for the Volmer step, and for the Heyrovsky and Tafel ones 40 and 30 mV/dec, respectively.[56–59] Therefore, the HER reaction for Ni-doped MoS_2/prGOAM-40%-500 and MoS_2/prGOAM-40%-500 likely follows a Volmer-Heyrovsky mechanism.

In general, the overpotential required to drive the overall reaction differs according to the reaction pathway, which is strongly dependent on the pH, and usually HER activity and exchange current densities are lower in alkaline rather than in acid solutions.[60–63] This is caused by the initial cleavage of the H–O–H bond in the Volmer step required in alkaline conditions (equation 7), which supplies H_{ad} to the following steps and is considered the rate-determining step of the overall reaction.[63] Also, in our undoped MoS_2/prGOAMs samples we observed better catalytic figures of merit in acid medium compared to alkaline conditions. On the contrary, the electroactivity of Ni-doped MoS_2/prGOAMs is significantly improved in alkaline conditions, likely because Ni dopants or NiO_x clusters supported on or within MoS_2, given their oxophilicity, can assist water adsorption and dissociation. The combination of MoS_2 and Ni based oxides (and more generally oxides of other transition metals) is not unusual in the literature. DFT calculations suggest that water is adsorbed on the oxide moiety and then it is electrochemically dissociated forming a hydroxide stabilized on the oxide and a H adatom on MoS_2.[64] This type of active bifunctional NiO_x/MoS_2 interface is present extensively in our materials as demonstrated by XPS and XRD data.

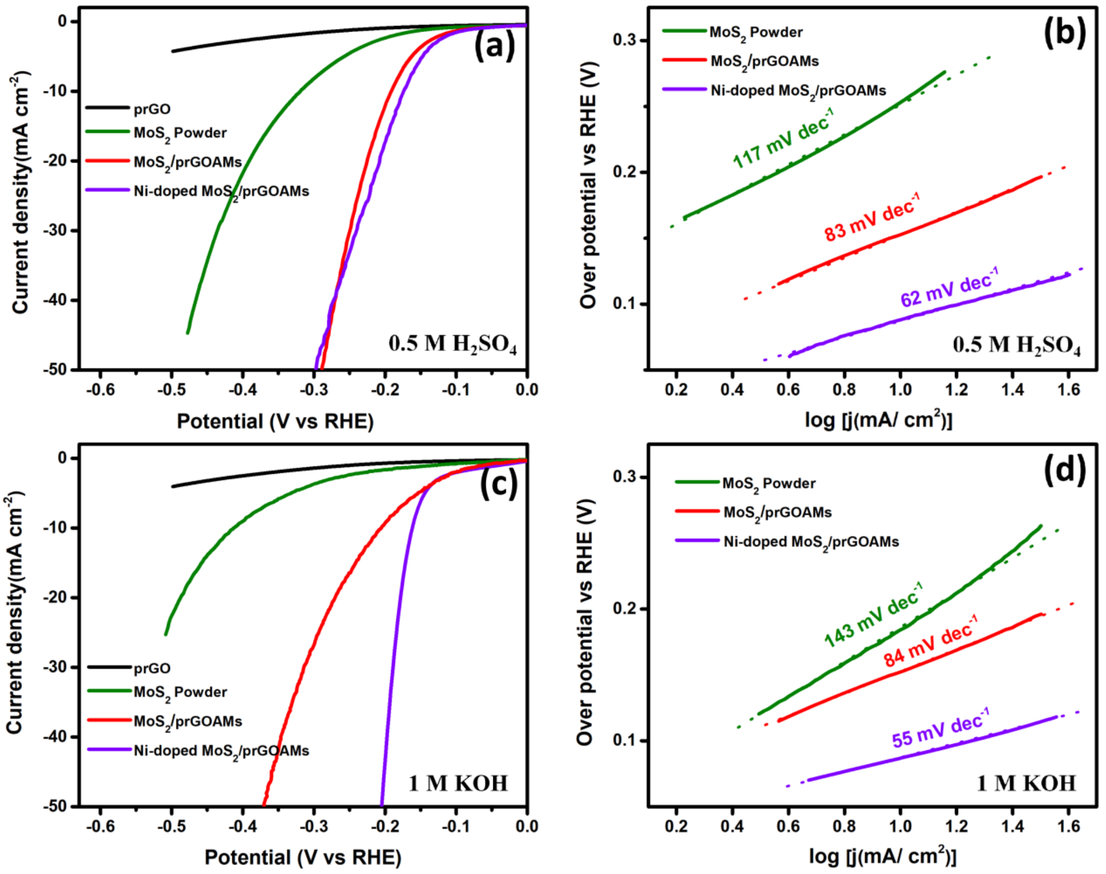

Figure 3.15 Polarization curves and Tafel plots in 0.5 M H_2SO_4 (a, b) and in 1 M KOH (c, d), respectively, for prGO, MoS_2 powder, MoS_2/prGOAM-40%-500 and Ni-doped MoS_2/prGOAM-40%-500.

The HER electrochemical activity of Ni-doped and undoped MoS_2/prGOAMs-x%-500 with different loading of MoS_2 was also evaluated. The η_{10} value of Ni-doped MoS_2/prGOAMs-x%-500 decreases from 262 mV to 174 mV (Fig 3.16a, in acid condition) and from 244 mV to 160 mV (Fig 3.16c, in alkaline condition) when the weight content of MoS_2 increases from 20% to 40%. This clearly indicates that the HER sites are related to MoS_2. However, when the MoS_2 loading is increased from 40% to 50%, η_{10} becomes slightly worse: changing from 174 mV to 179 mV (in acid condition) and from 160 mV to 178 mV (in alkaline condition), suggesting that the HER cannot indefinitely increase by adding more active phase. A similar trend can be deduced by the η_{10} values of the undoped MoS_2/prGOAMs-x%-500 samples. These data suggests that the MoS_2 nanoparticles tend to aggregate and grew in size so that the TMDC/graphene interaction becomes less effective with respect to the electron transfer [65] and the addition of MoS_2 above 40% does not produce the exposure of additional active sites.

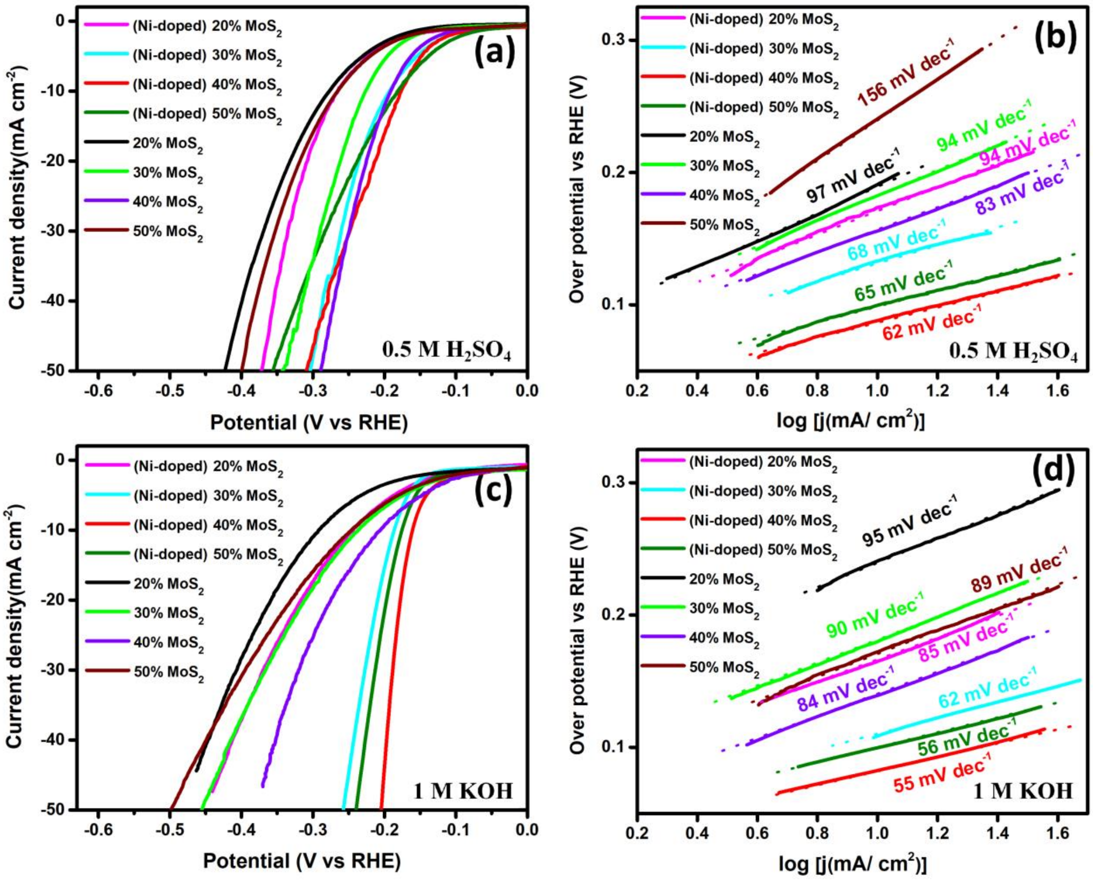

Figure 3.16 Polarization curves and Tafel plots in 0.5 M H_2SO_4 (a, b) and in 1 M KOH (c, d), respectively, for Ni-doped MoS_2/prGOAM-x%-500 and MoS_2/prGOAM-x%-500, (x= 20,30,40,50).

We also investigated the dependence of HER activity of Ni-doped and undoped MoS_2/prGOAM-40% on the reduction temperature, since this parameter can affect in a complex way many structural properties, e.g. the reduction degree of the graphene support, the crystallinity, size, and stoichiometry of the final MoS_2 nanoparticles. Figure 3.20a compares the electrochemical activity of Ni-doped MoS_2/prGOAM-40% samples (i.e. the best catalyst with respect to the loading), which were treated at different temperatures, namely 400, 500, 600 and 900 ℃ . The sample heated at 500 ℃ presents the best HER activity, with the lowest η_{10} value of 160 mV vs RHE in alkaline conditions. The same current density, in the case of 400 ℃, 600 ℃ and 900 ℃ electrodes can be only reached at significantly higher η_{10} values (243, 186 and 252 mV, respectively). The Tafel slopes (Figure 3.20b) confirm the trend observed for η_{10}. To determine if the optimal thermal treatment temperature changes without Ni doping, we also studied the dependence of the polarization curves of undoped MoS_2/prGOAM-40% after different reduction temperatures (Figure 3.17), obtaining the same trend observed in Ni-doped samples. Probably, 500℃ is the best temperature because it is sufficient to form MoS_2 from the ATM precursor and significantly reduced the GO scaffold, but low enough to prevent aggregation and coalescence of the active phase or an alteration of their stoichiometry and structure (e.g. excessive removal of oxygen, or phase separation).

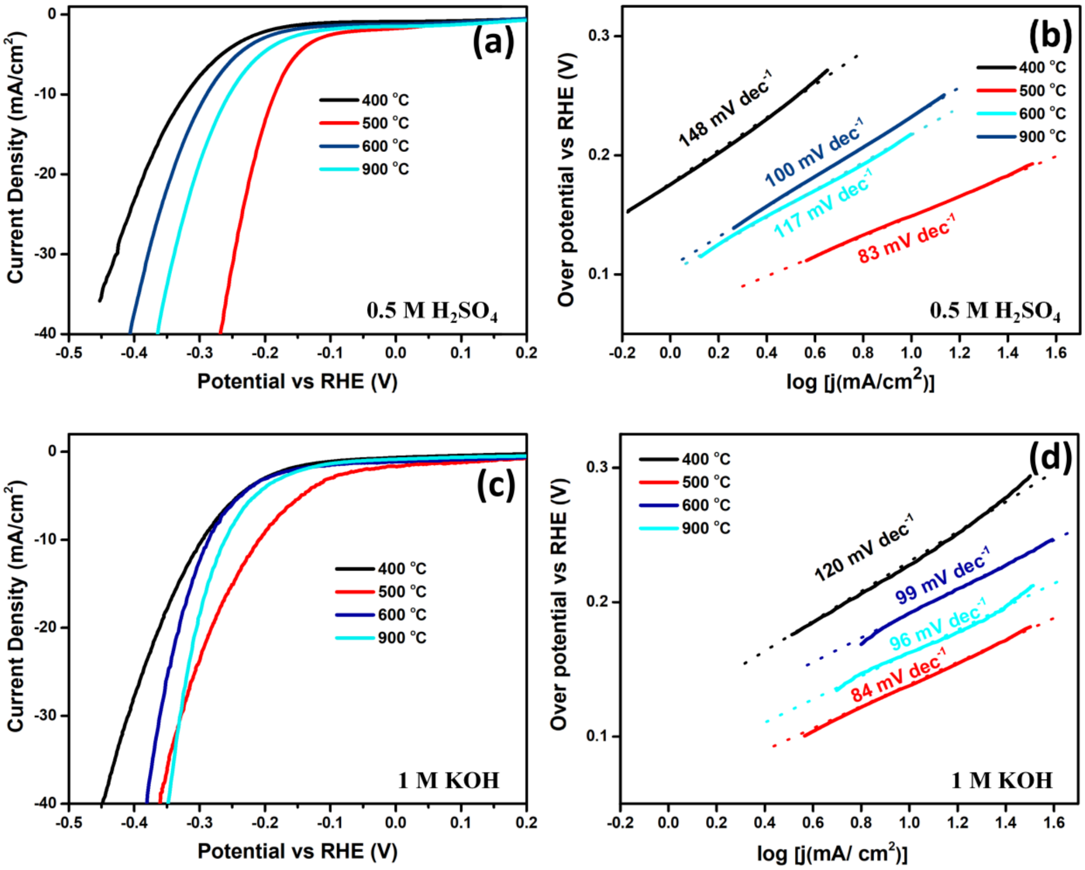

Figure 3.17 Polarization curves and Tafel plots in 0.5 M H_2SO_4 (a, b) and in 1 M KOH (c, d), respectively, for MoS_2/prGOAM-40% after different temperature thermal treatments at 400℃, 500℃, 600℃ and 900℃.

To facilitate the comparison of performance descriptors, Tafel slopes and η_{10} values are summarized in Table 3.6. It results that the Ni-doping increases the activity in all the explored cases, decreasing the η_{10} and increasing the current density. However, the nickel presence is particularly advantageous when the HER is carried out in alkaline medium.

The key role played by Nickel prompted us also to investigate the effect of nickel concentration in the HER performance, in particular we synthesized a series of samples with optimized parameters (Ni-doped MoS_2/prGOAM-40%-500) at varying Ni doping: 2.5%, 5% and 10% (Fig 3.18). It can be seen that the effect of nickel in acid condition is not very pronounced, whereas is quite critical in alkaline conditions, confirming that the nickel is key to promote water dissociation. In all media, the best performing system present a 5% doping, whereas the sample with lower doping shows a similar activity and low overpotential, but worse performance at high currents, probably because of the reduced number of bifunctional sites. When a 10% Ni doping is achieved, we observe a decreased of the performances, likely because the dopant amount increases does not produce additional sites, but just the formation of phase separated NiO_x phases as well as an excessive oxidation of the MoO_xS_y component.

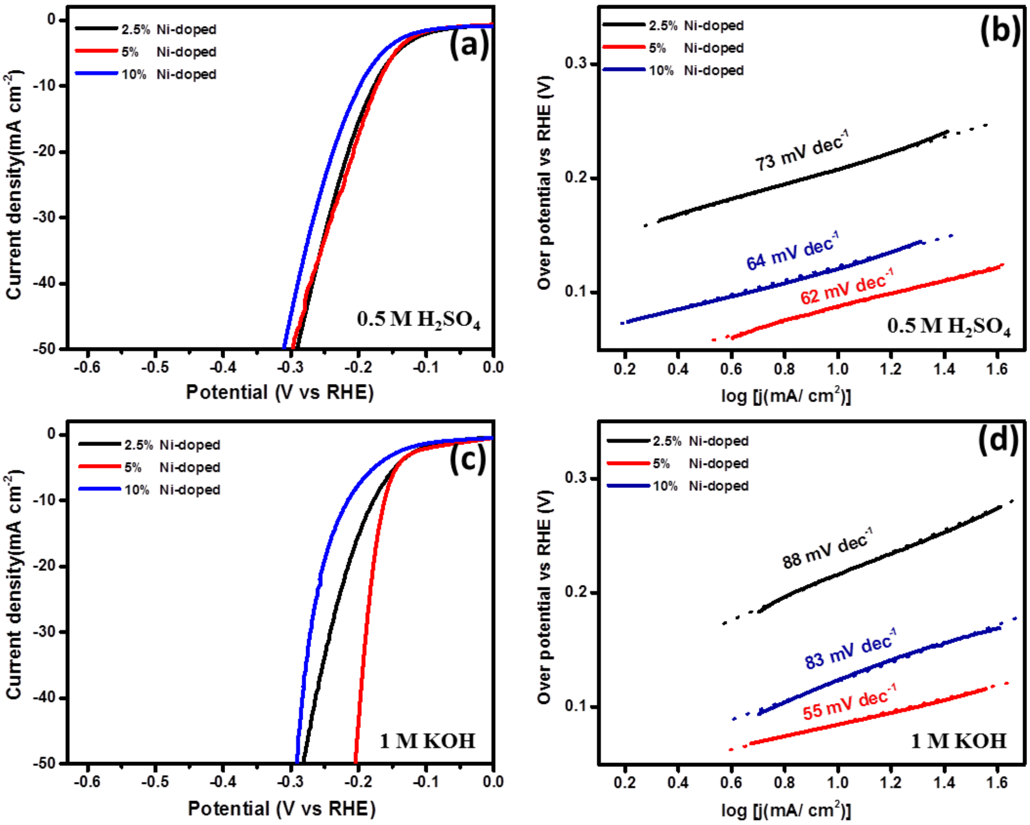

Figure 3.18 Polarization curves and Tafel plots in 0.5 M H_2SO_4 (a, b) and in 1 M KOH (c, d), respectively, for Ni-doped MoS_2/prGOAM-40%-500 at varying Ni doping: 2.5%, 5% and 10%.

To assess the role of the special centre diverging morphology of the microspheres, we prepared working electrodes using milled Ni-doped MoS_2/prGOAM-30%-500 and Ni-doped MoS_2/prGOAM-40%-500 powders. In both cases, the milled electrodes undergo a strong reduction of the catalytic performance (Figure 3.20c and d), especially in the case of the best catalyst, Ni-doped MoS_2/prGOAM-40%-500. This reduction is also evident in the undoped MoS_2/prGOAMs (Figure 3.19a and b).

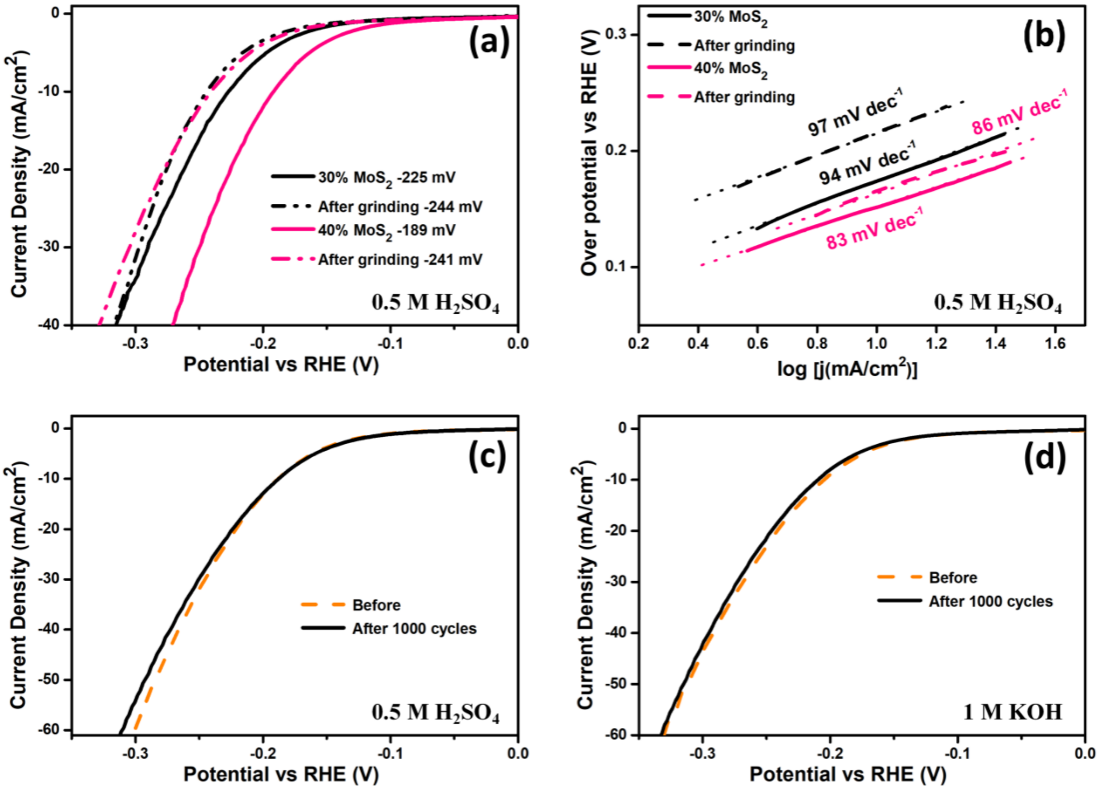

Figure 3.19 (a) HER activity tests for MoS_2/prGOAM-30%-500 and MoS_2/prGOAM-40%-500 before and after milling; (b) corresponding Tafel plots. (d) Polarization curves of MoS_2/prGOAM-40%-500 before and after 1000 cycles at a scan rate of 50 mV/s in 0.5 M H_2SO_4 (c) and in 1.0M KOH (d), respectively.

Finally, given its importance for practical applications, the long-term stability of the samples under HER working condition was investigated by chronopotentiometric measurements. Figure 3.20e and f show the V-t curves of Ni-doped MoS_2/prGOAM-40%-500 sample obtained in alkaline and acid environment, respectively. As observed in the undoped samples (Figure 3.19c and d), the electrodes present a high stability in both pH conditions. However, in alkaline medium the catalytic activity increases slightly with time, while a low decrease is observed in acid conditions. Notably, at the end of the durability test, Ni-doped MoS_2/prGOAM-40%-500 exhibits an outstanding η_{10} of 147 mV, corresponding to a mass activity of 50 mA/mg, which is about twice higher than other similar materials recently reported in the literature (see Table 3.7), e.g. Co- MoS_2 (η_{10} 137 mV, 59 mV dec^{-1}, 28.6 mA/mg) [66] and 1T-MoS_2/$Ni^{2+\delta}O_\delta(OH)^{2-\delta}$(1:1) ($\eta_{10}$ 73 mV, 77 mV dec^{-1}, 25 mA/mg).[67] This comparison confirms the exceptional properties of the prGOAMs as supporting scaffold, which allows an extremely efficient utilization of the active phase.

Finally, Table 3.8 compares the figures of merits (η_{10} and Tafel slope) of the catalysts investigated in this work with other relevant literature data, where an active MoS$_2$ phase is supported on different 2D or 3D Nickel or graphenic supports. The HER performance of the Ni-doped MoS$_2$/prGOAM-40%-500 catalyst compares very favourably to those observed for other non-noble-metal catalysts, e.g. 2D-MoS$_2$/Ni(OH)$_2$ (η_{10} 185 mV, 73 mV dec^{-1}),[64] MCM@MoS$_2$–Ni (η_{10} 263 mV, 82mV dec^{-1}),[68] MoS$_2$–MoO$_2$ hybrids (η_{10} 240 mV, 76 mV dec^{-1}),[69] MoS$_2$ on 3D-Ni (η_{10} 237 mV, 110 mV dec^{-1}) [70] and Ni-doped 3D-MoS$_2$ sample (η_{10} 220 mV, 65 mV dec^{-1}).[33]

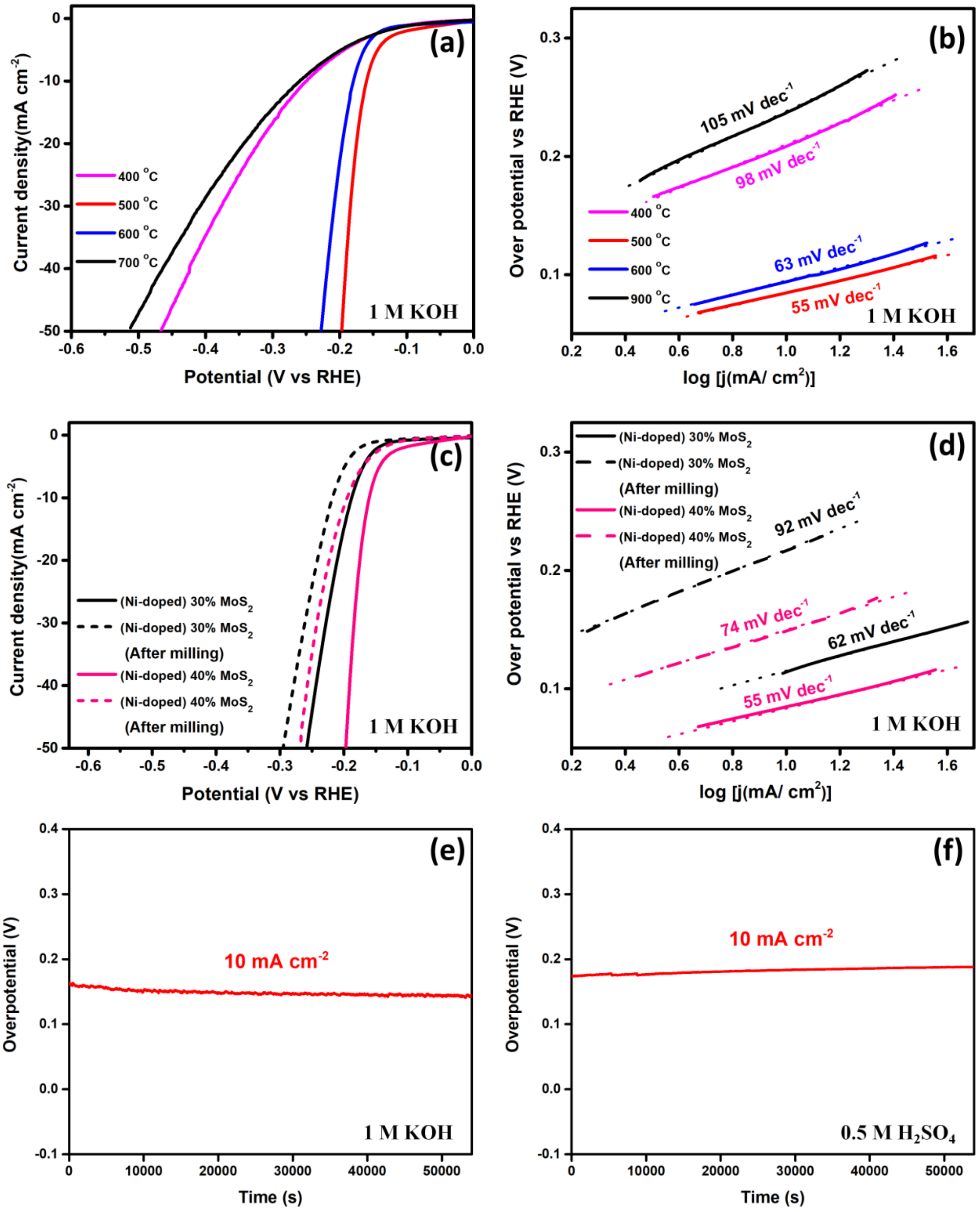

Figure 3.20 Polarization curves (a) and Tafel plots (b) in 1 M KOH, for Ni-doped

MoS_2/prGOAM-40% after different temperature thermal treatments at 400℃, 500℃, 600℃ and 900℃ . (c) Polarization curves for Ni-doped MoS_2/prGOAM-30%-500 and Ni-doped MoS_2/prGOAM-40%-500 in 1 M KOH before and after milling; (d) corresponding Tafel plots. Chronopotentiometric tests of Ni-doped MoS_2/prGOAM-40%-500 at a constant current density of 10 mA cm^{-2} for 15 h in 1.0M KOH (e) and in 0.5 M H_2SO_4 (f), respectively.

Table 3.6. HER overpotentials at 10 mA cm^{-2} (η_{10}) and Tafel slopes for the sample investigated ion the present study in 0.5 M H_2SO_4 and 1 M KOH.

Material	**Overpotential η_{10} (mV)**		**Tafel Slope (mV/dec)**	
	0.5 M H_2SO_4	**1 M KOH**	**0.5 M H_2SO_4**	**1 M KOH**
prGO+MoS_2 powder	325	416	117	143
MoS_2/prGOAM-20%-500	273	289	97	95
MoS_2/prGOAM-30%-500	225	238	94	90
MoS_2/prGOAM-40%-500	189	206	83	84
MoS_2/prGOAM-50%-500	263	246	156	89
MoS_2/prGOAM-40%-400	317	297	148	120
MoS_2/prGOAM-40%-500	189	206	83	84
MoS_2/prGOAM-40%-600	289	285	117	99
MoS_2/prGOAM-40%-900	250	260	100	96
Ni-doped MoS_2/prGOAM-20%-500	262	244	94	85
Ni-doped MoS_2/prGOAM-30%-500	189	187	68	62
Ni-doped MoS_2/prGOAM-40%-500	174	160	62	55
Ni-doped MoS_2/prGOAM-50%-500	179	178	65	56
Ni-doped MoS_2/prGOAM-40%-400	-	243	-	98

Ni-doped MoS_2/prGOAM-40%-500	-	160	-	55
Ni-doped MoS_2/prGOAM-40%-600	-	186	-	63
Ni-doped MoS_2/prGOAM-40%-900	-	252	-	105
Ni-doped MoS_2/prGOAM-40%-900	-	252	-	105
(2.5%) Ni-doped MoS_2/prGOAM-40%-500	177	178	73	88
(5%) Ni-doped MoS_2/prGOAM-40%-500	174	160	62	55
(10%) Ni-doped MoS_2/prGOAM-40%-500	196	213	64	83

Table 3.7 Comparison of HER activity data and mass activity for several literature data closely related to the present paper.

Catalyst	**η(mV) at 10 mA cm^{-2}**	**Tafel slope (mV/dec)**	**Mass activity (mA/mg)**	**References**
Ni-doped MoS_2/prGOAM-40%-500	147	55	50	*This work*
Co- MoS_2	137	59	28.6	*Angewandte Chemie 133.13 (2021): 7327-7334*
1T-$MoS_2/Ni^{2+\delta}O_\delta(OH)^{2-\delta}$(1:1)	73	77	25	*Advanced Science 5.2 (2018): 1700644*
FNHNs	450	108.76	65	*Small 13.6 (2017): 1602637*
FNHNs/Nickel Foam	140	81.63	*nickel foams	*Small 13.6 (2017): 1602637*

Table 3.8 Comparison of HER activity data for several literature data closely related to the present paper.

Catalyst	**η(mV) at 10 mA cm^{-2}**	**Tafel slope (mV/dec)**	**References**
Pt	10	33	*Carbon* 142 (2019): 206-216
Ni-doped MoS_2/prGOAM-40%-500	147	55	*This work*
Ni-doped MoS_2/prGOAM-40%-500 (milling)	198	74	*This work*
MoS_2/prGOAM-40%-500	189	83	*This work*
prGO and MoS_2 powder	304	117	*This work*
2D Layered MoS_2 -rGO Hybrids	250	79	*Scientific reports* 7 (2017): 1-13
1T − 2H MoS_2	290	65	*Advanced Energy Materials 8.25 (2018): 1801345*
MoS_2−MoO_2 nanohybrids	240	76	*Nanoscale 7 (2015): 5203-5208*
MoS_2-5	190	54	*Journal of Catalysis 391 (2020): 91-97*
MoS_2 on 3D-Ni	237	110	*International Journal of Hydrogen Energy* 44 (2019): 28143-28150
Hollow-rGO@MoS_2	240	105	*Nano-micro letters* 10 (2018): 62
Ni-doped 3D-MoS_2	220	65	*Surfaces 2.4 (2019): 531-545*
Ni-MoS_2 /RGO	168	69.5	*ChemSusChem 12.2 (2019): 457-466*
MCM@MoS_2 − Ni	263	82	*Advanced Functional Materials 28.51 (2018): 1807086*

2D-MoS_2/$Ni(OH)_2$	185	73	*Advanced Materials 30.28 (2018): 1801171*

3.4 Conclusion

In conclusion, we have demonstrated the successful fabrication of (5% Ni)-MoS_2 decorated carbon 3D architectures derived from prGOAMs through a facile and quick one pot method that combines electrospraying and in-situ freeze-drying technique. The use of a sophisticated carbon scaffold with centre diverging channels and intrinsic mesoporosity allows a very economical usage of the active phase, providing materials with excellent performances.

In general, the realization of advanced nanocatalysts with both controlled morphology and tailored chemical composition is performed with complex multistep procedures that rely mainly on solvothermal synthesis and/or chemical exfoliation of MoS_2 or other TMDCs, which are expensive, lengthy and with a low throughput.[64,71] The present method on the contrary, is quite fast, easily scalable and extremely versatile and does not need the use of expensive supports such as Nickel foams. Its effectiveness has been demonstrated for the preparation of Ni doped MoS_2/GO nanocomposites, but it can be easily extended to other metal dopants, different TMDCs, and a variety of 2D materials.[29,30,72]

After a careful optimization procedure, the best material, Ni-doped MoS_2/prGOAM-40%-500, achieved an excellent performance especially in alkaline conditions, where an η_{10} of 140 mV even after 15 h of continuous electrolysis.

The reason of such high activity can be traced back on the one hand to the special dandelion morphology of the carbon scaffold, and on the other hand to the presence of nickel, which assists the dissociation of water in the first step of the HER.

Actually, the obtained materials can be best described as Ni-Mo mixed oxysulfides that likely contain a large number of adjacent NiO_x and MoS_x centers. The former has good affinity for water and present a suitable adsorption energy for OH,[73] while the latter a convenient H adsorption energy, therefore making the composite material an excellent bifunction catalyst. Interestingly, given the high dispersion of Ni into MoO_xS_y the bifunctional effect is already achieved at a very low amount of Nickel, 5% w/w only, which is much lower than other NiO_x/MoS_2 catalysts in the literature.[64,67,74] This point is quite important for practical application because Nickel is not an environmental benign material, and its use should be minimized in practical applications.

References

(1) Joshi, A. S.; Dincer, I.; Reddy, B. V. Exergetic Assessment of Solar Hydrogen Production Methods. *Int. J. Hydrogen Energy* **2010**, *35* (10), 4901–4908. https://doi.org/10.1016/j.ijhydene.2009.09.067.

(2) Brandon, N. P.; Kurban, Z. Clean Energy and the Hydrogen Economy. *Philos. Trans. R. Soc. A Math. Phys. Eng. Sci.* **2017**, *375* (2098). https://doi.org/10.1098/rsta.2016.0400.

(3) Jiao, Y.; Zheng, Y.; Jaroniec, M.; Qiao, S. Z. Design of Electrocatalysts for Oxygen- and Hydrogen-Involving Energy Conversion Reactions. *Chem. Soc. Rev.* **2015**, *44* (8), 2060–2086. https://doi.org/10.1039/c4cs00470a.

(4) Dincer, I.; Zamfirescu, C. Sustainable Hydrogen Production. *Sustain. Hydrog. Prod.* **2016**, *305* (August), 1–479. https://doi.org/10.1016/b978-0-444-64203-5.00001-0.

(5) Walter, M. G.; Warren, E. L.; McKone, J. R.; Boettcher, S. W.; Mi, Q.; Santori, E. A.; Lewis, N. S. Solar Water Splitting Cells. *Chem. Rev.* **2010**, *110* (11), 6446–6473. https://doi.org/10.1021/cr1002326.

(6) Trasatti, S. Electrocatalysis of Hydrogen Evolution: Progress in Cathode Activation. *Adv. Electrochem. Sci. Eng.* **2008**, *2*, 1–85. https://doi.org/10.1002/9783527616763.ch1.

(7) Roger, I.; Shipman, M. A.; Symes, M. D. Earth-Abundant Catalysts for Electrochemical and Photoelectrochemical Water Splitting. *Nat. Rev. Chem.* **2017**, *1*. https://doi.org/10.1038/s41570-016-0003.

(8) Lin, L.; Sherrell, P.; Liu, Y.; Lei, W.; Zhang, S.; Zhang, H.; Wallace, G. G.; Chen, J. Engineered 2D Transition Metal Dichalcogenides—A Vision of Viable Hydrogen Evolution Reaction Catalysis. *Adv. Energy Mater.* **2020**, *10* (16), 1–24. https://doi.org/10.1002/aenm.201903870.

(9) Kim, Y.; Tiwari, A. P.; Prakash, O.; Lee, H. Activation of Ternary Transition Metal Chalcogenide Basal Planes through Chemical Strain for the Hydrogen Evolution Reaction. *Chempluschem* **2017**, *82* (5), 785–791. https://doi.org/10.1002/cplu.201700164.

(10) Gao, M. R.; Liang, J. X.; Zheng, Y. R.; Xu, Y. F.; Jiang, J.; Gao, Q.; Li, J.; Yu, S. H. An Efficient Molybdenum Disulfide/Cobalt Diselenide Hybrid Catalyst for Electrochemical Hydrogen Generation. *Nat. Commun.* **2015**, *6*. https://doi.org/10.1038/ncomms6982.

(11) Wang, H.; Kong, D.; Johanes, P.; Cha, J. J.; Zheng, G.; Yan, K.; Liu, N.; Cui, Y. $MoSe_2$ and WSe_2 Nanofilms with Vertically Aligned Molecular Layers on Curved and Rough Surfaces. *Nano Lett.* **2013**, *13* (7), 3426–3433. https://doi.org/10.1021/nl401944f.

(12) Voiry, D.; Yamaguchi, H.; Li, J.; Silva, R.; Alves, D. C. B.; Fujita, T.; Chen, M.; Asefa, T.; Shenoy, V. B.; Eda, G.; Chhowalla, M. Enhanced Catalytic Activity in Strained Chemically Exfoliated WS $_2$ Nanosheets for Hydrogen Evolution. *Nat. Mater.* **2013**, *12* (9), 850–855. https://doi.org/10.1038/nmat3700.

(13) Chhowalla, M.; Shin, H. S.; Eda, G.; Li, L. J.; Loh, K. P.; Zhang, H. The Chemistry of Two-Dimensional Layered Transition Metal Dichalcogenide Nanosheets. *Nat. Chem.* **2013**, *5* (4), 263–275. https://doi.org/10.1038/nchem.1589.

(14) Hinnemann, B.; Moses, P. G.; Bonde, J.; Jørgensen, K. P.; Nielsen, J. H.; Horch, S.; Chorkendorff, I.; Nørskov, J. K. Biomimetic Hydrogen Evolution: MoS_2 Nanoparticles as Catalyst for Hydrogen Evolution. *J. Am. Chem. Soc.* **2005**, *127* (15), 5308–5309. https://doi.org/10.1021/ja0504690.

(15) Jaramillo, T. F.; Jørgensen, K. P.; Bonde, J.; Nielsen, J. H.; Horch, S.; Chorkendorff, I. Identification of Active Edge Sites for Electrochemical H_2 Evolution from MoS_2 Nanocatalysts. *Science (80-.).* **2007**, *317* (5834), 100–102. https://doi.org/10.1126/science.1141483.

(16) Liu, Y.; Zhou, X.; Ding, T.; Wang, C.; Yang, Q. 3D Architecture Constructed via the Confined Growth of MoS_2 Nanosheets in Nanoporous Carbon Derived from Metal-Organic Frameworks for Efficient Hydrogen Production. *Nanoscale* **2015**, *7* (43), 18004–18009. https://doi.org/10.1039/c5nr03810c.

(17) Li, D. J.; Maiti, U. N.; Lim, J.; Choi, D. S.; Lee, W. J.; Oh, Y.; Lee, G. Y.; Kim, S. O. Molybdenum Sulfide/N-Doped CNT Forest Hybrid Catalysts for High-Performance Hydrogen Evolution Reaction. *Nano Lett.* **2014**, *14* (3), 1228–1233. https://doi.org/10.1021/nl404108a.

(18) Tan, Y.; Liu, P.; Chen, L.; Cong, W.; Ito, Y.; Han, J.; Guo, X.; Tang, Z.; Fujita, T.; Hirata, A.; Chen, M. W. Monolayer MoS $_2$ Films Supported by 3D Nanoporous Metals for High-Effi Ciency Electrocatalytic Hydrogen Production. *Adv. Mater.* **2014**, *26* (47), 8023–8028. https://doi.org/10.1002/adma.201403808.

(19) Liao, L.; Zhu, J.; Bian, X.; Zhu, L.; Scanlon, M. D.; Girault, H. H.; Liu, B. MoS_2 Formed on Mesoporous Graphene as a Highly Active Catalyst for Hydrogen Evolution. *Adv. Funct. Mater.* **2013**, *23* (42), 5326–5333.

https://doi.org/10.1002/adfm.201300318.

(20) Zhao, Y.; Zhou, J.; Jia, Z.; Huo, D.; Liu, Q.; Zhong, D.; Hu, Y.; Yang, M.; Bian, M.; Hou, C. In-Situ Growth of Gold Nanoparticles on a 3D-Network Consisting of a MoS_2/RGO Nanocomposite for Simultaneous Voltammetric Determination of Ascorbic Acid, Dopamine and Uric Acid. *Microchim. Acta* **2019**, *186* (2). https://doi.org/10.1007/s00604-018-3222-7.

(21) Wu, D.; Wang, Y.; Wang, F.; Wang, H.; An, Y.; Gao, Z.; Xu, F.; Jiang, K. Oxygen-Incorporated Few-Layer MoS_2 Vertically Aligned on Three-Dimensional Graphene Matrix for Enhanced Catalytic Performances in Quantum Dot Sensitized Solar Cells. *Carbon N. Y.* **2017**, *123*, 756–766. https://doi.org/10.1016/j.carbon.2017.07.086.

(22) Zhang, Q.; Xu, Z.; Lu, B. Strongly Coupled MoS_2-3D Graphene Materials for Ultrafast Charge Slow Discharge LIBs and Water Splitting Applications. *Energy Storage Mater.* **2016**, *4*, 84–91. https://doi.org/10.1016/j.ensm.2016.03.005.

(23) Carraro, F.; Calvillo, L.; Cattelan, M.; Favaro, M.; Righetto, M.; Nappini, S.; Píš, I.; Celorrio, V.; Fermín, D. J.; Martucci, A.; Agnoli, S.; Granozzi, G. Fast One-Pot Synthesis of MoS_2/Crumpled Graphene p-n Nanonjunctions for Enhanced Photoelectrochemical Hydrogen Production. *ACS Appl. Mater. Interfaces* **2015**, *7* (46), 25685–25692. https://doi.org/10.1021/acsami.5b06668.

(24) Geng, X.; Wu, W.; Li, N.; Sun, W.; Armstrong, J.; Al-Hilo, A.; Brozak, M.; Cui, J.; Chen, T. P. Three-Dimensional Structures of MoS_2 Nanosheets with Ultrahigh Hydrogen Evolution Reaction in Water Reduction. *Adv. Funct. Mater.* **2014**, *24* (39), 6123–6129. https://doi.org/10.1002/adfm.201401328.

(25) Zhu, W.; Zhang, R.; Qu, F.; Asiri, A. M.; Sun, X. Design and Application of Foams for Electrocatalysis. *ChemCatChem* **2017**, *9* (10), 1721–1743. https://doi.org/10.1002/cctc.201601607.

(26) Tang, C.; Pu, Z.; Liu, Q.; Asiri, A. M.; Luo, Y.; Sun, X. $Ni3S_2$ Nanosheets Array Supported on Ni Foam: A Novel Efficient Three-Dimensional Hydrogen-Evolving Electrocatalyst in Both Neutral and Basic Solutions. *Int. J. Hydrogen Energy* **2015**, *40* (14), 4727–4732. https://doi.org/10.1016/j.ijhydene.2015.02.038.

(27) Tiwari, A. P.; Yoon, Y.; Novak, T. G.; An, K. S.; Jeon, S. Continuous Network of Phase-Tuned Nickel Sulfide Nanostructures for Electrocatalytic Water Splitting. *ACS Appl. Nano Mater.* **2019**, *2* (8), 5061–5070. https://doi.org/10.1021/acsanm.9b00985.

(28) Kibsgaard, J.; Chen, Z.; Reinecke, B. N.; Jaramillo, T. F. Engineering the

Surface Structure of MoS $_2$ ToÂ Preferentially Expose Active Edge Sites ForÂ Electrocatalysis. *Nat. Mater.* **2012**, *11* (11), 963–969. https://doi.org/10.1038/nmat3439.

(29) Lunardon, M.; Ran, J.; Mosconi, D.; Marega, C.; Wang, Z.; Xia, H.; Agnoli, S.; Granozzi, G. Hybrid Transition Metal Dichalcogenide/Graphene Microspheres for Hydrogen Evolution Reaction. *Nanomaterials* **2020**, *10* (12), 1–15. https://doi.org/10.3390/nano10122376.

(30) Liao, S.; Zhai, T.; Xia, H. Highly Adsorptive Graphene Aerogel Microspheres with Center-Diverging Microchannel Structures. *J. Mater. Chem. A* **2016**, *4* (3), 1068–1077. https://doi.org/10.1039/c5ta09540a.

(31) Bao, X. Q.; Petrovykh, D. Y.; Alpuim, P.; Stroppa, D. G.; Guldris, N.; Fonseca, H.; Costa, M.; Gaspar, J.; Jin, C.; Liu, L. Amorphous Oxygen-Rich Molybdenum Oxysulfide Decorated p-Type Silicon Microwire Arrays for Efficient Photoelectrochemical Water Reduction. *Nano Energy* **2015**, *16*, 130–142. https://doi.org/10.1016/j.nanoen.2015.06.014.

(32) Luo, R.; Luo, M.; Wang, Z.; Liu, P.; Song, S.; Wang, X.; Chen, M. The Atomic Origin of Nickel-Doping-Induced Catalytic Enhancement in MoS $_2$ for Electrochemical Hydrogen Production. *Nanoscale* **2019**, *11* (15), 7123–7128. https://doi.org/10.1039/c8nr10023c.

(33) Mosconi, D.; Till, P.; Calvillo, L.; Kosmala, T.; Garoli, D.; Debellis, D.; Martucci, A.; Agnoli, S.; Granozzi, G. Effect of Ni Doping on the MoS_2 Structure and Its Hydrogen Evolution Activity in Acid and Alkaline Electrolytes. *Surfaces* **2019**, *2* (4), 531–545. https://doi.org/10.3390/surfaces2040039.

(34) Escalera-Lopez, D.; Niu, Y.; Yin, J.; Cooke, K.; Rees, N. V.; Palmer, R. E. Enhancement of the Hydrogen Evolution Reaction from Ni-MoS_2 Hybrid Nanoclusters. *ACS Catal.* **2016**, *6* (9), 6008–6017. https://doi.org/10.1021/acscatal.6b01274.

(35) Gaur, A. P. S.; Zhang, B.; Lui, Y. H.; Tang, X.; Hu, S. Morphologically Tailored Nano-Structured MoS_2 Catalysts via Introduction of Ni and Co Ions for Enhanced HER Activity. *Appl. Surf. Sci.* **2020**, *516* (March), 146094. https://doi.org/10.1016/j.apsusc.2020.146094.

(36) Müller, A.; Prasad, T. P.; Menge, R. Thermal Decomposition of $(NH_4)_2MoS_4$ and $(NH_4)_2WS_4$heat of Formation of $(NH4)_2MoS_4$. *ZAAC - J. Inorg. Gen. Chem.* **1972**, *391* (2), 107–112. https://doi.org/10.1002/zaac.19723910203.

(37) Brito, J. L.; Ilija, M.; Hernández, P. Thermal and Reductive Decomposition of Ammonium Thiomolybdates. *Thermochim. Acta* **1995**, *256* (2), 325–338.

https://doi.org/10.1016/0040-6031(94)02178-Q.

(38) R. H. Busey, W. F. G. The Equilibrium Reaction $NiCl_2 + H_2$. *J. Am. Chem. Soc.* **1953**, *376* (4), 5–8.

(39) Hoang-Van, C.; Kachaya, Y.; Teichner, S. J.; Arnaud, Y.; Dalmon, J. A. Characterization of Nickel Catalysts.Dta by Chemisorption Techniques, x-Ray Diffraction and Magnetic Measurements. Effects of Support, Precursor and Hydrogen Pretreatment. *Appl. Catal.* **1989**, *46* (2), 281–296. https://doi.org/10.1016/S0166-9834(00)81123-9.

(40) Zhang, L. S.; Wang, W. D.; Liang, X. Q.; Chu, W. S.; Song, W. G.; Wang, W.; Wu, Z. Y. Characterization of Partially Reduced Graphene Oxide as Room Temperature Sensor for H_2. *Nanoscale* **2011**, *3* (6), 2458–2460. https://doi.org/10.1039/c1nr10187k.

(41) Tao, Y.; Kanoh, H.; Abrams, L.; Kaneko, K. Mesopore-Modified Zeolites : Preparation , Characterization , and Applications. **2006**, 896–910.

(42) BY C. L. CHANG, Y. K. TAO, J. S. S. A. H. S. Oxygen Substitution in Sn and Ni Chevrel Phases. *acta Crystallogr. C* **1987**, No. 2.

(43) Huang, Y.; Sun, Y.; Zheng, X.; Aoki, T.; Pattengale, B.; Huang, J.; He, X.; Bian, W.; Younan, S.; Williams, N.; Hu, J.; Ge, J.; Pu, N.; Yan, X.; Pan, X.; Zhang, L.; Wei, Y.; Gu, J. Atomically Engineering Activation Sites onto Metallic 1T-MoS_2 Catalysts for Enhanced Electrochemical Hydrogen Evolution. *Nat. Commun.* **2019**, *10* (1), 1–11. https://doi.org/10.1038/s41467-019-08877-9.

(44) K. Chang, W. C. et al. L -Cysteine-Assisted Synthesis of Layered MoS_2 / Graphene Composites with Excellent Electrochemical Performances for Lithium Ion Batteries. *ACS Nano* **2011**, No. 6, 4720–4728.

(45) Lee, J. E.; Jung, J.; Ko, T. Y.; Kim, S.; Kim, S. Il; Nah, J.; Ryu, S.; Nam, K. T.; Lee, M. H. Catalytic Synergy Effect of MoS_2/Reduced Graphene Oxide Hybrids for a Highly Efficient Hydrogen Evolution Reaction. *RSC Adv.* **2017**, *7* (9), 5480–5487. https://doi.org/10.1039/c6ra26149c.

(46) Kong, D.; Wang, H.; Cha, J. J.; Pasta, M.; Koski, K. J.; Yao, J.; Cui, Y. Synthesis of MoS_2 and $MoSe_2$ Films with Vertically Aligned Layers. *Nano Lett.* **2013**, *13* (3), 1341–1347. https://doi.org/10.1021/nl400258t.

(47) Prasad, J.; Singh, A. K.; Haldar, K. K.; Gupta, V.; Singh, K. Electromagnetic Interference Shielding Effectiveness in 3D Flower-like MoS_2-RGO/Gadolinium-Doped Nanocomposites. *J. Alloys Compd.* **2019**, *788*, 861–872. https://doi.org/10.1016/j.jallcom.2019.02.246.

(48) Vrubel, H.; Merki, D.; Hu, X. Hydrogen Evolution Catalyzed by MoS $_3$ and MoS $_2$ Particles. *Energy Environ. Sci.* **2012**, *5* (3), 6136–6144. https://doi.org/10.1039/c2ee02835b.

(49) Wang, H. W.; Skeldon, P.; Thompson, G. E. XPS Studies of MoS_2 Formation from Ammonium Tetrathiomolybdate Solutions. *Surf. Coatings Technol.* **1997**, *91* (3), 200–207. https://doi.org/10.1016/S0257-8972(96)03186-6.

(50) Zheng, X.; Xu, J.; Yan, K.; Wang, H.; Wang, Z.; Yang, S. Space-Confined Growth of MoS_2 Nanosheets within Graphite: The Layered Hybrid of MoS_2 and Graphene as an Active Catalyst for Hydrogen Evolution Reaction. *Chem. Mater.* **2014**, *26* (7), 2344–2353. https://doi.org/10.1021/cm500347r.

(51) Liu, A.; Zhao, L.; Zhang, J.; Lin, L.; Wu, H. Solvent-Assisted Oxygen Incorporation of Vertically Aligned MoS_2 Ultrathin Nanosheets Decorated on Reduced Graphene Oxide for Improved Electrocatalytic Hydrogen Evolution. *ACS Appl. Mater. Interfaces* **2016**, *8* (38), 25210–25218. https://doi.org/10.1021/acsami.6b06031.

(52) Chang, Y. H.; Lin, C. Te; Chen, T. Y.; Hsu, C. L.; Lee, Y. H.; Zhang, W.; Wei, K. H.; Li, L. J. Highly Efficient Electrocatalytic Hydrogen Production by MoS_x Grown on Graphene-Protected 3D Ni Foams. *Adv. Mater.* **2013**, *25* (5), 756–760. https://doi.org/10.1002/adma.201202920.

(53) Weber, T.; Muijsers, J. C.; Van Wolput, J. H. M. C.; Verhagen, C. P. J.; Niemantsverdriet, J. W. Basic Reaction Steps in the Sulfidation of Crystalline MoO_3 to MoS_2, as Studied by X-Ray Photoelectron and Infrared Emission Spectroscopy. *J. Phys. Chem.* **1996**, *100* (33), 14144–14150. https://doi.org/10.1021/jp961204y.

(54) Yu, X. Y.; Feng, Y.; Jeon, Y.; Guan, B.; Lou, X. W. D.; Paik, U. Formation of Ni–Co–MoS_2Nanoboxes with Enhanced Electrocatalytic Activity for Hydrogen Evolution. *Adv. Mater.* **2016**, *28* (40), 9006–9011. https://doi.org/10.1002/adma.201601188.

(55) Weber, T.; Muijsers, J. C.; Niemantsverdriet, J. W. Structure of Amorphous MoS_3. *J. Phys. Chem.* **1995**, *99* (22), 9194–9200. https://doi.org/10.1021/j100022a037.

(56) Wang, D.; Zhang, X.; Shen, Y.; Wu, Z. Ni-Doped MoS_2 Nanoparticles as Highly Active Hydrogen Evolution Electrocatalysts. *RSC Adv.* **2016**, *6* (20), 16656–16661. https://doi.org/10.1039/c6ra02610a.

(57) Kosmala, T.; Mosconi, D.; Giallongo, G.; Rizzi, G. A.; Granozzi, G. Highly Efficient MoS_2/Ag_2S/Ag Photoelectrocatalyst Obtained from a Recycled DVD Surface. *ACS Sustain. Chem. Eng.* **2018**, *6* (6), 7818–7825.

https://doi.org/10.1021/acssuschemeng.8b00840.

(58) Eng, A. Y. S.; Ambrosi, A.; Sofer, Z.; Šimek, P.; Pumera, M. Electrochemistry of Transition Metal Dichalcogenides: Strong Dependence on the Metal-to-Chalcogen Composition and Exfoliation Method. *ACS Nano* **2014**, *8* (12), 12185–12198. https://doi.org/10.1021/nn503832j.

(59) Dai, X.; Du, K.; Li, Z.; Liu, M.; Ma, Y.; Sun, H.; Zhang, X.; Yang, Y. Co-Doped MoS_2 Nanosheets with the Dominant CoMoS Phase Coated on Carbon as an Excellent Electrocatalyst for Hydrogen Evolution. *ACS Appl. Mater. Interfaces* **2015**, *7* (49), 27242–27253. https://doi.org/10.1021/acsami.5b08420.

(60) Anantharaj, S.; Noda, S.; Jothi, V. R.; Yi, S. C.; Driess, M.; Menezes, P. W. Strategies and Perspectives to Catch the Missing Pieces in Energy-Efficient Hydrogen Evolution Reaction in Alkaline Media. *Angew. Chemie - Int. Ed.* **2021**, 2–28. https://doi.org/10.1002/anie.202015738.

(61) Wang, L.; Zhu, Y.; Zeng, Z.; Lin, C.; Giroux, M.; Jiang, L.; Han, Y.; Greeley, J.; Wang, C.; Jin, J. Platinum-Nickel Hydroxide Nanocomposites for Electrocatalytic Reduction of Water. *Nano Energy* **2017**, *31* (October 2016), 456–461. https://doi.org/10.1016/j.nanoen.2016.11.048.

(62) Zhang, B.; Liu, J.; Wang, J.; Ruan, Y.; Ji, X.; Xu, K.; Chen, C.; Wan, H.; Miao, L.; Jiang, J. Interface Engineering: The $Ni(OH)_2/MoS_2$ Heterostructure for Highly Efficient Alkaline Hydrogen Evolution. *Nano Energy* **2017**, *37* (March), 74–80. https://doi.org/10.1016/j.nanoen.2017.05.011.

(63) Wei, J.; Zhou, M.; Long, A.; Xue, Y.; Liao, H.; Wei, C.; Xu, Z. J. Heterostructured Electrocatalysts for Hydrogen Evolution Reaction Under Alkaline Conditions. *Nano-Micro Lett.* **2018**, *10* (4), 1–15. https://doi.org/10.1007/s40820-018-0229-x.

(64) Zhu, Z.; Yin, H.; He, C. T.; Al-Mamun, M.; Liu, P.; Jiang, L.; Zhao, Y.; Wang, Y.; Yang, H. G.; Tang, Z.; Wang, D.; Chen, X. M.; Zhao, H. Ultrathin Transition Metal Dichalcogenide/3d Metal Hydroxide Hybridized Nanosheets to Enhance Hydrogen Evolution Activity. *Adv. Mater.* **2018**, *30* (28), 1–7. https://doi.org/10.1002/adma.201801171.

(65) Zhang, X.; Zhang, M.; Tian, Y.; You, J.; Yang, C.; Su, J.; Li, Y.; Gao, Y.; Gu, H. In Situ Synthesis of MoS_2/Graphene Nanosheets as Free-Standing and Flexible Electrode Paper for High-Efficiency Hydrogen Evolution Reaction. *RSC Adv.* **2018**, *8* (19), 10698–10705. https://doi.org/10.1039/c8ra01226a.

(66) Duan, H.; Wang, C.; Li, G.; Tan, H.; Hu, W.; Cai, L.; Liu, W.; Li, N.; Ji, Q.; Wang, Y.; Lu, Y.; Yan, W.; Hu, F.; Zhang, W.; Sun, Z.; Qi, Z.; Song, L.; Wei,

S. Single-Atom-Layer Catalysis in a MoS $_2$ Monolayer Activated by Long-Range Ferromagnetism for the Hydrogen Evolution Reaction: Beyond Single-Atom Catalysis . *Angew. Chemie* **2021**, *133* (13), 7327–7334. https://doi.org/10.1002/ange.202014968.

(67) Zhang, X.; Liang, Y. Nickel Hydr(Oxy)Oxide Nanoparticles on Metallic MoS$_2$ Nanosheets: A Synergistic Electrocatalyst for Hydrogen Evolution Reaction. *Adv. Sci.* **2018**, *5* (2). https://doi.org/10.1002/advs.201700644.

(68) Zhang, H.; Yu, L.; Chen, T.; Zhou, W.; Lou, X. W. (David). Surface Modulation of Hierarchical MoS$_2$ Nanosheets by Ni Single Atoms for Enhanced Electrocatalytic Hydrogen Evolution. *Adv. Funct. Mater.* **2018**, *28* (51), 1–8. https://doi.org/10.1002/adfm.201807086.

(69) Yang, L.; Zhou, W.; Hou, D.; Zhou, K.; Li, G.; Tang, Z.; Li, L.; Chen, S. Porous Metallic MoO$_2$-Supported MoS$_2$ Nanosheets for Enhanced Electrocatalytic Activity in the Hydrogen Evolution Reaction. *Nanoscale* **2015**, *7* (12), 5203–5208. https://doi.org/10.1039/c4nr06754a.

(70) Kim, K.; Tiwari, A. P.; Hyun, G.; Novak, T. G.; Jeon, S. Improving Electrochemical Active Area of MoS$_2$ via Attached on 3D-Ordered Structures for Hydrogen Evolution Reaction. *Int. J. Hydrogen Energy* **2019**, *44* (52), 28143–28150. https://doi.org/10.1016/j.ijhydene.2019.09.071.

(71) Theerthagiri, J.; Senthil, R. A.; Senthilkumar, B.; Reddy Polu, A.; Madhavan, J.; Ashokkumar, M. Recent Advances in MoS$_2$ Nanostructured Materials for Energy and Environmental Applications – A Review. *J. Solid State Chem.* **2017**, *252* (May), 43–71. https://doi.org/10.1016/j.jssc.2017.04.041.

(72) Cheng, Y.; Zhan, Y.; Ran, J. J.; Wang, Z.; Agnoli, S.; Xia, H.; Granozzi, G. Hybrid MXene/Reduced Graphene Oxide Aerogel Microspheres for Hydrogen Evolution Reaction. *Ionics (Kiel).* **2021**, *27* (7), 3099–3108. https://doi.org/10.1007/s11581-021-04062-5.

(73) Subbaraman, R.; Tripkovic, D.; Chang, K. C.; Strmcnik, D.; Paulikas, A. P.; Hirunsit, P.; Chan, M.; Greeley, J.; Stamenkovic, V.; Markovic, N. M. Trends in Activity for the Water Electrolyser Reactions on 3d M(Ni,Co,Fe,Mn) Hydr(Oxy)Oxide Catalysts. *Nat. Mater.* **2012**, *11* (6), 550–557. https://doi.org/10.1038/nmat3313.

(74) Liu, J.; Yang, Y.; Ni, B.; Li, H.; Wang, X. Fullerene-Like Nickel Oxysulfide Hollow Nanospheres as Bifunctional Electrocatalysts for Water Splitting. *Small* **2017**, *13* (6), 1–6. https://doi.org/10.1002/smll.201602637.

Chapter 4

When morphology boosts electrocatalytic activity: CoAl-Layered Double Hydroxide Nanorings supported on 3D Reduced Graphene Oxide Aerogel Microspheres

4. When morphology boosts electrocatalytic activity: CoAl-Layered Double Hydroxide Nanorings supported on 3D Reduced Graphene Oxide Aerogel Microspheres

4.1 Introduction

The development of technologies for an highly-efficiency, low-cost hydrogen production is critical for the implementation of an energy infrastructure based on renewable sources.[1,2] Electrochemical water splitting provides a promising chemical route to enable the storage of intermittent renewable energy provided by sun, wind, tides etc..[3] The oxidative half reaction of water splitting, namely the OER, is kinetically sluggish since its requires four electron transfer steps. In general, a substantial overpotential (1.23 V, is the standard redox potential for water oxidation) is required to drive this reaction at rates that are suitable for practical applications. In addition, precious metal-based compounds such as RuO_2 and IrO_2 have been recognized as state-of-the-art OER electrocatalysts in acid conditions, but their scarcity inevitably increases the cost of energy conversion devices [4] limiting their practical application. Consequently, it is very important to develop highly-active, low-cost, earth-abundant, and very durable catalysts to replace precious metal oxides.

Transition metal compounds, including (hydro)oxides,[5,6] sulfides,[7,8] selenides [9,10] and phosphides,[11,12] have been widely studied for their remarkable activity in the OER, especially in alkaline environment, which is becoming a quite interesting application field, given the recent development of new anion exchange polymer membranes. In recent years, many studies have identified LDHs as suitable candidates for sustainable energy conversion and storage and indeed many works have been reported about their use in supercapacitors,[13–15] lithium-sulfur batteries,[16–18] electrocatalysis,[19–21] and so on. LDH materials are anionic layered compounds with the brucite structure, consisting of a cationic layer of mixed metal hydroxides, generally p- or s-block metals (e.g. Al, Mg) or transition metals (Ni, Zn, Co, Fe etc) and charge-balancing anions in the interlayer regions.[22] A great deal of experiments indicates that Co^{2+} cations in the LDH represent extremely active catalytic active sites towards water oxidation.[23–25] Furthermore, Co oxides/hydroxides have attracted extensive attention in OER research due to their large availability.[26,27] Indeed, many studies have focused on hydrotalcite based materials containing Co^{2+} ions either as dopants or constitutive element, as catalysts for the OER and even as bifunctional materials for the complete water splitting. For example, Wang et al. have reported, the high electrocatalytic activity and superior charge transfer properties of cobalt nickel-layered double hydroxide@polypyrrole−cotton pad (CoNi-LDH@PCPs);[28] while Han and coworkers used Fe-Co LDHs doped with different content of Zn^{2+} as outstanding OER electrocatalysts with superior stability;[29] moreover, Qiu et al. [30] prepared ZnCo-LDH nanosheets with enhanced OER activity. Several reports in the literature propose that starting from CoAl-LDH, which is *per se* limitedly active due to poor charge transfer properties,[31] it is possible to obtain high performance materials by acting on the morphology or chemical composition or by combination with additional components. Ring-like nanostructures have attracted particular attention, [32,33] because they have relatively larger surface areas, higher chemical accessibility and more active sites than plate-like counterparts.[34,35] Zhou et al.[36] have prepared ringlike CoAl-LDHs exploiting urea hydrolysis and verified that the nanoring structure provide a larger number of catalytically active sites for the OER.

LDH electrocatalysts are generally prepared by drop-casting the exfoliated LDH nanosheets onto a GCE. This procedure may result in the restacking of nanosheets, determining a poor electrical contact between the active phase and the GCE, resulting in low catalytic efficiency.[37,38] In addition to modifications of the LDHs, an appropriate support is generally required for anchoring firmly the nanocatalysts as well as dispersing them and preventing their aggregation. 3D porous electrocatalysts prepared by incorporation of active species into 3D porous scaffolds have attracted tremendous attention in water splitting.[39] In the previous chapter, we reported a successful route to disperse Ni-doped MoS_2 nanosheets within a graphene oxide aerogel having a special centre-diverging microchannel 3D structure.[40] Interestingly, the microspheres maintain their shape even after a thermal reduction process (providing prGOAMs). Adding an electrochemically active component during the GOAMs preparation step, catalysts/prGOAM hybrids can be obtained, which keep their special morphology even during the electrochemical work

Herein, we report the development of nanocomposites constructed by CoAl-LDH NR supported on GOAMs as highly efficient electrocatalysts for water oxidation. The CoAl-LDHs are prepared via the hydrothermal method in presence of urea and then are anchored on GOAMs under the combination of electrospraying and ice templating as previously done in the case of the chemically exfoliated nanosheets of TMDCs (see chapter 2). The presence of negatively charged GOAMs can play an import role in supporting and dispersing positively charged CoAl-LDH NR. The as-prepared electrocatalyst, denoted as CoAl-LDH NR/GOAMs, inherits the special centre-diverging microchannel 3D structure from GOAMs, with numerous CoAl-LDH NR decorating quite homogeneously the GO surface. As expected form previous results, both the CoAl-LDH NRs and GOAMs maintain their structure and morphology even after a thermal reduction process at 200 ℃ (providing CoAl-LDH NR/prGOAMs). As a result, the CoAl-LDH NR/prGOAMs exhibit a remarkable electrocatalytic activity in the OER, which is attributed both to the peculiar centre-diverging mesoporous structure of the carbon scaffold, which allows an easy access to the active sites and an optimal mass transport, and to the presence of many catalytically active sites associated with the nanorings. The CoAl-LDH NR/prGOAMs reach a remarkable η_{10} of 300 mV in 0.1 M KOH. Moreover, after chronopotentiometry tests (15 h) at a constant current density of 10 mA cm^{-2}, the η_{10} value is further improved to 270 mV in alkaline conditions, indicating an exceptional stability.

4.2 Experimental section

4.2.1 Synthesis of the CoAl-LDH and CoAl-LDH Nanoring

CoAl-LDHs were synthesized by a hydrothermal method. $Co(NO_3)_2 6H_2O$ (0.75 mmol), $Al(NO_3)_3 9H_2O$ (0.25 mmol) and $CO(NH_2)_2$ (20 mmol) were dissolved in 40 mL of deionized water and stirred to form a clear solution. Such solution was then transferred to a Teflon-lined stainless-steel autoclave, which was sealed, maintained at 120 ℃ for 12 h, and then allowed to cool to room temperature on its own. A brown solid precipitate was formed, which subsequently was rinsed with deionized water, ethanol for 5 min each time, with the assistance of ultrasonication. The so-prepared wet CoAl-LDH powders were freeze-dried overnight.

CoAl-LDH nanorings were synthesized by the same method of CoAl-LDH except the ratio of metal and urea and the different reaction temperature (moles of Metal: moles of Urea =1:30, 120 ℃ for 14 h).

4.2.2 Synthesis of the CoAl-LDH/prGOAMs and CoAl-LDH NR/prGOAMs

Scheme 4.1 illustrates the synthetic route for the preparation of CoAl-LDH NR/prGOAMs. 70 mg GO and 50 mg CoAl-LDH NR were added to 10 mL of deionized water, stirred and ultrasonicated at room temperature for 30 minutes to obtain a homogeneous suspension of 7.0 mg mL^{-1}. Starting from the precursor solution, a combination of electrospraying, ice templating and thermal annealing was used for the synthesis of the CoAl-LDH NR/prGOAMs composites. Regarding the electrospraying step, a beaker containing n-hexane was cooled down to -45℃ by an acetone/dry ice mixture and used as receiving liquid. Then, the CoAl-LDH NR /GO suspension was added to the injection pump of the electrospraying device, which was terminating with a small capillary (nozzle) connected to a high voltage power supply. The parameters for the electrospraying procedure were: flow rate = 7.5 mL h^{-1}; voltage = 10 kV, distance between the receiving liquid and the nozzle = 10 cm. Under the action of the electric field, the electrically conductive suspension was stretched forming a “Taylor cone”, which eventually split into smaller charged droplets that entered the cooling bath, where they were rapidly frozen, producing CoAl-LDH NR /GO /ice microspheres. Finally, after rapid filtration, the solid microspheres collected in the cooled n-hexane bath were transferred to a freeze dryer working at -50 ℃ and less than 20 Pa, for 48 h, eventually obtaining the dried CoAl-LDH NR/GOAMs. Finally, the dried CoAl-LDH NR/GOAMs were heated to 200 ℃ under an Ar (100 sccm) atmosphere for 1 h with a heating rate of 3 ℃/min. After the heat treatment, the GOAMs were transformed into prGOAMs, so the final CoAl-LDH NR/prGOAMs were obtained. For the preparation of a comparative sample of CoAl-LDH/prGOAMs, the same procedure was followed simply adding the CoAl-LDH with standard morphology to the initial solution.

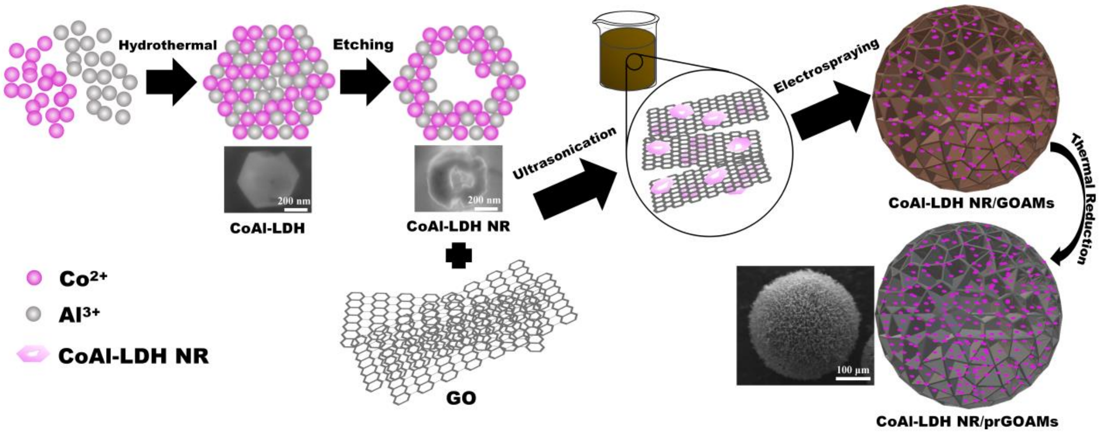

Scheme 4.1 Scheme summarizing the synthesis strategy of CoAl-LDH NR/prGOAMs.

4.2.3 Structural and Morphological Characterizations

SEM measurements were carried out with a Zeiss Supra VP35 FE-SEM, equipped with In-Lens, SE, and BSE detectors for the imaging (Zeiss, Jena, Germany). Micrographs were obtained with an acceleration voltage of 5 kV using in-lens high-resolution detection. EDX and mapping data were acquired with the same instrument. The surface area measurements were carried out with a Micromeritics ASAP 2020/2010 apparatus using the BET model for N_2 adsorption measurements. Prior to the adsorption run, the sample was outgassed at 373 K for 10 h.

XRD patterns were recorded in the diffraction angular range of 5–80° by a PANalytical X'Pert 3 diffractometer, working in the reflection geometry and equipped with a graphite monochromator on the diffracted beam (Cu Kα radiation, Pananlytical, Almelo, The Netherlands). Raman spectra were collected using a DXR Raman microscope system (Thermo Fisher Scientific, USA) with a 532 nm laser as the photoexcitation source, with 0.5 mW laser power at the sample and a 50× objective lens.

The surface chemical composition of the samples was investigated by XPS using a custom-made system working at a base pressure of 10^{-10} mbar and equipped with an EA 125 Omicron electron analyzer ending with a five channeltron detector. The XPS data were collected at room temperature using the Mg Kα line (hv = 1486.7 eV) of a non-monochromatized dual-anode DAR400 X-ray source. High resolution spectra were acquired using 0.1 eV energy steps, and 20 eV pass energy. The multipeak analysis of the C 1s, O 1s, Co 2p photoemission lines was performed by means of Voigt functions and subtracting a Shirley background using the XPSPEAK software.

4.2.4 Electrochemical Characterization

The electrochemical (EC) OER measurements were carried out in a custom designed three-electrode cell using an Autolab PGSTAT-204 potentiostat. Graphite was used as counter electrode, whereas an Ag/AgCl (3M KCl) electrode, calibrated with respect to the RHE, was the reference electrode. All electrochemical potentials reported in the text and figures are referred to the reversible hydrogen electrode (RHE) and corrected according to the equation: E(RHE) = E(Ag/AgCl) + 0.222 V + 13×0.059 pH. The EC experiments were carried out in Ar-saturated 0.1 M KOH solution prepared from high-purity reagents (Sigma-Aldrich) and ultrapure Milli-Q water. The working electrodes were prepared by painting 50 μL of the catalyst ink, (which was obtained by dispersing 1 mg of sample and 5 μL of Nafion in 200 μL of DMF, by ultrasonication for powder materials, whereas by gently shaking only for aerogel microspheres) on a 1×1 cm carbon cloth (Zoltek Tm PX30 Woven fabric, Hungary). The polarization curves were recorded at a 5 mV/s scan rate. The stability of the catalysts was tested by chronopotentiometry at 10 mA cm^{-2}. Curves were iR-corrected using the resistance determined by EIS.

4.3 Results and Discussion

4.3.1. Chemical and Structural Characterization

The LDHs are hydrotalcite-like materials composed of positively charged layers and charge-balancing interlayer anions (as shown in Figure 4.1a).[41] The as-prepared CoAl LDHs showed a homogeneous morphology consisting of thin hexagonal flakes with a uniform lateral size of *ca.* 500 nm (Figure 4.1 b and c). On the other hand, Figure 4.1 d and e demonstrated the morphology changed to a ring-like as a consequence of etching of metals during the growth process determined by the in situ urea hydrolysis, Actually, the locally high pH determined by urea dissociation into NH_4^+ and CO_3^{2-}determines the easy dissolution of amphoteric Al^{+3} ions, as alluminate, AlO_2^-. Notably, the cations distribution in the pristine hexagonal flake is not homogeneous, because in the used synthesis conditions, which are moderately alkaline, $Al(OH)_3$ is initially formed, which acts as nucleation center for the further growth of the CoAl-LDHs. This combination of initial gradient cation distribution and selective etching explains the obtained morphology (as shown in Figure 4.1f) as reported previously.[36] As shown in Figure 4.1d and 1e the dimension of the nanorings is essentially the same as the parent flakes i.e. *ca*. 500 nm.

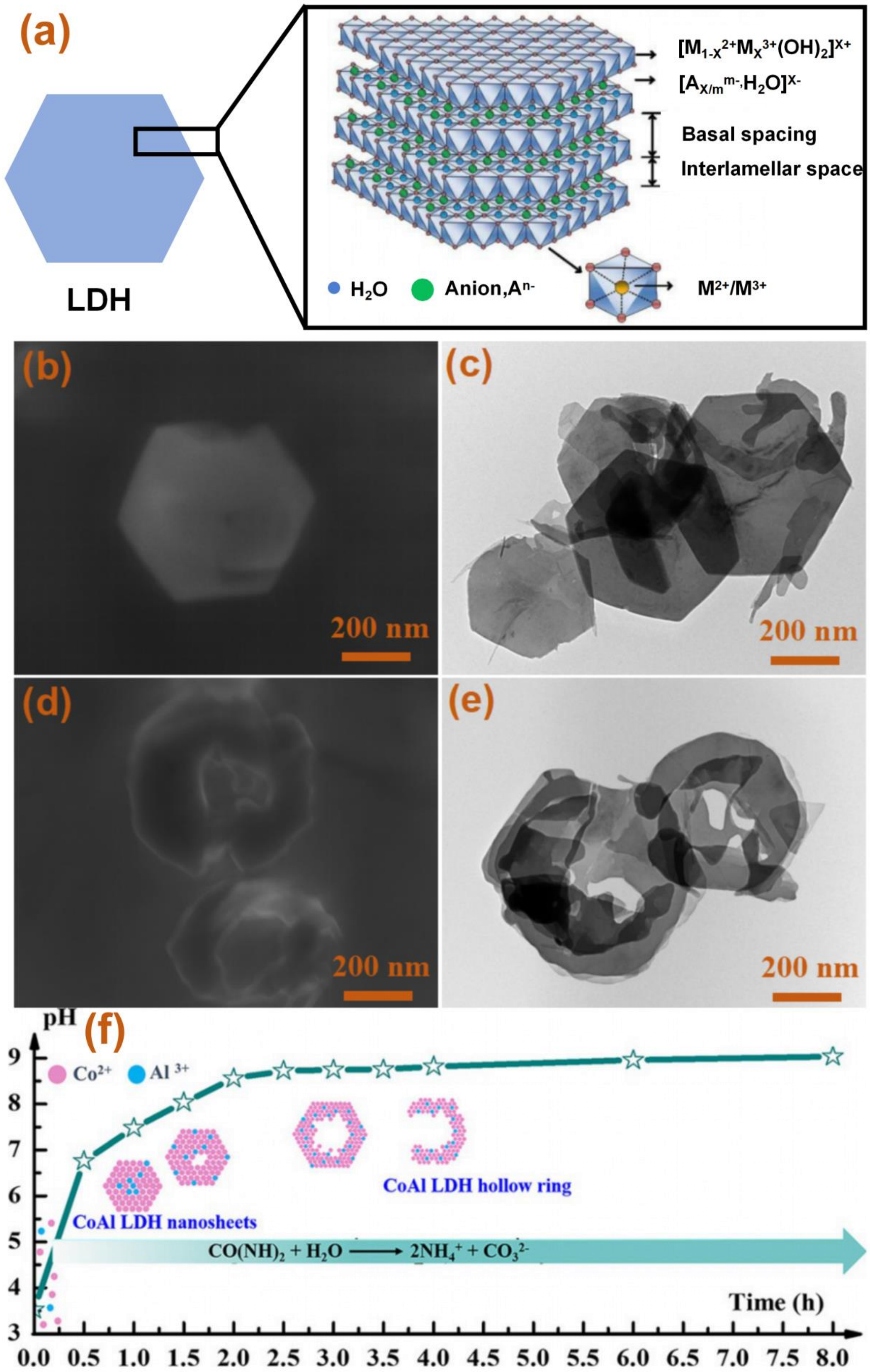

Figure 4.1 (a) The ball model of LDH taken from ref.[41] (b) SEM image of CoAl-LDH. (c) TEM image of CoAl-LDH. (d) SEM image of CoAl-LDH nanoring. (e)

TEM image of CoAl-LDH nanoring. (f) Proposed formation mechanism of the CoAl-LDH nanoring along with reaction time adapted from ref.[36]

Figure 4.2a and b show the SEM micrographs of CoAl-LDH NR/prGOAMs, where the typical spherical morphology of the materials (~ 300 μm sphere diameter) is easily recognizable. Figure 4.3a show the SEM micrographs of CoAl-LDH/prGOAMs with also ~ 300 μm diameter. Furthermore, the inner microstructure of CoAl-LDH NR/prGOAMs and CoAl-LDH/prGOAMs can be clearly observed in Figure 4.2c and Figure 4.3b, which consists of a highly porous network made up by interconnected GO sheets. Such structure, resembling a blowball, shows radially oriented microchannels that are the result of the uniform cooling from the outer surface toward the inner core, of the CoAl-LDH NR/GO/water or CoAl-LDH/GO/water microdroplet. Ice crystals grow in the radial direction physically forcing the self-assembly of CoAl-LDH NR/GO and CoAl-LDH/GO blocks. The radially oriented microchannel structure is then retained after the removal of the templating ice crystals during the lyophilization step, thanks to the formation of hydrogen bonds and van der Waals interactions between the GO nanosheets. The SEM images of CoAl-LDH NR/prGOAMs at larger magnification (reported in Figure 4.2d), show that the CoAl-LDH NR, are uniformly dispersed on the prGO surface. A further annealing at 200℃ is then needed to consolidate the structure promoting cross linking by condensation reactions. The same morphology is observed also for the CoAl-LDH/prGOAM samples, as shown in Figure 4.3c and d.

Figure 4.2e and f show the SEM image and the corresponding area averaged EDX spectra of CoAl-LDH NR/prGOAMs: the atomic ratio of Al/Co is 1.8 at/at whereas the atomic ratio of Al/Co on CoAl-LDH/prGOAMs surface is 2.3 at/at (reported in Figure 4.3e and f). The EDX data therefore, support the idea that the nanoring morphology is produced by the leaching of Al^{3+} cations promoted by the *in situ* produced OH^- derived from urea hydrolysis.[36] Overall, the SEM/EDX investigation suggests that CoAl-LDH and CoAl-LDH NR finely decorates the prGO sheets, which are efficiently interconnected creating a series of centre diverging channels.

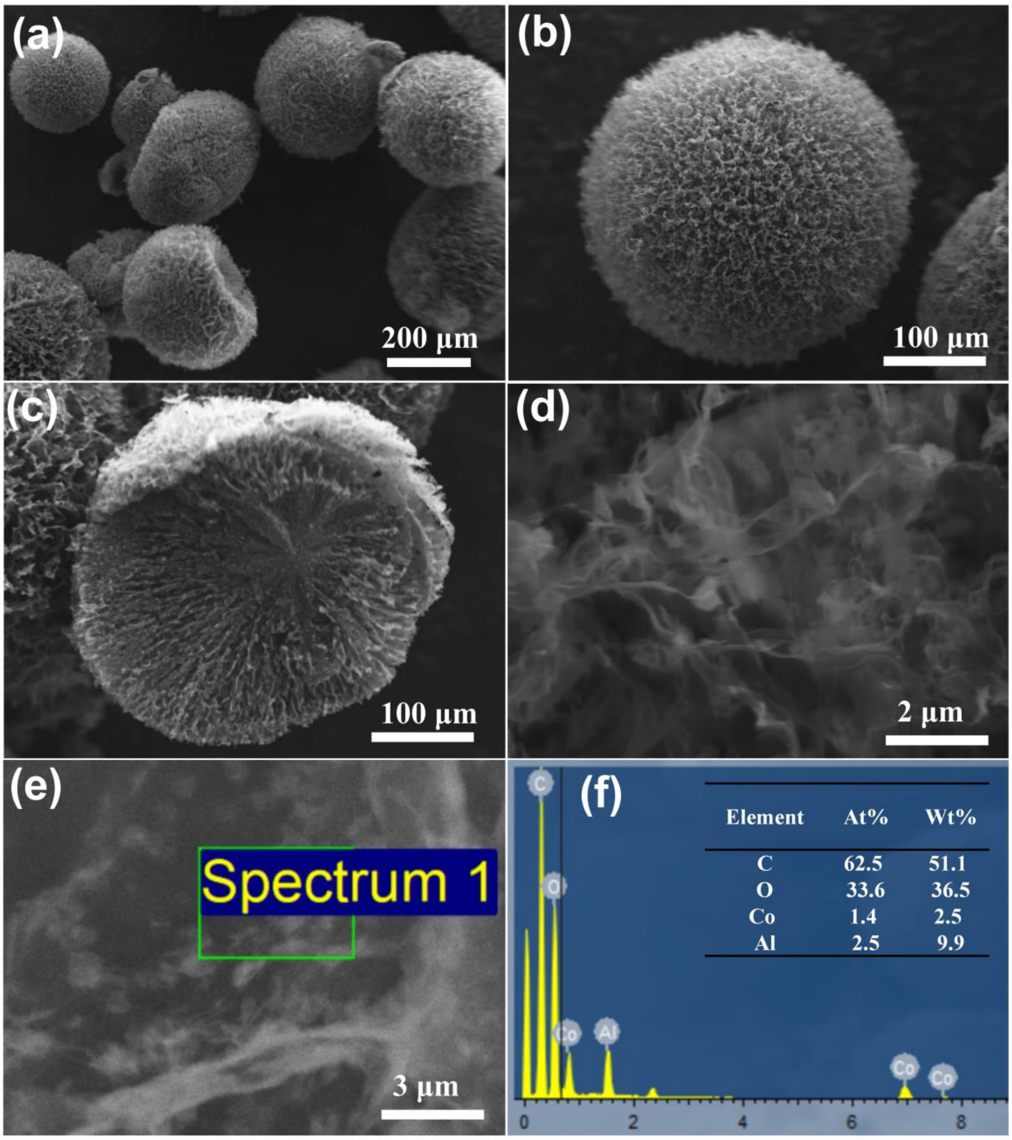

Element	At%	Wt%
C	62.5	51.1
O	33.6	36.5
Co	1.4	2.5
Al	2.5	9.9

Figure 4.2 (a and b) SEM images of typical CoAl-LDH NR/prGOAMs; (c) aerogel hemispheres; (c and d): higher magnification; (g and h) SEM image and EDX analysis of CoAl-LDH NR/prGOAMs.

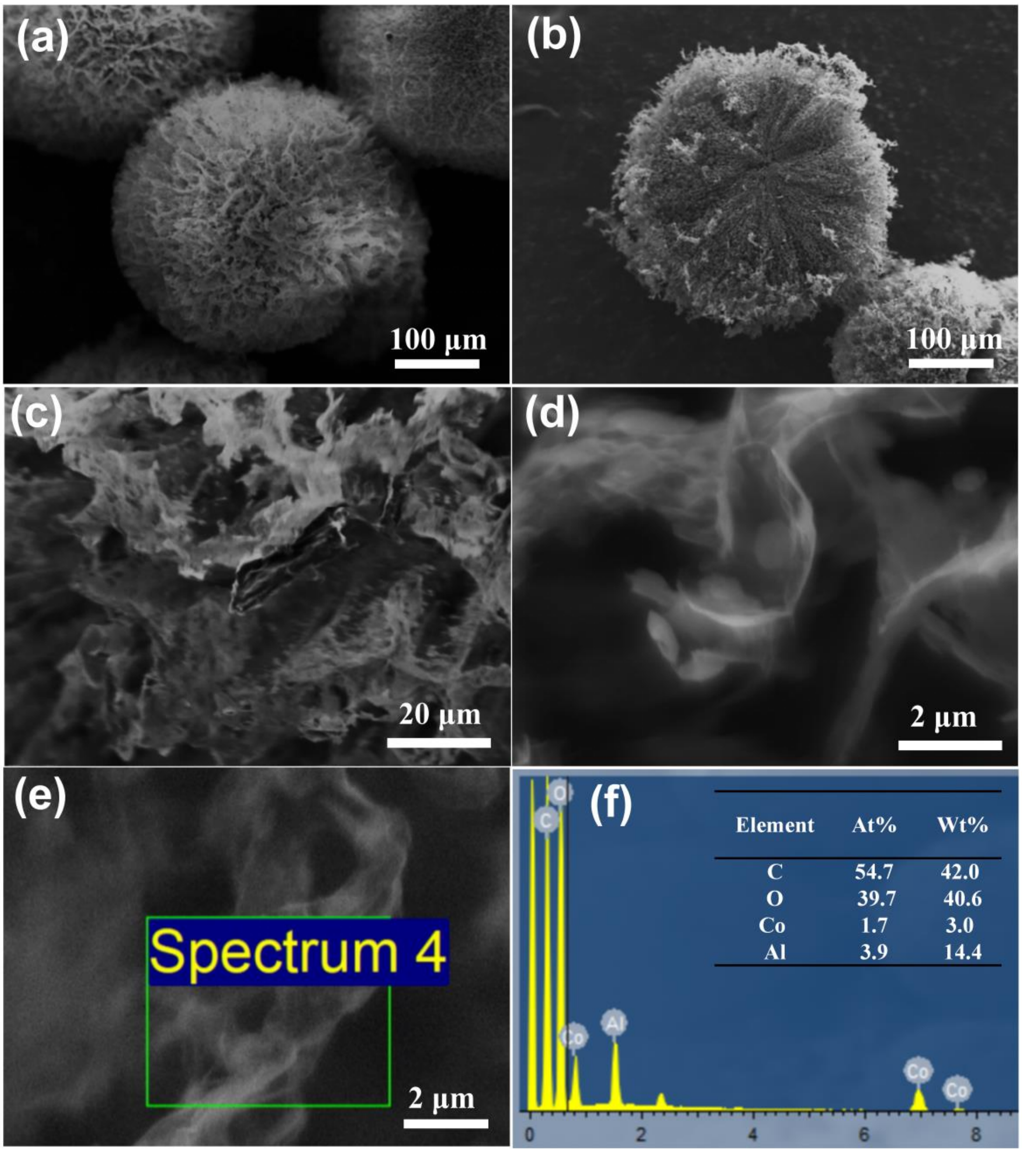

Element	At%	Wt%
C	54.7	42.0
O	39.7	40.6
Co	1.7	3.0
Al	3.9	14.4

Figure 4.3 (a) SEM images of typical CoAl-LDH/prGOAMs and (b) aerogel hemispheres at a lower magnification; (c and d): higher magnification; (g and h) SEM image and EDX analysis of CoAl-LDH/prGOAMs.

The elemental maps of CoAl-LDH NR/prGOAMs in Figure 4.4 confirm that the regions with brighter contrast in the SEM backscattered electron images correspond to the Co-Al-LDH, however it can be noted that the Al^{+3} and Co^{2+} spatial distributions sometimes do not always match. This supports the idea that the cation distribution inside the nanosheets is not perfectly homogeneous.

Figure 4.5 shows the TEM images of CoAl-LDH/prGOAMs and CoAl-LDH NR/prGOAMs that confirm an intimate association between the LDHs and the carbon nanosheets, as thin LDH flakes and nanorings cover the surface of the almost transparent prGO nanosheets (Figure 4.5c). The prGO and LDH nanosheets seem to be attached in a face-to-face fashion as expected by their 2D topology. The wrinkles of GO nanosheets are clearly visible in the TEM images (Figure 4.5b, d), however they do not seem to be preferential anchoring centers for the LDH flakes, at contrast with what is normally observed with simple nanoparticles. The LDHs, either nanorings or standard nanosheets, are scattered all over the prGO surface, however they show a certain tendency to stack together as well. This is somehow unexpected considering that the GO sheets are negatively charged, whereas the LDHs carry a positive charge, so electrostatic interactions should drive an assembly where same type of nanosheets repels each other. Probably, during the synthesis, the freezing of the microdroplets is so fast that the nanosheets do not have the time to assemble minimizing mutual interactions, and the LDHs are forced to stack together driven by the rapid gradient driven growth of the ice crystals.

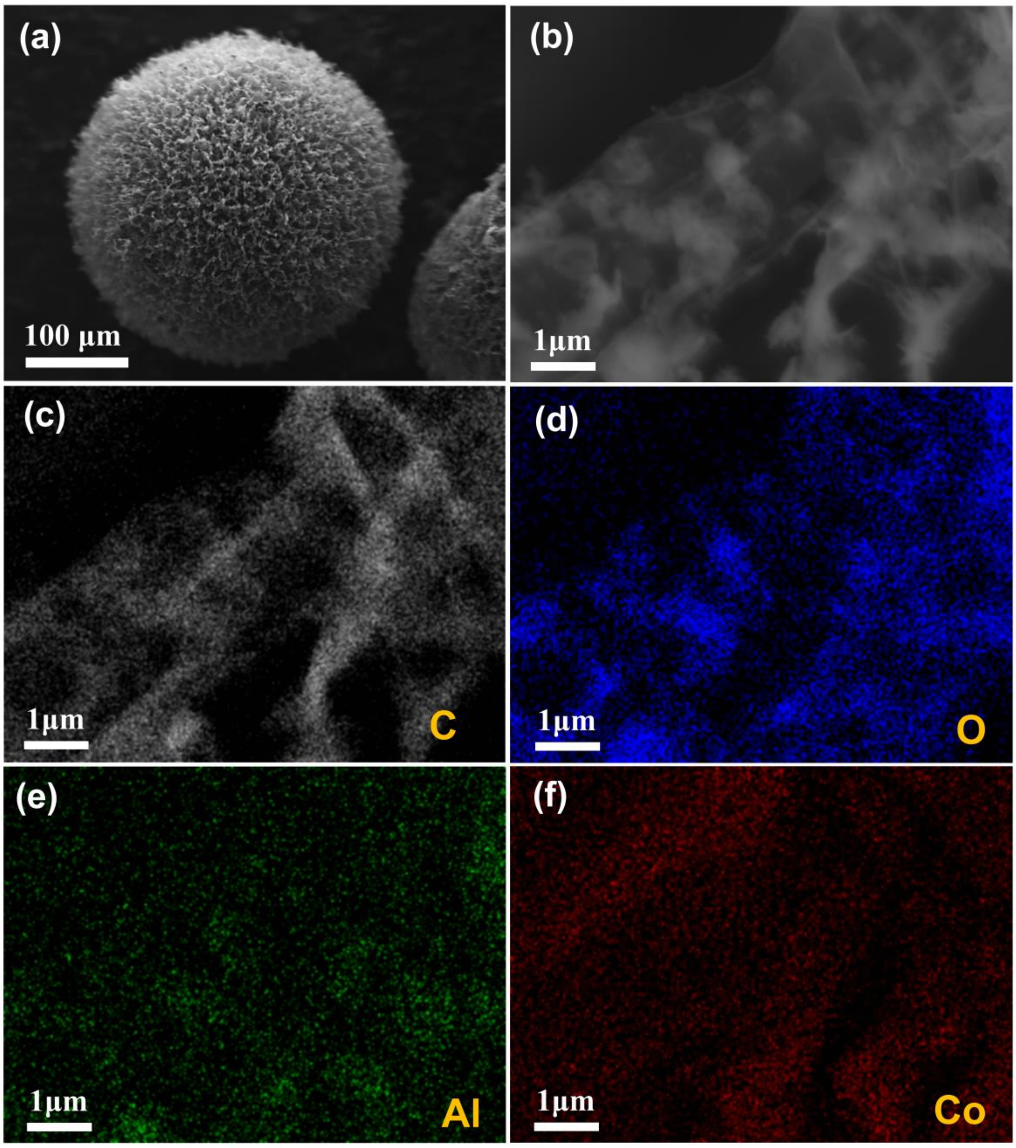

Figure 4.4 SEM images and EDX chemical map of the CoAl-LDH NR/prGOAMs. EDX showing the chemical maps of C (gray), O (blue), Al (green) and Co (red) signals.

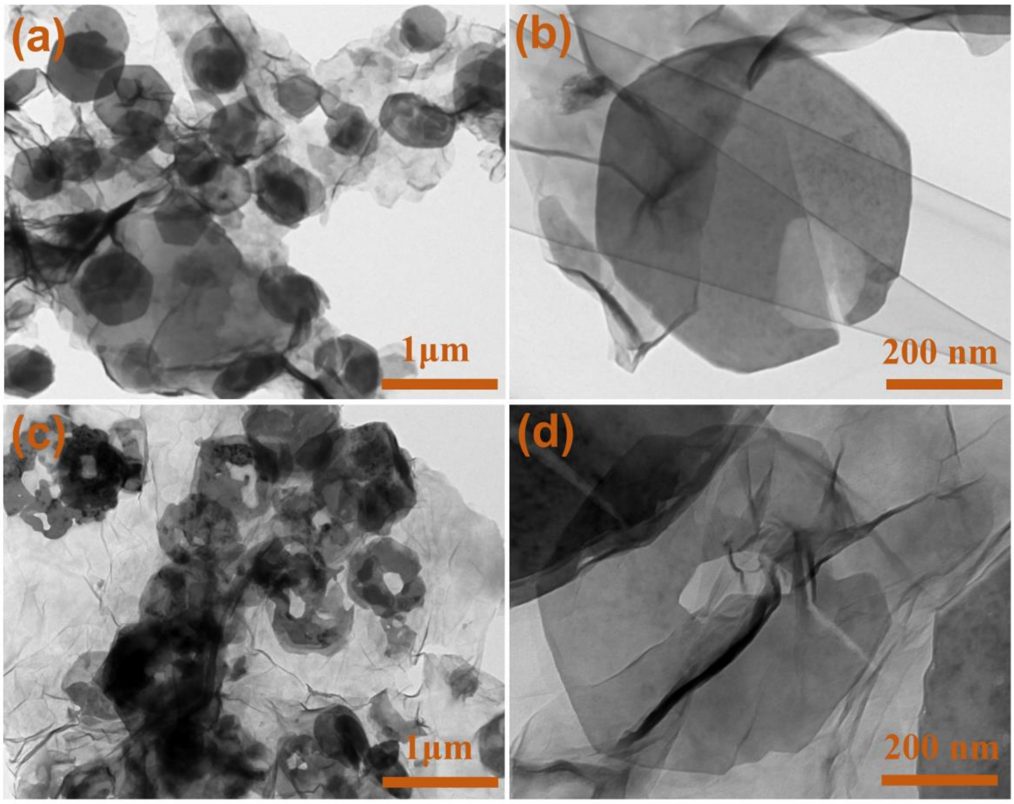

Figure 4.5 (a) and (b) TEM images of CoAl-LDH/prGOAMs. (c) and (d) TEM images of CoAl-LDH NR/prGOAMs.

The porosity of CoAl-LDH, CoAl-LDH NR and CoAl-LDH NR/prGOAMs was characterized using nitrogen adsorption experiments (Figure 4.6). The N_2 adsorption-desorption measurements revealed that the as-prepared CoAl-LDH NR has BET specific surface area of 30 m^2g^{-1} (Figure 4.6b), which is a higher value than that of CoAl-LDH of 22 m^2g^{-1} (Figure 4.6a). This confirms that the etching has produced newly exposed unsaturated sites poised for an efficient gas adsorption. The overall shape of the adsorption isotherm can be associated with an type II isotherm as expected for micrometric particles, however a small hysteresis can be observed as well, indicating also the presence of minority of nanometric pores. Actually, the pore-size distribution of CoAl-LDH and CoAl-LDH NR exhibits a dominant feature around 1-1.6 nm, and other weaker features at 15-40 nm (inset of Figure 4.6a and b), suggesting the presence of a small fraction of both micro- and meso-pores. When the LDHs are combined with the GOAMs the adsorption properties undergoes significant changes and are dominated by the features of the carbon moiety. CoAl-LDH

NR/prGOAMs have a BET specific surface area of 144 m^2g^{-1} (Figure 4.6d), which is higher than the value observed for prGOAMs, 123 m^2g^{-1} (Figure 4.6c). This result indicates that the well anchored CoAl-LDH on the prGO sheets, effectively prevents the restacking of the prGO nanosheets. The N_2 adsorption-desorption isotherm of the two samples showed a type IV isotherm (according to the IUPAC classification) with a small H3 hysteresis loop extending from P/P_0 = 0.30 to 0.95, demonstrating the presence of a mesoporous structure and slit-shaped pores[42], as widely documented in many other composite based on GOAMs (see the previous chapters of this thesis). The pore-size distribution of CoAl-LDH NR/prGOAMs and prGOAMs exhibits a dominant feature around 0.9-1.2 nm, but also some weaker peaks at 2-20 nm (inset of Figure 4.6c and d), suggesting the presence of both micro- and meso-pores.

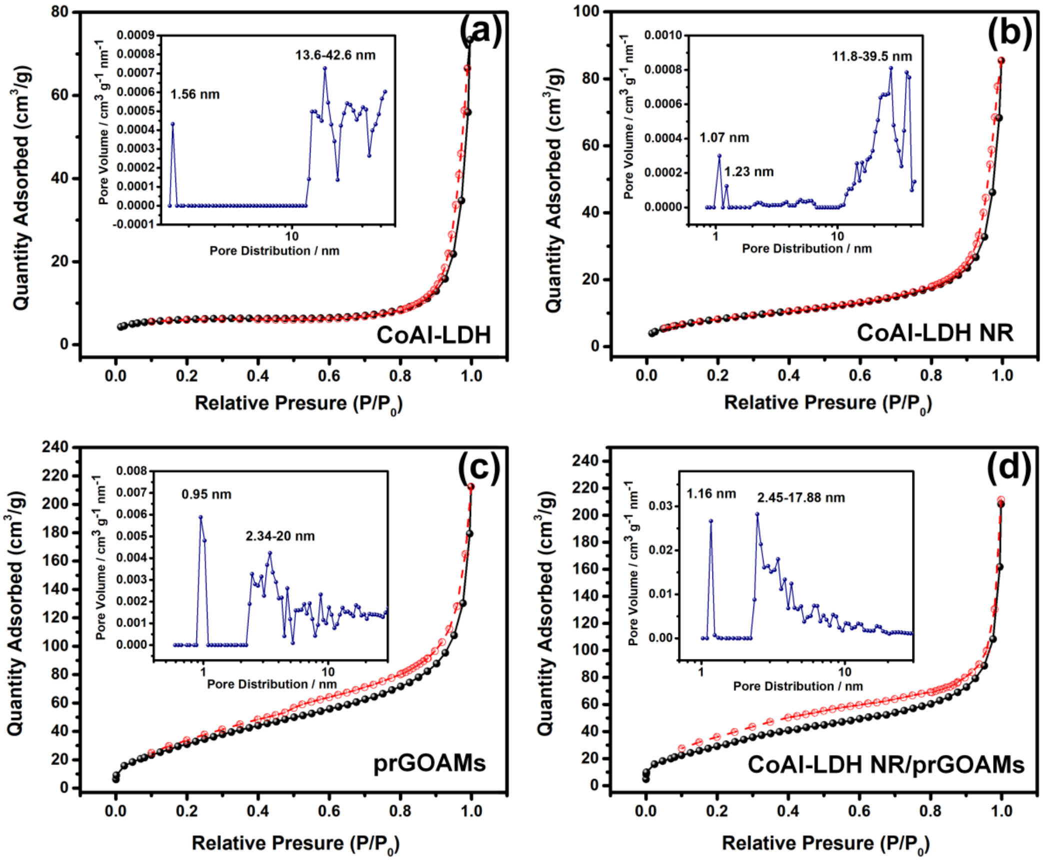

Figure 4.6 N_2 adsorption-desorption isotherm and pore-size distribution (inset) of (a) CoAl-LDH, (b) CoAl-LDH NR, (c) prGOAMs and (d) CoAl-LDH NR/prGOAMs.

The crystal structure of the CoAl-LDH, CoAl-LDH NR and CoAl-LDH NR/prGOAMs hybrid was characterized by XRD (Figure 4.7a). The XRD patterns of CoAl-LDH and CoAl-LDH NR are the same. The diffraction peaks at 11.7°, 23.5°, 34.5°, 39.3°, 46.8°, 60.3°and 61.6°are ascribed to the (003), (006), (012), (015), (018), (110) and (113) planes typical of hydrotalcite-like CoAl-LDH.[43] The basal plane spacing around 7.5 Å calculated from the (003) reflection indicates the intercalation of CO_3^{2-} ions into the interlayer space. The XRD pattern of CoAl-LDH NR/prGOAMs exhibits additionally a wide peak at 26°corresponding to the (002) plane of graphite oxide, whose position indicates that the oxygen-containing groups in the structure were mostly removed. The pronounced width of the peak is attributed to a turbostratic arrangement of graphene stacked sheets.[44] As revealed by Figure 4.7b, the 2θ position of the (003) diffraction peak is downward shifted (from 11.7° in the pure LDH samples to 11.4°in the composite with GO AMs), which corresponds to a larger spacing of the basal planes of CoAl-LDHs (from 0.75 to 0.77 nm).

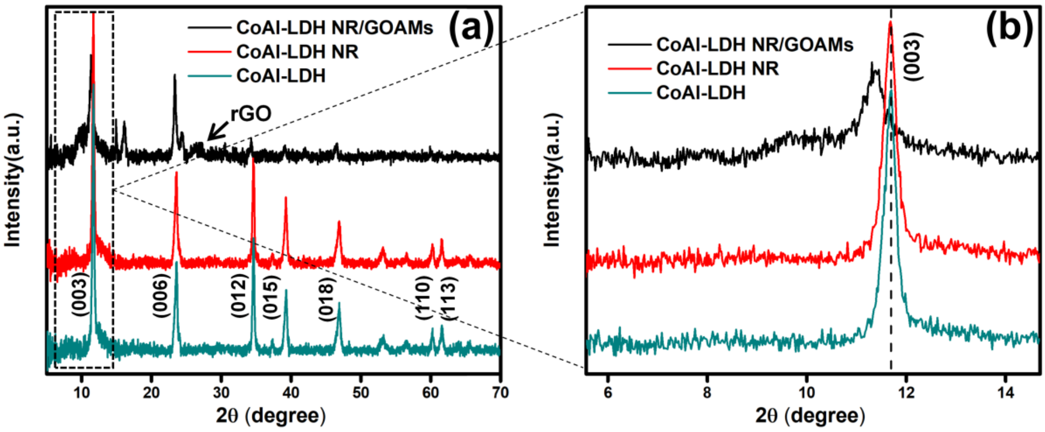

Figure 4.7 XRD pattern of CoAl-LDH, CoAl-LDH NR, CoAl-LDH NR/GOAMs and CoAl-LDH NR/prGOAMs.

The photoemission spectra of the C 1s, O 1s and Co 2p present in CoAl-LDH NR/prGOAMs and Co 2p presents in CoAl-LDH NR are presented in Figure 4.8, respectively. Figure 4.8a shows the BE energy region of the C 1s core level for CoAl-LDH NR/prGOAMs: different chemical species can be identified, i.e. C sp^2 at a BE of 284.2 eV, C sp^3 at 285.5 eV, C-O (epoxides and alcohols) at 286.5 eV, C=O (carbonyls) at 288.0 eV, HO-C=O (carboxyls) at 289.8 eV and the π-π* satellite at 290.8 eV. The observed relative intensity among the components suggests that the GO sheets have been substantially reduced during the thermal treatment. In the Co 2p spectrum (Figure 4.8d), the two deconvoluted peaks at 785.2 and 780.2 eV in the Co $2p_{3/2}$ region of CoAl-LDH NR can be ascribed to Co^{2+} and Co^{3+} ions in an octahedral environment, respectively.[45] Besides, two shake-up satellite peaks are present at 791.3 eV and 806 eV.[46] It is noteworthy that the Co $2p_{3/2}$ peak of CoAl-LDH NR/prGOAMs (Figure 4.8c) is shifted towards higher binding energy with respect to pure CoAl-LDH NR, suggesting that in the composite the LDH nanoring are slightly more oxidized.[47] This is also confirmed by the intensity ratio between the $Co^{2+}$and Co^{3+} components, which is higher in CoAl-LDH NR than in CoAl-LDH NR/prGOAMs. Previous works have pointed out that a lower ratio of Co^{2+}/Co^{3+} can improve the OER activity by producing active intermediates.[48] The Al 2p core level is not reported because it overlaps significantly with the Co 3s core level, so no significant information can be obtained. In any case, as confirmed by a large body of literature in all types of LDHs, Aluminum ions are redox innocent and always present as Al^{3+} either as hydroxides or oxides.[49] Finally, the O 1s photoemission spectrum of CoAl-LDH NR/prGOAMs in Figure 4.8b shows chemically shifted components centered at 530.8, 531.6, 532.8 and 534.2 eV, which are ascribed to metal-O, O-H, C-O bonds and chemisorbed water respectively.[50,51]

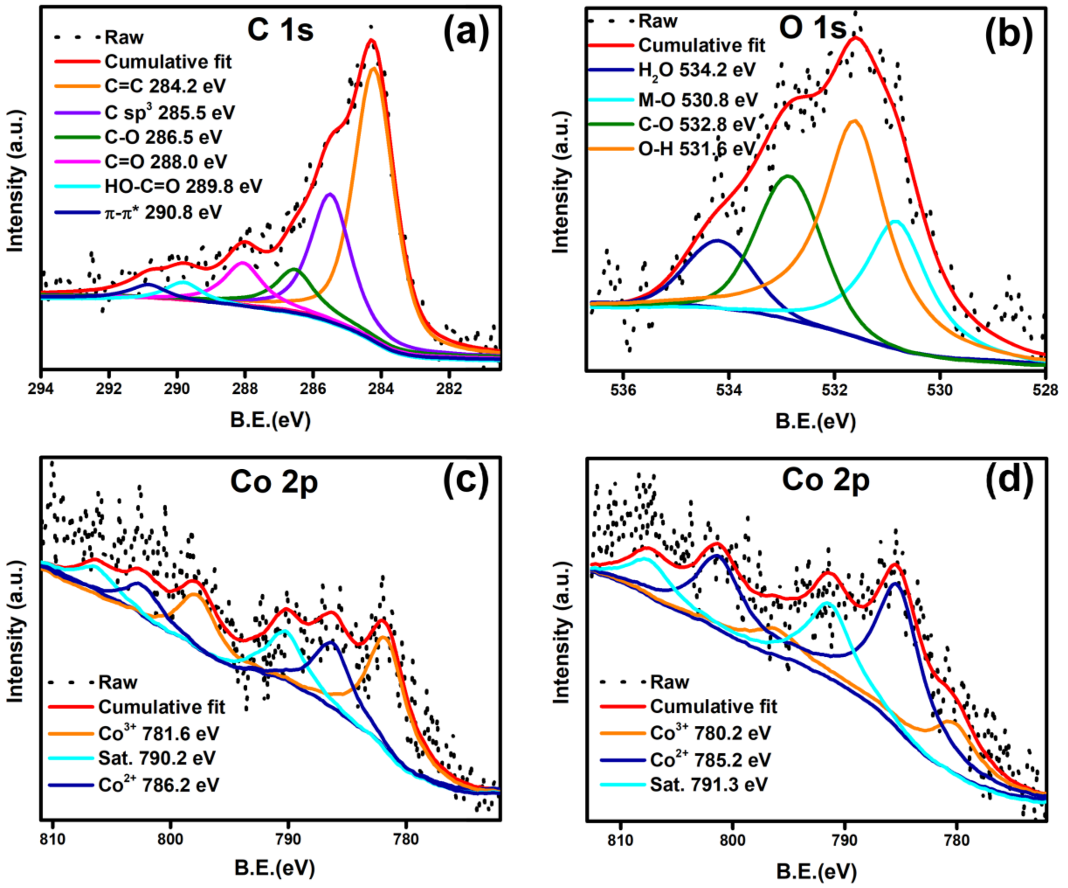

Figure 4.8 XPS data of the C 1s (a), O 1s (b) and Co 2p regions of CoAl-LDH NR/prGOAMs; Co 2p (d) region of CoAl-LDH NR, where the different fitted components are outlined.

4.3.2. Electrocatalytic HER Characterization

OER electrocatalytic characterization. The activity of CoAl-LDHs in the OER is well known, however the intrinsically scarce electron conductivity of these materials hinder their practical applications. The need to achieve large currents requires the use of a high loading of catalysts at the electrode in order to increase the number of active sites, however this also determines on the one hand the increase of the electrical resistance and also the restacking of the LDH setting a limit to the number of active sites effectively exposed. In the following by the comparison of different composite materials we will elucidate how the morphology of the LDH nanosheets and the structure of the supporting carbon scaffold affect the electrochemical performances. To this aim, Figure 4.9 reports the LSV curves in alkaline conditions (pH 13, 0.1 M KOH) in the potential window relevant for water oxidation of all the samples investigated in this study: i.e. CoAl-LDH and CoAl-LDH NR physically mixed with Vulcan carbon black powder, CoAl-LDH/GOAMs, CoAl-LDH/prGOAMs (200℃) (i.e treated in oven at 200 ℃ in inert atmosphere), CoAl-LDH NR/GOAMs, CoAl-LDH NR/prGOAMs (200 ℃) and CoAl-LDH NR/prGOAMs (400 ℃). The CoAl-LDH NR/GOAMs treated in oven at 400 ℃ in inert atmosphere is used as a comparison sample because GO can be reduced better at this temperature, but the LDH with carbonate as interlayer anion, at temperatures of 400-800 ℃ is converted to the simple single oxides or mixed spinel phase.[52] The CoAl-LDH NR/prGOAMs (200 ℃) sample clearly exhibits the best OER activity with an overpotential necessary to reach a current density of 10 mA cm^{-2} of 300 mV, whereas CoAl-LDH and CoAl-LDH NR physically mixed with Vulcan carbon black powder have a η_{10} of 500 mV and 380 mV, respectively. The unreduced samples, CoAl-LDH/GOAMs and CoAl-LDH NR/GOAMs have the worst activity (η_{10} of 540 mV and 480 mV respectively). Moreover, LDHs with nanoring morphology perform better than pristine materials with flake-like hexagonal morphology (e.g. the η_{10} of CoAl-LDH/prGOAMs 200℃ is 370 mV vs 300 mV for CoAl-LDH NR/prGOAMs) and samples annealed at 400℃, are less active than s ample annealed at 200℃ (see for example the η_{10} of 400 mV for CoAl-LDH NR/prGOAMs annealed at 400℃).

The OER kinetics of each sample was further analyzed by Tafel plots, as shown in Figure 4.9b. The CoAl-LDH/prGOAMs (200 ℃) exhibits a Tafel slope of 58 mV/dec, which is lower than that of CoAl-LDH and CoAl-LDH NR physically mixed with Vulcan carbon black powder (100 and 72 mV/dec, respectively), CoAl-LDH/GOAMs (100 mV/dec) CoAl-LDH/prGOAMs (200 ℃) (70 mV/dec), CoAl-LDH NR/GOAMs (93 mV/dec) and CoAl-LDH NR/prGOAMs (60 mV/dec).

Finally, given its importance for practical applications, the long-term stability of the samples under OER working conditions was investigated by chronopotentiometric measurements. Figure 4.9d shows the V-t curves of the CoAl-LDH/prGOAMs (200 ℃) sample: notably, at the end of the durability test not only we did not observed any deactivation, on the contrary an increase of the catalytic activity. Actually, the CoAl-LDH/prGOAMs (200℃) sample exhibits an outstanding η_{10} of 270 mV. The superior activity of CoAl-LDH/prGOAMs (200 ℃) compared to the other samples can be attributed to the following reasons: firstly, the nanoring structure of CoAl-LDH NRs provides a larger number of catalytically active sites for the electrochemical OER; secondly, the peculiar centre-diverging mesoporous structure of the prGOAMs allows an easy access of the electrolyte and fast removal of the produced gas to/from the active phase, finally the interconnected reduced graphene network facilitates a fast electron transport. The reason for the scarcer activity of the materials treated at 400℃ on the other hand is likely connected to the limi ted stability of LDH, which above 250℃ tend to be converted into more stable oxides, which typically are catalytically less active.[53]

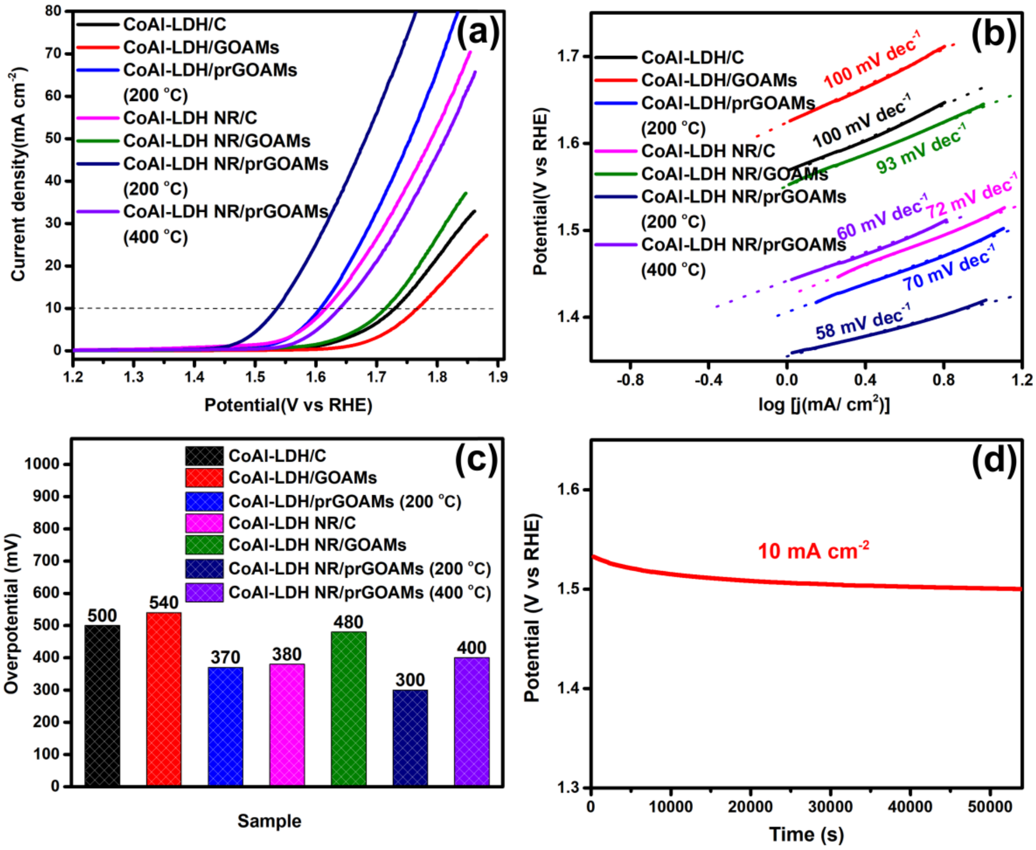

Figure 4.9 (a and b) Polarization curves and Tafel plots in 0.1 M KOH for CoAl-LDH, CoAl-LDH/GOAMs, CoAl-LDH/prGOAMs (200 ℃), CoAl-LDH NR, CoAl-LDH NR/GOAMs, CoAl-LDH NR/prGOAMs (200 ℃) and CoAl-LDH NR/prGOAMs (200 ℃); (c) The OER overpotentials at a current density of 10 mA cm^{-2}; (d) Chronopotentiometric tests of CoAl-LDH/prGOAMs (200 ℃) at a constant current density of 10 mA cm^{-2} for 15 h in 0.1 M KOH.

4.4 Conclusion

In conclusion, we have demonstrated the successful fabrication of CoAl-LDH NR decorated carbon 3D architectures with blowball morphology through a facile one-pot method starting from pre-formed nanosheets of GO and LDH NR, which combines electrospraying and in-situ freeze-drying. The material, CoAl-LDH NR/prGOAMs (200 ℃), achieved an excellent performance in alkaline conditions, where an η_{10} of 270 mV was achieved after 15 h of continuous electrolysis.

The mechanism of activation is not clear yet: it is possible that in the alkaline environment further Al^{3+} ions are etched exposing additional catalytic sites, however microscopic measurements after the electrochemistry are problematic because of the presence of the many components (especially Nafion) present in the ink formulation. Anyway, in the literature it is not reported any similar activation mechanism for CoAl-LDHs even though, our synthesis protocols of the nanorings would support the possibility of continuous etching.

Another possibility is that it takes time for the electrolyte to fully permeate inside the catalytic ink, in particular inside the smallest pores of the carbon support; an enhanced permeation with time would be also favoured by the progressive oxidation of carbon during OER conditions, which makes the surface more hydrophilic. So we can expect that as a function of time there is progressive increase of the effective electrochemical surface area, with consequent improvement of the catalytic performance.

The OER performance of the CoAl-LDH NR/prGOAMs catalyst compares very favourably to those observed for other cobalt oxides and LDH catalysts, e.g. Co-CoO_x/N-C NSAs (η_{10} 278 mV, 71.5 mV dec^{-1}),[54] $MoSe_2$-$CoSe_2$@CoAl-LDH (η_{10} 320 mV, 71mV dec^{-1}),[55] CoFe LDH/rGO (η_{10} 325 mV, 43 mV dec^{-1}),[56] NiCo LDH (η_{10} 290 mV, 113 mV dec^{-1}) [57] and CoMn LDH (η_{10} 324 mV, 43 mV dec^{-1}).[58] Although the OER performance of NiFeRu LDH/Ni foam (η_{10} 225 mV, 32.4 mV dec^{-1}) [53] and NiFe LDH/N-rGO (η_{10} 258 mV, 63 mV dec^{-1}) [59] are better than CoAl-LDH NR/prGOAMs, due to the use of expensive supports such as Nickel foams, the mass activity of NiFeRu LDH/Ni foam (8.3 mA/mg) [53] and NiFe LDH/N-rGO (27.8 mA/mg) [59] are much lower than ours (50 mA/mg) (see Table 4.1).

The reason of such high activity can be traced back on the one hand to the special dandelion morphology of the carbon scaffold, and on the other hand to the presence of nanoring structure of CoAl-LDH NR, which assists the dissociation of water in the step of the OER. This new type of nanocomposite catalysts could replace expensive catalysts such as Ru and Ir for the oxidative half reaction of water splitting. More importantly and significantly, the current synthesis route is rather simple fast and unexpensive therefore very suited for the preparation of large area electrodes for practical applications.

Table 4.1 Comparison of OER activity data and mass activity for several literature data closely related to the present paper.

Catalyst	**η_{10}(mV)**	**Tafel slope (mV/dec)**	**Mass activity (mA/mg)**	**Electrode**	**Ref.**
CoAl-LDH NR/prGOAMs	270	58	41	CC [1]	This work
Co-CoO$_x$/N-C NSAs	278	71.5	21.7	CC	[54]
MoSe$_2$-CoSe$_2$@CoAl-LDH	320	71	17.5	GC [2]	[55]
CoFe LDH/rGO	325	43	49	GC	[56]
Fe$_1$ Co$_1$ -ONS	350	36.8	27.7	GC	[60]
NiFeRu LDH/Ni foam	225	32.4	8.3	NF [3]	[53]
NiCo LDH	290	113	5.7	NF	[57]
NiCo LDH NA/CFP	307	64	12.5	CFP [4]	[61]
Exfoliated NiCo LDH	367	40	58.8	CFP	[62]
CoNi LDH/CoO	300	123	37.7	GC	[63]

NiFe LDH/N-rGO	258	63	27.8	NF	[59]
Ni$_3$ FeAl$_{0.91}$ LDH/Ni foam	304	57	20	--	[64]
CoMn LDH	324	43	70	GC	[58]
Co$_5$ Mn LDH/MWCNT	300	73.6	35	GC	[65]

Type of electrode: [1]Carbon cloth, [2]Glassy carbon, [3]Nickel foam, [4]Carbon fiber paper.

References

(1) Cui, X.; Gao, L.; Lei, S.; Liang, S.; Zhang, J.; Sewell, C. D.; Xue, W.; Liu, Q.; Lin, Z.; Yang, Y. Simultaneously Crafting Single-Atomic Fe Sites and Graphitic Layer-Wrapped Fe3C Nanoparticles Encapsulated within Mesoporous Carbon Tubes for Oxygen Reduction. *Adv. Funct. Mater.* **2021**, *31* (10), 1–9. https://doi.org/10.1002/adfm.202009197.

(2) Jiao, Y.; Zheng, Y.; Jaroniec, M.; Qiao, S. Z. Design of Electrocatalysts for Oxygen- and Hydrogen-Involving Energy Conversion Reactions. *Chem. Soc. Rev.* **2015**, *44* (8), 2060–2086. https://doi.org/10.1039/c4cs00470a.

(3) Faber, M. S.; Jin, S. Earth-Abundant Inorganic Electrocatalysts and Their Nanostructures for Energy Conversion Applications. *Energy Environ. Sci.* **2014**, *7* (11), 3519–3542. https://doi.org/10.1039/c4ee01760a.

(4) Shi, Q.; Zhu, C.; Du, D.; Lin, Y. Robust Noble Metal-Based Electrocatalysts for Oxygen Evolution Reaction. *Chem. Soc. Rev.* **2019**, *48* (12), 3181–3192. https://doi.org/10.1039/c8cs00671g.

(5) Song, F.; Bai, L.; Moysiadou, A.; Lee, S.; Hu, C.; Liardet, L.; Hu, X. Transition Metal Oxides as Electrocatalysts for the Oxygen Evolution Reaction in Alkaline Solutions: An Application-Inspired Renaissance. *J. Am. Chem. Soc.* **2018**, *140* (25), 7748–7759. https://doi.org/10.1021/jacs.8b04546.

(6) Morales, D. M.; Kazakova, M. A.; Dieckhöfer, S.; Selyutin, A. G.; Golubtsov, G. V.; Schuhmann, W.; Masa, J. Trimetallic Mn-Fe-Ni Oxide Nanoparticles Supported on Multi-Walled Carbon Nanotubes as High-Performance Bifunctional ORR/OER Electrocatalyst in Alkaline Media. *Adv. Funct. Mater.* **2020**, *30* (6), 1–12. https://doi.org/10.1002/adfm.201905992.

(7) Jiang, J.; Lu, S.; Wang, W. K.; Huang, G. X.; Huang, B. C.; Zhang, F.; Zhang, Y. J.; Yu, H. Q. Ultrahigh Electrocatalytic Oxygen Evolution by Iron-Nickel Sulfide Nanosheets/Reduced Graphene Oxide Nanohybrids with an Optimized Autoxidation Process. *Nano Energy* **2018**, *43* (November 2017), 300–309. https://doi.org/10.1016/j.nanoen.2017.11.049.

(8) Wang, Y.; Ge, Z.; Li, X.; Zhao, J.; Ma, B.; Chen, Y. Cu2S Nanorod Arrays with Coarse Surfaces to Enhance the Electrochemically Active Surface Area for Water Oxidation. *J. Colloid Interface Sci.* **2020**, *567*, 308–315. https://doi.org/10.1016/j.jcis.2020.02.030.

(9) Chen, Y.; Ren, Z.; Fu, H.; Zhang, X.; Tian, G.; Fu, H. NiSe-Ni0.85Se Heterostructure Nanoflake Arrays on Carbon Paper as Efficient Electrocatalysts for Overall Water Splitting. *Small* **2018**, *14* (25), 1–10. https://doi.org/10.1002/smll.201800763.

(10) Lin, L.; Chen, M.; Wu, L. Hierarchical Iron-Doped Nickel Diselenide Hollow Spheres for Efficient Oxygen Evolution Electrocatalysis. *ACS Appl. Energy Mater.* **2019**, *2* (7), 4737–4744. https://doi.org/10.1021/acsaem.9b00337.

(11) Xi, W.; Yan, G.; Lang, Z.; Ma, Y.; Tan, H.; Zhu, H.; Wang, Y.; Li, Y. Oxygen-Doped Nickel Iron Phosphide Nanocube Arrays Grown on Ni Foam for Oxygen Evolution Electrocatalysis. *Small* **2018**, *14* (42), 1–11. https://doi.org/10.1002/smll.201802204.

(12) Li, Y.; Zhao, C. Iron-Doped Nickel Phosphate as Synergistic Electrocatalyst for Water Oxidation. *Chem. Mater.* **2016**, *28* (16), 5659–5666. https://doi.org/10.1021/acs.chemmater.6b01522.

(13) Liang, H.; Lin, J.; Jia, H.; Chen, S.; Qi, J.; Cao, J.; Lin, T.; Fei, W.; Feng, J. Hierarchical NiCo-LDH@NiOOH Core-Shell Heterostructure on Carbon Fiber Cloth as Battery-like Electrode for Supercapacitor. *J. Power Sources* **2018**, *378* (November 2017), 248–254. https://doi.org/10.1016/j.jpowsour.2017.12.046.

(14) Zhou, J. J.; Li, Q.; Chen, C.; Li, Y. L.; Tao, K.; Han, L. Co3O4@CoNi-LDH Core/Shell Nanosheet Arrays for High-Performance Battery-Type Supercapacitors. *Chem. Eng. J.* **2018**, *350* (April), 551–558. https://doi.org/10.1016/j.cej.2018.06.023.

(15) Su, D.; Tang, Z.; Xie, J.; Bian, Z.; Zhang, J.; Yang, D.; Zhang, D.; Wang, J.; Liu, Y.; Yuan, A.; Kong, Q. Co, Mn-LDH Nanoneedle Arrays Grown on Ni Foam for High Performance Supercapacitors. *Appl. Surf. Sci.* **2019**, *469* (November 2018), 487–494. https://doi.org/10.1016/j.apsusc.2018.10.276.

(16) Chen, S.; Wu, Z.; Luo, J.; Han, X.; Wang, J.; Deng, Q.; Zeng, Z.; Deng, S. Constructing Layered Double Hydroxide Fences onto Porous Carbons as High-Performance Cathodes for Lithium–Sulfur Batteries. *Electrochim. Acta* **2019**, *312*, 109–118. https://doi.org/10.1016/j.electacta.2019.04.113.

(17) Tian, M.; Liu, C.; Neale, Z. G.; Zheng, J.; Long, D.; Cao, G. Chemically Bonding NiFe-LDH Nanosheets on RGO for Superior Lithium-Ion Capacitors. *ACS Appl. Mater. Interfaces* **2019**, *11* (39), 35977–35986. https://doi.org/10.1021/acsami.9b10719.

(18) Chen, S.; Han, X.; Luo, J.; Liao, J.; Wang, J.; Deng, Q.; Zeng, Z.; Deng, S. In Situ Transformation of LDH into Hollow Cobalt-Embedded and N-Doped Carbonaceous Microflowers as Polysulfide Mediator for Lithium-Sulfur Batteries. *Chem. Eng. J.* **2020**, *385* (September 2019), 123457. https://doi.org/10.1016/j.cej.2019.123457.

(19) He, K.; Tadesse Tsega, T.; Liu, X.; Zai, J.; Li, X. H.; Liu, X.; Li, W.; Ali, N.; Qian, X. Utilizing the Space-Charge Region of the FeNi-LDH/CoP p-n Junction to Promote Performance in Oxygen Evolution Electrocatalysis. *Angew. Chemie - Int. Ed.* **2019**, *58* (34), 11903–11909. https://doi.org/10.1002/anie.201905281.

(20) Liu, Q.; Huang, J.; Zhao, Y.; Cao, L.; Li, K.; Zhang, N.; Yang, D.; Feng, L.; Feng, L. Tuning the Coupling Interface of Ultrathin Ni 3 S 2 @NiV-LDH Heterogeneous Nanosheet Electrocatalysts for Improved Overall Water Splitting. *Nanoscale* **2019**, *11* (18), 8855–8863. https://doi.org/10.1039/c9nr00658c.

(21) Li, R.; Liu, Y.; Li, H.; Zhang, M.; Lu, Y.; Zhang, L.; Xiao, J.; Boehm, F.; Yan, K. One-Step Synthesis of NiMn-Layered Double Hydroxide Nanosheets Efficient for Water Oxidation. *Small Methods* **2019**, *3* (1), 3–7. https://doi.org/10.1002/smtd.201800344.

(22) Han, X.; Lin, Z.; He, X.; Cui, L.; Lu, D. The Construction of Defective FeCo-LDHs by in-Situ Polyaniline Curved Strategy as a Desirable Bifunctional Electrocatalyst for OER and HER. *Int. J. Hydrogen Energy* **2020**, *45* (51),

26989–26999. https://doi.org/10.1016/j.ijhydene.2020.07.006.

(23) Zhao, Z.; Wu, H.; He, H.; Xu, X.; Jin, Y. A High-Performance Binary Ni-Co Hydroxide-Based Water Oxidation Electrode with Three-Dimensional Coaxial Nanotube Array Structure. *Adv. Funct. Mater.* **2014**, *24* (29), 4698–4705. https://doi.org/10.1002/adfm.201400118.

(24) Liu, Y.; Zhang, M.; Hu, D.; Li, R.; Hu, K.; Yan, K. Ar Plasma-Exfoliated Ultrathin NiCo-Layered Double Hydroxide Nanosheets for Enhanced Oxygen Evolution. *ACS Appl. Energy Mater.* **2019**, *2* (2), 1162–1168. https://doi.org/10.1021/acsaem.8b01717.

(25) Khan, S. B.; Khan, S. A.; Asiri, A. M. A Fascinating Combination of Co, Ni and Al Nanomaterial for Oxygen Evolution Reaction. *Appl. Surf. Sci.* **2016**, *370*, 445–451. https://doi.org/10.1016/j.apsusc.2016.02.062.

(26) Li, Z.; Shao, M.; Yang, Q.; Tang, Y.; Wei, M.; Evans, D. G.; Duan, X. Directed Synthesis of Carbon Nanotube Arrays Based on Layered Double Hydroxides toward Highly-Efficient Bifunctional Oxygen Electrocatalysis. *Nano Energy* **2017**, *37* (April), 98–107. https://doi.org/10.1016/j.nanoen.2017.05.016.

(27) Jing, C.; Liu, X.; Yao, H.; Yan, P.; Zhao, G.; Bai, X.; Dong, B.; Dong, F.; Li, S.; Zhang, Y. Phase and Morphology Evolution of CoAl LDH Nanosheets towards Advanced Supercapacitor Applications. *CrystEngComm* **2019**, *21* (33), 4934–4942. https://doi.org/10.1039/c9ce00905a.

(28) Wang, W.; Lu, Y.; Zhao, M.; Luo, R.; Yang, Y.; Peng, T.; Yan, H.; Liu, X.; Luo, Y. Controllable Tuning of Cobalt Nickel-Layered Double Hydroxide Arrays as Multifunctional Electrodes for Flexible Supercapattery Device and Oxygen Evolution Reaction. *ACS Nano* **2019**, *13* (10), 12206–12218. https://doi.org/10.1021/acsnano.9b06910.

(29) Deng, X.; Li, H.; Huang, J.; Li, Y. Controllable in Situ Growth of Amorphous MoSx Nanosheets on CoAl Layered Double Hydroxides for Efficient Oxygen Evolution Reaction. *Electrochem. commun.* **2020**, *110* (December 2019), 106634. https://doi.org/10.1016/j.elecom.2019.106634.

(30) Qiu, C.; Cai, F.; Wang, Y.; Liu, Y.; Wang, Q.; Zhao, C. 2-Methylimidazole Directed Ambient Synthesis of Zinc-Cobalt LDH Nanosheets for Efficient Oxygen Evolution Reaction. *J. Colloid Interface Sci.* **2020**, *565*, 351–359. https://doi.org/10.1016/j.jcis.2019.12.070.

(31) Han, J.; Zhang, J.; Wang, T.; Xiong, Q.; Wang, W.; Cao, L.; Dong, B. Zn Doped FeCo Layered Double Hydroxide Nanoneedle Arrays with Partial Amorphous Phase for Efficient Oxygen Evolution Reaction. *ACS Sustain. Chem. Eng.* **2019**, *7* (15), 13105–13114. https://doi.org/10.1021/acssuschemeng.9b02297.

(32) Yan, F.; Goedel, W. A. The Preparation of Mesoscopic Rings in Colloidal Crystal Templates. *Angew. Chemie - Int. Ed.* **2005**, *44* (14), 2084–2088. https://doi.org/10.1002/anie.200460584.

(33) Li, F.; Ding, Y.; Gao, P.; Xin, X.; Wang, Z. L. Single-Crystal Hexagonal Disks and Rings of ZnO: Low-Temperature, Large-Scale Synthesis and Growth Mechanism. *Angew. Chemie - Int. Ed.* **2004**, *43* (39), 5238–5242.

https://doi.org/10.1002/anie.200460783.

(34) Kong, X. Y.; Ding, Y.; Yang, R.; Wang, Z. L. Single-Crystal Nanorings Formed by Epitaxial Self-Coiling of Polar Nanobelts. *Science (80-.).* **2004**, *303* (5662), 1348–1351. https://doi.org/10.1126/science.1092356.

(35) Liu, B.; Zeng, H. C. Semiconductor Rings Fabricated by Self-Assembly of Nanocrystals. *J. Am. Chem. Soc.* **2005**, *127* (51), 18262–18268. https://doi.org/10.1021/ja055734w.

(36) Zhou, D.; Zhang, Q.; Wang, S.; Jia, Y.; Liu, W.; Duan, H.; Sun, X. Hollow-Structured Layered Double Hydroxide: Structure Evolution Induced by Gradient Composition. *Inorg. Chem.* **2020**, *59* (3), 1804–1809. https://doi.org/10.1021/acs.inorgchem.9b03005.

(37) Song, F.; Hu, X. Exfoliation of Layered Double Hydroxides for Enhanced Oxygen Evolution Catalysis. *Nat. Commun.* **2014**, *5*. https://doi.org/10.1038/ncomms5477.

(38) Ma, W.; Ma, R.; Wang, C.; Liang, J.; Liu, X.; Zhou, K.; Sasaki, T. A Superlattice of Alternately Stacked Ni-Fe Hydroxide Nanosheets and Graphene for Efficient Splitting of Water. *ACS Nano* **2015**, *9* (2), 1977–1984. https://doi.org/10.1021/nn5069836.

(39) Chen, S.; Duan, J.; Jaroniec, M.; Qiao, S. Z. Three-Dimensional N-Doped Graphene Hydrogel/NiCo Double Hydroxide Electrocatalysts for Highly Efficient Oxygen Evolution. *Angew. Chemie - Int. Ed.* **2013**, *52* (51), 13567–13570. https://doi.org/10.1002/anie.201306166.

(40) Liao, S.; Zhai, T.; Xia, H. Highly Adsorptive Graphene Aerogel Microspheres with Center-Diverging Microchannel Structures. *J. Mater. Chem. A* **2016**, *4* (3), 1068–1077. https://doi.org/10.1039/c5ta09540a.

(41) Tronto, J., Bordonal, A. C., Naal, Z., & Valim, J. B. *Conducting Polymers/Layered Double Hydroxides Intercalated Nanocomposites*; 2013.

(42) Tao, Y.; Kanoh, H.; Abrams, L.; Kaneko, K. Mesopore-Modified Zeolites : Preparation , Characterization , and Applications. **2006**, 896–910.

(43) Hu, R.; Qiu, H.; Zhang, H.; Wang, P.; Du, X.; Ma, J.; Wu, T.; Lu, C.; Zhou, X.; Cui, G. A Polymer-Reinforced SEI Layer Induced by a Cyclic Carbonate-Based Polymer Electrolyte Boosting 4.45 V LiCoO2/Li Metal Batteries. *Small* **2020**, *16* (13), 1–8. https://doi.org/10.1002/smll.201907163.

(44) Bourlinos, A. B.; Gournis, D.; Petridis, D.; Szabó, T.; Szeri, A.; Dékány, I. Graphite Oxide: Chemical Reduction to Graphite and Surface Modification with Primary Aliphatic Amines and Amino Acids. *Langmuir* **2003**, *19* (15), 6050–6055. https://doi.org/10.1021/la026525h.

(45) Yu, C.; Cao, Z.; Chen, S.; Wang, S.; Zhong, H.; Ma, X. In Situ Selenylation of Molybdate Ion Intercalated Co-Al Layered Double Hydrotalcite for High-Performance Electrocatalytic Oxygen Evolution Reaction. *J. Taiwan Inst. Chem. Eng.* **2021**, *119*, 166–176. https://doi.org/10.1016/j.jtice.2021.01.022.

(46) Li, J.; Zhou, Q.; Zhong, C.; Li, S.; Shen, Z.; Pu, J.; Liu, J.; Zhou, Y.; Zhang, H.; Ma, H. (Co/Fe)4O4 Cubane-Containing Nanorings Fabricated by Phosphorylating Cobalt Ferrite for Highly Efficient Oxygen Evolution

Reaction. *ACS Catal.* **2019**, *9* (5), 3878–3887. https://doi.org/10.1021/acscatal.9b00293.

(47) Gang, C.; Chen, J.; Chen, Q.; Chen, Y. Heterostructure of Ultrafine FeOOH Nanodots Supported on CoAl-Layered Double Hydroxide Nanosheets as Highly Efficient Electrocatalyst for Water Oxidation. *J. Colloid Interface Sci.* **2021**, *600*, 594–601. https://doi.org/10.1016/j.jcis.2021.05.041.

(48) Zhou, J.; Zheng, H.; Luan, Q.; Huang, X.; Li, Y.; Xi, Z.; Lu, G.; Xing, L.; Li, Y. Improving the Oxygen Evolution Activity of Co3O4 by Introducing Ce Species Derived from Ce-Substituted ZIF-67. *Sustain. Energy Fuels* **2019**, *3* (11), 3201–3207. https://doi.org/10.1039/c9se00541b.

(49) Jin, Z.; Li, Y.; Ma, Q. CoAl LDH@Ni-MOF-74 S-Scheme Heterojunction for Efficient Hydrogen Evolution. *Trans. Tianjin Univ.* **2021**, *27* (2), 127–138. https://doi.org/10.1007/s12209-020-00269-1.

(50) Lim, C. S.; Chua, C. K.; Sofer, Z.; Klímová, K.; Boothroyd , C.; Pumera, M. Layered Transition Metal Oxyhydroxides as Tri-Functional Electrocatalysts. *J. Mater. Chem. A* **2015**, *3* (22), 11920–11929. https://doi.org/10.1039/c5ta02063h.

(51) Ding, Y.; Zhao, J.; Zhang, W.; Zhang, J.; Chen, X.; Yang, F.; Zhang, X. Single-Walled Carbon Nanotubes Wrapped CoFe2O4 Nanorods with Enriched Oxygen Vacancies for Efficient Overall Water Splitting. *ACS Appl. Energy Mater.* **2019**, *2* (2), 1026–1032. https://doi.org/10.1021/acsaem.8b01338.

(52) Tianhu, C.; Huifang, X.; Yifeng, W.; Chengsong, Q.; Mingde, F.; Gang, C. Structural Evolvement of Heating Treatment of Mg/Al-LDH and Preparation of Mineral Mesoporous Materials. *Acta Geol. Sin. - English Ed.* **2010**, *80* (2), 170–174. https://doi.org/10.1111/j.1755-6724.2006.tb00226.x.

(53) Chen, G.; Wang, T.; Zhang, J.; Liu, P.; Sun, H.; Zhuang, X.; Chen, M.; Feng, X. Accelerated Hydrogen Evolution Kinetics on NiFe-Layered Double Hydroxide Electrocatalysts by Tailoring Water Dissociation Active Sites. *Adv. Mater.* **2018**, *30* (10). https://doi.org/10.1002/adma.201706279.

(54) Li, S.; Xie, W.; Song, Y.; Shao, M. Layered Double Hydroxide@Polydopamine Core-Shell Nanosheet Arrays-Derived Bifunctional Electrocatalyst for Efficient, Flexible, All-Solid-State Zinc-Air Battery. *ACS Sustain. Chem. Eng.* **2020**, *8* (1), 452–459. https://doi.org/10.1021/acssuschemeng.9b05754.

(55) Yu, C.; Cao, Z.; Chen, S.; Wang, S.; Zhong, H.; Ma, X. In Situ Selenylation of Molybdate Ion Intercalated Co-Al Layered Double Hydrotalcite for High-Performance Electrocatalytic Oxygen Evolution Reaction. *J. Taiwan Inst. Chem. Eng.* **2021**, *119*, 166–176. https://doi.org/10.1016/j.jtice.2021.01.022.

(56) Han, X.; Yu, C.; Yang, J.; Zhao, C.; Huang, H.; Liu, Z.; Ajayan, P. M.; Qiu, J. Mass and Charge Transfer Coenhanced Oxygen Evolution Behaviors in CoFe-Layered Double Hydroxide Assembled on Graphene. *Advanced Materials Interfaces*. 2016. https://doi.org/10.1002/admi.201500782.

(57) Jiang, J.; Zhang, A.; Li, L.; Ai, L. Nickel–Cobalt Layered Double Hydroxide Nanosheets as High-Performance Electrocatalyst for Oxygen Evolution Reaction. *J. Power Sources* **2015**, *278*, 445–451.

https://doi.org/10.1016/j.jpowsour.2014.12.085.

(58) Song, F.; Hu, X. Ultrathin Cobalt–Manganese Layered Double Hydroxide Is an Efficient Oxygen Evolution Catalyst. *J. Am. Chem. Soc.* **2014**, *136* (47), 16481–16484. https://doi.org/10.1021/ja5096733.

(59) Zhan, T.; Liu, X.; Lu, S. S.; Hou, W. Nitrogen Doped NiFe Layered Double Hydroxide/Reduced Graphene Oxide Mesoporous Nanosphere as an Effective Bifunctional Electrocatalyst for Oxygen Reduction and Evolution Reactions. *Applied Catalysis B: Environmental*. 2017, pp 551–558. https://doi.org/10.1016/j.apcatb.2017.01.010.

(60) Zhuang, L.; Ge, L.; Yang, Y.; Li, M.; Jia, Y.; Yao, X.; Zhu, Z. Ultrathin Iron-Cobalt Oxide Nanosheets with Abundant Oxygen Vacancies for the Oxygen Evolution Reaction. *Adv. Mater.* **2017**, *29* (17), 1606793. https://doi.org/10.1002/adma.201606793.

(61) Yu, C.; Liu, Z.; Han, X.; Huang, H.; Zhao, C.; Yang, J.; Qiu, J. NiCo-Layered Double Hydroxides Vertically Assembled on Carbon Fiber Papers as Binder-Free High-Active Electrocatalysts for Water Oxidation. *Carbon N. Y.* **2016**, *110*, 1–7. https://doi.org/10.1016/j.carbon.2016.08.020.

(62) Liang, H.; Meng, F.; Cabán-Acevedo, M.; Li, L.; Forticaux, A.; Xiu, L.; Wang, Z.; Jin, S. Hydrothermal Continuous Flow Synthesis and Exfoliation of NiCo Layered Double Hydroxide Nanosheets for Enhanced Oxygen Evolution Catalysis. *Nano Lett.* **2015**, *15* (2), 1421–1427. https://doi.org/10.1021/nl504872s.

(63) Wu, J.; Ren, Z.; Du, S.; Kong, L.; Liu, B.; Xi, W.; Zhu, J.; Fu, H. A Highly Active Oxygen Evolution Electrocatalyst: Ultrathin CoNi Double Hydroxide/CoO Nanosheets Synthesized via Interface-Directed Assembly. *Nano Research*. 2016, pp 713–725. https://doi.org/10.1007/s12274-015-0950-4.

(64) Liu, H.; Wang, Y.; Lu, X.; Hu, Y.; Zhu, G.; Chen, R.; Ma, L.; Zhu, H.; Tie, Z.; Liu, J.; Jin, Z. The Effects of Al Substitution and Partial Dissolution on Ultrathin NiFeAl Trinary Layered Double Hydroxide Nanosheets for Oxygen Evolution Reaction in Alkaline Solution. *Nano Energy* **2017**, *35*, 350–357. https://doi.org/10.1016/j.nanoen.2017.04.011.

(65) Jia, G.; Hu, Y.; Qian, Q.; Yao, Y.; Zhang, S.; Li, Z.; Zou, Z. Formation of Hierarchical Structure Composed of (Co/Ni)Mn-LDH Nanosheets on MWCNT Backbones for Efficient Electrocatalytic Water Oxidation. *ACS Appl. Mater. Interfaces* **2016**, *8* (23), 14527–14534. https://doi.org/10.1021/acsami.6b02733.

Chapter 5

Conclusion

Conclusions and futures perspectives

In this thesis, we have rationally designed and synthesized in high yield special 3D graphene nanoarchitectures to be used as advanced supports for heterogeneous catalysis. The most notable features of these nanomaterials is their spherical morphology with diameter ranging from 100 to >500 µm associated with the presence of center diverging nanochannels. These materials have fairly large surface area (up to almost 200 m^2/g) and present both micro and mesopores. This type of structures has been formed by combining electrospraying and freeze drying starting from GO suspensions; however a thermal treatment after synthesis is needed in order to consolidate their mechanical stability. Actually, the formation of such peculiar *blowball* morphology is driven by the self-assembly of GO sheets that are pushed together by rapidly growing ice crystals during the freezing step. Once the ice is removed by lyophilization, the GO sheets are kept together by hydrogen bonds and dispersive interactions. However, these rather weak and somehow labile interactions can be replaced by covalent bonds after a mild thermal annealing that promotes condensation and crosslinking reactions. This synthesis method is extremely robust, so the ice-templating step that prominently impart the spherical morphology and formation of microchannels is little sensitive to the nature of chemical compound in the precursor solution.

Actually, we have demonstrated that it is possible to create nanocomposites with the same microsphere morphology simply by adding other nanosheets besides GO to the precursor solution. In this way, we have obtained GOAMs loaded with a variety of other 2D materials such as TMDCs (MoS_2, WS_2, $MoSe_2$, etc), LDHs and MXenes.[1,2] It has to be remembered however, that the ratio between the amount of GO and of the other type of nanosheets must be carefully tuned. Actually, it is the GO with its polar surface groups, poised for hydrogen bonds and dispersive interactions, which is essential to form a mechanically stable framework.

On the other hand, as detailed reported in the third chapter of this thesis, we have also proposed an even more versatile route that is based on a *fully bottom-up* approach. In this case the second phase was assembled starting from molecular species directly present in the initial GO suspension.

As an exemplary case, we have prepared advanced nanocomposites made up by mesoporous graphene oxide microspheres with usual morphology that were decorated by nickel doped molybdenum oxysulfide nanoparticles.

At first sight, this system may seem overly complicated because it combines a control of morphology from the nano to the mesoscale and a fine tuning of the chemical composition down to single atom dopants. However, it could be prepared using a one pot strategy mixing a GO suspension with ATM and nickel chloride and then adopting the usual protocol made up by electrospraying, freeze drying and thermal treatment.

In this way, starting from cheap and easily available precursors (i.e. GO and simple soluble metal salts) it has been possible to produce in a fast and continuous matter a large quantity of materials of exquisite complexity. This is a quite unique and remarkable feature of such technique, which can be used to fill the gap between lab scale and industrially oriented production.

Quite interestingly, the stoichiometric ratio of the reactants in the precursor solution is maintained also in the final material allowing therefore a quite precise and simple control of the chemical properties of the final materials. This type of one-pot procedure can likely be extended to other doped TMDCs, but also other materials such as complex oxides (spinels or perovskites), carbides, metal alloys: potentially any material that can be obtained from the thermal treatment of a solid xerogel/aerogel phase, as it usually happens during the inorganic-sold gel routes (e.g. citrate method).

Actually it is still unexplored, but our synthesis protocol, since it already entails two steps of the sol-gel method (i.e. drying and firing), with due changes, could be adapted to prepare many materials usually synthesized through standard sol-gel method.

The common feature of the all composite materials presented in this thesis is the presence of a spherical morphology with center diverging channels. As discussed previously, the specific surface area is good, but not excellent (graphene aerogel with specific surface areas of almost 1000m^2/g have been reported and the nominally surface area of monolayer graphene is theoretically more than 2600 m^2/g). However, we reported that for some of the prepared composites, the specific surface area was higher than that of the analogous bare GOAMs, despite the high density of the second phase added. This suggests that there is still large room for the improvement of our GOAM scaffolds and the use of thinner GO stacks forming the framework structure could lead to material with improved surface area. Actually, very recently we have mixed GO sheets with phenyl diboronic acid in the precursor solution, which are known to easily bind to epoxy groups, in order to functionalize the GO surface with phenyl spacer to prevent the direct stacking of the sheets. Preliminary BET measurements indicated that this simple strategy is effective to increase the specific surface area, which almost double, while maintaining the *blowball* morphology.

The applications of GOAMs and their nanocomposites in this thesis have been focused mainly on electrochemistry. The reasons are quite simple: the chemical nature and interconnection of the carbon scaffold guarantees an efficient electron transport, while the presence of mesoporosity allows for a fast electrolyte transportation. These two factor are essential to develop electrodes capable to achieve high performances, namely high current, in electrocatalysis. In all the examples reported, both for the OER and HER, the prGOAMs based nanocomposites resulted to be better performing than other carbon supports. This has been proved by comparing the activity of other ink prepared using different sources of carbon (plain prGO sheets or Vulcan) or by grinding the GOAMs themselves destroying their microstructures. In all cases worse performance compared to prGOAMs has been reported. Notably, *post-mortem* characterization of the electrodes has shown that the *blowball* morphology is rather resistant in working conditions remaining unaltered after prolonged catalytic tests.

As extendedly reported in the previous chapters, the overall performances obtained by our materials are comparable to the best catalysts reported in the literature, if not always in absolute values of overpotential, but in term of mass activity. Actually, as evident for the characterization provided, the prGOAMs allow a very good distribution of the active phases allowing a very thrifty use.

Despite the already proved excellent performances, we can envisage that with further synthesis optimization, catalytic activity could be increased even more. Actually, we tried to keep as simple as possible the synthesis procedure; however, introducing further steps for the control of the surface properties of the carbon scaffold, additional properties such as (super)aerophilicity (useful for CO_2 reduction reaction or ORR) or aerophobicity (useful for OER and HER) [3-5] could be imparted. In the present protocol consisting of a single thermal treatment step, a compromise on the annealing temperature must be reached: a high temperature will lead to better electron conductivity, but on the other hand, to the partial collapse of the pores and to the formation of a highly hydrophobic surface preventing a good interaction with the electrolyte. Most probably, adding a surface functionalization step would allow to tune the surface properties of the GOAMs independently from the thermal treatment.

Further improvement of the materials could be obtained by playing with the initial GO sheets. Our choice of Hummer’s GO was based on practical convenience: nowadays GO suspensions are commercially available and getting cheaper and cheaper, therefore suitable for up-scaling. On the other hand, there is a wide range of chemically modified graphenes that could be used, first of all doped (nitrogen, sulfur, boron) graphenes, which are known to have improved physico-chemical properties (better electron conductivity, improved interaction with supported nanoparticles or electrolytic species etc…) and are known to have a catalytic activity on their own. Actually, the type of bifunctional mechanisms outlined in Chapter 3, which was so critical to boost the performances, can then be exploited by involving the carbon support as well.

Overall, low-cost, efficient and durable electrocatalysts for green hydrogen production by electrochemical water splitting are strategical for the transition towards renewable energy sources. Our work exemplifies the enormous potential of electrospray and freeze casting for the preparation of highly sophisticated electrocatalytic materials. This technique is extremely cheap and quick, very suitable to a rather fast and continuous production (e.g. hundreds of mg per hour of material produced with lab scale equipment, but easily transferred to industrial scale). However, these high productivity and cost effectiveness are not at the expenses of materials properties. We have shown that materials with exquisite complexity can already be prepared but there is still much to be done.

Finally, we want to mention that the type of nanocomposites presented in this thesis can also have quite interesting applications beyond electrochemistry.

Once again the special *blowball* morphology is the key. Previous works have demonstrated that GA can be used for water remediation, mainly using the carbon phases as an absorbent for pollutants. The special morphology would come in handy in more demanding applications such as filtration. Actually, in filtration is required a fast mass transport trough a stationary phase, which could be easily achieved through the numerous open ended microchannels that are distinctive of the GOAMs. In this case mechanical and chemical filtration could be combined in a single material. Furthermore, the possibility of imparting (photo)catalytic activity or selective chemical adsorption properties to the GOAMs by incorporating a second phase without perturbing the overall morphology would widen further the spectrum of applications.

As a further perspective we want to mention that so far no work has been devoted to the assembly of the GOAMs themselves. Given the synthesis protocol the microsperes are formed as single entities, completely detached one form the other.

However, in our experiments we noticed that the microspheres have actually amphiphilic properties and spontaneous assemble at the water/liquid or oil/water interfaces leading to the formation of thin film. Once suitable means for bonding to each other, it would be possible to create membranes and self-standing thin films or even monoliths further expanding the applications.

Reference

(1) Lunardon, M.; Ran, J.; Mosconi, D.; Marega, C.; Wang, Z.; Xia, H.; Agnoli, S.; Granozzi, G. Hybrid Transition Metal Dichalcogenide/Graphene Microspheres for Hydrogen Evolution Reaction. Nanomaterials 2020, 10 (12), 1 – 15.

(2) Cheng, Y.; Zhan, Y.; Ran, J. J.; Wang, Z.; Agnoli, S.; Xia, H.; Granozzi, G. Hybrid MXene/Reduced Graphene Oxide Aerogel Microspheres for Hydrogen Evolution Reaction. Ionics (Kiel). 2021, 27 (7), 3099 – 3108.

(3) Zhou, D.; Zhang, Q.; Wang, S.; Jia, Y.; Liu, W.; Duan, H.; Sun, X. Hollow-Structured Layered Double Hydroxide: Structure Evolution Induced by Gradient Composition. Inorg. Chem. 2020, 59 (3), 1804 – 1809.

(4) Zhou, D., Cai, Z., Lei, X., Tian, W., Bi, Y., Jia, Y., Sun, X., Duan, X. NiCoFe – layered double hydroxides/N – doped graphene oxide array colloid composite as an efficient bifunctional catalyst for oxygen electrocatalytic reactions. Adv. Energy Mater. 2018, 8(9), 1701905.

(5) Yuan, Z., Bak, S. M., Li, P., Jia, Y., Zheng, L., Zhou, Y., Cai, Z., Sun, X. Activating layered double hydroxide with multivacancies by memory effect for energy-efficient hydrogen production at neutral pH. ACS Energy Lett. 2019, 4(6), 1412-1418.

List of Publications

1. Marco Lunardon, **JiaJia Ran**, Dario Mosconi, Carla Marega, Zhanhua Wang, Hesheng Xia, Stefano Agnoli, Gaetano Granozzi*. Hybrid transition metal dichalcogenide/graphene microspheres for hydrogen evolution reaction[J] *Nanomaterials*, 2020, 10(12): 2376.

2. Yu Cheng, Yanhu Zhan, **JiaJia Ran**, Zhanhua Wang*, Stefano Agnoli, Hesheng Xia*, Gaetano Granozzi. Hybrid MXene/reduced graphene oxide aerogel microspheres for hydrogen evolution reaction[J] *Ionics*, 2021: 1-10.

3. Dario Mosconi, Matís Blanco, **JiaJia Ran**, Marco Sturaro, Marco Bersani*, Gaetano Granozzi. Selective and scaled-up continuous flow synthesis of manganese oxide nanocatalysts for single electron transfer reactions[J] *Chemical Engineering Journal*, 2021, 417: 129063.

4. **JiaJia Ran**, Leonardo Girardi, Zhanhua Wang, Stefano Agnoli*, Hesheng Xia and Gaetano Granozzi. The Effect of the 3D Nanoarchitecture and Ni-doping on the Hydrogen Evolution Reaction in MoS_2/reduced GO Aerogel Hybrid Microspheres produced by a simple one-pot electrospraying procedure. *Small*. (Submitted)

5. **JiaJia Ran**, Stefano Agnoli*, Gaetano Granozzi. When morphology boosts electrocatalytic activity: CoAl-Layered Double Hydroxide Nanorings supported on 3D Reduced Graphene Oxide Aerogel Microspheres. (Submit soon)

Acknowledgments

In the beautiful city of Padova, I spent an unforgettable three years of my life. Since COVID-19 (coronavirus) has been declared a global epidemic in 2020, our work and life have been greatly affected and changed. Here, I would like to first thank all the staff of the University of Padua for providing us with a relatively safe environment for experimentation and learning. In particular, thanks to frontline health workers for anti-epidemic.

In the past three years, I have gained knowledge and improved my research capabilities. At the end of my Ph.D, I would like to express my heartfelt thanks to everyone who has helped me.

Firstly, I would like to thank Prof. Agnoli, my supervisor, for his careful guidance over the past three years. His rigorous working attitude of excellence, the tireless pursuit of scientific research has profoundly affected me, and I have benefited all my life. In the past three years, my progress has been inseparable from his careful training and strict requirements. From determination of the project, the design of the experiment, the analysis of the data and writing of the thesis, his help is everywhere. At the same time, I would also like to sincerely thank Prof. Granozzi and thank him for the good scientific research platform he has provided for us and for the careful check of the thesis draft. It was my luck to join Granozzi's group. This thesis was also completed under the joint guidance of Prof. Agnoli and Prof. Granozzi, and I would like to express my sincere gratitude. In addition, I would also like to thank Prof. Laura Calvillo and Prof. Gian Andrea Rizzi.

Thanks to the members of the research group Panjuan Tang, Jijin Yang, Leonardo Girardi, Davide Salvò, Hongqing Liang, Claudio Cometto, Biagio Di Vizio, Giuliaalice Volpato, Marco Lunardon, Tomasz Kosmala, and Matias Blanco Fernandez. Thank you for your company and help. I am grateful to the China Scholarship Council for providing scholarships to give me the opportunity to study abroad.

Finally, I would like to thank my family for their continuous support and understanding, long-term commitment and waiting, selfless care and love, especially my father who is far away in heaven.